The relationship between biogenic silica diagenesis and the physical properties of sediments studied using seismic and well data

Raluca Cristina Neagu

Submitted in partial fulfilment of the requirements for the degree of Ph.D.

Cardiff University

- March 2011 -

UMI Number: U567215

UMI

Dissertation Publishing

ProQuest

DECLARATION

This work has not previously been accepted in substance for any degree and is not concurrently submitted in candidature for any degree.

Signed ....(candidate) Date................

STATEMENT 1:

This thesis is being submitted in partial fulfilment of the requirements for the degree of PhD.

Signed ....(candidate) Date................

STATEMENT 2:

This thesis is the result of my own independent work/investigation, except where otherwise stated. Other sources are acknowledged by explicit references.

Signed ....(candidate) Date................

STATEMENT 3:

I hereby give consent for my thesis, if accepted, to be available for photocopying and for inter-library loan, and for the title and summary to be made available to outside organisations.

Signed ....(candidate) Date................

Mamei mele

To my mother

Acknowledgements

TABLE OF CONTENTS

LIST OF FIGURES

LIST OF TABLES

ABSTRACT

By integrating seismic and well data, two major aspects of biogenic silica diagenesis are investigated: its role on the evolution of the physical properties of the sediments during burial and deformation and the temperature as a controlling factor of diagenesis, with implications on the 'fossilisation' of reaction fronts.

Selected scientific drill sites are examined in order to identify the silica diagenesis transition zones, characterised by important changes of the physical properties of the sediments. The criteria for the identification of these zones are proposed and the factors controlling their thickness are analysed. It is argued that some diagenetic transition zones are presently 'fossilised'.

The quantification of the magnitude of the porosity loss during silica diagenesis is done by using a novel technique based on 3 – D seismic data. It is demonstrated that the fault planes were passively rotated into shallower dips due to diagenesis, allowing the quantification of the vertical compaction strain. In addition, the impact of silica diagenesis on the fault growth is considered. Deviations from classical Mohr – Coulomb behaviour may be expected during diagenesis and associated porosity collapse, possibly sufficient to promote continued fault growth.

Three styles of deformation demonstrate that the opal –A to opal – CT reaction front in Norwegian Sea is 'fossilised'. The identification of the 'fossilisation' time is attempted by recognising the stratal surface concordant to the opal –A to opal – CT reflection, presumably the paleo – seabed when the reaction became inactive. The proposed causes are the change in the geothermal gradient or the presence of overpressure.

Chapter 1.
INTRODUCTION

1. INTRODUCTION

1.1. Rationale

Biogenic silica diagenesis represents the mineralogical alteration of biogenic opal – A to opal – CT (cristobalite and tridymite) and quartz, the stable mineralogical phase.

Biosiliceous sediments are a significant constituent of Neogene sediments around the world, therefore investigating the role of silica diagenesis on the evolution of sediment physical properties during burial and deformation is important for basin analysis. This is mainly because of the implications on fluid overpressure, fluid flow, and thermal evolution of sedimentary basins. From an economic perspective, the study of biogenic silica diagenesis is relevant because biosiliceous mudstones, porcelanites and cherts can represent significant hydrocarbon reservoirs (e.g. Monterey Formation, California) or shale – gas systems (e.g. Barnett Formation, Texas).

Silica diagenesis has been widely researched during the past four decades, largely stimulated by the Deep Sea Drilling Project (DSDP) (e.g. Pisciotto, 1981) and the Monterey Formation (e.g. Bramlette, 1946). The motivation for these studies was related to different aspects: on the one hand, the hard chert layers were an important drilling hazard for DSDP; on the other hand, the Monterey Formation presented an economic importance, its biosiliceous rocks representing the source rock and reservoir for almost all the oil in California. These studies have been mainly based on core, field or experimental data (e.g. Murata and Larson, 1975; Isaacs, 1981; Williams and Crerar, 1985; Williams et al., 1985; Hinman, 1990; Compton, 1991; Eichhubl and Boles, 2000). Less attention has been paid to the seismic expression of silica diagenesis, even though the remarkable changes in physical properties of the biosiliceous sediments during the diagenetic pathways commonly result in a prominent seismic reflection marking the silica diagenetic boundary (e.g. Lonsdale, 1990; Bohrmann et al., 1992; 1994; Davies and Cartwright, 2002; 2007).

More than 100 Ocean Drilling Program (ODP) and Deep Sea Drilling Project (DSDP) sites have drilled silica diagenesis boundaries around the globe. Since an inventory of these sites is not available, one of the aims of this thesis is to compile such a database, with the purpose of analysing the physical and chemical properties of the silica diagenesis transition zones. This is important because of the implications that the remarkable changes in physical properties over a narrow depth range have on sediment shear strength, compaction and fluid flow.

Of particular importance is the porosity contrast resulting from diagenesis, because it allows the quantification of compaction strain, which is an essential element in basin analysis. So far, small – scale methods have been employed to estimate compaction strains, e.g. from the deformation of bedding around nodules (Craig, 1987), or from ptygmatic folding of sandstone dykes (Parize and Beaudoin, 1988). On a slightly larger scale, differential compaction of isolated channel sand bodies encased in a muddier host lithology has also been used to infer vertical flattening strains (Hillier and Cosgrove, 2002). One of the aims of this research is to estimate the compaction strain due to diagenesis using a large – scale method based on the flattening of fault planes identified on 3 – D seismic data.

One of the most important outstanding questions in silica diagenesis research is the identification of 'active' and 'fossilised' diagenetic fronts. Due to the potential significance of recognising a 'fossilised' diagenetic front for a better understanding of the silica diagenetic process and thermal evolution of basins in which the opal – A to opal – CT reaction front is developed, it is important to develop a set of interpretational criteria to allow the distinction of a 'fossilised' reaction front from an active front.

The present study integrates seismic and well data to investigate two principal aspects of biogenic silica diagenesis: the physical properties changes across the diagenetic transition zone and the temperature as a controlling factor of diagenesis with implications on the 'fossilisation' of a reaction front.

The next section presents the overview of the literature covering the topics presented this thesis, followed by the statement of the aims of this study.

1.2. Overview

1.2.1. Biogenic silica diagenesis

Diagenesis is defined as all the chemical, physical and biological processes operating on a sediment from the time of its deposition until it enters the realm of metamorphism (Giles, 1997).

Biosiliceous sediment is an important constituent of Neogene sediments of high – latitude and equatorial regions (Fig. 1.1). It is the dominant sediment type where surface plankton productivity is high and the seafloor lies below the carbonate compensation depth. Biosiliceous sediments are mainly composed of diatom frustules and radiolarian tests.

Radiolarians and diatoms are common in coastal upwelling zones, while radiolarians dominate equatorial belts in the Pacific and Indian Oceans (Kastner, 1981). High diatom productivity results in a belt of siliceous sediments at approximately $60°$ S (Kastner, 1981). The shape of the Atlantic Ocean prohibits the development of equatorial current divergence, thus biogenic silica production is relatively low and there is no Atlantic equatorial belt of siliceous sediments (Spinelli et al., 2004). Biosiliceous sediments represent approximately 6% of the mass of the pelagic sediments, and 3% of the mass of all seafloor sediments (Hay et al., 1988).

Diatom frustules and radiolarian tests consist of biologically precipitated opal – A, or hydrous silica that is crystallographically amorphous to X – ray diffraction. This is an unstable silica polymorph, and, during the first kilometre of sediment burial, dissolves and reprecipitates as opal – CT (hydrous silica composed of interlayered cristobalite and tridymite) and then to the stable phase, quartz (generally cryptocrystalline, microcrystalline, or chalcedonic quartz) (Behl, 1999) (Fig. 1.2). The diagenetic transformations consist of two dissolution and reprecipitation reactions (Murata and Larson, 1975; Kastner et al., 1977; Isaacs, 1981; Williams and Crerar, 1985; Williams et al., 1985; Tada, 1991).
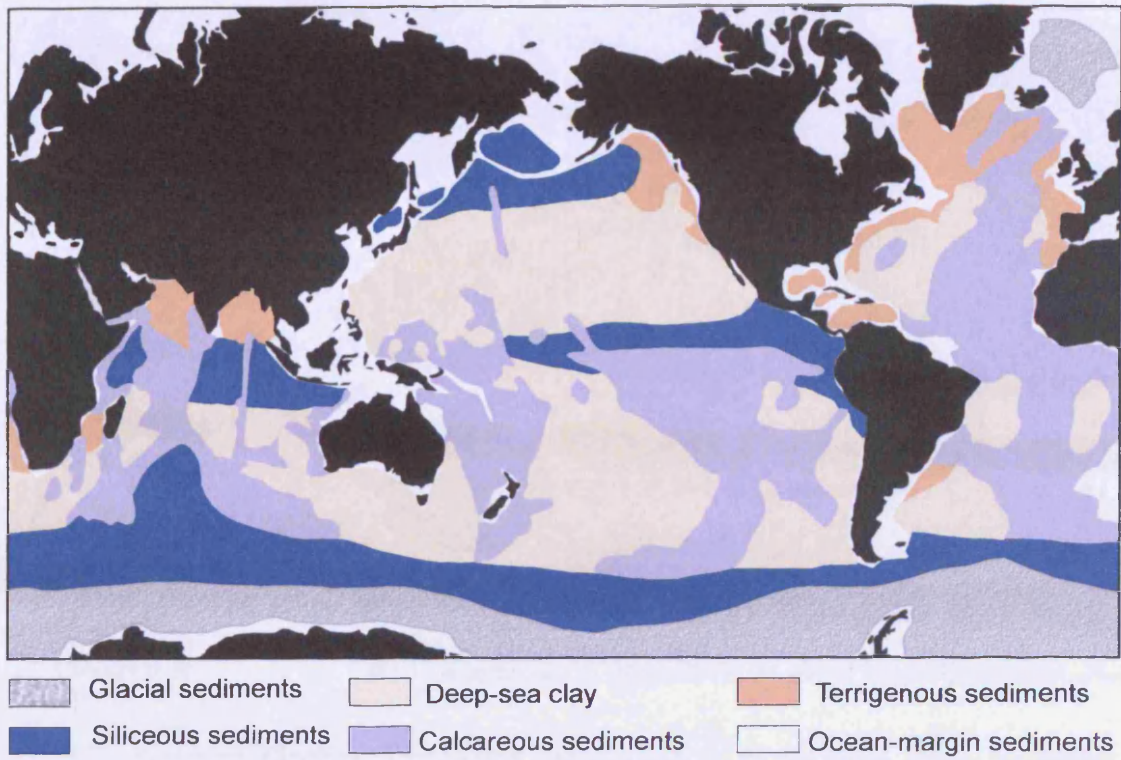
Fig. 1.1. Distribution of dominant sediment types on the present – day deep – sea floor (modified from Fütterer, 2000).
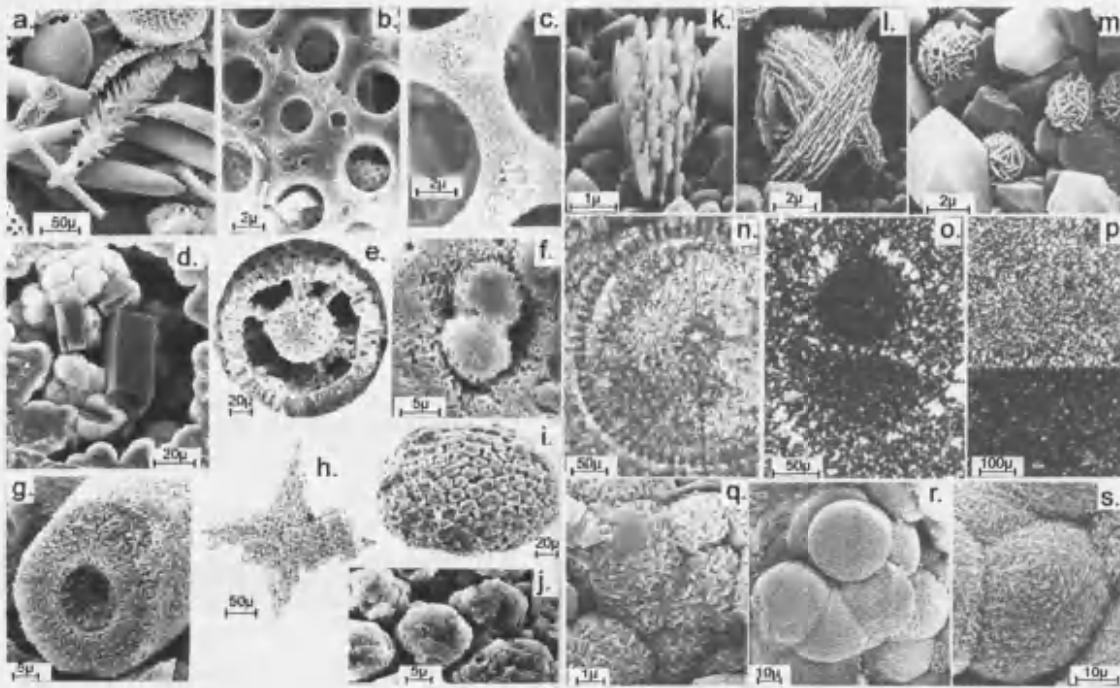
Fig. 1.2. Scanning Electron Microscope (SEM) images of biogenic silica diagenesis (modified from Riech and von Rad, 1979). (a) Unaltered siliceous microfossils; (b) Radiolarian skeleton; (c) Slightly altered diatom test; (d) Relic of dissolved radiolarian ('ghost') filled with opal – CT lepispheres; (e) Opal – CT replaced radiolarian skeleton; (f) Detail of Fig. 1.2e; (g) Quartz – replaced sponge spicule; (h) Quartz – replaced radiolarian; (i) Radiolarian cast consisting of amorphous silicate and smectite; (j) Detail of Fig. 1.2i showing opal – CT blades and lepispheres where the original siliceous skeleton was dissolved; (k) Individual opal – CT blades; (l) Opal – CT blades interweaved according to the twinning laws of tridymite; (m) Moderately silicified chalk with a few small, early – diagenetic, individual lepispheres growing on euhedral calcite crystals and coccoliths; (n) Well – preserved radiolarian in calcareous porcelanite with chert bands; (o) Incipient quartzification in zoned chalk – porcelanite – chert nodule; (p) Well defined boundary between porcelanite (black) with scattered quartz nuclei (white) and microcrystalline quartz chert (top); (q) Ghost of radiolarian filled by lepispheres; (r) Quartz – replaced lepispheres with well – preserved gross morphology from the original opal – CT stage; (s) Quartzified lepisphere with relic surface indicative of an opal – CT precursor stage.

1.2.1.1. The controlling factors of silica diagenesis reaction

The key concepts of silica diagenesis were developed by the research done in the 1970's and 1980's on the Monterey Formation (e.g. Kastner et al., 1977; Murata and Larson, 1975; Isaacs 1981; 1982; Isaacs et al., 1983; Williams and Crerar, 1985; Williams et al., 1985) and NE Pacific sites (e.g. Mizutani, 1977; Hein et al., 1978). These studies concluded that the two dissolution – reprecipitation reactions (opal – A to opal – CT and opal – CT to quartz) are controlled by temperature, time, sediment surface area, host sediment composition and pore water chemistry.

A reaction rate depends exponentially on temperature, as expressed by the Arrhenius equation (e.g. Atkins and de Paola, 2006), and as demonstrated by Williams and Crerar (1985). The temperature required for opal – A to opal – CT transformation varies from 2 to 56 °C (Hein et al., 1978; Keller & Isaacs, 1985; Nobes et al., 1992; Bohrmann et al., 1994; Behl, 1999), and the temperature for the opal – CT to quartz transformation ranges from 46 to 56 °C (Hesse 1988; Nobes et al., 1992) (Fig. 1.3). Based on downhole temperature measurements, Hein et al. (1978) concluded that the temperature of opal – A to opal – CT conversion is 35 – 50 °C. Using oxygen isotopic compositions, Murata et al. (1977) and Pisciotto (1981) determined that the precipitation of opal – CT takes place at 37 – 51 °C and that of quartz at 44 – 77 °C. These results were later argued by Matheney and Knauth (1993) who found that the precipitation of opal – CT takes place at much lower temperatures, between 17 – 21 °C. Moreover, the purest diatomaceous ooze converts into hard, brittle opal – CT and quartz cherts at temperatures as low as 2 – 33 °C and 36 – 76 °C, respectively (Behl and Garrison, 1994; Bohrmann et al., 1994).

In conclusion, given these wide temperature ranges, it is likely that the exact temperature value for each reaction depends on other factors, such as host sediment lithology, pore water chemistry, surface area, sediment permeability and sediment age, as discussed in various studies (e.g. Kastner et al., 1977; Hein et al., 1978; Keller and Isaacs, 1985; Williams et al., 1985; Pisciotto et al., 1992).
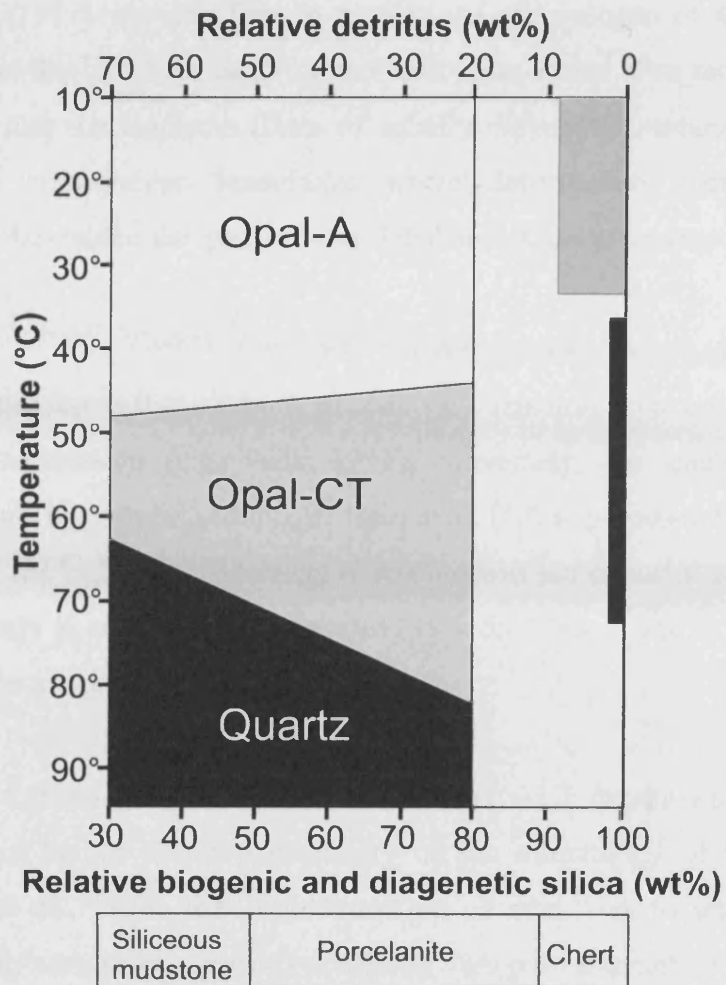
Fig. 1.3. Diagram showing the relative timing and temperatures of silica phase changes (modified after Behl, 1999).

Mizutani (1977) was the first to discuss the dependence of the silica diagenetic reaction on the thermal history of the sediments, rather than temperature alone. He proposed that the isopleths (lines of equally diagenetic maturation of cristobalite) cross the stratigraphic boundaries where deformation occurred shortly after sedimentation, since the parts of the deformed strata experienced different thermal histories.

The current view is that opal – A to opal – CT reaction occurs at lower temperatures in older successions (e.g. Tada, 1991); conversely, the reaction requires higher temperatures in younger sediments. Hein et al. (1978) proposed that the formation of opal – CT for highly to moderately siliceous deep sea deposits takes place within 10 million years at moderate temperatures (35 – 55 °C) and within 30 million years or more at low temperatures (< 30 °C).

The rate of transformation of opal – A to opal – CT depends also on geochemical factors such as the solution chemistry or the mineralogy of the host sediments (Kastner et al., 1977). The transformation of opal – A to opal – CT is greatly enhanced in carbonate sediments compared with pure siliceous oozes; in contrast, the presence of reactive clay minerals retards the transformation (Kastner et al., 1977).

1.2.1.2. Silica diagenesis transition zone

The research based on ODP data highlighted an important aspect of silica diagenesis: the physical properties contrast resulting from the conversion of opal – A into opal – CT (e.g. O'Brien et al., 1989; Compton, 1991; Nobes et al., 1992; Guerin and Goldberg, 1996; Gerland et al., 1997; Chaika and Dvorkin, 2000; Chaika and Williams, 2001).

The two silica phase transitions (opal – A to opal – CT and opal – CT to quartz) result in important changes of the physical properties of the sediments. The present research focuses on the transformation of opal – A to opal – CT, which results in a dramatic reduction in porosity (e.g. Chaika and Dvorkin, 2000). Typical ODP boreholes calibrating this diagenetic transformation show ranges from 5 – 40 %

reduction in porosity values, with the lower values relating to lesser proportions of opaline silica in the bulk sediment. It was demonstrated that this porosity reduction results from diagenesis and not from gradual mechanical compaction due to increasing sediment load (e.g. Isaacs, 1981). In other words, the biosiliceous sediments are resistant to mechanical compaction, showing a remarkably retention of high porosity during burial (Hamilton, 1976). The rigid framework created by the interweaving of the diatom tests collapses as a result of the diagenetic dissolution – reprecipitation reactions, allowing sediment consolidation.

The decrease in porosity is correlated to an increase in bulk density and compressional velocity of the sediments (e.g. Nobes et al., 1992; Chaika and Dvorkin, 2000). Most of the ODP reports of the sites where the silica boundary was drilled highlighted the physical properties change due to biogenic silica diagenesis (e.g. Mayer et al., 1992; Mountain et al., 1994; D'Hondt et al., 2003). In addition, several studies have analysed in detail the impact of silica diagenesis on the physical properties of the sediments for specific sites (O'Brien et al., 1989; Littke et al., 1991; Nobes et al., 1992; Guerin and Goldberg, 1996; Gerland et al., 1997; Kim et al., 2007).

The change of physical properties due to opal – A to opal – CT transformation usually takes place over a narrow depth interval. This does not have a consistent name in the existing literature; it was called a 'diagenetic front' (Thein and von Rad, 1987); a 'phase transition zone' (Keller and Isaacs, 1985) and represents the zone in which interbedded strata have different silica phases. The stratigraphic co – occurrence of silica phases is explained by compositionally controlled variation in the kinetics of the phase transformations (Behl, 1999). Two of the aims of this thesis are to determine the typical thickness of these transition zones and to establish their physical and chemical properties, by integrating the data from different sites.

1.2.1.3. Seismic expression of silica diagenesis

The increase in bulk density and compressional velocity of the sediments associated with the two diagenetic reactions (opal – A to opal – CT and opal – CT to quartz) results in acoustic impedance contrasts, allowing these reaction fronts to be imaged as reflectors on seismic reflection data (Hein et al., 1978; Bohrmann et al., 1992; Brekke, 2000; Davies and Cartwright, 2002). Generally, the opal – A to opal – CT transformation is imaged on seismic data as a high – amplitude reflector that crosscuts stratigraphy.

The opal – CT to quartz diagenetic transformation results in less significant changes of the physical properties, but can also create a seismic reflection from the phase boundary, as demonstrated by Mayerson and Crouch (1994), Pegrum et al. (2001) and, more recently, by Meadows and Davies (2008). The importance of the study of these seismic reflections arises from the fact that the diagenetic zones are associated with the expulsion of fluids (Volpi et al., 2003; Davies et al., 2008), trapping of hydrocarbons (McGuire et al., 1983) and the potential for forming fractured petroleum reservoirs (Mayerson et al., 1995).

The reflection associated with the opal – A to opal – CT diagenetic reaction front (referred to here as the A/CT reflection) has been recognised in various basins worldwide (e.g. Hein et al., 1978; Hammond and Gaither, 1983; Lonsdale, 1990; Bohrmann et al., 1992; Kuramoto et al., 1992; Nobes et al. 1992; Brekke 2000; Davies and Cartwright 2002; Volpi et al., 2003; Berndt et al., 2004; Nouzé et al. 2009; Ireland et al., 2010a; Meadows and Davies, 2010b) (Fig. 1.4). Most of these studies have characterised the A/CT reflection as being generally parallel to the present – day seafloor, i.e. a sea bottom – simulating reflector (BSR). Consequently, criteria for distinguishing a BSR related to silica diagenesis from the more common gas hydrates BSR have been discussed (Berndt et al., 2004; Nouzé et al., 2009).

One of the aims of the present study is to re – evaluate the relationship of the opal – A to opal – CT reflection to the present – day seafloor in order to demonstrate the reflection is not a typical BSR.

One of the most profound implications is that diagenetic processes can be studied on a basinal scale, with all the constraints that result from high precision mapping of the boundary in three dimensions, without the lack of continuity that hinders comparable efforts based on outcrop data. The combination of seismic and well data provides constraints on the geometry of the diagenetic boundary in the context of local stratigraphy and structure. In the last decade, the high – resolution of 3 – D reflection data allowed the study of silica diagenesis over the scale of sedimentary basins (e.g. Davies and Cartwright, 2002; 2007).

1.2.1.4. Fossilisation of diagenetic reaction fronts

Several studies in the past two decades have suggested that the A/CT reflection is not related to an active diagenetic reaction front, but is in fact 'fossilised' in its current position. The first to propose this hypothesis were Rundberg (1989) and Roaldset and He (1995) who suggested that the opal – A to opal – CT reaction fronts in the North Sea and Barents Sea, respectively are 'fossilised', based on disequilibrium with present day temperature relationships. The idea of 'fossil' or 'relict' chert layers was also proposed by Mayer et al. (1992) and Littke et al. (1991), based on ODP data. Brekke (2000) observed that the opal – A to opal – CT reaction front in the Norwegian Sea is not parallel to the sea floor, but is generally concordant to the units occurring just below the Late Pliocene unconformity. He also noted that the opal – A to opal – CT reaction front was deformed by the latest phase of Late Miocene flexuring along this continental margin. From this, Brekke (2000) argues that the diagenesis took place in the Late Miocene to Early Pliocene and has been inactive thereafter. Importantly, he concluded that the 'fossilised' opal – A to opal – CT reaction front records a higher temperature gradient in Late Miocene – Early Pliocene than at present, possibly due to an event of increased heat flow in Mid – Miocene times caused by an unknown mechanism.

1 - Norwegian Sea *(Brekke, 2000; Berndt et al., 2004);* 2 - Faeroe-Shetland Basin *(Davies and Cartwright, 2002);*

3 - South Korea Plateau *(Lee et al., 2003);* 4 - Fairway Basin *(Exon et al., 2007;Nouzé al., 2009);*

5 - Weddell Sea *(Bohrmann et al., 1992);* 6 - Antarctic Peninsula *(Volpi et al., 2003; Neagu et al., 2008);*

7 - Bermuda Rise *(Thein and von Rad, 1987);* 8 - Eastern Equatorial Pacific *(Mayer et al., 1992)*

9 - Japan Sea *(Tamaki et al., 1990; Kuramoto et al., 1992);* 10 - Offshore Sakhalin *(Meadows and Davies, 2007)*

11 - Labrador Sea *(Bohrmann and Stein, 1989);* 12 - Bering Sea *(Hein et al., 1978; Hammond and Gaither, 1983)*

13 - Antarctica *(Lonsdale, 1990);* 14 - Argentine Basin *(Zimmerman et al., 1979);*

15 - Indian Ocean *(Littke et al., 1991); 16 - Offshore California (Yeats et al., 1981)*

Fig. 1.4. The global distribution of the seismic reflectors associated with the opal – A to opal – CT diagenesis.

Davies and Cartwright (2002) proposed that the A/CT transformation within the Faeroe – Shetland Basin is 'fossilised' based on discordant structural and stratigraphic relationships between the A/CT reflection and its host sediments. They followed Brekke (2000) in linking the cause of the arrested diagenesis to changes in thermal regime, either resulting from heating from below or cooling from the water column.

The significance of discordant geometry has recently been challenged by Meadows and Davies (2008; 2010b) who suggested that the A/CT reflection within the Sea of Okhotsk, although generally discordant to the present seabed, is not 'fossilised', and has instead been subject to a significant decrease in the rate of conversion in the latest phase of basin evolution.

Recognising 'fossilised' diagenetic fronts and identifying the reasons for their 'arrest' is important for a better understanding of the silica diagenetic process and thermal evolution of sedimentary basins since they could be used to help constrain paleo – geothermal events.

1.2.2. Polygonal faulting

1.2.2.1. Definition and structural analysis

Polygonal fault systems are laterally extensive arrays of normal faults arranged in polygonal patterns in map view and confined to a specific stratigraphic interval (Cartwright and Dewhurst, 1998). They have been recognised in more than 50 basins worldwide (Cartwright et al., 2003) (Fig. 1.5).

Polygonal faults have been extensively studied in recent years based mainly on reflection seismic data (e. g. Henriet et al., 1991; Cartwright, 1994, 1996; Cartwright and Dewhurst, 1998; Dewhurst et al., 1999; Watterson et al., 2000; Goulty, 2001, 2002; Stuevold et al., 2003; Goulty and Swarbrick, 2005; Ireland et al., 2010b; 2010c), but there has been only limited investigation of the relationship between

polygonal faulting and silica diagenesis (Davies et al., 1999; Davies, 2005; Davies et al., 2008).

There is evidence that polygonal faults develop at shallow burial depth (Cartwright and Lonergan, 1996; Cartwright et al., 2004), in fine – grained sediments, commonly smectite – rich claystones or biogenic mudstones, however they have also been recognised in sandstones (Cartwright, 2007). The characteristic of this type of faults is that they develop in sediments that have been subjected to passive subsidence and burial in passive deposition settings, with no tectonic extension.

1.2.2.2. Genetic mechanisms

The genesis of polygonal fault is a matter of active debate (for reviews see Cartwright et al., 2003; Goulty, 2008). Several mechanisms have been proposed: gravity sliding (Clausen et al., 1999), density inversion (Henriet et al., 1989; Watterson et al., 2000), syneresis (Dewhurst et al., 1999) and low coefficients of residual friction in fine – grained lithologies (Goulty, 2001, 2002; Goulty & Swarbrick, 2005).

Gravity sliding would produce faults with strikes oriented orthogonal to the direction of sliding, and the characteristic of polygonal faults is that there is no preferential orientation of their strikes. Consequently, this hypothesis is not considered viable (e.g. Cartwright et al., 2003; Goulty, 2008).

In the density inversion hypothesis, faults would result from overpressured sediment layers overlain by normal compacted layers. The density inversion would cause the folding of the sediments and, subsequently, the development of fractures of the folded regions. This hypothesis was rejected on mechanical basis (Goulty, 2002) and because of the mismatch of strain and the absence of a universal correlation between folds and faults (Cartwright et al., 2003).

Syneresis is the spontaneous contraction of the solid network in a gel, with expulsion of liquid when internal forces of attraction are greater than the internal forces of
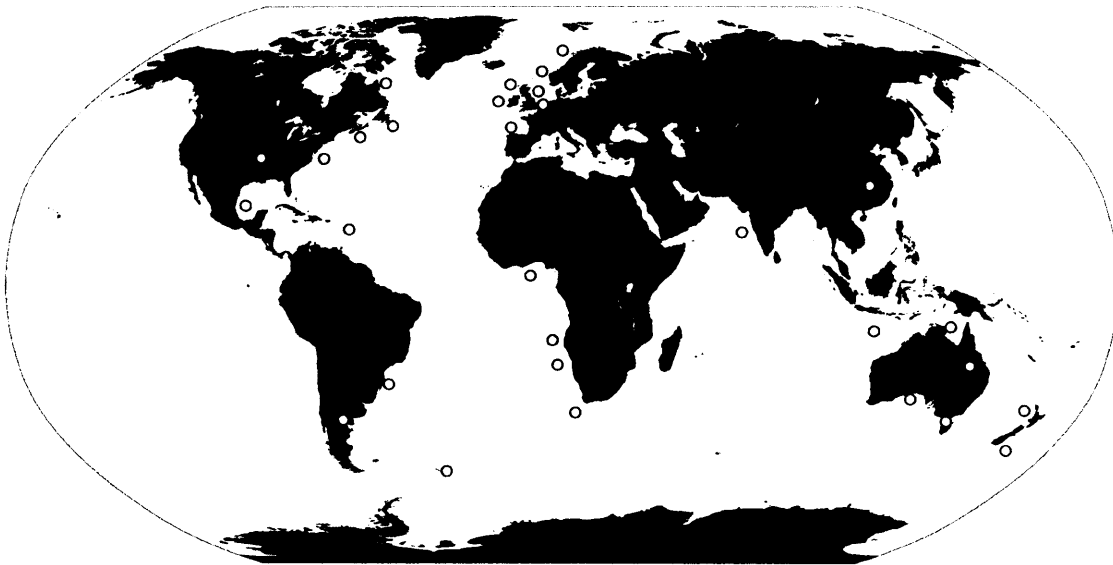
Fig. 1.5. The global distribution of polygonal fault systems as recognized from seismic data or field evidence (from Cartwright et al, 2003).

repulsion between the solid particles. It was proposed as a genetic mechanism because the fine – grained sediments in which the polygonal faults develop fall into the range of colloidal material (e.g. Dewhurst et al., 1999, Cartwright et al., 2003). According to Goulty (2008), this hypothesis has two weaknesses: the variety of lithofacies in which polygonal faults develop and the development of faults in sequences of hundreds of metres in thickness.

Another hypothesis proposed as responsible for the propagation of these faults is based on the low coefficients of friction of the sediments. However, this only applies to faults already generated. Once faults have nucleated, they can grow with increasing overburden stress, under laterally confined conditions, provided the coefficient of earth pressure at rest is less than the function of the residual coefficient of friction (Goulty, 2008).

1.2.2.3. The relationship between biogenic silica diagenesis and polygonal faulting

Polygonal faults systems are interesting features because they develop in sediments in the absence of tectonic stresses. Their existence seems paradoxical because shear failure is not considered possible under normal geomechanical burial conditions, unless the state of stress is modified by the presence of tectonic stresses. However, a recent study (Shin et al., 2008) has shown that particle – scale volume contraction associated with mineral dissolution and precipitation (e.g. silica diagenesis reactions) is a potential cause of shear failure in uncemented particulate materials. This could explain natural fracture systems (e.g. polygonal faults systems) without invoking regional tectonics.

Recent work by Davies et al. (2009) has shown that polygonal faults could be initiated as a result of silica diagenesis. However, as recognised by the authors, this genetic mechanism is applicable only in some biosiliceous sediments, due to the particular morphology of the A/CT diagenetic boundary necessary for the development of differential subsidence and growth of polygonal faults.

The genetic mechanism of polygonal faults will not be discussed further in this thesis, as it does not constitute one of its aims. However, the relationship between polygonal faults and biogenic silica diagenesis will be analysed in Chapter 5, with special emphasis on the impact that silica diagenesis has on the shear strength of the sediments and polygonal fault growth. In addition, in Chapter 6, polygonal faults will be analysed as one of the three styles of deformation associated with the A/CT reflection that argue for the 'fossilisation' of silica diagenesis in the Norwegian Sea.

1.3. Aims of study

The research presented in this thesis is aimed at analysing two important, and yet poorly understood aspects of silica diagenesis: (a) the physical properties contrast across the diagenetic transition zone, with a special focus on the porosity change and compaction, and (b) the temperature as a controlling factor of diagenesis and the implications on the 'fossilisation' of a reaction front and the thermal evolution of sedimentary basins. The specific aims of this thesis are:

- the compilation of a database of scientific drill sites that have penetrated the opal – A to opal – CT diagenetic boundary (Chapter 4);
- the definition of the criteria that could be used to infer the presence of a silica diagenesis front where only limited data are available (Chapter 4);
- the physical and chemical characterisation of the opal – A to opal – CT transition zones (Chapter 4);
- the development of a novel method to quantify the compaction strain due to diagenesis based on 3 – D seismic data (Chapter 5);
- the evaluation of the impact that silica diagenesis has on the shear strength of the sediments and the growth of polygonal faults (Chapter 5);
- the evaluation of the temperature as the dominant control of silica diagenesis (Chapters 4 and 6);
- the examination of the evidence for a 'fossilised' opal – A to opal – CT reaction front on the mid – Norwegian margin (Chapter 6);
- the development of a set of interpretational criteria to allow the identification of a 'fossilised' silica diagenetic front (Chapter 6);

- the investigation of the causes of the 'fossilisation' of a silica diagenetic front (Chapter 6).

A combination of seismic data (2 – D and 3 – D) and well data (exploration and scientific boreholes) was selected as the most adequate methodology to fulfil the scientific aims of this thesis. The main aim of Chapter 4 was to define and characterise the diagenetic transition zones from different locations around the globe. Therefore, the methodology of this chapter was based on ODP data, making use of the information available from numerous scientific boreholes that have penetrated the silica diagenetic boundaries in all of the world's oceans.

In Chapter 5, a combination of 3 – D seismic, exploration and scientific wells was used to develop a new method to estimate the compaction strain associated with the conversion of opal – A to opal – CT. The main observations (i.e. the systematic change of the fault plane dips across the diagenetic front) were made based on the seismic data; the sonic logs from the exploration wells were used for the crucial time to depth conversion of the quantitative data extracted from the seismic; finally, scientific drilling data were used for the validation of the method.

For answering the interesting question of the 'fossilisation' of the diagenetic boundary (Chapter 6), 3 – D and 2 – D seismic data allowed the identification and analysis of the regional structural criteria used to demonstrate the hypothesis that the boundary is a 'fossilised' feature. Geothermal data derived from the exploration wells in the study area were used to constrain the thermal history and provided further testing of the work hypothesis.

In summary, a combination of several data types allows the integration of different scales of resolution and areal extensions needed to approach the aims of this thesis.

1.4. Thesis structure

In this chapter, a summary of the literature covering the topics of this thesis was presented, followed by a statement of the aims of this research. Chapter 2 gives an overview of the data and methods used and Chapter 3 presents the geological setting. The results of this research project are presented in Chapters 4 – 6. Chapter 7 is an integrated discussion of the main scientific results of this thesis. Chapter 8 presents the conclusions of this research. Appendices A1 – A3 include additional data to support the conclusions of Chapters 4 – 6.

Two of the results chapters of this thesis have been published as scientific papers in international journals. The current status of each publication is:

- Chapter 5 has been published as *'Measurement of diagenetic compaction strain from quantitative analysis of fault plane dip'*. Raluca Cristina Neagu, Joe Cartwright, Richard Davies. Journal of Structural Geology 32 (2010), 641 – 655. (Appendix A5)

- Chapter 6 has been published as *'Fossilisation of a silica diagenesis reaction front on the mid – Norwegian margin'*. Raluca Cristina Neagu, Joe Cartwright, Richard Davies, Lars Jensen. Marine and Petroleum Geology 27 (2010), 2141 – 2155. (Appendix A6)

Although each article is jointly authored with the project supervisors, they are the work of the lead author (R.C.N). Project supervisors provided editorial support in accordance with a normal thesis chapter. Lars Jensen from Statoil is acknowledged in his position as a fourth author for providing permission to use the seismic data, and discussions at a preliminary stage of the project with the supervisors.

Chapter 2.

DATA AND

METHODOLOGY

2. DATA AND METHODOLOGY

The data used for this project consist of industry multichannel reflection seismic (2 – D and 3 – D), exploration wells and scientific (ODP and DSDP) boreholes. An overview of the dataset and methodology is given in this chapter, while the details on the specific methodologies employed for every chapter is presented in the relevant section (i.e. Chapters 4 – 6).

2.1. Seismic reflection data

2.1.1. Overview

The 2 – D seismic data set used in this study is composed of a regional grid of 214 profiles covering an area of approximately 66×10^3 km^2 of the Møre and Vøring Basins, on the mid – Norwegian continental margin (Fig. 2.1). The 3 – D seismic data consist of seven surveys (Tab. 2.1), covering a total area of 13×10^3 km^2. However, over three of the surveys, the sediments containing the opal – A to opal – CT diagenetic boundary have been eroded by the numerous slope failures of the Late Pleistocene to Holocene (Bryn et al., 2005). Consequently, only the other four 3 – D seismic surveys were analysed in this thesis (i.e. Gjallar, Ormen Lange, Grip High and pl251). The data are time migrated, and, since they are industry data, unfortunately no details on processing were available. The zero – phase nature of the data was determined by examining the seabed reflection (e.g. Ormen Lange and pl251 surveys) (Fig. 2.2a; b), the reflections associated with igneous intrusions (e.g. Gjallar survey) (Fig. 2.2c) or the reflection from the top of the basement (e.g. Grip High survey) (Fig. 2.2d). In all the cases, the reflections have a clear symmetrical waveform, consisting of a peak with side lobes that are low and symmetrical (Brown, 2004). In other words, the maximum amplitude of the wavelet coincides with the water – sediment, sediment – igneous intrusions or sediment – basement interfaces. The data are displayed with either a positive Society of Exploration Geophysicists (SEG) polarity, or a reverse SEG polarity (Tab. 2.1).
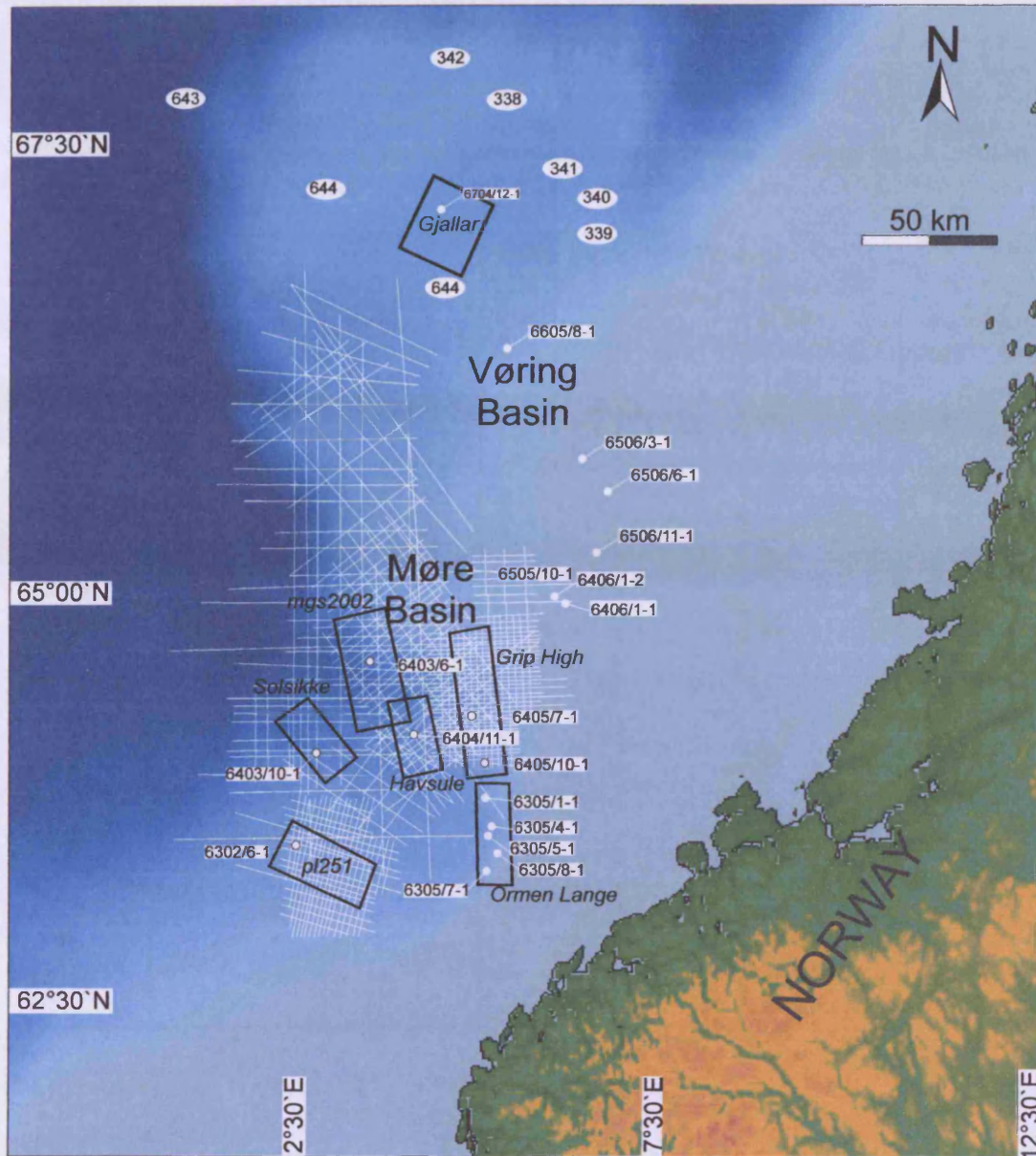
Fig. 2.1. Location map of the seismic data (2 – D profiles drawn in white and 3 – D surveys outlined in black) on the Norwegian continental margin. Exploration wells (white dots) and ODP and DSDP data (white ellipses) are also shown. Basemap built using Global Mapper software: Mercator Projection, WGS84 Datum and SRTM Worldwide elevation data. Bathymetry from NOAA (Amante and Eakins, 2008).

Tab. 2.1. Parameters of the seismic surveys.

*The vertical resolution is estimated based on an average velocity of 1800 m $\cdot$ s^{-1}; the horizontal resolution is equal to the CDP bin size.
** In case of the 2 – D surveys, the lateral resolution was calculated using Eq. 2.1, where $t_0 =$ 1s and V = 1800 m $\cdot$ s^{-1}.

Survey name	2D/ 3D	Area (km^2)	Line spacing, CDP spacing (m)	Sampling rate (ms)	Polarity (SEG convention)	Dominant frequency (Hz)	Resolution vertical* /horizontal (m)
Gjallar	3D	1900	18.75/18.75	4	+	50	9/18.75
Grip High	3D	2500	25/25	4	-	45	10/25
Ormen Lange	3D	1500	22.79/12.50	4	-	36	13/12.50
pl251	3D	2000	12.50/12.50	4	+	36	13/12.50
Havsule	3D	1300	24.98/25	4	+	40	11/25
Solsikke	3D	1300	25/25	4	-	50	9/25
mgs2002	3D	2600	25/25	4	+	45	10/25
e2d (157 lines)	2D	~57000	–	4	+	36	13/150**
g2d (57 lines)	2D	~9300	–	4	+	36	13/150**
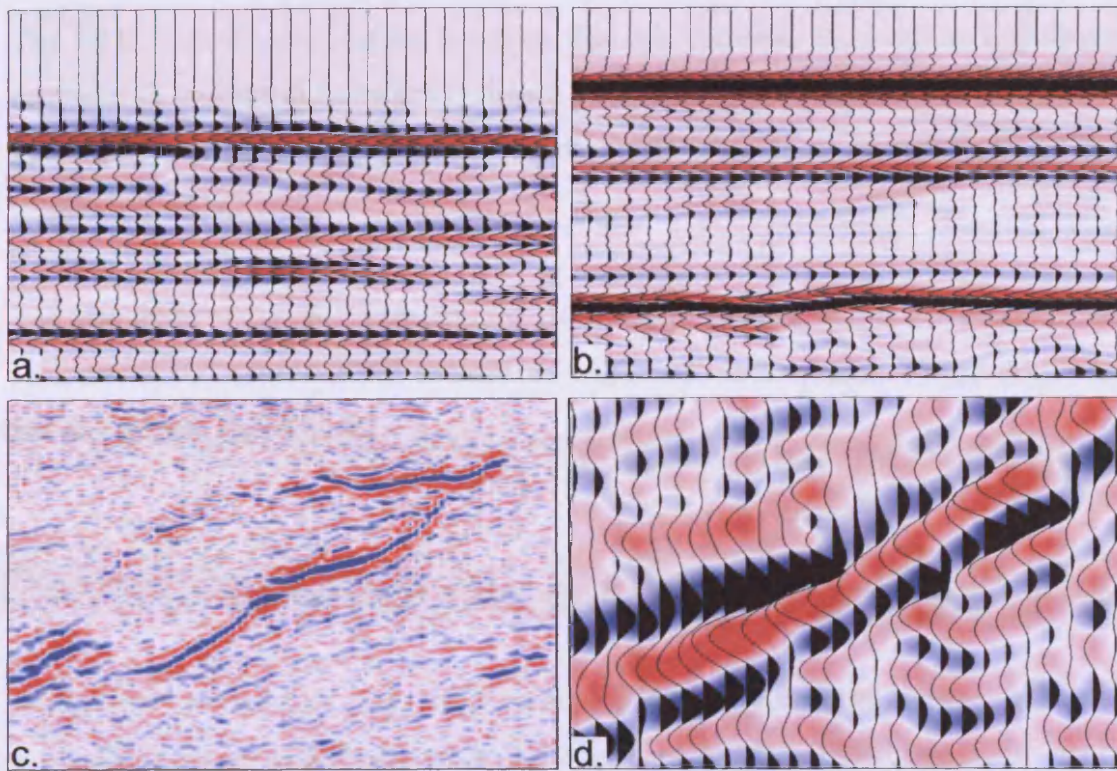
Fig. 2.2. The zero – phase nature of the data was determined by examining (a) the seabed reflection in Ormen Lange survey; (b) the seabed reflection in pl251 survey; (c) the reflection associated with the top of an igneous intrusion in the Gjallar survey; (d) the reflection from the top of the basement in Grip High survey.

The SEG polarity convention specifies that an increase in acoustic impedance represents a positive polarity and is displayed as a peak in the seismic wavelet, while a decrease in acoustic impedance represents a negative polarity and is displayed as a trough (Fig. 2.3).

The resolution of the data refers to how close two points can be, yet be distinguished (Yilmaz, 2001). The vertical resolution (Fig. 2.4a) is a quarter of the dominant wavelength (λ), defined by:

$$\lambda = \frac{v}{f},$$

<div align="right">(Eq. 2.1)</div>

where v is the velocity and f the dominant frequency. Seismic wave velocities generally increase with depth, while the dominant frequencies decrease with depth (Yilmaz, 2001). However, the thickness and areal extent of beds below the resolution limit and the sub – seismic faults can be mapped based on the amplitude changes. Lateral or horizontal resolution (Fig. 2.4b) refers to how close two reflecting points can be, yet be recognised as distinct points (Yilmaz, 2001). It is represented by the Fresnel zone (Fig. 2.4c), which is the part of the reflector that contributes to a constructive interference of the total energy arriving at a detector. The radius of the Fresnel zone is:

$$r = \left(\frac{1}{2} \cdot \lambda \cdot h_0 \right)^{1/2} = \frac{1}{2} \cdot v \cdot \left(\frac{t}{f} \right)^{1/2}$$

<div align="right">(Eq. 2.2)</div>

where λ is the dominant wavelength, h_0 is the depth, t the arrival time, v the average velocity and f the frequency (Sheriff and Geldart, 1995). Migration tends to collapse the Fresnel zone to approximately the dominant wavelength (Yilmaz, 2001). When the reflector dimensions are smaller than the Fresnel zone, the response is that of a diffracting point (Fig. 2.4b) (Sheriff and Geldart, 1995).

The parameters (area covered, bin size, polarity, phase, dominant frequency, vertical and lateral resolutions) of all the surveys are presented in Tab. 2.1.

Acoustic impedance   Reflection coefficient   Zero-phase wavelet   Minimum-phase wavelet
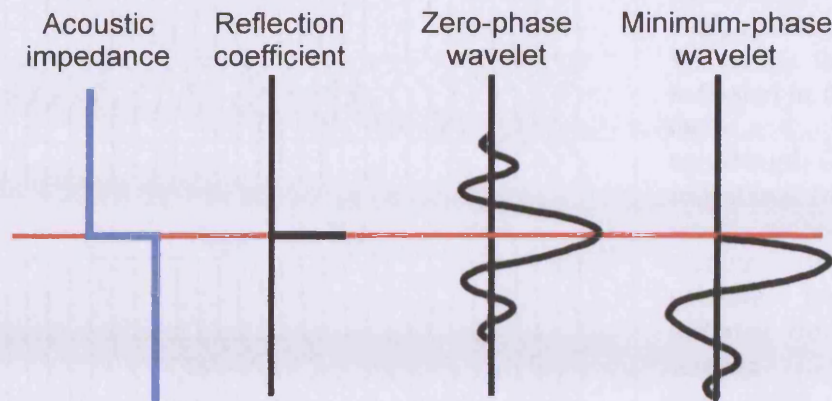
Fig. 2.3. Typical minimum – phase and zero – phase wavelets. The minimum – phase wavelet has the seismic energy located directly below the reflecting interface. For the zero – phase wavelet, the peak in seismic energy corresponds to the reflecting interface.
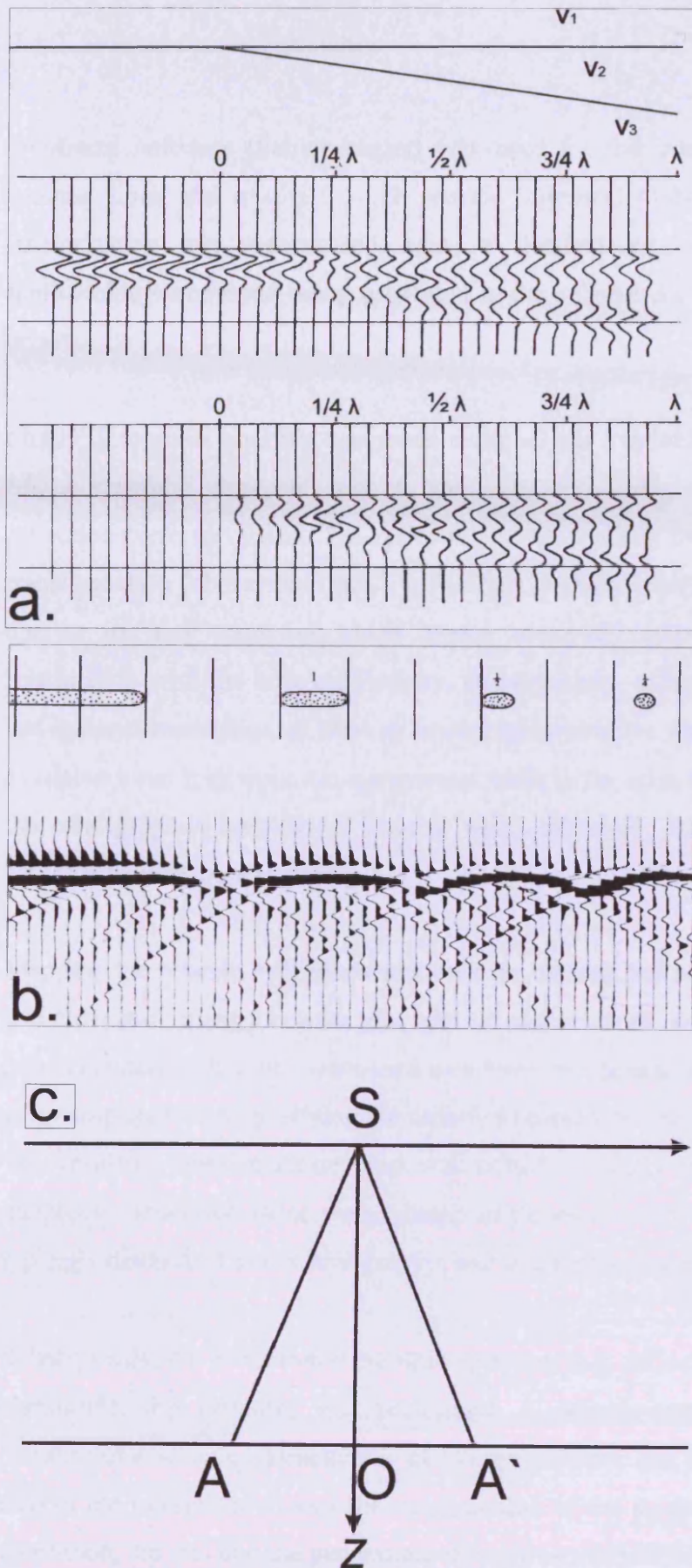
Fig. 2.4. Vertical and horizontal resolution (modified from Sheriff and Geldart, 1995). (a) reflections illustrating vertical resolution. Reflections from the wedge where $v_3 > v_2 > v_1$; wedge thickness is indicated in fractions of the dominant wavelength (λ). Below, reflections from a thin wedge embedded in a medium of different velocity ($v_3 = v_1$ different from v_2); (b) seismic reflections from strips of varying widths (expressed in terms of Fresnel – zone width); (c) schematic representation of the Fresnel zone (AA') where S – source, O – reflection point, z – depth.

2.1.2. Seismic data interpretation

Geoframe software (Schlumberger) was used for the interpretation of the 2 – D seismic lines and of the 3 – D seismic volumes. Only the main steps of the interpretation are summarised next, a detailed explanation of the specific methodology employed being presented in the subsequent chapters (i.e. Chapters 5 and 6).

Firstly, a regional analysis was made using all the available seismic and well data. Major structural elements, such as anticlines and faults, and the silica diagenesis reflection were identified. The reflection corresponding to opal – A to opal – CT transformation (abbreviated A/CT reflection) is easily identified on the seismic data due to its high amplitude, high lateral continuity and commonly crosscutting relationship with the host stratigraphy. Subsequently, using the available well data, the regional correlation of the key stratigraphic markers was undertaken. Using the available sonic logs from the commercial wells in the area, the interval velocities for the stratigraphic interval of interest were extracted; these were used for the conversion from time to depth.

Mapping the seismic reflections was done by manual picking of a horizon on inlines and crosslines, using a regular grid, and on random lines, where necessary. The seed points created in this way were used as a basis for the autotracking operation, which was completed after specifying the criteria to control the picking (e.g. time window). The resulting time structure map was edited manually to correct the automatic mispicks. Generally, these were related to the opal – A/CT horizon, because it is typically discordant to the stratigraphy, and to the presence of faults.

Subsequently, the extraction of seismic attributes (e.g. reflection time, amplitude, dip magnitude, dip azimuth) was performed. A seismic attribute is a quantitative measure of a seismic characteristic of interest (Chopra and Marfurt, 2005). The next step in the interpretation was the manipulation of the seismic attribute maps (time, amplitude, dip etc) and the generation of isochron and isochore maps.

The faults present in the interval of interest (i.e. the polygonal faults of Kai and Brygge Formation) were identified on seismic attribute maps (mainly dip magnitude, azimuth, amplitude and coherence maps). The dip and azimuth attributes represent the magnitude and, respectively, the direction of the time gradient vector computed at each trace of the picked horizon (c.f. Neves et al., 2004). In general, a fault is visible on the dip attribute map when the dip direction of the fault plane differs from the dip of the horizon. On coherence maps, the discontinuities in the data are enhanced, allowing their identification. These discontinuities are characterised by low – coherence values and they can be related to geological (e.g. faults) or geophysical (e.g. low signal – to – noise areas) features.

Once identified on the attribute maps, the faults were interpreted on seismic cross – section with confidence to a positioning accuracy equivalent to the lateral resolution, from a series of stacked cutoffs of stratal reflections in both the hangingwall and the footwall (Chapter 5). Imaging of the fault cutoffs was consistently excellent throughout the survey areas, and there were no problems with imaging artefacts beneath the fault planes, such as fault shadows.

2.1.2.1. Quantitative measurements based on seismic data

Based on seismic cross sections, two types of measurements (i.e. dip angle of the fault planes and the throw values for selected horizons) were extracted.

The dip angle of the fault planes was measured on seismic cross – sections orthogonal to fault strikes as identified on the attribute maps of the A/CT reflection (details in Chapter 5). The interval velocities derived from the available sonic logs from the commercial wells in the area, were used for the time to depth conversion of the measurements, which allowed the calculation of the true dip angle of the faults. Throw values of selected faults were measured on seismic profiles by taking the two – way travel time of reflections from the footwall and hangingwall cutoffs of selected horizons (details in Chapter 5).

2.1.2.2. Sources of error and limitations

There are several limitations in the interpretation of the seismic data. The data quality in some areas (e.g. Ormen Lange 3 – D survey) is affected by the presence of gas anomalies. Both the signal – to – noise ratio and the frequency content are reduced over these areas, hindering the seismic interpretation.

Several potential sources of error are associated with the velocity values used for the time to depth conversion of the measurements (i.e. fault dips and throws in Chapter 5, the thickness of sediments within a stratigraphic interval in Chapter 6) based on seismic data. Firstly, a limited number of wells were available for the study area (Fig. 2.1). Consequently, the interval velocities derived from the sonic logs had to be extrapolated to the area where no well data were available. Secondly, the interval velocities represent simplified values, in reality both vertical and lateral velocity variations being present. This can be related to the variation of a range of parameters, such as lithology, density, porosity etc. The pressure due to burial depth is another source of vertical velocity variations, together with the effects of age, frequency and temperature (Sheriff and Geldart, 1995).

An important limitation for the interpretation of the data and the extraction of quantitative measurements is the resolution (vertical and lateral) of the seismic data (Tab. 2.1). However, the resolution limit for detecting the fault offsets is better than the vertical resolution because the identification of fault offsets depends on the sampling frequency and the quality of the migration, and not on the dominant wavelength, which determines the stratigraphic resolution (Stuevold et al., 2003). Other possible limitations and sources of error related to specific methodologies are discussed in the relevant chapters.

2.2. Well data

The exploration wells available from the Norwegian Petroleum Directorate (http://www.npd.no) or from confidential industry reports have provided lithological and chronostratigraphic calibration for this study (Chapters 5 and 6). Where

32

available, the sonic logs from these wells have allowed the extraction of interval velocities used for the time to depth conversion (Chapters 5 and 6). In addition, the sonic and the density log from well 6407/7 – 1 were used for computing a synthetic seismogram needed to illustrate the detailed acoustic response of the opal – A to opal – CT reaction front (Chapter 6).

The scientific boreholes (ODP and DSDP) available from http://www-odp.tamu.edu/ and http://www.deepseadrilling.org/ were used for regional correlation of some key stratigraphic markers (Chapters 5 and 6), estimation of the physical properties of the sediments (Chapters 4 and 5), the physical and chemical characterisation of the silica diagenesis transition zone and the compilation of a database of the silica diagenesis boundaries that were drilled worldwide (Chapter 4). The details of the specific methodologies employed in each of these applications are presented in the subsequent chapters.

Chapter 3.

GEOLOGICAL SETTING

3. GEOLOGICAL SETTING

3.1. Introduction

This research focuses on the Møre and Vøring Basins, part of the Norwegian passive continental margin. This area has been considerably studied in the last decades due to its hydrocarbon prospectivity (e.g. Spencer et al., 1999), submarine sliding (Hjelstuen et al., 2004; Mienert et al., 2005), gas hydrate accumulations (Bünz et al., 2005; Mienert et al., 2005; 2010) and fluid migration processes (Berndt et al., 2003; Gay and Berndt, 2007; Hustoft et al., 2007). Less attention has been paid to the study of biogenic silica diagenesis (Brekke, 2000; Berndt et al., 2004; Davies and Cartwright, 2007; Ireland et al., 2010a; 2010b).

3.2. Regional geology and tectonic setting

The Møre and Vøring Basins (Fig. 3.1) are oriented NE – SW and are flanked by paleo – highs and platforms (e.g. Møre and Vøring Marginal highs). The basins are separated by the Jan Mayen Fracture Zone, which represents a major offset in the Mid – Atlantic Ridge and has been active since the early Tertiary continental breakup (Berndt et al., 2001). To the north, Vøring Basin is delimited by the Bivrost Lineament. To the southeast, Møre Basin is delimited by the Møre – Trøndelag Fault Complex, to the west by the Faeroe – Shetland Escarpment, to the south by the northern termination of Tampen Spur in the North Sea and to the east by the mainland.

The Vøring Basin is bisected by the Fles Fault Complex that runs along the basin axis between Bivrost and Jan Mayen Lineaments (Brekke et al., 1999). Gjallar Ridge, located in the west of the Vøring Basin, is an elevated complex of rotated fault blocks formed in the Late Cretaceous that runs parallel to the continent – ocean boundary for about 250 km. It trends N – S in its southern part and NE – SW in its central and northern parts (Corfield et al., 2004). The Vøring and Møre basins are

controlled by NE – SW master normal faults that dip towards the oceanic domain located to the northwest (Gómez and Vergés, 2005).

The present structural configuration of the Norwegian margin is the result of several rifting episodes that started in the Permian – Early Triassic (e.g. Brekke and Riis, 1987; Skogseid and Eldholm, 1989; Doré and Lundin, 1996). Three main rifting episodes were identified: Carboniferous to Permian, late Mid – Jurassic to Early Cretaceous and Late Cretaceous to Early Eocene (Brekke et al., 2000 and references therein). In Carboniferous to Early Cretaceous extensional tectonics were related to continental rifting.

The rifting terminated in the Late Paleocene – Early Eocene (~55 Ma) with the onset of seafloor spreading in the North Atlantic (Skogseid et al., 1992; Blystad et al., 1995). The final continental break – up and subsequent thermal subsidence led to the development of the Vøring and Møre sedimentary basins (Brekke and Riis, 1987; Skogseid et al., 1992; Brekke, 2000). The basins are filled with more than 10 km of Cretaceous and Cenozoic sediments (Scheck – Wenderoth et al., 2007). The volcanic – related Vøring and Møre marginal highs were also created during continental break – up (Hjelstuen et al., 2004).

Møre Basin has been a major depocentre since the Late Jurassic, the main phase of basin subsidence having been initiated in the Middle Cretaceous, with more than 10 km of post – Jurassic sediments (Eldholm et al., 1987). The Vøring Basin developed as a depocentre in the Late Triassic – Early Jurassic time, however, except in local sub – basins, the younger sedimentary cover is relatively thin. The total Cenozoic sediment sequence shows a maximum thickness of about 3.5 km in the Møre Basin, while in the Vøring Margin the sediment cover rapidly thickens away from the coast, approaching an average value of about 2 – 2.5 km. The variation in thickness is often associated with the underlying structures. The marginal highs are covered by much thinner sediment sections than the landward basins.

Norwegian Margin was subjected to inversion tectonics during the Neogene, expressed by large – scale domes and elongated anticlines, such as Ormen Lange

Dome, the Helland Hansen Arch, Vema Dome etc (Blystad et al., 1995; Doré and Lundin, 1996). The compressional deformation may have begun in the Eocene, but maximum growth of the large inversion anticlines occurred during the Middle – Miocene (Brekke et al., 2000; Løseth and Henriksen, 2005). In the Vøring Basin, there is seismic and biostratigraphical evidence for regional uplift and intrabasinal erosion prior to this Middle – Miocene compression (Brekke et al., 1999). The Miocene compressional phase had important consequences for the hydrocarbon systems along the Norwegian margin (Løseth and Henriksen, 2005). In the context of the research presented in this thesis, this episode of regional compression is important because the latest stages of folding deformed both the basin fill and the regionally extensive A/CT reflection.

Throughout the Miocene, the sedimentation was characterised by the deposition of fine – grained material under a current influenced regime, creating contourite deposits (Hjelstuen et al., 2005). In the Late Miocene, important deposits of muds and siliceous oozes filled the depressions created by the Middle Miocene folding, onlapping and burying the tectonically created topography, such as Helland – Hansen Arch (Brekke et al., 1999). Silica was probably supplied to the ocean from land due to an enhanced chemical weathering during a warm and humid climate (Laberg et al., 2005).

The Late Miocene to early Pliocene period was characterised by important shifts between opal – and carbonate – dominated accumulations, indicating alternating periods of decreased surface water circulation with a relative isolation of deep water (opal – dominated), and periods of increased surface and deep – water circulation (carbonate – dominated) (Laberg et al., 2005). The Miocene – Late Pliocene boundary coincides with an important change in the depositional regime, as the post – Miocene sediments mainly have been transported to the continental slope from an easterly source area, as revealed by the westward prograding wedges on the Vøring margin (Hjelstuen et al., 2004).

Over large parts of the Norwegian continental shelf, there was a period of non – deposition or erosion during the Early to Late Pliocene. This was probably related to

the onset of glaciations and uplift of the continent (Brekke et al., 1999; Eidvin et al., 2000; Brekke, 2000). On the mainland and in shallow parts of the continental margin, the Late Pliocene unconformity is related to uplift and erosion. In the deeper parts of the continental margin, this unconformity corresponds to a period of non – deposition (Brekke et al., 1999).

During Late Pliocene a thick prograding sediment wedge was built out westward from the mainland across the entire shelf (Brekke, 2000). This unit occupies the Trøndelag Platform region in the Vøring Margin and is much narrower in the Møre Margin (Gómez and Vergés, 2005). The sediment wedge can be up to 1.75 km thick and is limited at its base by the Late Pliocene unconformity (Gómez and Vergés, 2005).

The rapid deposition of the prograding wedge produced differential compaction in the underlying Tertiary and Mesozoic sediments, resulting in lateral flow, mud diapirism and fracturing in the underlying sediments in front of the wedge (Gómez and Vergés, 2005 and references therein).

Fig. 3.1. Structural map of the Norwegian Sea continental margin (modified from Blystad et al., 1995). Location of Fig. 3.2 shown by the red line.

3.3. Seismic stratigraphy

The research in this thesis focuses on Brygge and Kai Formations, both of which contain a significant fraction of biogenic silica and have been affected by diagenesis (Brekke, 2000; Berndt et al. 2004).

The Brygge Formation is Early Eocene to Early Miocene in age and is part of the Hordaland Group. It consists of biosiliceous mudstones, claystones and minor sandstones (Dalland et al., 1988; Brekke, 2000).

The Kai Formation is Early Miocene to Early Pliocene in age and is part of the Nordland Group. It is composed of fine – grained hemipelagic sediments, which are part of contourite sediment drifts that developed free from the interaction with downslope processes (Rokoengen, 1995; Hjelstuen, 1997; Bryn et al., 2005). The Kai Formation represents mostly deep – water basinal sedimentation, onlapping the continental slope and the Mid – Miocene domes (Bryn et al., 2005).

Both Brygge and Kai Formations are extensively deformed by a system of polygonal faults (Fig. 3.2.). In addition, several huge crater structures have been identified in the ooze sediments of the Kai and Brygge Formations (Riis et al., 2005).

The uppermost stratigraphic unit is Naust Formation (Late Pliocene – Pleistocene), which comprises glacial sediments (tills and debris flows) and slide deposits (e.g. Berg et al., 2005). These form thick prograding packages of sediment, as a result of the considerable erosion caused by Neogene uplift of the Norwegian mainland and continental shelf (Hovland et al., 1998).

Current – controlled fine – grained sediments deposited along the slope during deglaciation are interbedded with glacigenic downslope – transported debris flow deposits (Bünz et al., 2005). The slide units, comprising Storegga Slide, have been the focus of numerous studies (e.g. Evans et al., 1996; Riis et al., 2005; Bryn et al., 2005; Bünz et al., 2005; Bull et al., 2009; Lawrence and Cartwright, 2009).
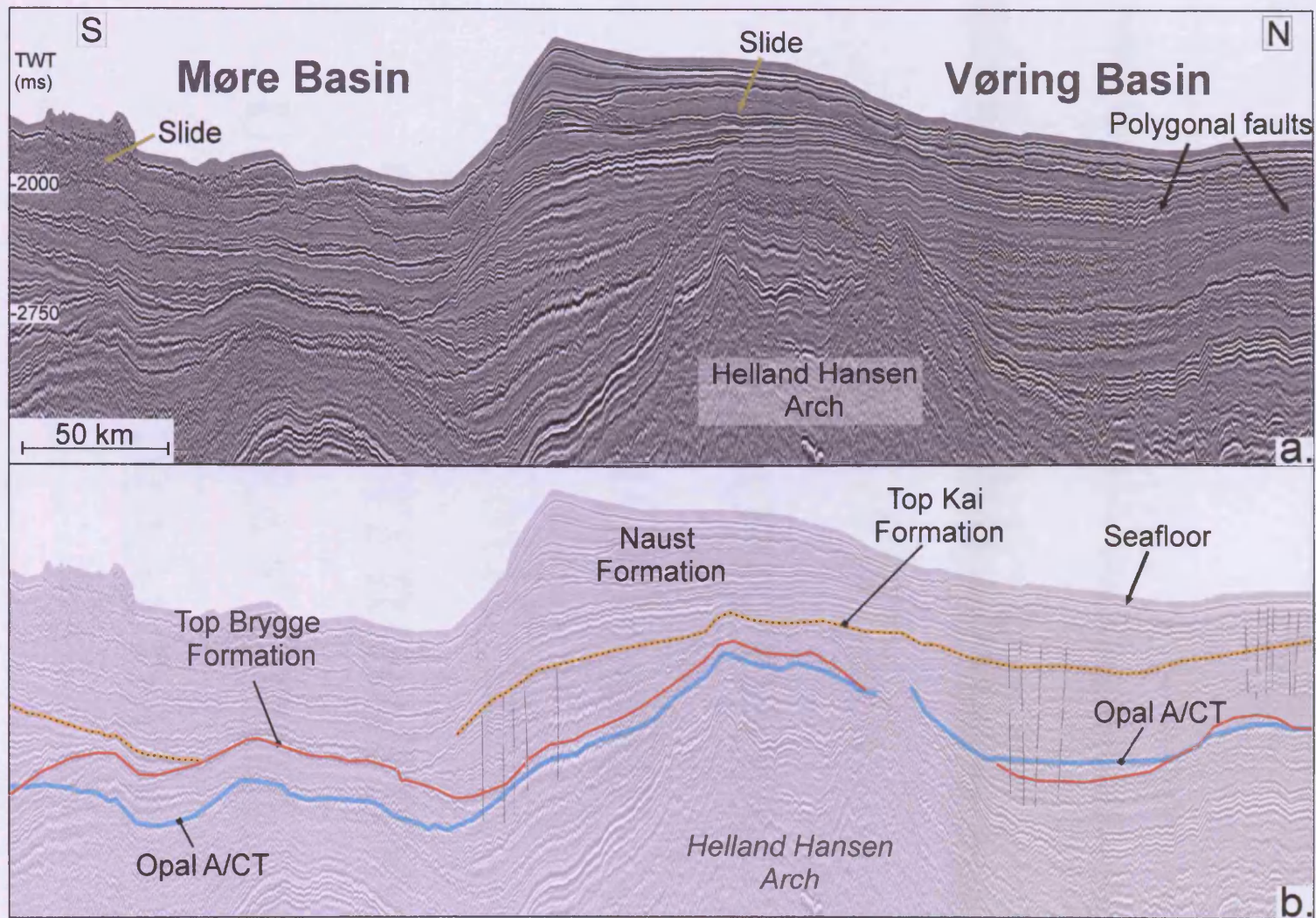
Fig. 3.2. (a) Regional 2 – D seismic profile crossing Møre and Vøring Basins. Location in Fig. 2.1; (b) Interpretation. Note that the reflection from the opal – A to opal – CT diagenesis crosscuts the hosting stratigraphy.

Chapter 4.

BIOGENIC SILICA DIAGENESIS TRANSITION ZONES – A PHYSICAL AND CHEMICAL CHARACTERISATION USING OCEAN DRILLING PROGRAM DATA

4. BIOGENIC SILICA DIAGENESIS TRANSITION ZONES – A PHYSICAL AND CHEMICAL CHARACTERISATION USING OCEAN DRILLING PROGRAM DATA

4.1. Abstract

A total of 33 ODP sites from various global locations are examined in order to identify silica diagenesis transition zones. These zones represent narrow depth ranges where the physical properties of the sediments change sharply as a result of opal – A to opal – CT diagenesis. Based on physical and chemical properties, the criteria for the identification of a silica diagenesis transition zone are proposed. Moreover, the factors that control the thickness of these zones are analysed. Evidence is shown that some of the diagenetic transition zones were formed as a response to higher paleo – geothermal gradients, supporting the view that they are presently 'fossil' or 'relict'. Due to the implications that the physical properties contrast has on compaction in sedimentary basins and overpressure, a summary of the physical properties of these diagenetic zones should prove useful for any future study investigating the diagenesis of biosiliceous sediments.

Keywords: opal – A, opal – CT, silica diagenesis, physical properties, Ocean Drilling Program

4.2. Introduction

The opal – A to opal – CT transformation results in significant changes to the physical properties of sediments (e.g. Nobes et al., 1992; Chaika and Dvorkin, 2000), while the opal – CT to quartz transformation does not create such a sharp physical property contrast (Isaacs et al., 1983; Nobes et al., 1992). The change of physical properties due to opal – A to opal – CT transformation usually takes place over a narrow depth interval. This does not have a consistent name in the existing literature; it was called a 'diagenetic front' by Thein and von Rad (1987); a 'phase

transition zone' by Keller and Isaacs (1985); a 'transition zone' by Littke et al. (1991); Nobes et al. (1992); Rice et al. (1995); a 'reaction zone' by Davies and Cartwright (2007); Davies et al. (2008), or a 'transformation zone' by Ireland et al. (2010a). There is also an inconsistency regarding the definition and, consequently, the thickness of the opal – A to opal – CT transition zone.

Silica diagenesis transition zones have been recognised and analysed from microscopic level (X – Ray diffraction or XRD analyses) (e.g. von Rad et al., 1978), core samples (e.g. Nobes et al., 1992), to outcrop (e.g. Isaacs, 1982) and seismic data (e.g. Davies et al., 2008). In general, the opal – A to opal – CT transition zones are narrow depth intervals, tens of meters thick (e.g. Murata and Larson, 1975; Hein et al., 1978; Littke et al., 1991; Nobes et al., 1992; Rice et al., 1995). However, some authors (e.g. Keller and Isaacs, 1985; Ireland et al., 2010a) have reported silica diagenesis transition zones of hundreds of meters in thickness.

The authors who have reported thin opal – A to opal – CT transition zones defined them as the interval over which opal – A and opal – CT coexist (Nobes et al., 1992); the interval separating the sediments containing only opal – A as the silica phase from sediments where opal – CT predominates (Littke et al., 1991); or as the transitional beds between the base of the zone of diatomaceous mudstones and the top of the diatom – free porcelanites (Murata and Larson, 1975).

Keller and Isaacs (1985) identified the phase – transition zones as 'zones in which interbedded strata have different silica phases'. Based on outcrop data, they estimated the thickness of the opal – A to opal – CT transition zone in the compositionally heterogeneous sequences of the Monterey Formation, California, as being 200 m thick. Ireland et al. (2010a) suggested that the silica diagenetic transformation zone on the Gjallar Ridge (Norwegian Sea) is hundreds of meters thick, based on seismic data interpretation. The authors define the transformation zone as 'the volume of sediment in which silica diagenetic reactions occur', referring to the entire sequence of transformation from opal – A to quartz, so strictly this definition does not equate to the opal – A to opal – CT transition.

It is important to understand what controls the thickness of the opal – A to opal – CT transition zone because the temperature ranges of the opal – A/CT transformation can be inferred based on the depth and thickness of the transition zone. A thin transition zone means temperature is the dominant control of diagenesis. Conversely, for a thicker transition zone, the temperature is probably less important than other controls, for example lithology (Keller and Isaacs, 1985), surface area (Williams et al., 1985) or age (e.g. Hein et al., 1978).

The opal – A to opal – CT boundary is sampled by more than 100 Ocean Drilling Program (ODP) and Deep Sea Drilling Project (DSDP) boreholes worldwide. For most of the sites, physical properties measurements on core samples and/or downhole measurements are available for the intervals of interest. In addition, some of the sites also have XRD analyses or Scanning Electron Microscope (SEM) images from the transition zone and pore water chemistry analyses. It is, therefore, possible to use this extensive database to make a physical and chemical characterisation of the diagenetic transition zones (Appendices A1.2 and A1.3).

Most of the ODP reports of the sites where the silica boundary was drilled mentioned the physical properties changes due to biogenic silica diagenesis (e.g. Mayer et al., 1992; Mountain et al., 1994; D'Hondt et al., 2003). Several studies have analysed in detail the impact of silica diagenesis on the physical properties of the sediments for specific ODP sites (O'Brien et al., 1989; Littke et al., 1991; Nobes et al., 1992; Guerin and Goldberg, 1996; Gerland et al., 1997; Kim et al., 2007). Other studies have focused on the chemical characterisation of the silica diagenesis transition zone (Kastner et al., 1977; Henrich et al., 1989; Hinman, 1990; Murray et al., 1992a; b; Murray, 1994) or the seismic expression of the diagenetic boundary (Hammond and Gaither, 1983; Larue et al., 1987; Bohrmann and Stein, 1989; Bohrmann et al., 1992; Lee et al., 2003; Volpi et al., 2003). A study of the physical and chemical properties of the opal – A to opal – CT transition zones has not been done so far, despite the silica diagenetic boundaries being present worldwide.

The main aims of the research presented in this chapter are:
- to define the opal – A to opal – CT transition zone;

- to make a characterisation of the transition zones from a physical and chemical point of view.

Establishing what a transition zone represents is imperative because the physical and chemical characterisation of the sediments undergoing silica diagenesis depends on how the transition zone is defined. The physical and chemical characterisation of the transition zones will provide the criteria that could be used to infer the presence of a silica diagenesis front where only limited data are available. This is important because of the implications that the remarkable change in physical properties over a narrow depth range has on sediment compaction, fluid flow in sedimentary basins and overpressure studies.

4.3. Specific data and methodology

Based on the ODP Initial Reports, 33 sites where the silica diagenetic fronts were drilled in Pliocene to Eocene sediments, were selected (Fig. 4.1). A database containing information regarding lithology, physical properties, interstitial water chemistry etc for the interval of interest was compiled. The methodology used for every type of measurement was presented in the ODP technical notes (Fisher and Becker, 1988; Mazzullo and Graham, 1988; Gieskes et al., 1991 and Blum, 1997).

In this study, the transition zone from opal – A to opal – CT ($TZ_{A/CT}$) refers to the depth interval where opal – A and opal – CT silica phases coexist, following the definition of Nobes et al. (1992). This interval is associated with sharp physical properties changes. Qualitatively, the top and base of the $TZ_{A/CT}$ were defined by the depth where there is a great deflection of the curve indicating the variation of a certain physical property. In the case of the porosity curve, for example, the top of the $TZ_{A/CT}$ is defined by a deflection to lower values (a negative deflection), while the base of the $TZ_{A/CT}$ is defined by a subsequent deflection to higher values (a positive deflection) (Fig. 4.2). Quantitatively, the $TZ_{A/CT}$ is defined by the highest gradient between two adjacent values within a specific lithostratigraphic interval, with the exception of isolated peaks.
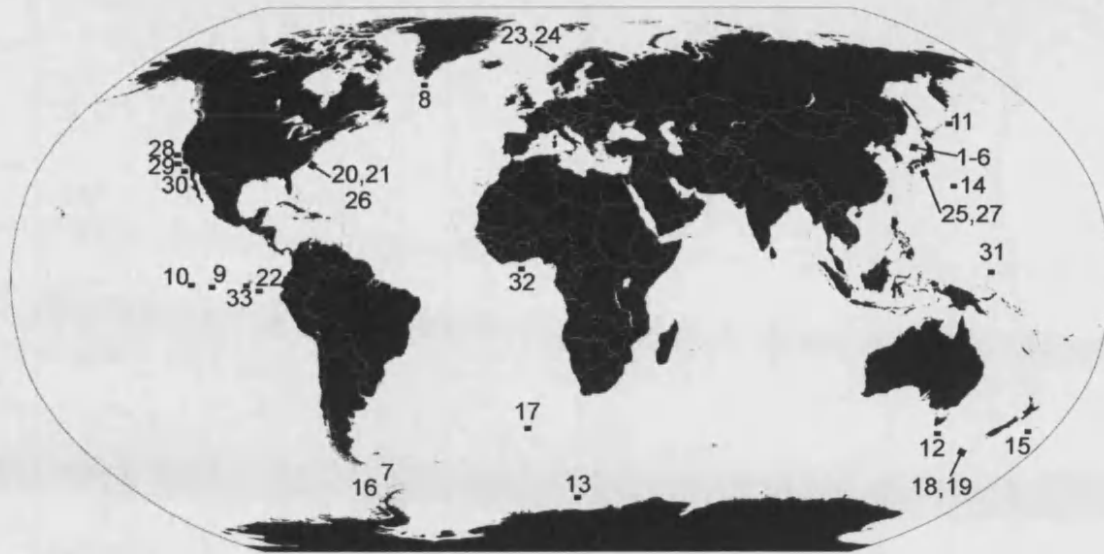
Fig. 4.1. Location map of the Ocean Drilling Program (ODP) sites analysed. 1) 799/128; 2) 794/127; 3) 795/127; 4) 796/127; 5) 797/127; 6) 798/128; 7) 696/113; 8) 647/105; 9) 1226/201; 10) 1225/201; 11) 1207/198; 12) 1170/189; 13) 1165/188; 14) 1149/185; 15) 1122/181; 16) 1095/178; 17) 1090/177; 18) 1171/189; 19) 1172/189; 20) 903/150; 21) 904/150; 22) 846/138; 23) 642/104; 24) 643/104; 25) 1150/186; 26) 902/150; 27) 1173/190; 28) 1022/167; 29) 1016/167; 30) 1010/167; 31) 869/143; 32) 959/159; 33) 847/138.
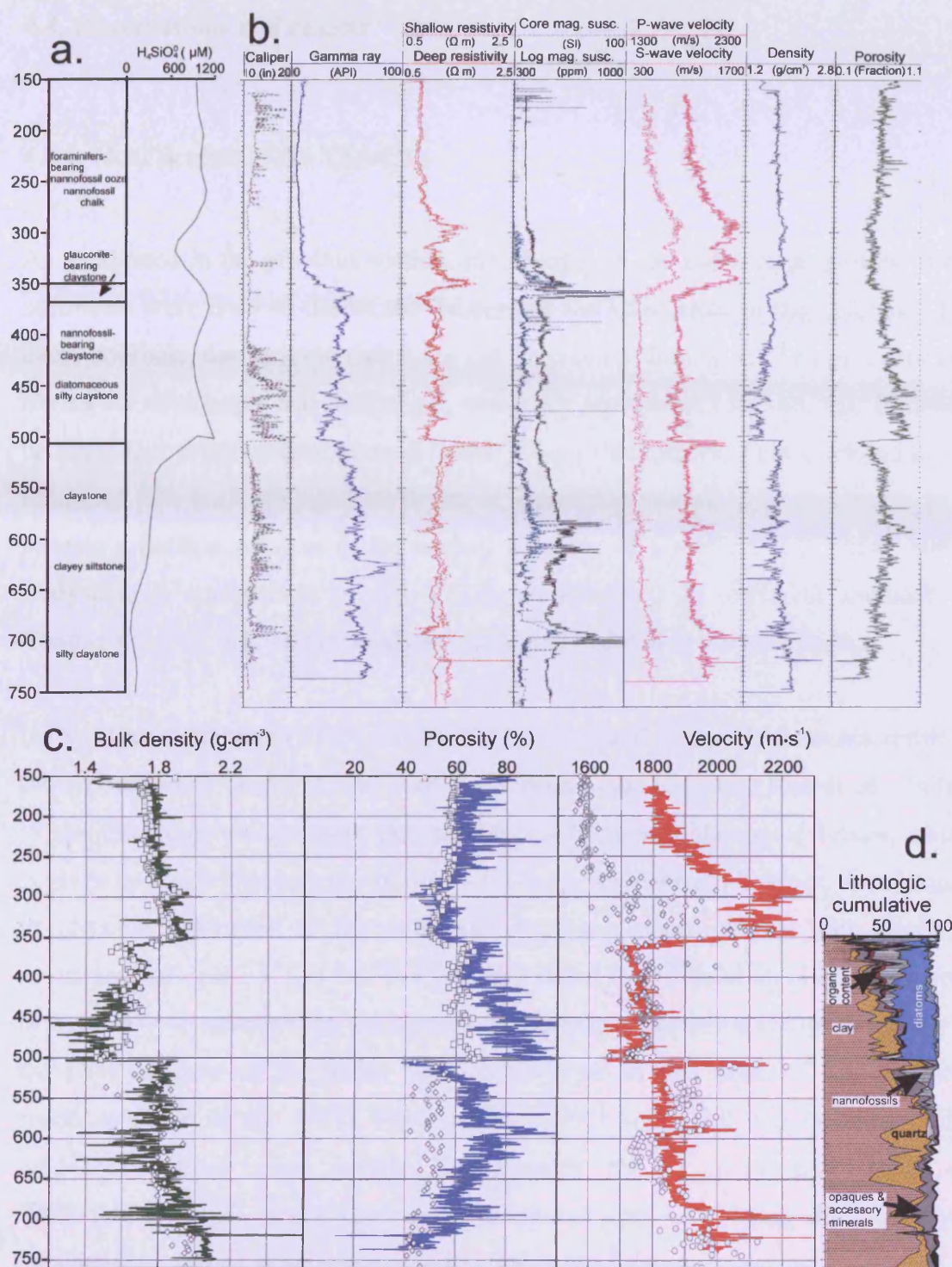
Fig. 4.2. Example of a representative ODP drill site (ODP site 1172/Leg 189) crossing the opal – A to opal – CT boundary (at 500 mbsf in this example) showing the (a) variation of the silica concentration of the interstitial waters with depth (expressed in meters below the seafloor); (b) geophysical logs (caliper, gamma ray, resistivity, magnetic susceptibility, P – wave velocity, bulk density and porosity). Note the sharp contrast of these properties across the opal – A to opal – CT boundary; (c) a comparison of the wet bulk density, porosity and P – wave velocity measured at discrete intervals on core samples (open symbols) and the same properties measured by downhole measurements (curves); (d) the results of the smear – slide analyses of the sediments. Note the disappearance of diatoms at 500 mbsf.

4.4. Observations and results

4.4.1. Identification of the TZA/CT

As mentioned in the previous section, the changes in the physical properties of the sediments were used to define the $TZ_{A/CT}$ for the ODP sites in the database. For every borehole, one or more data types can be used to identify the $TZ_{A/CT}$, every one having its advantages and limitations, which are summarised in Tab. 4.3. It should be noted that every method gives different $TZ_{A/CT}$ thicknesses. This is related to the sampling rate (e.g. chemical analyses of interstitial water), data resolution (e.g. seismic reflection data) or to the limited accuracy of a method (e.g. smear slides analyses). A comparison of the $TZ_{A/CT}$ as identified by different methods is illustrated in Fig. 4.4. The methods are presented in detail in the next section.

(a) X – Ray diffraction (XRD) analyses of opal – A and opal – CT mixtures result in the separation of opal – A and opal – CT peak areas (e.g. von Rad et al., 1978). Where these data are available, they can be used to identify the top of $TZ_{A/CT}$, which is given by the first occurrence of opal – CT in the sediments. However, the changes in physical properties of the sediments do not always coincide with the first occurrence of opal – CT, a fact that was also noted by Nobes et al. (1992) and Rice et al. (1995). In other words, the porosity and density records the abrupt transition in the physical state of the rocks, but not the onset or end point of the chemical reactions (Rice et al., 1995). Nobes et al. (1992) suggested that is because the diagenetic process is not uniform. Consequently, the $TZ_{A/CT}$ identified based on XRD data is usually larger, the first occurrence of opal – CT being shallower than the changes in physical properties used to define the $TZ_{A/CT}$.

(b) Physical properties measurements on discrete core samples, as well as downhole measurements allow a very good identification of the $TZ_{A/CT}$ (e.g. Compton, 1991; O'Brien et al., 1989; Littke et al., 1991; Nobes et al., 1992; Chaika and Williams, 2001; Kim et al., 2007). This is due to their high sampling intervals, 0.75 to 1.5 m for the Moisture and Density Station, usually 2 to 4 cm for the Multisensor Track Station and about 30 cm for the downhole logging tools (Blum, 1997).
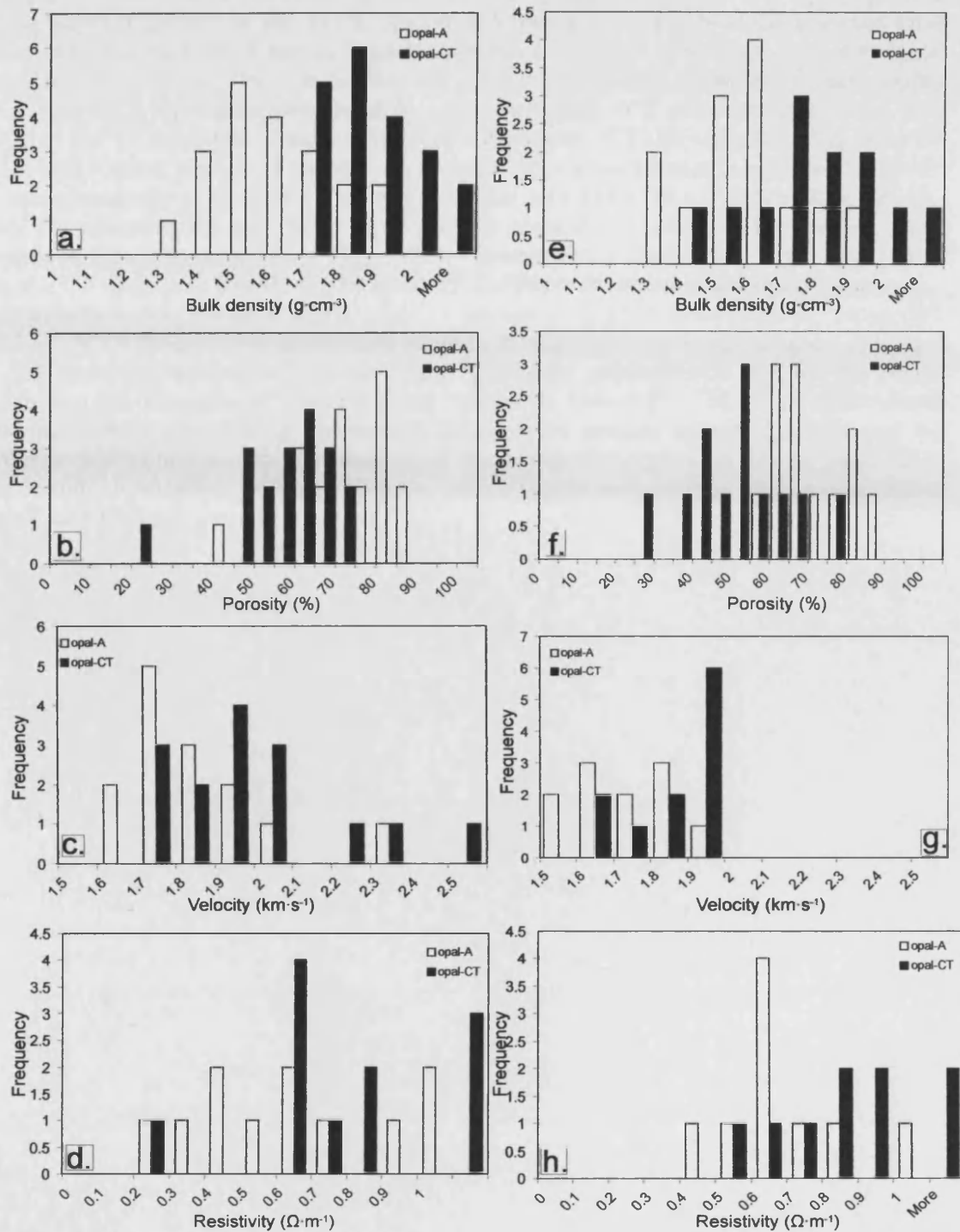
Fig. 4.3. Histograms showing the variation of the mean values of physical properties in the opal – A and opal – CT sediments in clay – rich (a; b; c; d) and carbonate – rich (e; f; g; h) lithologies for all the analysed ODP sites. (a) and (e) bulk density; (b) and (f) porosity; (c) and (g) P – wave velocity; (d) and (h) resistivity. Summary statistics are shown in Appendix A1.1.

Tab. 4.1. *(shown on the next two pages)* Parameters (opal – A to opal– CT depth, age, heat flow, physical properties etc) of the opal–A and opal–CT sediments at the analysed ODP sites. The values were extracted from or computed based on data from the ODP Initial Reports. Mean bio. si. (%) = mean biogenic silica content (wt % – percent of total weight); Por. A or CT (%) = mean porosity of the opal – A or opal – CT rich sediments; Dens. A or CT (g · cm^{-3}) = mean bulk density of the opal – A or opal – CT rich sediments; Vel. A or CT (km · s^{-1}) = mean velocity of the opal – A or opal – CT rich sediments; Res. A or CT (Ω · m) = mean resistivity of the opal – A or opal – CT rich sediments; Dens./Por./Vel./Res. diff. (g · cm^{-3}) = difference between the density / porosity /velocity/ resistivity of the opal – CT and opal – A rich sediments; Temp. TZ$_{A/CT}$ (°C) = present – day temperature of the opal – A to opal – CT diagenetic boundary; Thickness TZ$_{A/CT}$ (m) = thickness of the opal – A to opal – CT transition zone; Geoth. Grad (°C · km^{-1}) = present – day geothermal gradient; Temp. diff. TZ$_{A/CT}$ (°C) = difference of temperature between the top and the base of the opal – A to opal – CT transition zone; Sed. Rate (m · M.y.$^{-1}$) = mean sedimentation rate for the period following the deposition of biogenic silica; Approx th. history (°C · M. y.$^{-1}$) = approximate thermal history representing the product between the present thermal gradient and the average sedimentation rate for the period following the deposition of biogenic silica (according to Mizutani, 1970 and Pisciotto, 1981). Digital data are presented in Appendices A1.2. and A1.3.

No.	Water depth (m)	Lithology	$TZ_{A/CT}$ depth (mbsf)	Age (M. y.)	Mean bio. si.(%)	Porosity A (%)	Porosity CT (%)	Porosity diff. (%)	Dens. A (g·cm^{-3})	Dens. CT (g·cm^{-3})	Dens. diff.(g·cm^{-3})	Vel. A (km·s^{-1})	Vel. CT (km·s^{-1})	Vel. diff. (km·s^{-1})	Res. A (Ω·m)	Res. CT (Ω·m)	Res. Diff. (Ω·m)	Temp. $TZ_{A/CT}$ (°C)	Thickness $TZ_{A/CT}$ (m)	Geoth. Grad (°C·km^{-1})	Heat flow (mW·m^2)	Temp. diff. $TZ_{A/CT}$ (°C)	Sed. Rate (m M.y^{-1})	Approx th. history (C M.y.$^{-1}$)
1	2085	clay	450	8.5	60	77	57	20	1.5	1.8	0.3	-	-	-	-	-	-	46	40	98	77	3.9	70	6.86
2	2822	clay	290	8.5	60	85	70	15	1.27	1.7	0.43	1.6	1.7	0.1	0.4	0.6	0.2	37	40	125	98	5.0	39.5	4.9375
3	3310	clay	325	5	40	80	55	25	1.75	1.85	0.1	-	-	-	-	-	-	43	40	133	113	5.3	56	7.448
4	2596	clay	224	5.5	40	70	55	15	1.55	1.9	0.35	1.7	1.9	0.2	0.6	0.8	0.2	40	30	178	156	5.3	62	11.036
5	2876	clay	300	8	50	85	65	20	1.4	1.8	0.4	1.75	2	0.25	0.4	0.6	0.2	36	30	121	101	3.6	49.5	5.9895
6	911	clay	450	3.4	35	65	55	10	1.7	1.85	0.15	2	2.3	0.3	0.17	0.17	0	37	35	83	98	2.9	121	10.043
7	661	clay	520	11	60	70	45	25	1.45	2	0.55	1.65	1.85	0.2	-	-	-	27	25	52	63	1.3	38	1.976
8	3869	clay	240	28.5	50	75	63	12	1.45	1.8	0.35	1.6	1.65	0.05	-	-	-	8	20	35	-	0.7	20	0.7
9	3297	carb.	370	13	-	80	65	15	1.55	1.7	0.15	1.75	1.8	0.05	0.55	0.75	0.2	25	15	67	48	1.0	15	1.005
10	3772	carb.	275	13	50	80	70	10	1.45	1.55	0.1	1.52	1.55	0.03	0.55	0.65	0.1	8	15	30	15.5	0.5	43	1.29
11	3112	carb.	160	16.5	20	60	55	5	1.9	2.18	0.28	1.5	1.7	0.2	0.45	0.5	0.05		20	-	-	-	5	-
12	2716	carb.	500	37.5	20	62	50	12	1.65	1.8	0.15	1.7	1.9	0.2	-	-	-	28	40	52	56	2.1	10	0.52
13	3549	carb.	600	19.5	20	55	45	10	1.75	2	0.25	1.7	1.85	0.15	0.7	0.9	0.2	32	15	32	51.4	0.5	13.5	0.432
14	5829	clay	180	14	-	70	20	50	1.5	2	0.5	-	-	-	0.9	1.8	0.9	7	28	33	-	0.9	10	0.33
15	4432	clay	585	15	-	40	-	-	1.85	2.05	0.2	2.3	2.5	0.2	-	-	-	-	20	-	-	-	20	-
16	3863	clay	490	6.5	20	57	45	12	1.75	1.9	0.15	1.7	1.9	0.2	0.65	0.7	0.05	15	20	30	-	0.6	110	3.3
17	3710	carb.	290	35	40	83	77	6	1.25	1.35	0.1	-	-	-	-	-	-	2	15	8	-	0.1	30	0.24

18	2159	carb.	340	24.5	30	75	55	20	1.4	1.7	0.3	1.6	1.9	0.3	0.6	2	1.4	21	35	62	68	2.2	8	0.496
19	2633	carb.	500	44	30	65	53	12	1.55	1.75	0.2	1.85	1.9	0.05	1	1.15	0.15	23	35	46.6	55	1.6	18	0.8388
20	703	carb.	1050	25.5	25	65	45	20	1.6	1.9	0.3	1.8	1.9	0.1	-	-	-	42	40	40	-	1.6	12.5	0.5
21	577	clay	525	42.5	20	60	50	10	1.7	1.95	0.25	1.85	2.2	0.35	1	1.5	0.5	21	10	40	-	0.4	12.5	0.5
22	3387	carb.	370	13.5	40	70	60	10	1.55	1.7	0.15	1.75	1.85	0.1	0.55	0.8	0.25	14	20	39	-	0.8	15	0.585
23	1292	clay	275	28.5	40	80	60	20	1.4	1.8	0.4	1.7	1.7	0	-	-	-	11	22	40	-	0.9	18	0.72
24	2768	clay	270	19	60	80	60	20	1.4	1.65	0.25	1.5	2	0.5	-	-	-	11	12	40	-	0.5	30	1.2
25	2692	clay	1050	8.3	35	70	60	10	1.55	1.7	0.15	1.8	2	0.2	1	1.4	0.4	25	25	25	20	0.6	70	1.75
26	808	clay	680	28.5	30	60	45	15	1.85	2.05	0.2	1.9	2	0.1	-	-	-	27	25	40	-	1.0	13	0.52
27	4802	clay	350	3.5	-	65	50	15	1.6	1.8	0.2	1.7	1.8	0.1	0.3	0.55	0.25	60	50	170	180	8.5	52	8.84
28	2325	clay	360	8	10	-	-	-	1.55	1.75	0.2	-	-	-	0.55	0.8	0.25	12	-	-	84	-	-	-
29	4162	clay	300	7.2	-	75	65	10	1.4	1.65	0.25	-	-	-	0.5	0.6	0.1	7	-	-	88	-	30	-
30	3690	clay	180	13.1	70	77	67	10	1.5	1.7	0.2	-	-	-	-	-	-	22	-	122	118	-	15	1.83
31	4838	carb.	140	37.5	-	60	40	20	1.3	1.5	0.2	1.55	1.55	0	-	-	-	-	5	173	-	-	5	0.865
32	2102	carb.	430	31.5	20	60	30	30	1.5	1.9	0.4	1.5	1.75	0.25	0.8	0.9	0.1	22	25	48	56	1.2	-	-
33	3346	carb.	233	8.5	30	-	-	-	1.45	-	-	-	-	-	-	-	-	-	-	-	-	-	-	-

Tab. 4.2. Parameters of the opal – A to opal – CT transition zone (TZ$_{A/CT}$). The abbreviation used represent: No. = the identification number of the ODP site presented in Tab. 4.1, Temp. (°C) = present – day temperature at the depth of the TZ$_{A/CT}$; Thick. TZ$_{A/CT}$ = thickness of the transition zone measured in metres; C = core data; DM = downhole measurements. The last column describes the type of data used to calculate the present – day temperature at the TZ$_{A/CT}$. G.G. = geothermal gradient; Temp. = temperature.

No.	TZ$_{A/CT}$ depth (mbsf)	Temp. (°C)	Thick. TZ$_{A/CT}$ (m)	Method used for TZ$_{A/CT}$ identification	Estimation of temp. of the TZ$_{A/CT}$
1	450	46	40	C	G.G. 95 °C · km^{-1}
2	290	37	40	C	G.G. 125 °C · km^{-1}
3	325	43	40	C	G.G. 132 °C · km^{-1}
4	224	40	30	C	G.G. 171 °C · km^{-1}
5	300	36	30	C	G.G. 121 °C · km^{-1}
6	450	37	35	C	G.G. 138 °C · km^{-1}
7	520	27	25	C	G.G. 53 °C · km^{-1}
8	240	8	20	C	G.G. 35 °C · km^{-1}
9	370	25	15	C	14 °C (based on the temp. log) – 25 C (estimated). G.G. 67 °C · km^{-1}
10	275	8	15	C	Measured by the temp. probe G.G. 30 °C · km^{-1}
11	160	–	20	DM	No data
12	500	28	40	C	G.G. of 52 °C · km^{-1}
13	600	32	15	DM	Measured by the temp. probe G.G. 32 °C · km^{-1}
14	180	31	28	DM	Measured by the temp. probe G.G. 33 °C · km^{-1}
15	585	–	20	DM	No data
16	490	15	20	C	Measured by the temp. probe. G.G. 30 °C · km^{-1}
17	290	2	15	C	G.G. 8 °C · km^{-1} at nearby Site 1094
18	340	21	35	C	G.G. 62 °C · km^{-1}
19	500	23	35	C	G.G. 46.6 °C · km^{-1}
20	1050	15	40	C	G.G. of 14 °C · km^{-1}
21	525	21	10	DM	G.G. of 40 °C · km^{-1}
22	370	14	20	DM	G.G. of 39 °C · km^{-1}
23	275	11	22	C	G.G. of 40 °C · km^{-1}
24	270	11	12	C	G.G. of 40 °C · km^{-1}
25	1050	25	25	DM	Measured by the temp. probe. G.G. 25 °C · km^{-1}
26	680	27	25	C	G.G. of 39 °C · km^{-1}
27	345	60	50	C	Extrapolated from shallower measured temp. G.G. 170 °C · km^{-1}
28	360	12	–	–	Measured by the temperature probe
29	300	7	–	–	Measured by the temperature probe
30	180	22	–	–	G.G. of 122 °C · km^{-1}
31	140		5		G.G. 173 °C · km^{-1}

32	430	16	25	C	G.G. of 51 °C $\cdot$ km^{-1}
33	233	–	–	–	No data

Tab. 4.3. Summary of the advantages and drawbacks of the different methods used to identify the presence and thickness of the $TZ_{A/CT}$.

Data type	Advantages	Disadvantages
XRD analyses	Are relatively accurate indicators of opal – CT occurrence.	Do not represent an exact opal – A indicator (c.f. von Rad et al., 1978). XRD analyses are only available for a limited number of ODP sites.
Physical properties measurements	Have a high sampling rate, allowing an accurate identification of the $TZ_{A/CT}$. Combinations of measurements can be very good indicators of silica diagenesis, especially the resistivity and magnetic susceptibility (e.g. Kim et al., 2007) and resistivity and gamma ray (e.g. Nobes et al., 1992). Are available for most ODP sites.	In some cases, sampling interval problems can arise from poor core recovery. Sediments are not in their in situ conditions for the measurements on core samples. Downhole measurements record the response of an area around the borehole, which is affected by drill – created disturbances. Every downhole logging tool has a characteristic depth of investigation.
Smear slides analyses	Are rough indicators of opal – A presence in the sediments. If no lithological changes are present, the disappearance of opal – A marks the base of the $TZ_{A/CT}$.	Are qualitative rather than quantitative data, so opal – A percentages do not represent absolute values.
Analyses of interstitial water chemistry	The silica concentration in pore waters is a very good indicator of the onset of opal – CT precipitation, marking the top of the $TZ_{A/CT}$. Other elements like Sr^{2+}, Li^+, can indicate the presence of silica diagenesis.	Changes in pore water chemistry are not a good proxy for the $TZ_{A/CT}$ thickness, usually because of the large sampling interval. Cannot accurately define the base of the $TZ_{A/CT}$. Are not available for all the sites.
Lithological description of cores	The presence of a first porcelanite or chert layer in diatomaceous sediments roughly indicates the top of the $TZ_{A/CT}$.	Do not allow an exact identification of the $TZ_{A/CT}$.
Seismic reflection data	Can be used, in some cases, to identify the presence of silica diagenesis, especially if the reflection from the diagenetic front crosscuts stratigraphy (e.g. Volpi et al., 2003).	The $TZ_{A/CT}$ is usually below the resolution of the data.
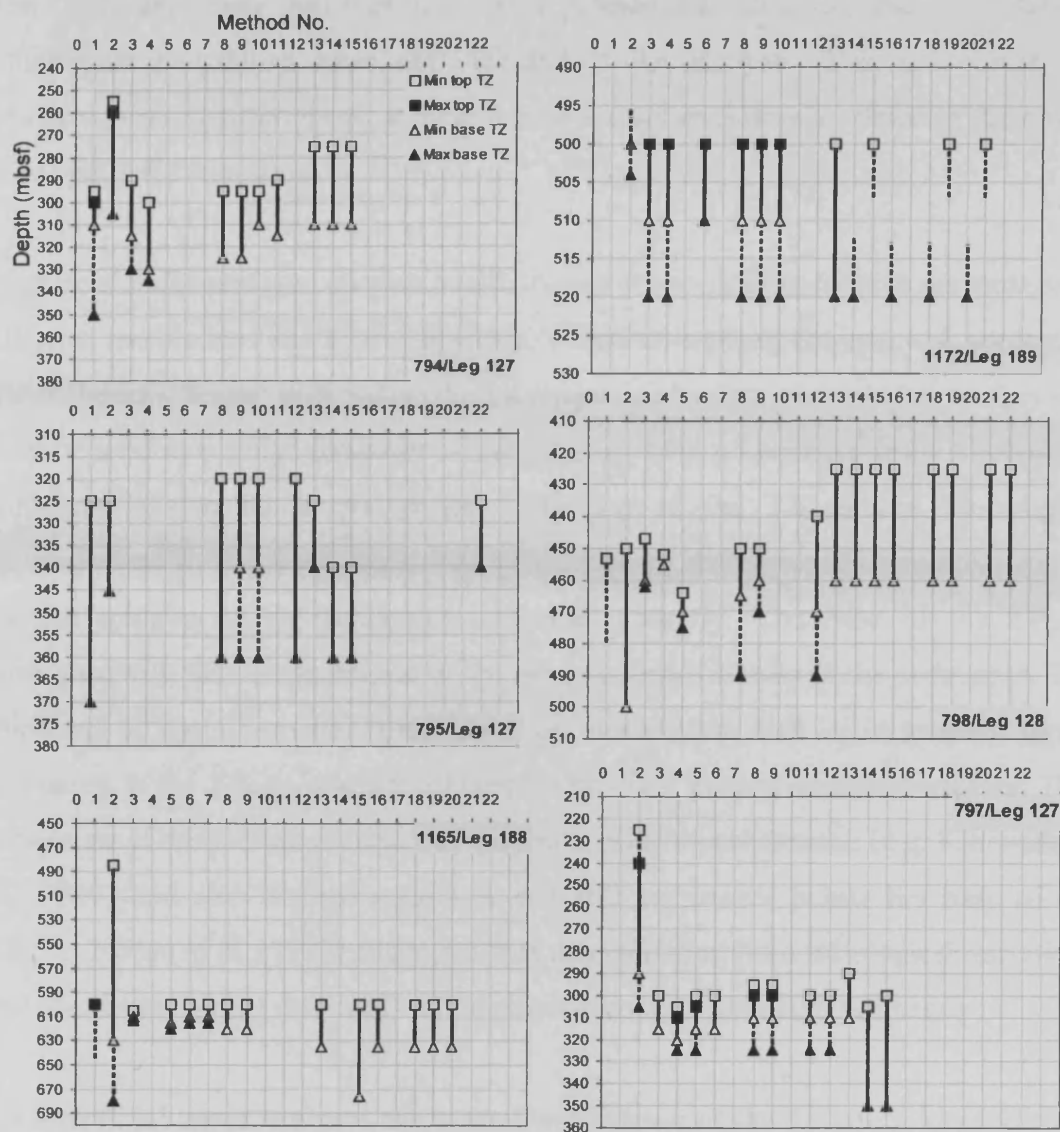
Fig. 4.4. Comparison of the thickness of the $TZ_{A/CT}$ determined based on different methods for six representative ODP sites. The ordinate of the graphs represents the depth (mbsf). The numbers on the abscissa represent different methods used for the identification of the $TZ_{A/CT}$ thickness where 1 = XRD analyses; 2 = smear slides analyses; 3 – 7 = downhole measurements (3 = bulk density; 4 = P – wave velocity; 5 = gamma ray; 6 = porosity; 7 = resistivity); 8 – 12 = measurements on discrete core samples (8 = wet bulk density; 9 = porosity; 10 = P – wave velocity; 11 = gamma ray; 12 = thermal conductivity); 13 – 22 = pore water chemistry analyses (13 = silica; 14 = lithium; 15 = strontium; 16 = salinity; 17 = pH; 18 = calcium; 19 = magnesium; 20 = potassium; 21 = manganese; 22 = alkalinity).

The ODP sites where the onset of silica diagenesis coincides with unconformities or lithological boundaries were not included in the analysis. This is because the physical properties variations at these depths are not exclusively related to the opal – A to opal – CT transition.

(c) Smear slides analyses allow a qualitative estimation of the relative percentage of diatoms, radiolarians and sponge spicules, which are a proxy for opal – A content of the sediments. Smear slide values do not represent absolute percentages, so they can only be used as a rough indicator of the $TZ_{A/CT}$ where no changes from siliceous to carbonate – rich facies are present. The top of the $TZ_{A/CT}$ can be roughly approximated to the depth where the proportion of diatoms and/or radiolarians or sponge spicules in the sediments decreases abruptly. The base of the $TZ_{A/CT}$ coincides with the disappearance of the siliceous microfossils in the sediments. The thickness of the $TZ_{A/CT}$ identified based on smear slide data is, in general, larger compared to the $TZ_{A/CT}$ identified based on physical properties measurements. This is because of the limited accuracy of the smear slide measurements (e.g. Kinoshita et al., 2009) and also because opal – A can still be present below the base of the $TZ_{A/CT}$. Nobes et al. (1992) suggested that this can arise from lithological variations and also from the fact that opal – CT precipitation does not occur uniformly.

(d) Interstitial water analyses allow the identification of the $TZ_{A/CT}$, a key indicator being the concentration of silica (e.g. Murray et al., 1992). High concentration of dissolved silica of the interstitial water reflects the dissolution of the siliceous microfossils (opal – A). A sharp decrease in the silica concentration marks the onset of opal – CT precipitation and the top of the $TZ_{A/CT}$. The disappearance of silica from the pore waters usually coincides with the precipitation of quartz and the end of the silica diagenesis process. Due to the porosity and permeability changes associated with opal – CT precipitation, other interstitial – water chemical profiles may be affected (Murray et al., 1992). These profiles include Sr^{2+}, Li^+, Cl^- etc. (e.g. Gieskes et al., 1991). Interstitial water analyses are available for a limited number of boreholes of the database. Where available, the thickness of the $TZ_{A/CT}$ identified based on these data is larger compared to the $TZ_{A/CT}$ identified based on physical

properties measurements (Fig. 4.4). This could be due to the large sampling interval that does not allow an accurate identification of the $TZ_{A/CT}$.

(e) Lithological description of cores can offer a rough estimate for the top of the $TZ_{A/CT}$. The appearance of the first porcelanite or chert layer in diatomaceous sediments usually coincides with the onset of silica diagenesis and the top of the $TZ_{A/CT}$ (e.g. Behl and Garrison, 1994). These data were only used as a first indication of the presence of silica diagenesis, and are not sufficient to accurately define the $TZ_{A/CT}$.

(f) On seismic reflection data, the transition from opal – A to opal – CT is usually marked by a reflection, due to the bulk density and acoustic velocity contrast between the two opal phases (e.g. Hammond and Gaither, 1983; Bohrmann et al., 1992). However, due to its thin thickness, the $TZ_{A/CT}$ is, in general, below the resolution of the seismic data.

4.4.2. The TZA/CT

4.4.2.1. Overview

The depth of the $TZ_{A/CT}$ is within the range of 90 to 1050 metres below seafloor (mbsf). At most drill sites, the $TZ_{A/CT}$ are located at a depth between 200 and 600 mbsf (Fig. 4.5 and Tab. 4.1). It should be noted that this is the present – day burial depth, and, in the cases where erosion and/or uplift is part of the burial history, it is plausible that this is not the maximum burial depth attained by the sediments.

The thickness of the $TZ_{A/CT}$ varies between 5 and 50 m, the mean value being 26 m (Fig. 4.6a). Remarkably, it was found that all values are less than 40 m, only Site 1173/Leg 190 having a $TZ_{A/CT}$ of about 50 m thick. The sediments in which the $TZ_{A/CT}$ is embedded have biogenic silica contents between 10 and 60 %, with the exception of site 1010/Leg 167 where it reaches 70 % (Fig. 4.6b). An important observation is that the thickness of the $TZ_{A/CT}$ in boreholes with different dominant

lithology (clay – or carbonate – rich) or with different age falls within the same range of values (Fig. 4.6a). No correlation was found between the biogenic silica content of the sediments and the thickness of the $TZ_{A/CT}$ (Fig. 4.7a).

However, when the $TZ_{A/CT}$ thickness was compared with the temperature values, a very good correlation between the two datasets was found (Correlation coefficient = 0.75 for all sites; 0.83 for the sites with clay – dominated lithology and 0.48 for sites with carbonate – dominated lithology), the thicker $TZ_{A/CT}$ corresponding to higher temperature values (Fig. 4.7b).

4.4.2.2. Physical properties of the $TZ_{A/CT}$ sediments

(a) The bulk density contrast across the transition zone varies between 0.05 and 1 g $\cdot$ cm^{-3}, the mean value being 0.29 g $\cdot$ cm^{-3} (Tab. 4.1 and Fig. 4.8a). The values are higher for the sites with carbonate – dominated lithologies than for clay – dominated lithologies (Tab. 4.1).

The bulk density values of the opal – A sediments are within the range 1.25 to 1.9 g $\cdot$ cm^{-3}, with a mean value of 1.5 g $\cdot$ cm^{-3}, while those of the opal – CT sediment are between 1.35 and 2.3 g $\cdot$ cm^{-3}, with a mean value of 1.8 g $\cdot$ cm^{-3}. A weak correlation was found between the density difference across the $TZ_{A/CT}$ and the biogenic silica content of the sediments (correlation coefficient = 0.27 for all sites, 0.5 for sites with clay – dominated lithology, however, no correlation for sites with carbonate – dominated lithology): the higher biogenic silica contents of the sediments, the higher the density difference across the $TZ_{A/CT}$ (Fig. 4.9a). In addition, a correlation exists between the density contrast across the $TZ_{A/CT}$ and the $TZ_{A/CT}$ thickness (correlation coefficient = 0.34 for all sites, 0.24 for sites with clay – dominated lithology and 0.4 for sites with carbonate – dominated lithology). The higher density contrast across the $TZ_{A/CT}$ corresponds to thicker $TZ_{A/CT}$ (Fig. 4.10a).

(b) The porosity contrast across the transition zone varies between 5 and 40 %, the mean value being 15 % (Tab. 4.1 and Fig. 4.8b). The difference has higher values for clay – dominated lithologies than for carbonate – dominated lithologies. The

60

porosities of the opal – A sediments are within the range 40 and 85 % and those of the opal – CT sediment within the range 30 to 77 %. A good positive correlation between the biogenic silica content of the sediments and the porosity difference from opal – A to opal – CT only for the sites with a clay – dominated lithology (correlation coefficient = 0.6) (Fig. 4.9b). A weak correlation (correlation coefficient 0.34) exists between the porosity difference across the $TZ_{A/CT}$ and its thickness (Fig. 4.10b).

(c) The difference in the P – wave velocity across the $TZ_{A/CT}$ varies from 0 to 0.5 km · s^{-1}, the mean value being 0.17 km · s^{-1} (Tab. 4.1 and Fig. 4.8c). The velocity contrast falls within similar ranges of values for both clay – and carbonate – dominated lithologies. The typical velocity values in the opal – A sediments are 1.5 to 2.3 km · s^{-1}, with a mean of 1.7 km · s^{-1} and, in the opal – CT sediment, 1.55 to 2.5 km · s^{-1}, with a mean of 1.9 km · s^{-1}. No correlations were found between the velocity contrast across the $TZ_{A/CT}$ and its thickness or the biogenic content of the sediments (Figs. 4.10c and 4.9c).

(d) The resistivity contrast across the $TZ_{A/CT}$ is between 0 and 1.4 Ω · m, with the mean value of 0.27 Ω · m (Tab. 4.1 and Fig. 4.8d). Similar to the porosity values, the resistivity difference has higher values for clay – dominated lithologies than for carbonate – dominated lithologies. The opal – A sediment resistivity is between 0.17 and 1 Ω · m, the mean value being 0.61 Ω · m. The opal – CT sediment resistivity is between 0.17 and 2 Ω · m, with a mean value of 0.88 Ω · m. No correlation was found between the resistivity contrast across the $TZ_{A/CT}$ and its thickness or the opal – A content of the sediments (Figs. 4.10d and 4.9d).

	Clay-rich	Carbonate-rich	All sites
Mean	402.2	400.6	401.6
Standard Error	46.1	66.9	37.7
Median	337.5	370.0	350.0
Mode	450.0	370.0	370.0
Standard Deviation	205.9	241.2	216.8
Sample Variance	42414.7	58175.8	47000.3
Kurtosis	4.1	4.0	3.3
Skewness	1.8	1.6	1.6
Range	870.0	960.0	960.0
Minimum	180.0	90.0	90.0
Maximum	1050.0	1050.0	1050.0
Sum	8044.0	5208.0	13252.0
Count	20.0	13.0	33.0
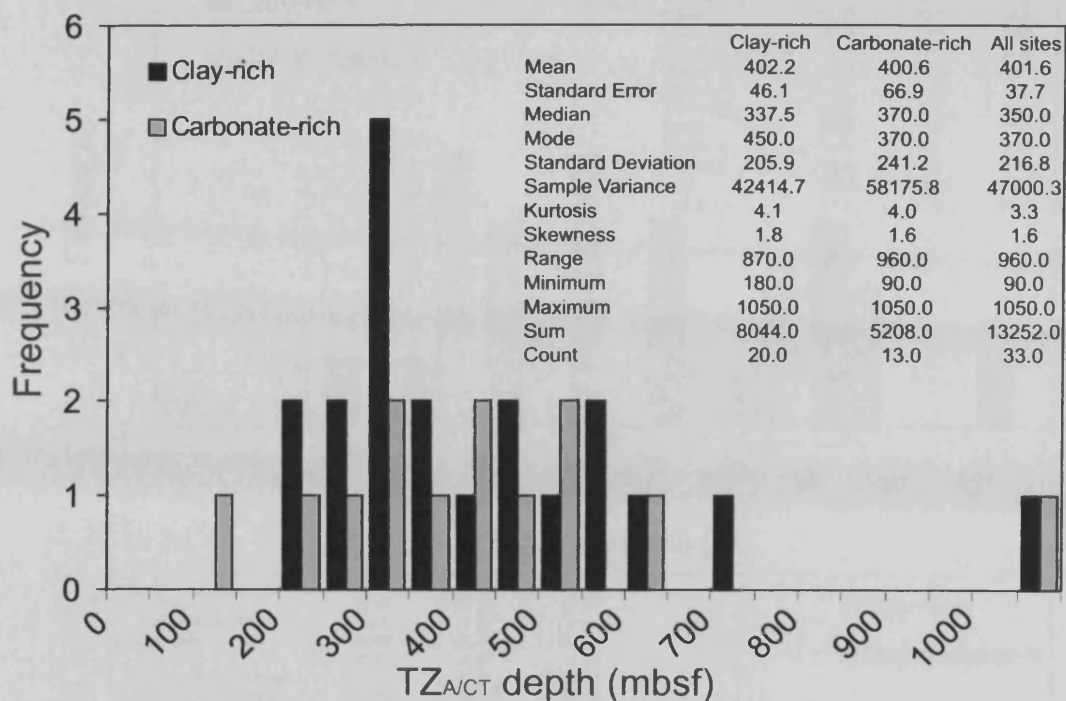
Fig. 4.5. Histogram showing the distribution of the $TZ_{A/CT}$ depth (metres below sea floor) in clay – rich sediments (black bars) and carbonate – rich sediments (grey bars). Summary statistics for both cases are also shown, together with the summary statistics for all the ODP sites, regardless of their dominant lithology.
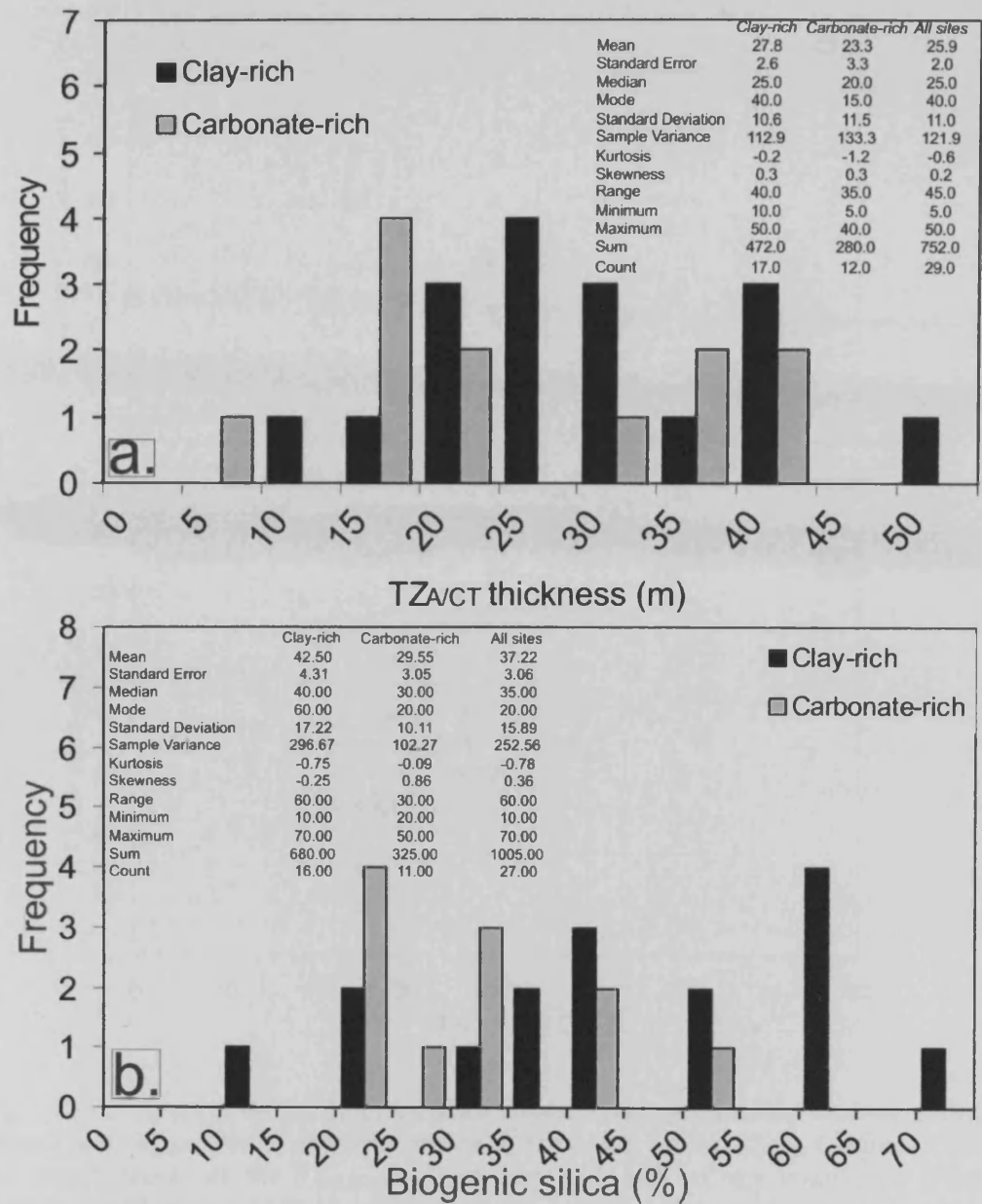
Fig. 4.6. Histograms showing the distribution of (a) the TZ$_{A/CT}$ thickness (measured in metres) and (b) biogenic silica content (measured in percentage of the total weight) in clay – rich sediments (black bars) and carbonate – rich sediments (grey bars). Corresponding summary statistics are are also shown.
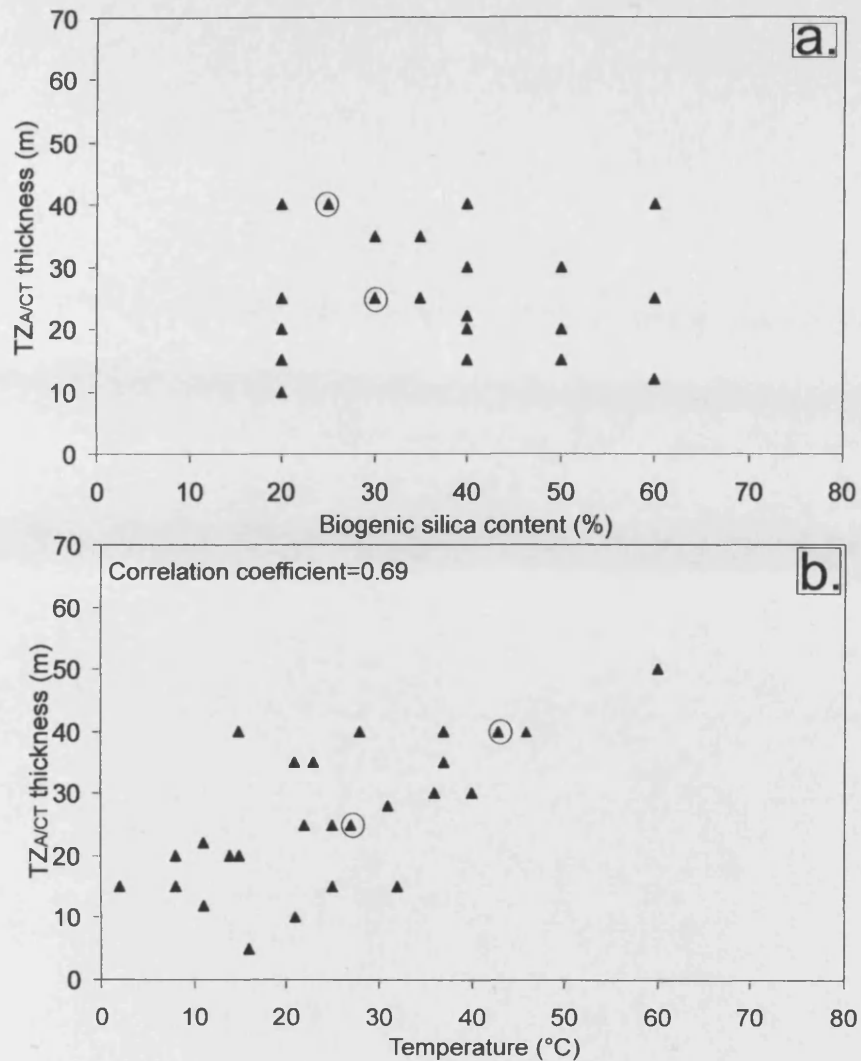
Fig. 4.7. Cross – plots of the (a) biogenic silica content (percentage of the total weight of the sediment) and (b) present – day temperature at the depth of the $TZ_{A/CT}$ (degrees Celsius) versus the thickness of the $TZ_{A/CT}$ (metres). Note the lack of any correlation (Pearson correlation coefficient = 0.08) in case (a) and the presence of a good correlation (Pearson correlation coefficient = 0.75) in case (b). Circled data points refer to sites 902/Leg 150 and 903/Leg 150 where the position of the $TZ_{A/CT}$ is uncertain due to the presence of unconformities. These data points might not be representative for the analysis.
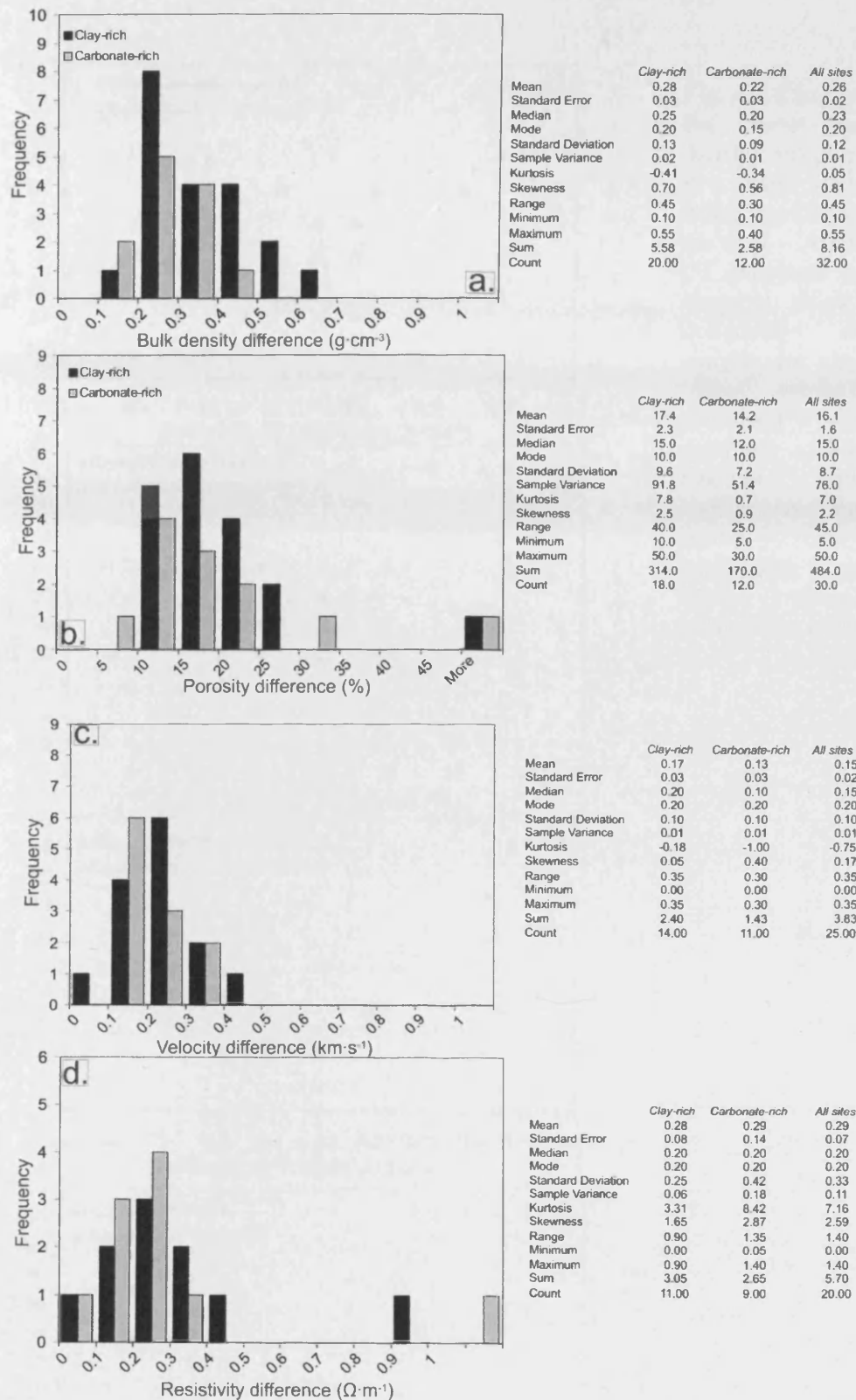
Fig. 4.8. Histograms showing the distribution of the mean (a) bulk density; (b) porosity; (c) P – wave velocity; (d) resistivity differences of the opal – A and opal – CT sediments for clay – rich (black bars) and carbonate – rich (grey bars) lithologies. Corresponding summary statistics are also shown.
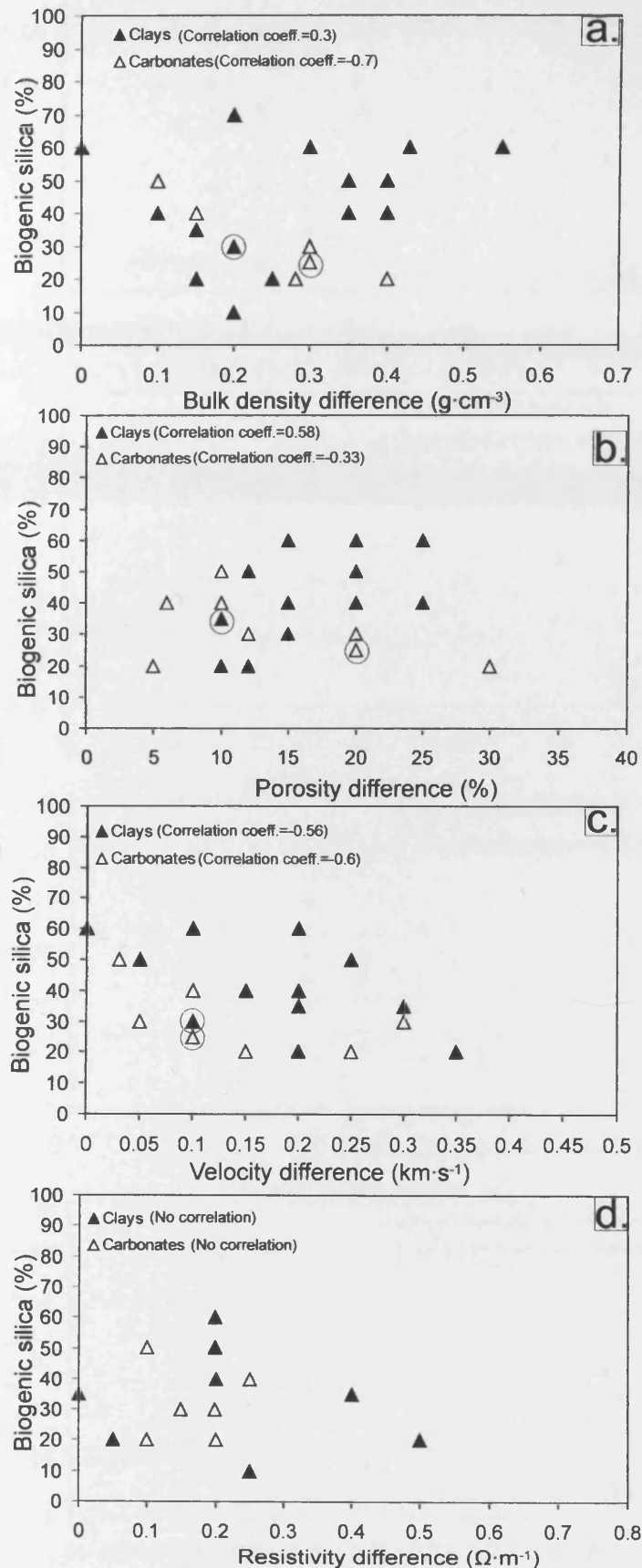
Fig. 4.9. Cross – plots of the mean (a) bulk density; (b) porosity; (c) P – wave velocity; (d) resistivity differences of the opal – A and opal – CT sediments versus the biogenic silica content (percentage of total weight) for clay – rich (filled symbols) and carbonate – rich (open symbols) lithologies. Pearson correlation coefficients are also shown. For the explanation of the circled data points please refer to Fig. 4.7.
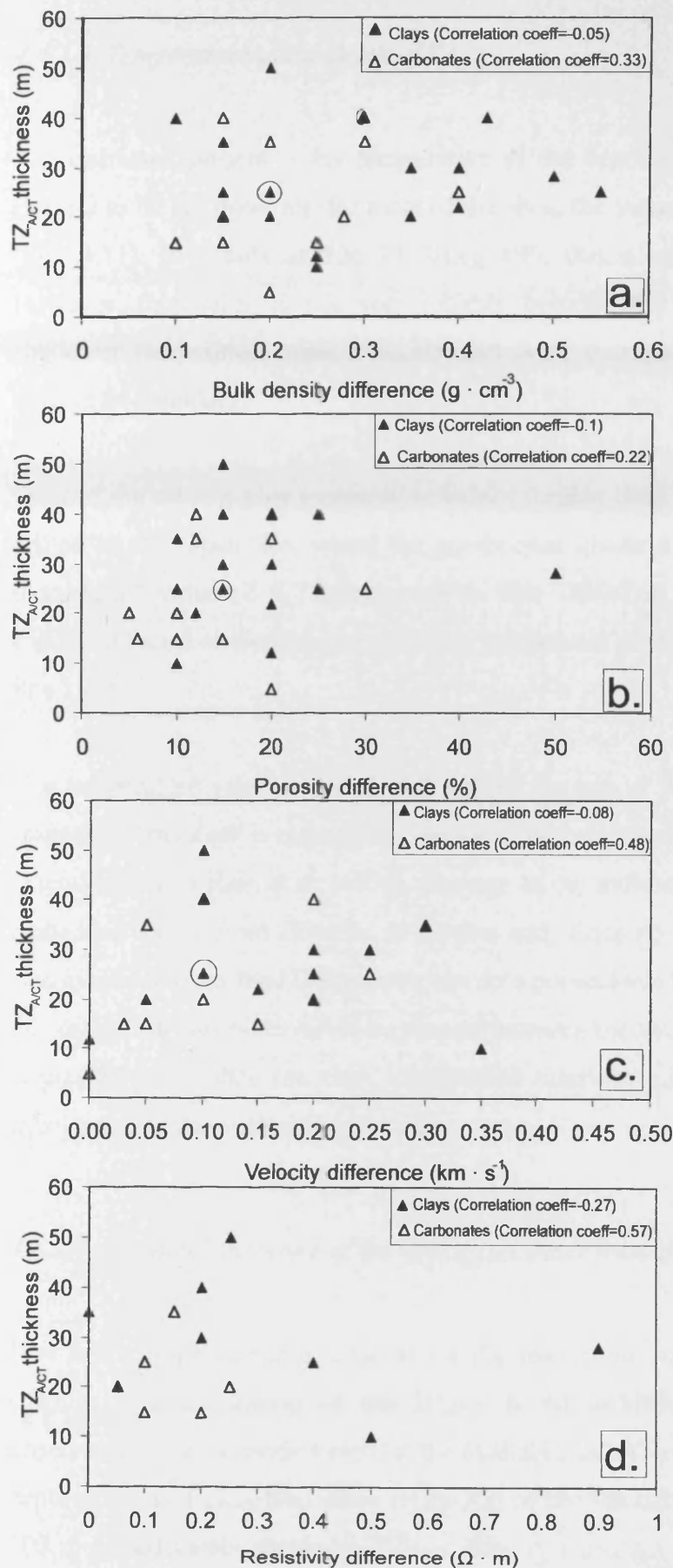
Fig. 4.10. Cross – plots of the mean (a) bulk density; (b) porosity; (c) P – wave velocity; (d) resistivity differences of the opal – A and opal – CT sediments versus the thickness of the $TZ_{A/CT}$ for clay – rich (filled symbols) and carbonate – rich (open symbols) lithologies. Pearson correlation coefficients are also shown. For the explanation of the circled data points please refer to Fig. 4.7.

4.4.2.3. Temperature at the depth of $TZ_{A/CT}$

The estimated present – day temperature at the depth of the $TZ_{A/CT}$ is within the range 2 to 60 °C, however, for most of the sites, the values are between 7 and 46 °C (Fig. 4.11). It is only at Site 1173/Leg 190, that a value of 60 °C was found. However, this value is not very reliable because the temperature is based on shallower temperature measurements that were extrapolated to the depth of the diagenetic boundary.

Most of the other higher temperature values (higher than 35 °C) are from boreholes drilled in the Japan Sea, where the geothermal gradient is very high. The lowest temperature value (2 °C) corresponds to Site 1090/Leg 177, Antarctica, and was estimated based on the anomalously low geothermal gradient (8 °C · km^{-1}) at nearby Site 1094.

The temperature values were plotted against the age of the sediments in which the diagenetic boundary is embedded. The result is shown in Fig. 4.12 and represents an extended plot of Hein et al. (1978). The age of the sediments in which the $TZ_{A/CT}$ is embedded varies from Pliocene to Eocene and, since no precise age determination was available from the ODP reports, the data points have large errors bars. Even so, no correlation was observed to be present between the two variables. No correlation is present even when the clay – dominated lithology and carbonate – dominated lithology sites are evaluated separately.

4.4.2.4. Chemical signature of the interstitial water from the $TZ_{A/CT}$ sediments

Due to the large sampling interval for the interstitial water analyses, an accurate chemical characterisation of the $TZ_{A/CT}$ is not achievable. Nevertheless, some observations can be made based on the available data (Tab. 4.4). At all the sites the concentration of dissolved silica ($H_4SiO^0_4$) of the interstitial water increases in the 100 m of sediments above the $TZ_{A/CT}$, then it decreases abruptly at the top of the $TZ_{A/CT}$. In general, this decrease reduces the silica concentration below the top of the

$TZ_{A/CT}$ to less than half the concentration above the $TZ_{A/CT}$. Other profiles, like alkalinity, calcium (Ca^{2+}) and potassium (K^+) show systematic changes across the $TZ_{A/CT}$. With the exception of Site 1170/Leg 189, the alkalinity profiles decrease across the $TZ_{A/CT}$. The Ca^{2+} concentrations increase across the $TZ_{A/CT}$, with the exception of Site 1172/Leg 189, while the K^+ concentrations decrease, except at Site 1165/Leg 188. Other interstitial – water chemical profiles show variations across the $TZ_{A/CT}$, however these are not consistent at the analysed sites (Tab. 4.4). At most sites the lithium concentrations (Li^+) and pH increase with depth, across the $TZ_{A/CT}$, while the strontium (Sr^{2+}), sodium (Na^+) and chlorine (Cl^-) concentrations decrease.
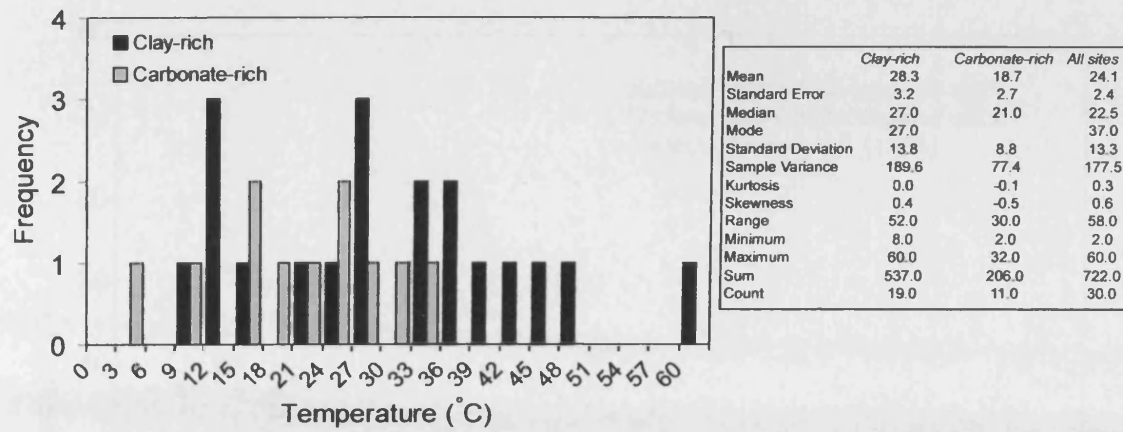
Fig. 4.11. Histogram illustrating the distribution of the present – day temperature (degrees Celsius) at the depth of the TZA/CT for clay – rich (black bars) and carbonate – rich (grey bars) lithologies. Summary statistics are also shown.
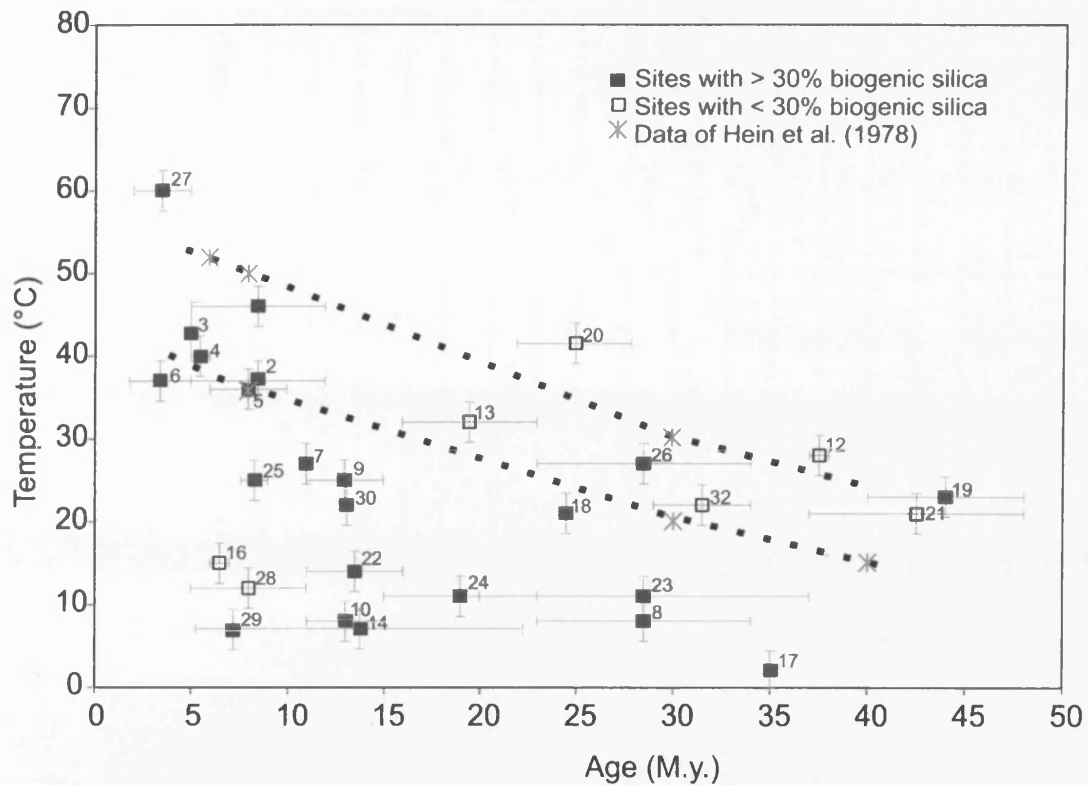
Fig. 4.12. Relationship between present – day temperatures (degrees Celsius) at the depth of the $TZ_{A/CT}$ and age of the corresponding sediments (million years) for ODP sites with more than 30 % biogenic silica (filled symbols) and less than 30 % biogenic silica (open symbols). The data from Hein et al. (1978) are shown for comparison. The number next to every data point corresponds to the site number in Fig. 4.1. The x-error bars represent the possible age range of the sediments; the y-error bars represent standard errors. The dotted lines represent the limits of opal – CT stability as defined by Hein et al. (1978). It can be observed that the data points of the ODP sites analysed in this study approximately correspond only to the top of this stability zone.

Tab. 4.4. Variation of different interstitial water elements molar concentration across the transition from opal – A to opal – CT sediments. μM = micromolar; mM = millimolar; D = decrease in concentration from the opal – A to opal – CT sediments; I = increase in concentration from the opal – A to opal – CT sediments. No. = the identification number of the ODP site presented in Tab. 4.1.

No	Silica (μM)	Lithium (μM)	Strontium (μM)	Chlorine (mM)	Sodium (mM)	pH	Calcium (mM)	Potassium (mM)	Alkalinity (mM)
1	D 1600/800	No data	No data	No data	No data	No data	No data	No data	No data
2	D 1400/700	I 100/200	D 275/160	D 525/505	No data	I 5.5/6.5	I 5/7	D 5/4	D 20/10
3	D 1500/750	I 80/90	I 80/100	No data	I 440/470	I 7.4/7.6	No data	D 3.5/2.5	No data
4	No data	I 160/250	I 150/200	No data	No data	D 7.75/7.55	No data	D 6.5/3.5	D 15/10
5	D 1500/650	No data	No data	No data	No data	No data	No data	No data	No data
6	D 1250/800	D 95/80	I 100/140	No data	No data	No data	No data	D 4/3	D 15/10
7	No data	D 900/790	I 150/215	No data	No data	No data	I 11/13	D 13/10.5	D 22/19
9	D 1250/500	No data	No data	No data	No data	No data	No data	No data	No data
10	D 1050/1000	I 17.5/20	D 1250/225	No data	No data	No data	I 10/12	No data	D 3/2
11	D 700/450	No data	D 175/160	No data	No data	No data	No data	No data	No data
12	D 1150 to 190	I 17.5/19	D 260/240	D 565/558	D 482/472	No data	I 11.2/11.8	D 10.9/10.8	D 4.2/ 4.1
13	D 800/400	I 50/400	D 800/350	D 550/500	D 470/430	I 7.58/7.81	I 14/14.8	D 9/5	I 3.9/4.8
14	No data	D 70/25	D 260/100	No data	D 455/440	No data	I 30/40	I 2/4	D 3.5/2.5
16	D 900/850	No data	No data	No data	No data	No data	No data	No data	No data
17	D 1100/900	No data	D 130/120	No data	No data	No data	I 60/70	D 4/3	D 3.5/2
18	D 1050/650	I 32/57	I 350/850	I 565/570	I 480/485	I 7.85/7.9	I 20/38	D 9/6	D 2.5/2
19	D 1000/400	I 80/120	D 340/290	D 555/548	D 485/474	I 7.45/7.6	No data	No data	D 7/5.6
20	D 1380/800	D 540/430	D 375/275	D 575/500	D 480/415	I 7/7.75	D 27/22	D 7.5/ 4.2	D 10/4
21	D 1500/850	No data	I 820/980	No data	No data	No data	I 28/34	D 12.2/11.5	No data

72

22	D 1300/650	No data	I 390/430	I 920/930	No data	I 6.5/6.7	I 16.5/17	D 10.7/10.2	D 26/22
23	No data	I 20/22	D 210/190	No data	No data	No data	I 10/12	D 10/8	D 3.4/2
26	No data	D 370/340	I 220/240	D 320/310	No data	No data	I 17/20	D 6.2/6	D 6/3.5
27	D 1100/200	No data	No data	No data	No data	No data	No data	No data	No data
28	No data	No data	No data	D 563/553	D 510/480	No data	No data	D 5/3	No data
32	D 1000/800	No data	No data	No data	No data	No data	No data	No data	No data
33	No data	I 20/22	D 380/370	No data	No data	No data	I 18/20	D 6.5/6	D 19/17

4.5. Discussion

4.5.1. Criteria for identifying the TZA/CT

According to ODP data, the $TZ_{A/CT}$ can be found, typically, but not exclusively, at 200 to 600 mbsf, in sediments of Pliocene to Eocene age and at present – day temperatures between 2 and 60 °C. Based on the observation presented in the previous section, if the following criteria are fulfilled, then the presence of a silica diagenesis transition zone is possible.

- The smear slide data should confirm that siliceous microfossils are present in a proportion higher than 10 %, regardless of the dominant lithology (clay or carbonate).

- The profile of silica concentration in the interstitial water should increase with depth, because of the dissolution of siliceous microfossils (opal – A), then it should decrease sharply, due to opal – CT precipitation. According to the observations made, the silica concentration generally decreases to half its value.

- If on the lithostratigraphic profile this sharp decrease in silica concentration does not correspond to a facies change (e.g. siliceous to carbonate – rich) or an unconformity, then the presence of a silica diagenesis transition zone is probable.

- By examining the physical properties profiles, $TZ_{A/CT}$ can be accurately defined due to the physical properties contrast. Generally, the bulk density and the compressional velocity increase and the porosity decreases. Other profiles, such as resistivity or thermal conductivity are also likely to change because of the porosity variation.

- If XRD analyses are available, they can confirm the presence of opal – CT in the $TZ_{A/CT}$ sediments. However, it was observed that the first occurrence of opal – CT usually precedes the sharp change of the physical properties.

- Other chemical profiles, such as the pH, alkalinity, potassium, calcium, sodium and chlorine profiles systematically change across the $TZ_{A/CT}$, suggesting they might also reflect the silica diagenesis.

- If seismic data are available, the $TZ_{A/CT}$ is usually marked by a single reflection. Due to its narrow thickness, it is, in general, below the resolution of the seismic data, for its top and base to be imaged by two separate reflections.

4.5.2. What controls the thickness of the TZA/CT?

The controlling factors of silica diagenesis are temperature, sediment age, host sediment lithology, pore water chemistry etc. (e.g. Kastner et al., 1977; Hein et al., 1978; Keller and Isaacs, 1985; Williams et al., 1985), so it is likely that they also control the $TZ_{A/CT}$ thickness. The temperature is the most important control, the reaction rate depending exponentially on temperature as expressed by the Arrhenius equation (e.g. Atkins and de Paola, 2006). This means that a reaction can become instantaneous in geological time at high temperature (e.g. Giles, 1997).

One of the most important observations is that all the sites examined in this study have thin $TZ_{A/CT}$ thicknesses (generally less than 40 m), regardless of the dominant lithology of the host sediments, their age or their biogenic silica content. This implies that the dominant controlling factor is a first – order control, which can be either the temperature or the pressure. According to Littke et al. (1991), a thin (about 20 m in their case) opal – A to opal – CT transition zone implies that the temperature is the dominant control of the $TZ_{A/CT}$ thickness, local variations in sediment and pore – water chemistry having only minor importance.

Based on the existing literature, the pressure is not listed as one of the controlling factors of silica diagenesis (e.g. Hein et al., 1978), and this was confirmed by the absence of any correlation between the overburden pressure and the $TZ_{A/CT}$ thicknesses (Fig. 4.13a). In contrast, the very good correlation (Correlation coefficient = 0.75) between the thickness of the $TZ_{A/CT}$ and the present – day temperatures (Fig. 4.7b) supports the hypothesis that temperature is the controlling factor of the $TZ_{A/CT}$ thickness.
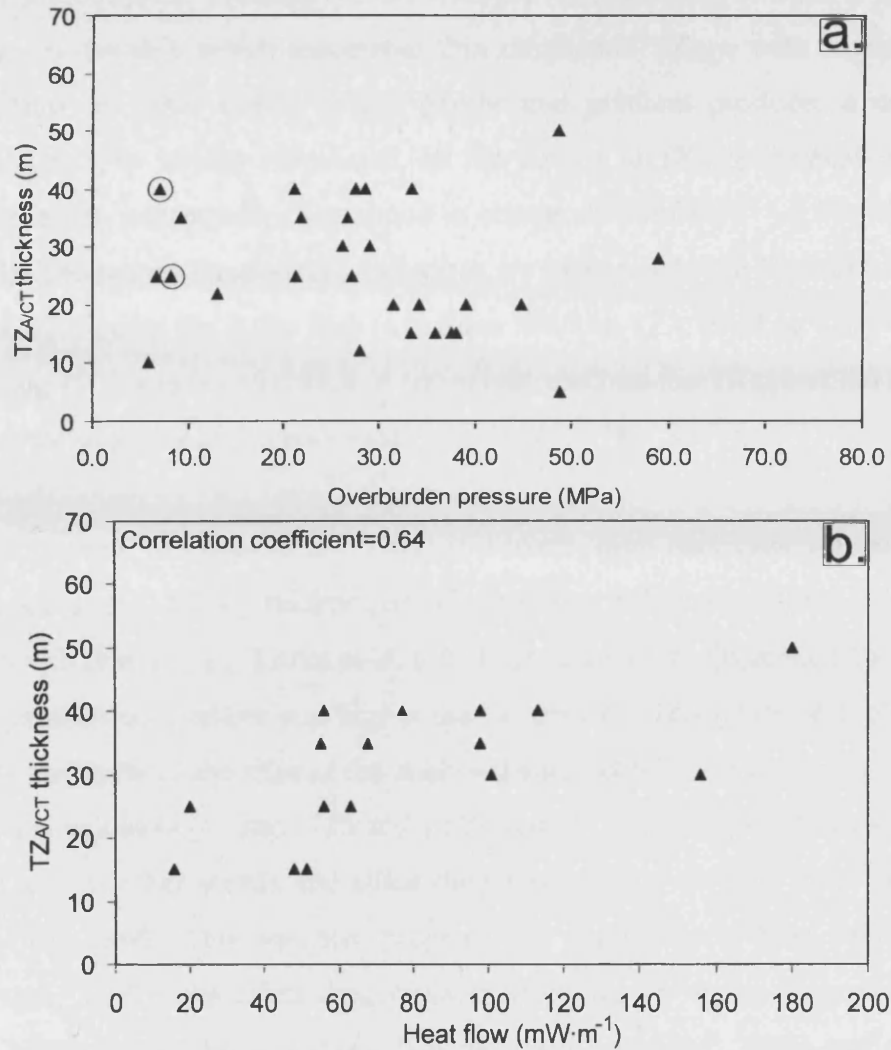
Fig. 4.13. Cross – plots of the (a) overburden pressure (megapascals) and (b) present – day heat flow (milliwatt per metre) versus the thickness of the $TZ_{A/CT}$ (metres) at the ODP sites analysed. Note the lack of any correlation in case (a) and the presence of a good correlation (Pearson correlation coefficient = 0.64) in case (b). For the explanation of the circled data points please refer to Fig. 4.7.

This result might appear in disagreement with previous findings (Littke et al., 1991 and references therein), which associated thin diagenetic $TZ_{A/CT}$ with regions with high heat flow; in other words, a high geothermal gradient produces a narrower $TZ_{A/CT}$. However, as already mentioned, all the $TZ_{A/CT}$ in $TZ_{A/CT}$ the analysed data set are thin zones, representing variations in temperature of $0.12 - 5.50$ °C (mean value 2 °C). The largest temperature variations are associated with highest heat flow values, exemplified by the Japan sites (e.g. Sites 795/Leg 127, 797/Leg 127). Only at site 1173/Leg 190 there is a variation of temperature across the $TZ_{A/CT}$ of 8.5 °C, due to the presence of a very high geothermal gradient (170 °C $\cdot$ km^{-1}).

If the interpretation of Littke et al. (1991) is correct, high heat flow values should have associated thin $TZ_{A/CT}$ thicknesses. Conversely, if low heat flow values are associated with thin $TZ_{A/CT}$, Littke et al. (1991) proposed that diagenesis took place when the geothermal gradient was higher than at present. This possible explanation might apply to some of the sites in the analysed data set which are characterised by low heat flow values (e.g. Sites 1225 and 1226/Leg 20, 1150/Leg 186), while having a thin $TZ_{A/CT}$. In other words, the silica diagenesis fronts at these sites might be 'relict' or 'fossilised'. This was also proposed for cherts on the East Pacific Rise (Mayer et al., 1992), the silica diagenesis reaction fronts in the Norwegian Sea (Brekke, 2000), Faroe Shetland Basin (Davies and Cartwright, 2002) and offshore Sakhalin (Meadows and Davies, 2010b).

The proposed criteria for identifying a 'fossilised' reaction front were based on seismic data (e.g. Davies and Cartwright, 2002) and cannot be applied here due to the limited availability of the ODP seismic data. Instead, the available chemical analyses can be used to verify whether the $TZ_{A/CT}$ have an associated chemical signature in the present – day interstitial water.

At most of the sites of the analysed data set, the silica concentration in the pore water suggests the silica diagenesis is an ongoing process (cf. Mayer et al., 1992), the high concentration of silica above the $TZ_{A/CT}$ reflecting opal – A dissolution, and the sharp decrease in the silica content at or near the top of the $TZ_{A/CT}$ indicating the

precipitation of opal – CT. From this, it could be inferred that the $TZ_{A/CT}$ are not relict features, but are related to ongoing diagenetic processes.

However, the presence of a chemical signature of opal – CT precipitation in the pore waters is dependent on the rates of molecular diffusion and/or the presence of advection. In mudrocks, due to their low permeability, diffusion is the main transport mechanism (Pearson, 1999). Consequently, the presence in the pore water of a chemical signature associated with silica diagenesis is dependent on the diffusion coefficient (McManus et al., 1995).

On the one hand, for a low diffusion coefficient, for example, the chemical signature of the present – day pore water might represent 'relict' chemical processes (i.e. diagenesis). On the other hand, in rocks with a higher permeability than that of mudrocks, pore water advection can be present. In this case, the pore water bearing the chemical signature of active diagenesis could have been transported from deeper in the sediment column and, therefore, it might not be representative for the pore water from the top of the $TZ_{A/CT}$.

It is assumed that diagenesis is an active process at the sites with high heat flow values The temperature contrast over the $TZ_{A/CT}$ varies within the range 0.12 – 8.5 °C, the mean value being 2 °C (Tab. 4.1, Fig. 4.14). This variation suggests that, along with temperature, other secondary factors might control the $TZ_{A/CT}$ thickness. Possible factors previously mentioned (e.g. Kastner et al., 1977; Hein et al., 1978; Keller and Isaacs, 1985; Williams et al., 1985) are age, host lithology, pore water chemistry and permeability.

Due to the variability of the physical and chemical conditions and temperature histories, it is likely that every site will have one or more different concurring factors controlling the thickness of the $TZ_{A/CT}$. In order to identify them, every site should be treated separately, this being beyond the purpose of the present study. The results of this study suggest that the heat flow or the temperature is likely to be the main controlling factor of the $TZ_{A/CT}$ thickness for all the sites analysed, any other factor or combination of factors having only a secondary role.
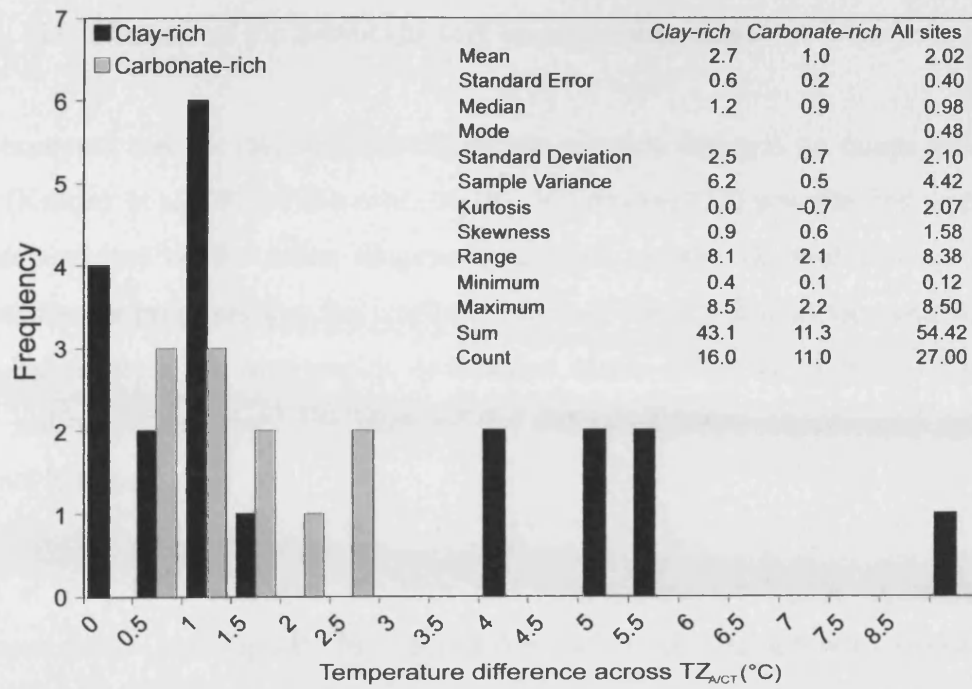
Fig. 4.14. Histogram of the present – day temperature differences between the top and the base of the $TZ_{A/CT}$ for the ODP sites analysed and the corresponding summary statistics. Black bars represent clay – rich sites and grey bars represent carbonate – rich sites.

4.5.3. The influence of the thermal history on silica diagenesis

It is accepted that the rate of silica diagenesis reaction depends on temperature and time (Kastner et al, 1977; Hein et al., 1978). Mizutani (1977) was the first to discuss the dependence of the silica diagenetic reaction on the thermal history of the sediments. He proposed that the isopleths (lines of equally diagenetic maturation of cristobalite) cross the stratigraphic boundaries where deformation occurred shortly after sedimentation, since the parts of the deformed strata experienced different thermal histories.

Hein et al. (1978) estimated the time and temperature for highly to moderately siliceous deep – sea deposits from 6 different locations. The authors proposed that the formation of opal – CT takes place within 10 million years at moderate temperatures (35 – 55 °C) and within 30 million years or more at low temperatures (< 30 °C). To verify if this relationship fits the data set examined here, the temperature and age values for the sites with more than 30 % biogenic silica were plotted on the original graph of Hein et al. (1978) (Fig. 4.12).

It can be observed in Fig. 4.12 that the new data points only fit the original (Hein et al., 1978) upper boundary of the time – temperature field. The low temperature data points, however, are placed outside the lower boundary of this field, regardless of the uncertainties associated with age determination. This mismatch can be explained by several hypotheses: (a) the location of the data points is not accurate, either because of the temperature or because of the age estimation; (b) the time versus temperature relationship defined by Hein et al. (1978) is not valid; (c) the present – day temperatures at some of the sites are not representative for an active silica diagenesis process.

On one hand, it is possible for the temperature values to have associated errors, because the temperature was estimated from shallower measurements, extrapolated to the depth of the diagenetic boundary. On the other hand, the age of the sediments in which the $TZ_{A/CT}$ is embedded is usually approximated; hence, the data points have large errors bars. Nevertheless, the presence of the error bars for both

temperature and age values does not alter the conclusion that no correlation between age and temperature is present (Fig. 4.12).

Since Hein et al. (1978) plot has only 6 data points, it is plausible that the exact definition of the time – temperature field needs to be modified, if more data points are added, as admitted by the authors themselves. However, the inverse relationship between time and temperature, valid for all diagenetic processes (e.g. Giles, 1997), should be present, even if the actual values which define the extension of the time – temperature field are different.

The absence of a relationship between time/age and temperature could be explained if the present – day in situ temperatures are not the temperatures when the active transformation of opal – A to opal – CT took place. In other words, some of the silica diagenesis transition zones represent relict or 'fossil' features, as discussed in the previous section. An accurate reconstruction of the temperature history is needed before determining which of the data points on the plot in Fig. 4.12 refer to 'fossilised' or 'relict' diagenetic fronts, however it can be inferred that the sites with a low temperature (< 25 °C) and relatively young age (e.g. Miocene) are the most likely candidates.

It seems plausible that the absence of a relationship between age and temperature values indicates that at least some of the temperature values do not characterise active diagenetic processes. Hence, some of the diagenetic transition zones could have been formed as a response to a higher paleo – geothermal gradients, associated with unknown past events.

In order to further investigate this, the approximate thermal history for the analysed sites was estimated, multiplying the sedimentation rate and the geothermal gradient, as proposed by Mizutani (1970) and Pisciotto (1981). The resulting data points were plotted versus the age of the sediments hosting the silica diagenetic fronts, as illustrated by the Fig. 4.15a.

a.

Legend

Data from *Pisciotto (1981)*
△ *nodular cherts and porcelanite in calcareous ooze, chalk or limestone*
▽ *silicified calcareous ooze, chalk, limestone or marl*
○ *chert and porcelanite in radiolarian mud and mudrocks*
□ *chert and porcelanite in diatomaceous mud and mudrocks*
• *silicified turbidite muds and calcarenites*
× *silicified tuffs and volcanogenic clays*
★ **ODP Data - this study**

b.

$y=48.089x^{-1.318}$

$R^2=0.7463$

Fig. 4.15. Relationship between age (million years) and approximate thermal history for (a) opal – CT sediments at the analysed ODP sites (black stars) compared to the DSDP siliceous rocks analysed by Pisciotto (1981); (b) opal – CT sediments at the analysed ODP sites only. The number next to every data point corresponds to the site number in Fig. 4.1. The x – error bars represent the possible age range of the sediments; the y – error bars represent standard errors.

A power function fits the data points (dotted curve). It can be observed that diagenetic fronts embedded in Oligocene – Eocene sediments are characterised by low geothermal gradients and slow burial rates. Interestingly, diagenetic fronts embedded in Miocene or younger sediments are characterised by a wide range of values for the thermal history.

82

A power function fits the data points, with a good correlation coefficient ($R^2 = 0.74$). High geothermal gradients and rates of burial characterise the ODP sites where the diagenetic fronts are embedded in younger sediments (in general, Miocene or younger) (Fig. 4.15b). It can be observed that the diagenetic fronts embedded in Miocene or younger sediments are characterised by a wide range of values for the thermal history. The diagenetic fronts in older sediments (Oligocene to Eocene) are characterised by a low geothermal gradient and sedimentation rates (Fig. 4.15b), reflected by constant values of the approximate thermal history.

The same correlation was found for DSDP sediments by Pisciotto (1981) (Fig. 4.15a) who proposed that high thermal gradients and rates of burial promote rapid transformations. Assuming this is a valid interpretation, active silica diagenesis is taking place at lower temperatures in older sediments and higher temperature in younger sediments. The sites characterised by lower temperatures, but younger age, do not fit this time – temperature relationship. A possible explanation for this misfit could be that they represent 'fossilised' reaction fronts, and were formed when the geothermal gradient was higher than at present.

4.6. Conclusions

A number of ODP sites from various locations worldwide where examined in order to identify the presence of silica diagenesis transition zones. These zones represent narrow depth ranges (usually between 10 and 40 m) where the opal – A and opal – CT phases coexist and their main characteristic is that the physical properties of the sediments change sharply. Based on their physical and chemical properties, the criteria for identifying the presence of a silica diagenesis transition zone were proposed:

- The smear slide data should confirm that siliceous microfossils are present in a proportion higher than 10 %.
- In homogenous lithology and in the absence of unconformities, the profile of silica concentration in the interstitial water should decrease sharply, due to opal – CT precipitation, marking the top of the $TZ_{A/CT}$.

- Generally, the bulk density and the compressional velocity values increase and the porosity values decrease at the top of the $TZ_{A/CT}$.

- Other chemical profiles (e.g. pH, alkalinity, potassium, calcium, sodium and chlorine) systematically change across the $TZ_{A/CT}$.

- If seismic data are available, the $TZ_{A/CT}$ is usually marked by a single reflection.

The controls on the thickness of the opal – A to opal – CT transition zone were analysed and the temperature gradient results to be the main controlling factor, other factors like lithology, pore – water chemistry, etc having only a secondary role. As one of the aims of this study, the temperature versus age plot of Hein et al. (1978) was re – evaluated. The new data points do not fit the previously accepted time – temperature field. One of the possible explanations is that some of the diagenetic transition zones were formed as a response to higher paleo – geothermal gradients and are presently 'fossilised' or inactive. The likely candidates are the diagenetic fronts at sites with a low present – day temperature and relatively young age (Miocene or younger) of the sediments hosting the $TZ_{A/CT}$ (e.g. ODP sites 1225, 1149, 846 identified by numbers 10, 14, 22 in Figs. 4.12 and 4.15).

Silica diagenesis transition zones were intersected by more than 100 ODP and DSDP boreholes (for a review see Warme et al., 1981), most of them confirming the presence of important physical properties contrast over narrow depth intervals. Due to the implications that the physical properties contrast has on compaction in sedimentary basins, this study should prove useful for any future study investigating the diagenesis of biosiliceous sediments.

Chapter 5.

MEASUREMENT OF DIAGENETIC COMPACTION STRAIN FROM QUANTITATIVE ANALYSIS OF FAULT PLANE DIP

5. MEASUREMENT OF DIAGENETIC COMPACTION STRAIN FROM QUANTITATIVE ANALYSIS OF FAULT PLANE DIP

5.1. Abstract

A novel technique for quantifying the amount of porosity loss during diagenetic transformation of opal – A to opal – CT is developed. The technique is based on 3 – D seismic data from offshore Norway, where the widely developed biosiliceous sediments of the Brygge and Kai Formations are deformed by a polygonal fault system. Evidence is shown from three study areas that the dip of the polygonal fault planes reduces abruptly across the opal – A to opal – CT diagenetic boundary, suggesting that the fault planes were passively rotated into shallower dips due to diagenesis. The reduction of fault plane dips is used to quantify the vertical compaction strain due to diagenesis. Using an independent assessment of the magnitude of the porosity loss, the method based on fault plane dips is validated. In addition, the hypothesis that the porosity loss might result in an exclusively vertical strain is evaluated. Furthermore, the impact of silica diagenesis on the shear strength of the sediments and fault growth is investigated. Evidence is presented that deviations from classical Mohr – Coulomb behaviour may be expected during the combined processes of diagenesis and porosity collapse, and may indeed be sufficient to promote continued fault growth.

Keywords: biogenic silica diagenesis, polygonal faults, fault dip, compaction strain

5.2. Introduction

It is well established that listric curvature of fault planes can result from compactional flattening of the fault plane as a passive marker during burial, either during or after the main phase of fault activity (Jones and Addis, 1984; Davison, 1987; Xiao and Suppe, 1989). This compactional effect may explain at least some of

the widely observed listric fault geometries exhibited by normal faults in shallow parts of sedimentary basins (e.g. Shelton, 1984). Compactional flattening of fault planes is likely to be most pronounced where a fault transects a dominantly fine − grained sedimentary succession, because the magnitude of compaction due to consolidation is greater for finer − grained than for coarser lithofacies (Rieke and Chilingarian, 1974; Velde, 1996). The quantification of compaction strain is an important element in basin analysis, because it accrues as a result of the advective loss of pore fluid from the originally deposited sediment, and this flux is a critical input into analyses of pore fluid overpressure, fluid flow, and thermal evolution of sedimentary basins (Audet and Fowler, 1992; Bayer and Wetzel, 1989, Bethke and Corbet 1988).

Based on normal faults from an outcrop in the Recôncavo Basin (NE Brazil), Davison (1987) recognised that early normal faults in shale act like passive markers when subjected to compaction. He suggested that their dip shallows due to compaction and discussed the decompaction of the fault plane dips. Xiao and Suppe (1989) used well logs to demonstrate the role of compaction in the flattening of growth normal faults from Louisiana, U.S. The authors underline the fact that slip on faults that flatten by compaction produces no rollover or hangingwall folding. The present study takes further the observations of Davison (1987) and Xiao and Suppe (1989), applying them to a much larger scale, by the use of 3 − D seismic data.

In general, small scale methods have been employed to estimate vertical flattening strains, e.g. from the deformation of bedding around nodules (Craig, 1987), or from ptygmatic folding of sandstone dykes (Parize and Beaudoin, 1988). On a slightly larger scale, differential compaction of isolated channel sand bodies encased in a muddier host lithology has also been used to infer vertical flattening strains (Hillier and Cosgrove, 2002). Recently, forward modelling of differential compaction folding due to irregular advancement of a silica diagenetic front has been undertaken to quantify the effects observed during diagenetic transformation of opal − A to opal − CT (Davies, 2005; Meadows et al., 2008). This diagenetic transformation involves a relatively sudden loss of a considerable fraction of the porosity, due to mineral dissolution and precipitation over a narrow depth interval of, typically, a few tens of

metres (Isaacs, 1981; Chaika and Dvorkin, 1997; Nobes et al., 1992; Davies et al., 2008).

This chapter focuses on the impact of this diagenetically induced compaction on fault plane dips, where a pre – existing fault is embedded in a biosiliceous sedimentary succession that undergoes diagenesis.

The main aims of this chapter are:

- to document the nature of the relationship between fault plane dip and porosity loss due to silica diagenesis;
- to develop a method for quantifying the amount of porosity loss from measurement of fault plane dip.

By attempting an independent assessment of the magnitude of the porosity loss, the method based on fault plane dips can be validated, and, also, the hypothesis that the porosity loss results in an exclusively vertical strain can be evaluated. A purely one – dimensional flattening would be the predicted result for classical models of soil or sediment consolidation (Terzaghi and Peck, 1948; Skempton, 1981), rather than a three – dimensional strain, which might be expected for chemical compaction where cementation is a major process for reduction of porosity (Cartwright and Lonergan, 1996).

The method for estimating the compaction strain during diagenesis is based on observations of fault plane dip using 3 – D seismic data from the Norwegian continental margin, in which widely developed biosiliceous sediments of the Kai and Brygge Formation (Brekke, 2000) are deformed by a polygonal fault system. Evidence from three study areas demonstrate that the dip of the polygonal fault planes reduces abruptly across the opal – A to opal – CT diagenetic boundary (from here abbreviated A/CT). A central theme of this chapter is that this reduction in dip is due to the diagenetic loss of porosity.

A secondary aim of this chapter is to investigate the effect of silica diagenesis on the shear strength of the sediments and whether, if at all, this influences fault growth e.g. through changing the physical properties of the deforming sediments. For example, it is relevant to ask whether slip accumulation on the faults is reduced or even stopped, either as a result of the reduction in fault plane dip or due to the change in physical properties, once opal − A has been converted into opal − CT. Investigations of the role of diagenesis on the evolution of sediment physical properties during burial and deformation are in their infancy (Shin et al., 2008), so the quantification here of the relationship between fault plane dip and physical property changes due to diagenesis may help promote further research on these complex, coupled phenomena.

5.3. Specific data and methodology

The data used in this chapter consists of 3 − D seismic surveys from Møre and Vøring Basins and well data (Fig. 5.1 and Tab. 5.1). The seismic surveys from three study areas cover 6000 km² in total. The parameters of the surveys (bin size, sampling rate, polarity, resolution etc) were presented in Tab. 2.1 of Chapter 2. Lithological and chronostratigraphic calibration for this study is provided by industry boreholes 6704/12 − 1, 6405/7 − 1 and 6305/5 − 1 (available from Norwegian Petroleum Directorate, http://www.npd.no, and from industry reports), and ODP Site 642, Leg 104 (Eldholm et al., 1987) (Fig. 5.1).

The seismic data were interpreted to produce a series of time structure, dip and amplitude maps through the interval of interest (e.g. Fig. 5.2; Appendices A2.1 − A2.12), which is represented by the Brygge and Kai Formations. These maps allowed the definition of faults in this interval, which exhibit the typical characteristics of polygonal fault systems (Cartwright and Dewhurst, 1998). The faults could be interpreted on seismic profiles with confidence to a positioning accuracy equivalent to the lateral resolution (varying from 13 to 25 m, depending on the survey) (Tab. 2.1 in Chapter 2) from a series of stacked cutoffs of stratal reflections in both hangingwall and footwall. Imaging of fault cutoffs was excellent

throughout the survey areas, and there were no problems with imaging artefacts beneath the fault planes, such as fault shadows.

Based on the dip maps of the A/CT reflection (Fig. 5.2), a series of seismic cross – sectional profiles orthogonal to the fault strike were selected in order to measure the true dip angle of the fault planes (Fig. 5.3 and Appendices A2.14 – A2.17). It was assumed that the faults are predominantly dip – slip (Cartwright et al., 2003). From the seismic sections, the TWT value (in ms) of the upper and lower fault tips and of the A/CT reflection were noted, and the height of the fault both above and below the A/CT reflection (in the opal – A and opal – CT sediments respectively) was calculated (Fig. 5.3f). The heave values (in m) were measured on the basemap (accuracy 0.1 m related to the positioning of the cursor on the screen).
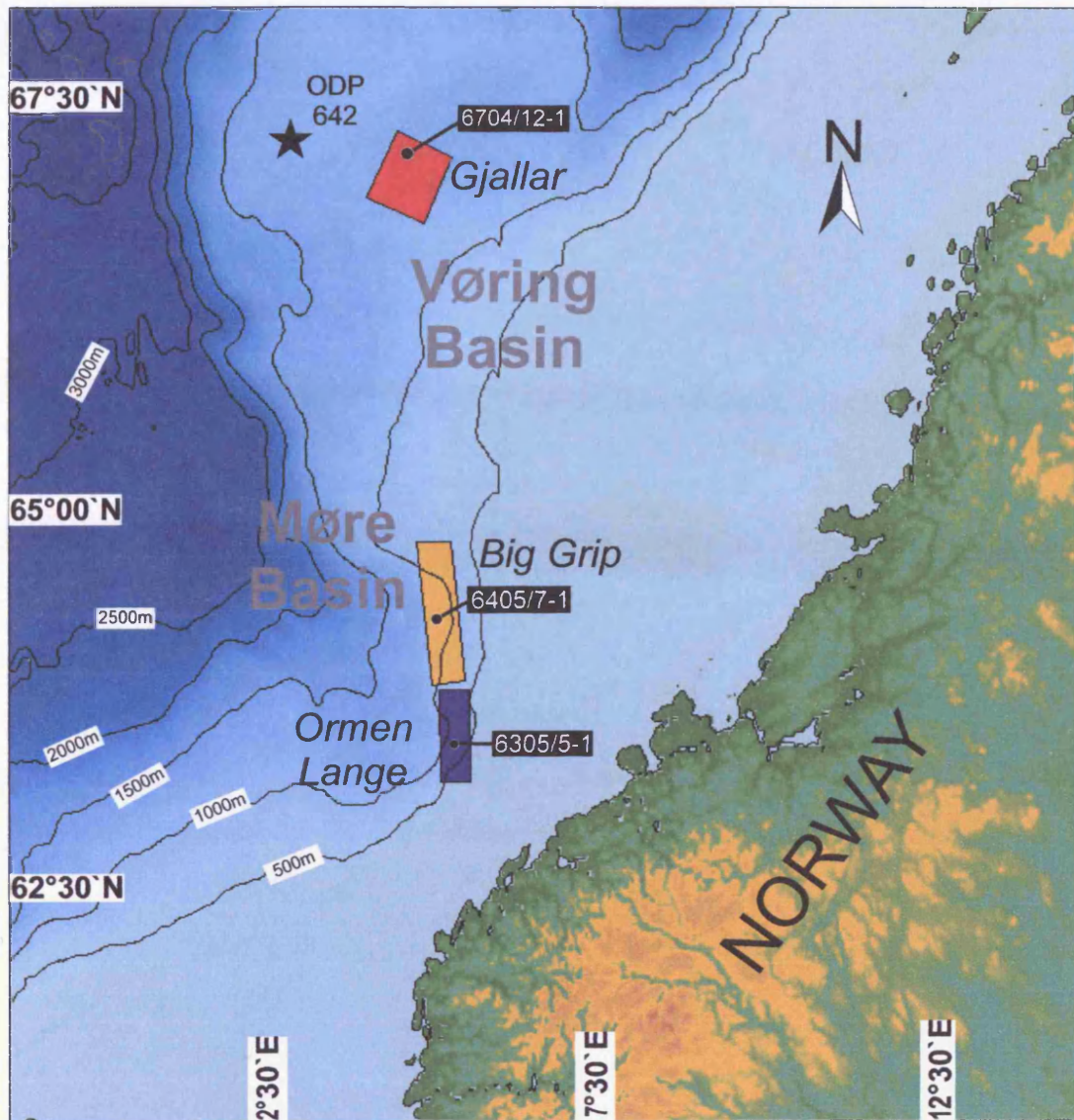
Fig. 5.1. (a) Map showing the location of the three study areas. Basemap built using Global Mapper software: Mercator Projection, WGS84 Datum and SRTM Worldwide elevation data. Bathymetry from NOAA (Amante and Eakins, 2008); *(continues on the next page)*
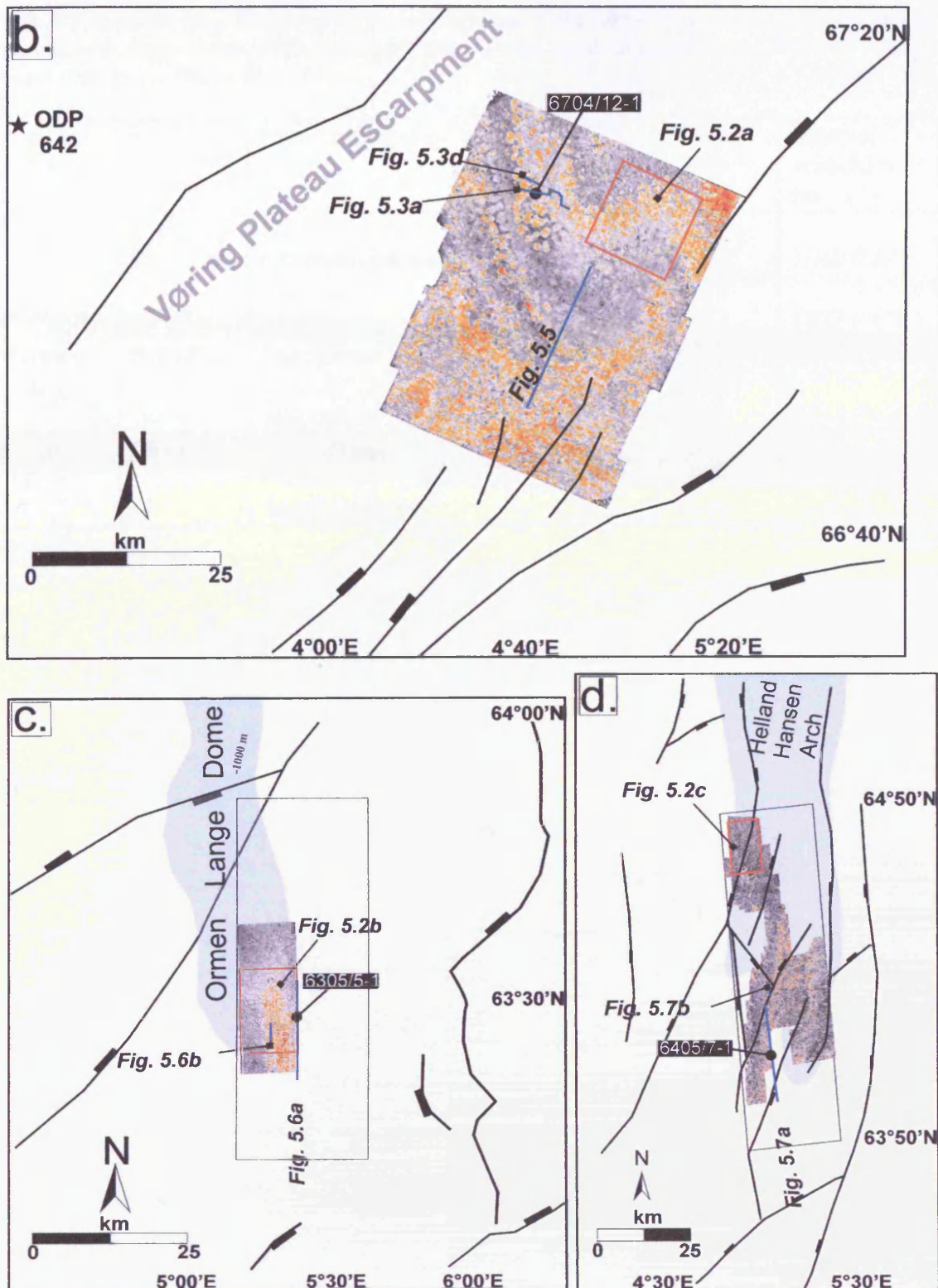
Fig. 5.1. *(continued)* (b) Outline of the Gjallar Ridge survey; (c) Outline of the Ormen Lange survey; (d) Outline of the Grip High survey. The main structural features are from Eldholm (1991) and Blystad et al. (1995). The location of wells 6704/12 – 1, 6405/7 – 1, 6305/5 – 1 and ODP site 642 is indicated, as well as the location of subsequent figures.

Tab. 5.1. Interval velocities used for the conversion of the two – way travel time into depth for the three study areas. TVD represents true vertical depth in metres and TWT two – way travel time in milliseconds.

Survey area	Well	Marker horizons	TVD (m)	TWT (ms)	Interval velocities $(m \cdot s^{-1})$
Gjallar	6704/12-1	Base Late Middle Miocene (intra Kai)	1590	2138	1640 ('A')
		Opal A/CT	1745	2327	
		Top Brygge	1920	2512	1892 ('CT')
Ormen Lange	6305/5-1	Base Naust	1617	1925	1854 ('A')
		Opal A/CT	1910	2226	
		Top Balder	2294	2625	1924 ('CT')
Grip High	6405/7-1	Top Brygge	1935	2372	1770 ('A')
		Opal A/CT	2150	2615	
		Top Eocene	2506	3010	1803 ('CT')
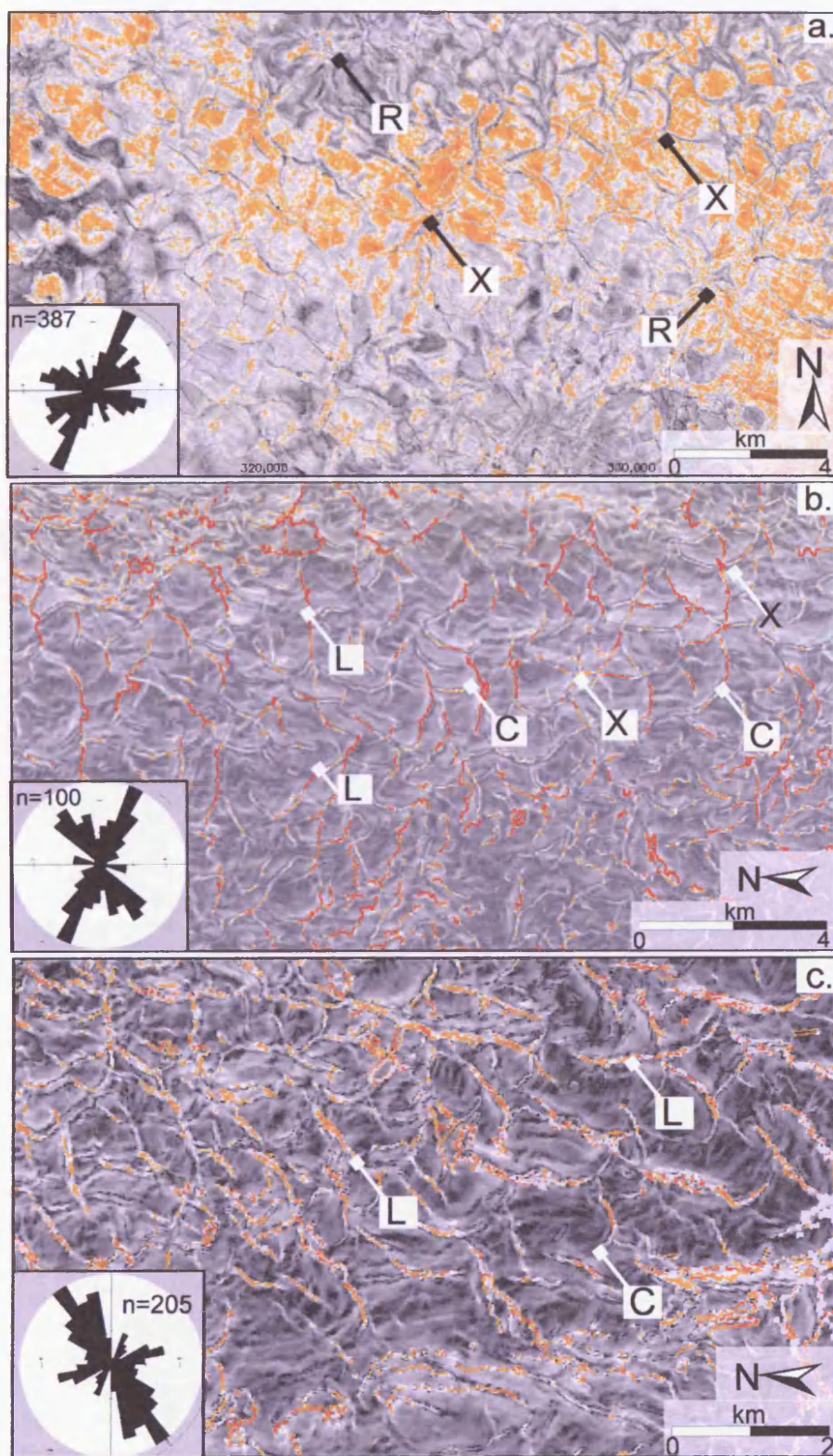
Fig. 5.2. Representative examples of maps of the A/CT reflection. (a) acoustic amplitude map (orange – high amplitudes, grey – low amplitudes) from the Gjallar Ridge survey; (b) dip map (black – low dip values, red – high dip values) from the Ormen Lange survey; (c) dip map (black – low dip values, red – high dip values) from the Grip High survey. The map inserts are rose diagrams representing the strike of the measured polygonal faults in the corresponding 3 – D survey. Polygonal faults are highlighted in dark grey to black on the amplitude map and in yellow and red on the dip maps. Examples of curved, linear and radial fault traces are marked with 'C', 'L' and respectively 'R'. Examples of orthogonal fault trace intersections are marked with an 'X'.
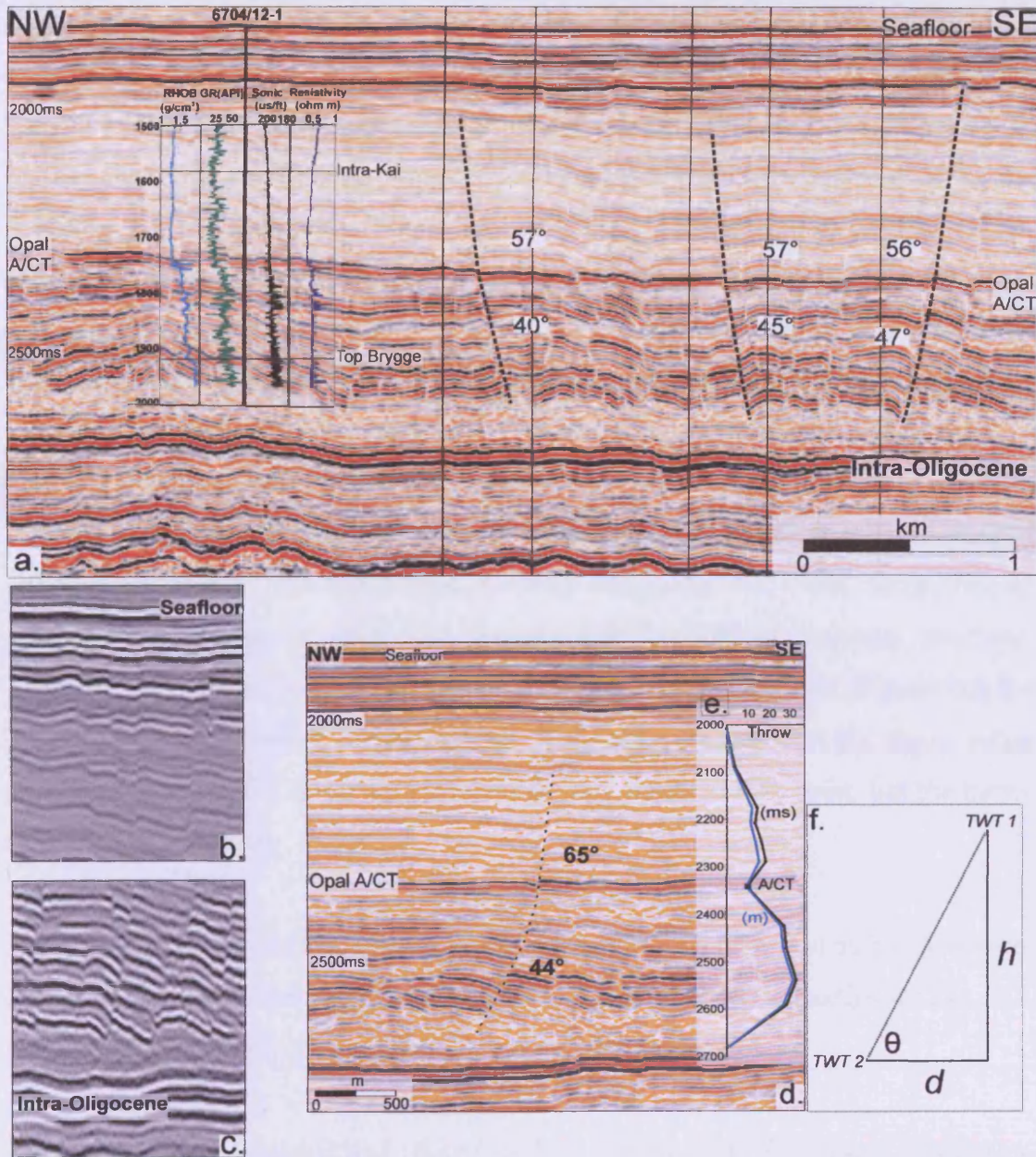
Fig. 5.3. (a) Composite seismic cross – section from the Gjallar Ridge (location in Fig. 5.1b). The vertical axis represents two – way travel time in milliseconds. The wireline logs (Density or RHOB, Gamma ray, Sonic and Resistivity) of exploration well 6704/12 – 1 are shown. Fault planes are marked with black dashed lines. The seismic cross – sectional profile is orthogonal to the fault strikes. Close – up of the (b) upper and (c) lower tips of the polygonal faults; (d) Seismic cross – section orthogonal to the strike of the fault 97 located nearby well 6704/12 – 1 (location in Fig. 5.1b). The two – way travel time is in milliseconds; (e) Vertical throw distribution plot for Fault 97 representing the throw value in milliseconds (black line) and metres (blue line) plotted against two – way travel time. Note that the throw value corresponding to the A/CT is not the true stratigraphic throw at that point, but the throw on the A/CT reflection; (f) Schematic representation of the method of measurement of the dip angle on the seismic cross – section. Explanation of symbols is: θ = dip angle of the fault segment (either in the opal – A or the opal – CT sediments); h = height of the fault computed by subtracting TWT 1 from TWT 2 (in milliseconds); d = heave (in metres) measured on basemap.

Using the available sonic logs from the industry wells in the area, the interval velocities in the opal – A rich sediments and in the opal – CT sediments were extracted (Tab. 5.1). They were used for the conversion of the fault height from time (ms) to depth (m) and the calculation of the true dip angles of the faults in the opal – A and opal – CT sediments. Where the fault plane was curved rather than planar, several readings at approximately 100 m intervals were taken, and the mean value was used. This typically involved a variation of < 10° and was mainly within the fault plane segment in the opal – CT sediments. A variation of ± 10 % in the interval velocities translates into a variation of ± 3° in the calculated dip angles (Tab. 5.2).

Throw values of selected faults were measured on seismic profiles oriented orthogonally with respect to the fault strike by taking the two – way travel time of reflections from the footwall and hangingwall cutoffs of selected horizons. Typically, 10 – 15 horizons were mapped and thus provided the cutoff positions for these throw measurements for every fault. It should be noted that the throw value equivalent to the A/CT is not the true stratigraphic throw at that point, but the throw on the A/CT reflection.

The throw (expressed in ms) versus two – way travel time (TWT in ms) values were converted to depth values (expressed in m) using the interval velocities in Tab. 5.1. The throw versus depth ('T – z plots') are presented in Fig. 5.4.

Possible errors of measurement related to drag folding (e.g. Walsh and Watterson, 1987; Mansfield and Cartwright, 1996) were minimised by not including the drag displacement in the throw measurement. The measurement precision is related to the sample rate of the seismic data (± 4 ms), the resolution of the seismic data (see for details/description Baudon and Cartwright, 2008) and to the accuracy of the cursor positioning on the screen (± 1ms); it was estimated that the overall measurement precision is ± 4 ms.

Tab. 5.2. Interval velocities from Tab. 5.1 varied by ± 10 %. Interval velocity 'A' or 'CT' = interval velocity in the opal – A or opal – CT sediments.

Survey area	Well	Interval velocity 'A' (m · s^{-1})		Interval velocity 'CT' (m · s^{-1})	
		Min.	Max.	Min.	Max.
Gjallar	6704/12-1	1476	1804	1703	2081
Ormen Lange	6305/5-1	1668	2039	1731	2116
Grip High	5405/7-1	1593	1947	1623	1983
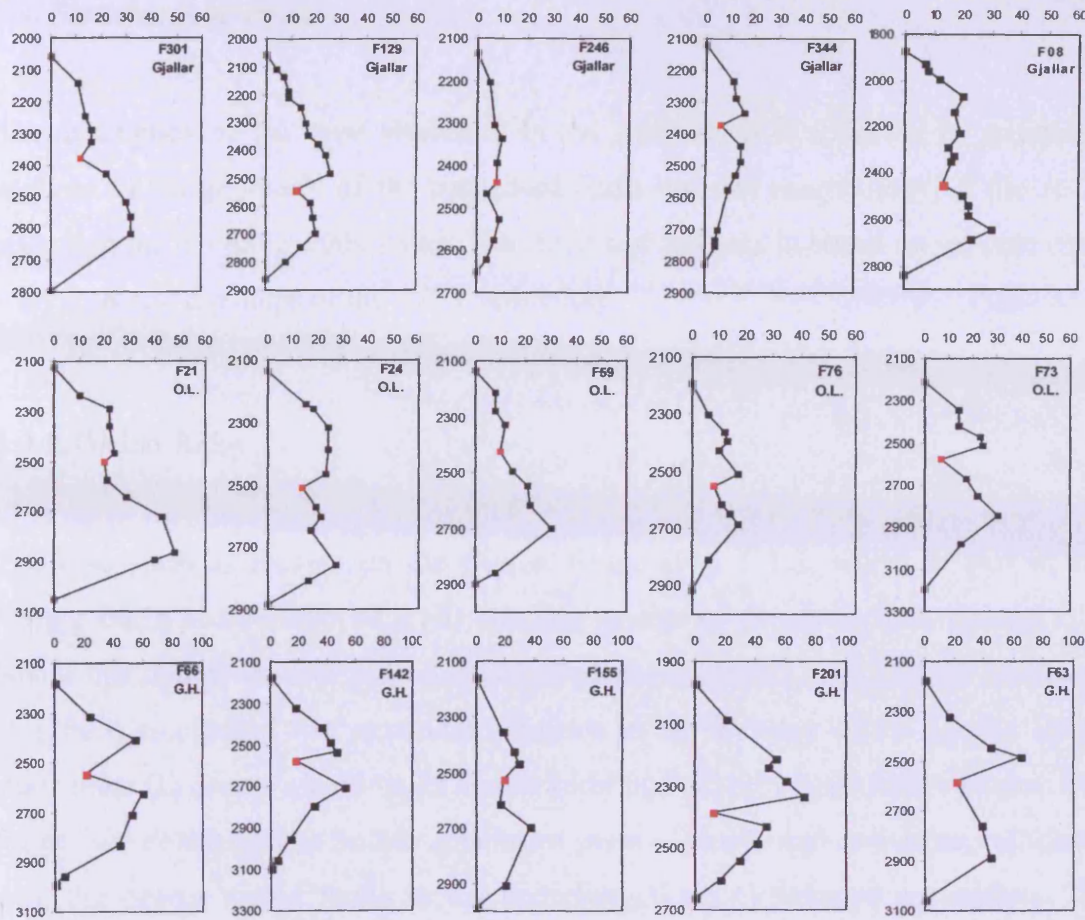
Fig. 5.4. Vertical throw distribution plots for 15 selected faults from the three case study areas (O.L. – Ormen Lange survey; G.H. – Grip High survey). The abscise represents the throw values (milliseconds) and the ordinate the two – way travel time (milliseconds). The throw values at the level of the A/CT reflection are marked by a red square. Note the significant local minimum throw values at this level. Data shown in Appendix A2.17.

5.4. Structural analysis

The description of the main structures in the study areas is followed by a detailed analysis of the geometry of the polygonal faults and the morphology of the A/CT reflection for the three study areas. The structural analysis is based on seismic cross – sections and dip maps of the A/CT reflection.

5.4.1. Gjallar Ridge

The case study is located on the Gjallar Ridge (Fig. 5.1a), which is part of the Vøring Basin and consists of a NE trending system of deeply eroded, rotated fault blocks that mainly involve pre – Tertiary sequences (Blystad et al., 1995). Hansen et al. (2005) recognised two structural elements in the Tertiary of the Gjallar Ridge study area: (1) deep – seated faults and flexures and (2) polygonal fault systems. The former are considered to be the uppermost parts of faults and anticlines associated with the deeper seated faults in the underlying Late Cretaceous succession. The polygonal faults are layer bound i.e. they are developed entirely within the Kai and Brygge Formations, deforming slope to basinal sediments of Oligocene to Pliocene age (Fig. 5.3a). They are part of a basin – wide polygonal fault system that is confined to this stratigraphic interval (Cartwright and Dewhurst, 1998; Brekke, 2000; Berndt et al., 2003) that consists exclusively of small normal faults (throws of up to 70 – 80 m). In some areas, they have been reactivated in the Pleistocene to Holocene, possibly by loading under rapid sedimentation (Gay and Berndt, 2007).

Within the survey area, a pronounced seismic reflection with a strong positive polarity (positive acoustic impedance contrast) is calibrated by well 6704/12 – 1 as resulting from the A/CT boundary. The boundary is set within Early Miocene sediments of the Kai Formation, and is clearly crosscut and offset by a set of polygonal faults (Figs. 5.3a). The A/CT reflection is concordant to the stratigraphy in some areas (Fig. 5.3d), but it is more typically discordant (Fig. 5.5). It crosscuts the stratigraphy across regions that are most deformed by the latest phase of the Neogene folding (c.f. Davies and Cartwright, 2002).
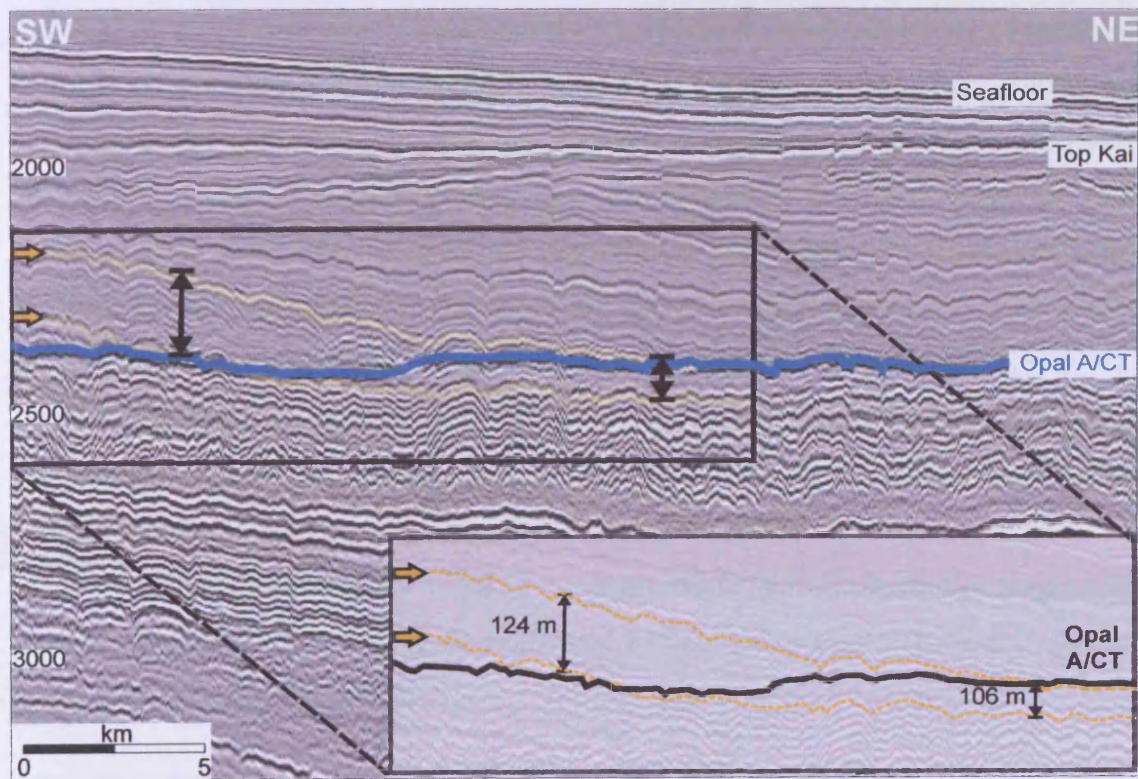
Fig. 5.5. A seismic cross – section (location in Fig. 5.1b) and associated line drawing showing the A/CT reflection discordant to the host stratigraphy.

The A/CT reflection is clearly not parallel to the present – day seabed and, therefore, is not in equilibrium with the present day thermal regime. Instead, it appears to be parallel to the reflections in the Kai Formation just below the Late Pliocene unconformity (Fig. 5.3a), suggesting that the boundary has been fixed in this position from this time onward, as previously suggested by Brekke (2000). Importantly, the magnitude of the throw of the polygonal faults measured at the A/CT reflection is less than the true stratigraphic throw at that position (Fig. 5.3e). The A/CT reflection separates two intervals of the faulted tier that are characterised by different seismic amplitudes. The lower interval has high seismic amplitudes compared to the upper interval, presumably due to the transformation of the opal – A in the mudstones to opal – CT (Davies and Cartwright, 2007). A similar amplitude response has been observed in neighbouring basins along this continental margin (Davies and Cartwright, 2002).

The majority of the faults in this area (> 90 %) do not propagate above the Late Pliocene unconformity, suggesting that they have been inactive since this time. The upper tips of the faults can be clearly identified in most cases: they terminate at different stratigraphic intervals within the Kai Formation, but are usually located at about 250 – 300 ms TWT below the seafloor (approximately 200 – 240 m). Growth packages have only been identified at the upper tips of the largest faults. The upper tips (Fig. 5.3b) are generally characterised by monoclinal tip folds typical of upper tips of small blind normal faults observed elsewhere (c.f. Baudon and Cartwright, 2008). The lower tip regions of the faults are located in a package of the Brygge Formation characterised by low seismic amplitude (Intra – Oligocene on Fig. 5.3c) and it is unclear whether there are local detachments at this level or whether the lower tips terminate against the underlying unfaulted Oligocene units.

Many of the polygonal faults exhibit an unusual, bimodal planar cross – sectional geometry, with two adjacent planar segments with contrasting dip magnitudes. The relatively abrupt change of dip magnitude occurs at or close to the position of the A/CT reflection, with a steeper fault segment in the opal – A sediments compared to that in the opal – CT sediments (e.g. Fig. 5.3). A small number of faults are limited to the upper part of the deformed interval (i.e. in the opal – A sediments), and these

are universally planar. There is no preferential orientation of the fault dip or throw direction, as can be seen, for example, from the seismic profile presented in Fig. 5.3a. The regional distribution and planform pattern of the polygonal faults is illustrated with the dip attribute map of the A/CT reflection in Fig. 5.3a. The dip map shows a uniform distribution of the faults over the area. Most of the fault segments are between 1 and 2 km in length, and are mainly linear (e.g. fault marked 'L' in Fig. 5.3a), with only a small proportion that are curved in planview (e.g. fault marked 'C' in Fig. 5.3a). The planform is polygonal and most fault intersections are orthogonal or at a high angle, as is typical of many polygonal fault systems (Lonergan et al., 1998; Cartwright et al., 2003). Some faults (e.g. fault marked 'R' in Fig. 5.3a) have a radial distribution pattern, they are correlated with deep – seated basement faults and mud diapirs (Hansen et al., 2005). Fault strikes show more than one set of preferred orientations, with trends WNW – ESE, NE – SW and SW – NE (insert of Fig. 5.3a).

5.4.2. Ormen Lange

The second case study is located on the Ormen Lange Dome, one of the major anticlines in the Møre Basin (Fig. 5.1a) resulting from the Neogene regional tectonic phase that affected the entire margin (Doré and Lundin, 1999; Brekke, 2000). This structure has a wavelength of the order of approximately 20 – 30 km and is elongated with a N – S trending axis. It is underlain by extensional faults that were mainly active during the Late Jurassic, but were reactivated during the Eocene to Miocene (Stuevold et al., 2003).

The opal – A to opal – CT diagenetic transformation is sharply expressed on the seismic data as a high – amplitude positive reflection, calibrated in four wells in or close to the study area, and hosted within the biosiliceous mudstones of the Kai and Brygge Formations (Fig. 5.6a). The biosiliceous mudstones of the Brygge Formation are characterised by high seismic amplitudes and partly host the polygonal fault system. The polygonal faults tier is bounded above by the top Kai Formation marker and below by the Top Balder marker, which corresponds to the early Eocene (Stuevold et al., 2003).

102
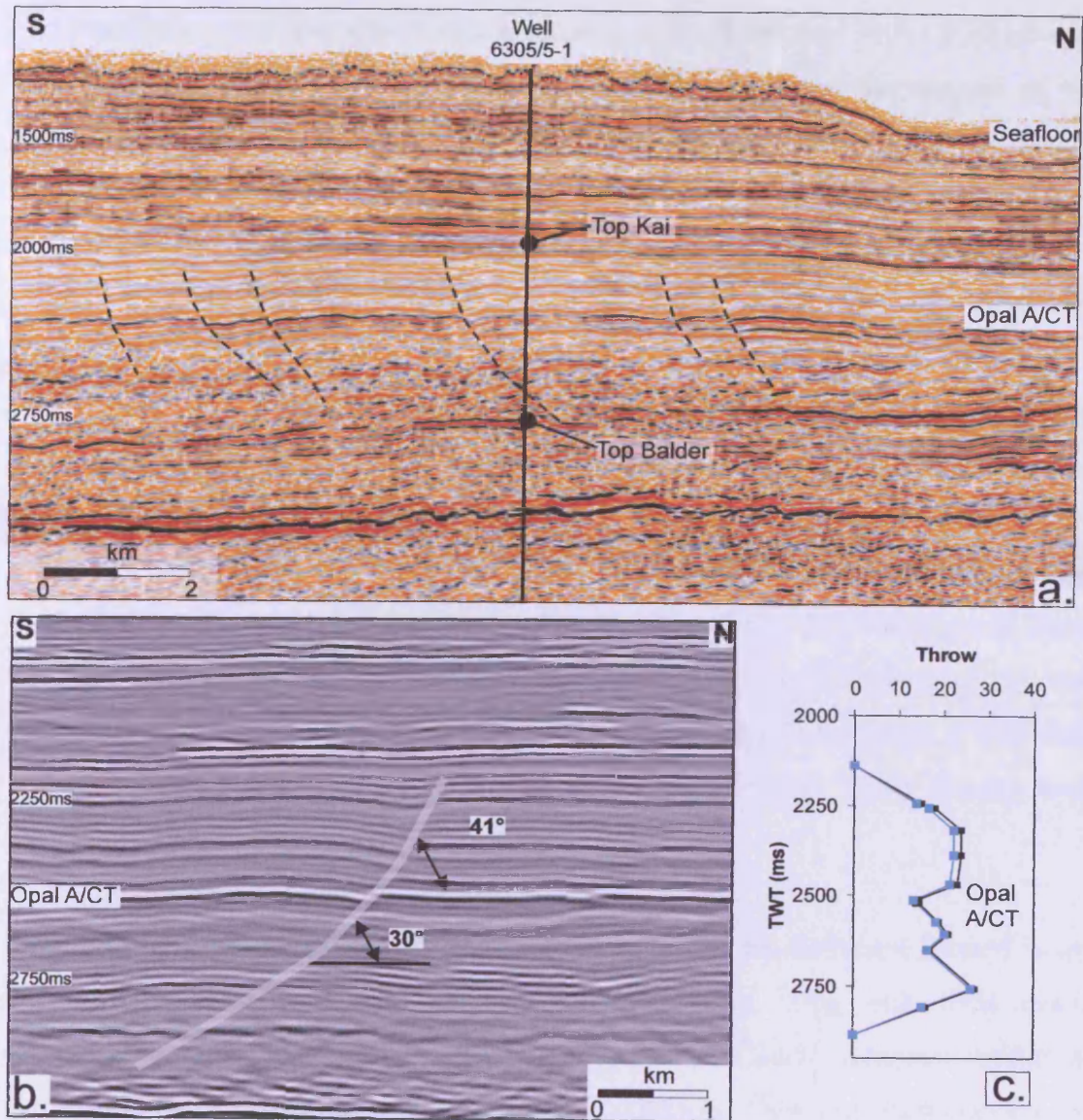
Fig. 5.6. (a) Seismic cross – section from the Ormen Lange survey (location in Fig. 5.1c). The vertical axis represents two – way travel time in milliseconds. The location of well 6305/5 – 1 is shown. Several fault planes are marked with dashed black lines. (b) Seismic cross – section orthogonal to the strike of Fault 24 (location in Fig. 5.1c), marked with a white line. The two – way travel time is in milliseconds. The change in fault dip corresponds to the A/CT reflection. (c) Vertical throw distribution plot for Fault 24 representing the throw value in milliseconds (black line) and in metres (blue line) plotted against two – way travel time in milliseconds.

The distribution and geometrical characteristics of the polygonal faults is illustrated with the dip map of the A/CT reflection (Fig. 5.3b). The areal distribution of the faults is fairly uniform, with the exception of the western edge of the survey, where the fault density decreases. The fault network consists of large (1.5 – 2 km long) and small (less than 700 m) fault segments, with orthogonal to high angle intersections (Fig. 5.3b). The majority of fault traces are curved and have two preferred orientations NE – SW and SE – NW (insert of Fig. 5.3b).

The majority of the polygonal faults that transect the A/CT reflection have a crudely step – like cross – sectional geometry with steeper segments within the opal – A rich interval, similar in general shape to the faults in the other two case study areas. The fault dip changes abruptly at the A/CT reflection (Fig. 5.6b). The faults range from 630 – 720 m in height and have a regular strike distribution, both in the opal – A and opal – CT sediments. The majority of faults dip upslope (Fig. 5.6a), a common feature of polygonal fault systems elsewhere (Cartwright, 1994; Goulty and Swarbrick, 2005).

Similar to the Gjallar Ridge study area, the lower tips of the faults are located in an interval characterised by low seismic amplitudes (Fig. 5.6), thus their exact geometry cannot be interpreted. The upper tips of the faults terminate within a narrow interval towards the top of the Kai Formation. They are characterised by tipline folds (monoclinal), with no obvious growth packages in their hangingwalls. With few exceptions, the maximum throw values are in the range of 17 – 68 ms TWT, and are usually located in the opal – CT sediments.

5.4.3. Grip High

Grip High is a SSW – NNE trending, elongated structural high, and was formed by large – scale faulting during the Middle Jurassic – Early Cretaceous rifting episode (Blystad et al., 1995). The A/CT boundary is visible on the seismic data as a high – amplitude, continuous seismic reflection that generally crosscuts the stratigraphy, and was calibrated by well 6405/7 – 1 (Figs. 5.1d and 5.7a).
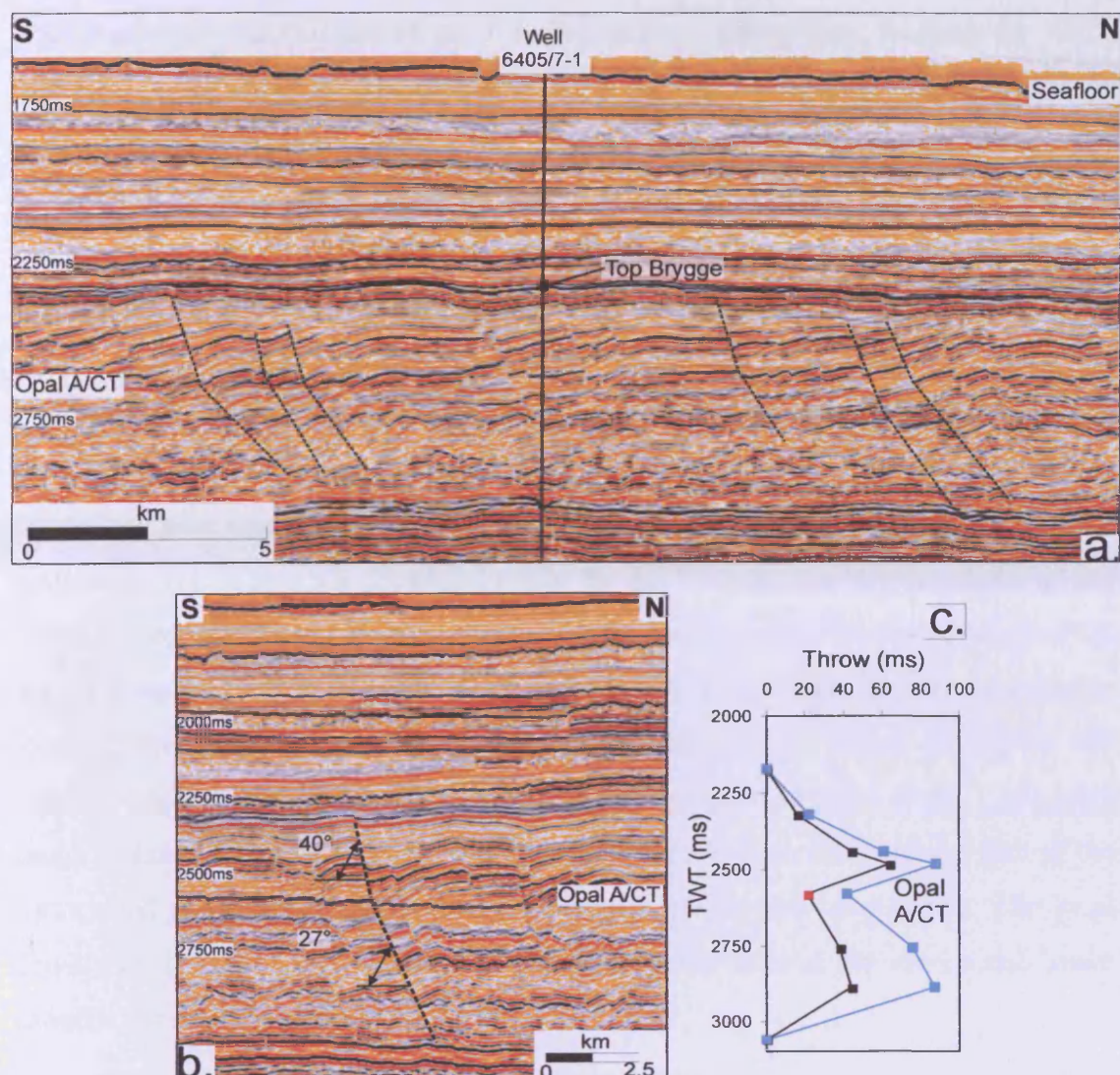
Fig. 5.7. (a) Seismic cross – section from the Grip High survey (location in Fig. 5.1d). The vertical axis represents two – way travel time in milliseconds. The location of well 6405/7 – 1 is shown and several fault planes are marked with dashed black lines. (b) Seismic cross – section orthogonal to the strike of Fault 63 (location in Fig. 5.1d). The two – way travel time is in milliseconds. The change in fault dip corresponds to the A/CT reflection. (c) Vertical throw distribution plot for Fault 63 representing the throw value in milliseconds (black line) and in metres (blue line) plotted against two – way travel time in milliseconds.

The biosiliceous mudstones of the Kai and Brygge Formations, hosting the A/CT reflection, were folded as a result of the Neogene regional tectonics that affected the entire margin (Doré and Lundin, 1996; Brekke, 2000). The wavelength of the folds is of the order of approximately 20 – 30 km. Brygge Formations has a relatively constant thickness, but the Kai Formation is thinning toward the crests of the folds, onlapping it (Fig. 5.7a). As in the case of the Gjallar survey, the A/CT reflection is also folded, but its structural relief is smaller than that of the units in which it is embedded.

Due to the poor signal to noise ratio in the north – eastern and southern parts of the seismic survey, it was not possible to map the A/CT reflection for the extent of the entire survey. The examples presented are from the northern and central parts of the survey (location in Fig. 5.1d), where the quality of the dip map permits an accurate identification and description of the polygonal faults. These examples are representative to the distribution and geometrical characteristics of the polygonal faults of the entire survey. The dip map in Fig. 5.2c is from the northern part of the survey and shows an irregular areal distribution of the fault population. The areal density of the fault population is higher in the central area of the survey and lower towards the edges of the survey.

It can be observed in Fig. 5.2c that the polygonal fault network is less developed than in the Gjallar area, the fault intersections being relatively rare, especially in the northern area of the survey. However, when fault intersections are present, they tend to be orthogonal. The fault pattern is composed by the interweaving of long fault traces (about 2 km) and shorter fault traces (less than 1 km), characterised by a large range of orientation of their strikes. The largest faults can have a NE – SW or an ENE – WSW preferential orientation (insert of Fig. 2c). The pattern of the fault traces on the dip map is, in general, linear, only the largest faults displaying a curved geometry (Fig 2c).

The polygonal faults develop within a tier bounded, at the lower limit, by the top Balder marker, and, at the upper limit, by the top of the Kai Formation. There is another set of polygonal faults developed within a lower tier. These faults deform

Cretaceous units and are not considered further in any detail, since they do not represent the object of this study.

The majority of the polygonal faults that traverse the A/CT reflection do not propagate below the Top Balder marker, with very few exceptions of faults that propagate from the Cretaceous units (Fig. 5.7a). The faults have a linear to gently listric cross – section with mean dip angles in the range of 25° to 42°, the lower values corresponding to the opal – CT rich interval. The majority of faults dip upslope, in a NE direction, but anthythetic faults are also present. The lower tip is contained in a low amplitude package, similar to the other two study areas; hence, their exact geometry cannot be accurately determined.

Most of the faults terminate at the level of or below the reflection from the top of the Kai Formation, which is at approximately 650 ms TWT (approximately 600 m considering an interval velocity of 1800 m · s^{-1}) below the present seabed. As in the other two study areas, the upper tips of the faults are characterised by fold – like bending of the reflections with no growth packages. The faults are, in general, about 600 m high (resulting from the conversion of c. 650 ms TWT using an interval velocity of 1800 m · s^{-1}) and present a uniform distribution, within both the opal – A and opal – CT rich intervals. The maximum throw values are in the range of 30 – 70 ms TWT, and are, in general, located in the opal – A rich interval.

5.4.4. Vertical variation in throw on the polygonal faults

In addition to the general observation of the abrupt change of dip at the A/CT reflection in all the study areas, it was also generally observed that the throw values at the level of the A/CT boundary are always smaller than the throw of stratal reflections at the same position on the fault. This latter observation has been made previously in other areas along this margin of the NE Atlantic, and has been attributed to the arrest of the upward migration of the diagenetic front prior to the last period of movement on the polygonal faults (Cartwright, 2007).

In order to quantify this relationship in more detail, vertical throw distributions were measured for 64 representative faults (of which 15 examples are shown in Fig. 5.4) from the three case study areas. The results were plotted as throw vs. depth (T – z) plots. These plots were all constructed through the maximum throw position of each fault and show that the maximum throw measured at the A/CT reflection ranges from a few m (6 – 7 ms) up to approximately 31 m (33 ms). In contrast, the stratigraphic throw at the equivalent position on the measured faults ranges from 8 – 64 m (approximately 8 – 72 ms). The effect of this reduction is to produce a local minimum at the position of the A/CT reflection obviously distinct from the general pattern of throw on the true stratigraphic markers (Fig. 5.4). The maximum throw values occur both in the opal – A rich interval (e.g. fault 129 Gjallar, 201 G.H. in Fig. 5.4) and in the opal – CT rich interval (e. g. fault 21 O.L., fault 301 Gjallar in Fig. 5.4).

In general, the vertical throw profiles for the 64 faults are not strictly similar to the C – type or M – type (e.g. Muraoka and Kamata, 1983; Baudon and Cartwright, 2008), but exhibit elements of both types of end member profiles. The C – type is characterised by a symmetrical shape with a gentle change of displacement with depth, while the M – type has a broad central section with no significant change of slope, and adjacent segments with an abrupt change of displacement. A good example of a C – type is fault 129 Gjallar, and an M – type is fault 24 O.L. (Fig. 5.4). Strongly asymmetric profiles are common; with approximately 40 % of the faults exhibiting a pronounced maximum in the opal – CT sediments and within 200 – 300 m of the basal tip (e.g. faults 301 Gjallar, 201 O.L. and 59 O.L. in Fig. 5.4). The asymmetric profiles tend to be those whose faults transect the entire tier. The vertical variation in throw is reasonably smooth, with the exception of the region at or close to the A/CT reflection.

These throw profiles show conclusively that there is a significant local minimum at the level of the A/CT reflection. They also show that a substantial proportion (quantified in Appendix A2.13) of the total throw of each fault accrued on the fault surfaces after the upward migration of the A/CT diagenetic front had effectively ceased (Brekke, 2000; Cartwright, 2007). This raises the interesting question of

whether the arrest of upward migration of the front, implies that all silica diagenesis had ceased in the opal – CT sediments. This question is important because in all the measured cases, especially the case of the highly asymmetric throw profiles – asymmetry that could be explained by a partial slip along the fault – it is evident that in this post – arrest phase of fault growth, throw actively accumulated in both the opal – A and opal – CT rich sediments.

5.4.5. Fault plane dip

One of the most important observations noted in the previous section is that the abrupt reduction of dip of the polygonal fault planes occurs at the A/CT boundary (Figs. 5.3ac, 5.6ab and 5.7ab). This was observed systematically throughout all the seismic surveys presented in this chapter, and has also been observed on a number of other 3 – D seismic surveys distributed more widely in the Møre and Vøring Basins.

To evaluate the significance of this abrupt change, the dip angle of 689 fault planes from the three seismic surveys was measured. The results are presented in Fig. 5.8a for the fault plane segments in the opal – A sediments (dip 'A') and for those in the opal – CT sediments (dip 'CT').

The histogram (Fig. 5.8b) and cross – plot of dip 'A' versus dip 'CT' (Fig. 5.8c) illustrate that there is a large scatter of dip values for both upper and lower segments. The dip 'A' values range from 24° to 73°, and the dip 'CT' values range from 11° to 57°. The ranges and mean values for the individual case studies are presented in Tab. 5.3. An important conclusion from this data is that the dip 'A' value is greater than the dip 'CT' in 95 % of the cases and of equal value in the remaining 37 faults (to within 2°). This is most clearly illustrated on the cross – plots of dip 'A' versus dip 'CT' (Fig. 5.8c). Within error, the dip of the lower segment is never found to be larger than that in the upper segment. The range of fault dips of both the upper and lower segments is clearly much greater than the range that could be due to errors in depth conversion or fault interpretation. The data are presented with error bars in Fig. 5.8d to illustrate this point, and show that typical errors are of the order of ± 2 to 3°.
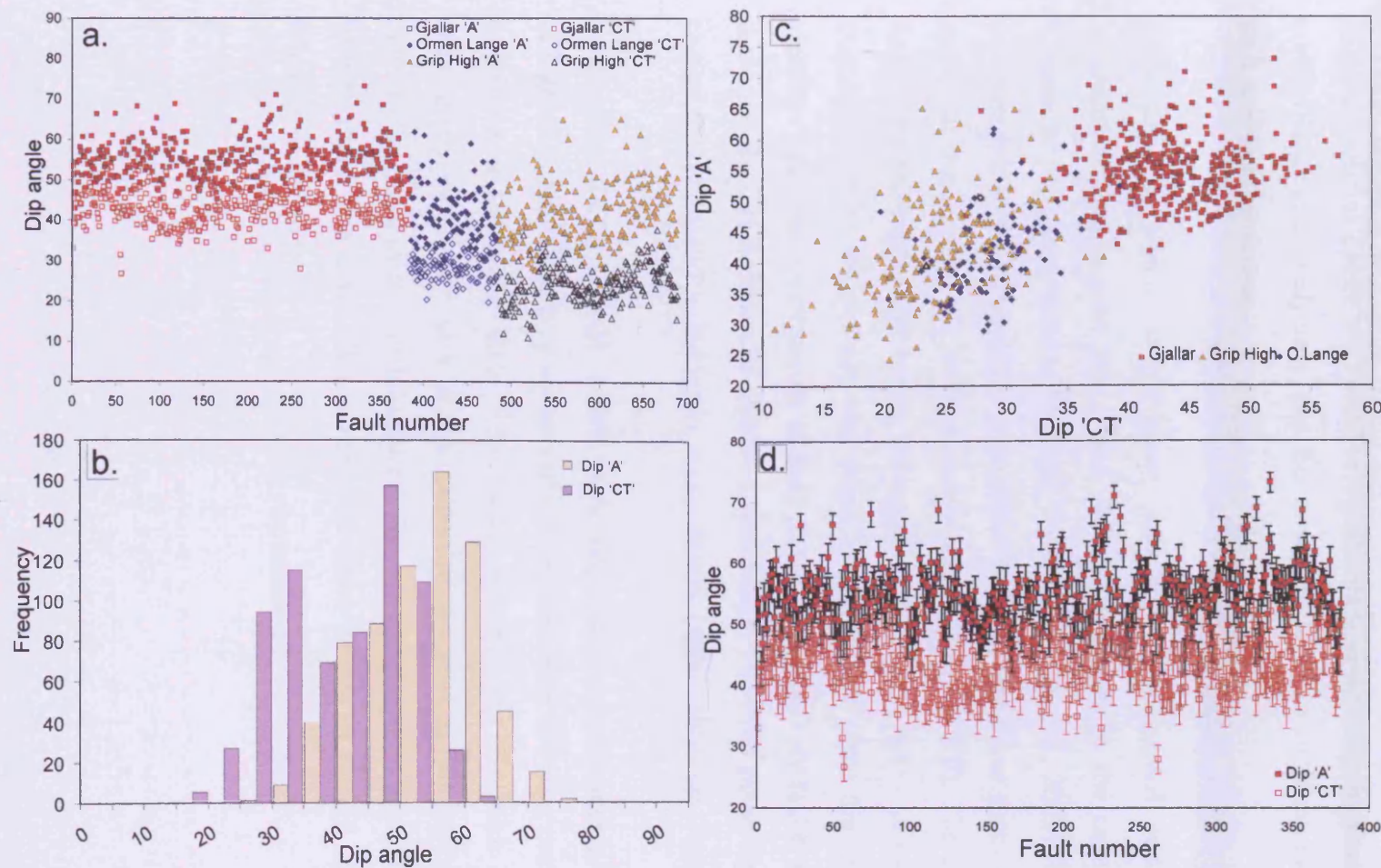
Fig. 5.8. (a) The values of the dip angles of the selected faults in the three surveys (red squares – Gjallar Ridge, blue rhombi – Ormen Lange; yellow triangles – Grip High). The dips of the fault segments located within the opal – A rich sediments (dip 'A') are marked with filled symbols, while the dips of the fault segments located within the opal – CT rich sediments (dip 'CT') are marked with open symbols. The ranges of values are presented in Tab. 5.3. Associated data are presented in Appendix A2.14; (b) Histogram showing the frequency of the 'A' dip angles (yellow bars) and 'CT' dip angles (purple bars);

(c) Cross – plot of dip 'CT' versus dip 'A' values for the three surveys; (d) Dip angles of the faults in the Gjallar survey with the associated error bars corresponding to a variation of ± 10 % of the interval velocity used for the depth conversion (Tab. 5.2).

110

It is apparent from Fig. 5.8a and Tab. 5.3 that the faults from the Grip High and Ormen Lange case studies exhibit a range of dip angles that is generally towards the lower end of the total range of the combined dataset. There is a shift of approximately 12 – 17° compared to those from the Gjallar Ridge survey.

From a comparison of wireline log characteristics, the lithology of the deformed Brygge and Kai Formations is similar in the three areas, but the faults in the Grip High and Ormen Lange are buried to significantly greater depths than those in the Gjallar Ridge case study area, and this is suggested as an explanation for this bulk shift to lower dip values.

Some previous studies of polygonal fault systems suggested that there is an azimuthal dependence of fault plane dip, for example, in the case of the Late Cretaceous polygonal faults of the Møre Basin (Stuevold et al., 2003). To investigate this possibility, the dip against fault plane strike measured at maps of the A/CT reflection was plotted, but no relationship was found (Fig. 5.9). The distribution of faults with contrasting dip values for segment 'A' (in the opal – A sediments) was examined, but no relationship was found between fault plane dip magnitude and location: there was no clustering of fault planes with relatively higher dips, nor was there any distinct zonation of higher or lower dips. The fault plane dip was plotted against maximum throw, but again, no systematic relationship was observed.

In summary, the large range in fault plane dips observed for segments 'A' and 'CT' in both areas appears to be a scatter that does not correlate to strike, maximum throw or position in the survey area. Since the lateral continuity of seismic reflections in each survey area is very high, this suggests that any marked lithological variation is only on the scale of tens of kilometres. The random distribution of fault segments with high and low dips indicates that this scatter cannot be related to any obvious lithological variation.

Tab. 5.3. Summary statistics for the calculated dip angles of the fault segments in the opal –
A sediment (dip 'A') and in the opal – CT sediment (dip 'CT') for the three study areas.

Survey Parameters	Gjallar		Ormen Lange		Grip High	
	Dip 'A'	Dip CT	Dip 'A'	Dip 'CT'	Dip 'A'	Dip 'CT'
Mean	55	43	42	29	42	25
Standard error	0	0	1	0	1	0
Median	55	43	41	29	41	25
Mode	56	43	44	–	–	25
Standard deviation	5	5	7	3	7	5
Sample variance	26	21	48	12	53	23
Kurtosis	1	0	0	0	0	0
Skewness	0	0	1	0	0	0
Range	31	31	33	20	41	27
Minimum	42	27	29	20	24	11
Maximum	73	57	62	39	65	38
Sum	20978	16688	4193	2874	8565	5039
Count	384	384	100	100	205	205

112
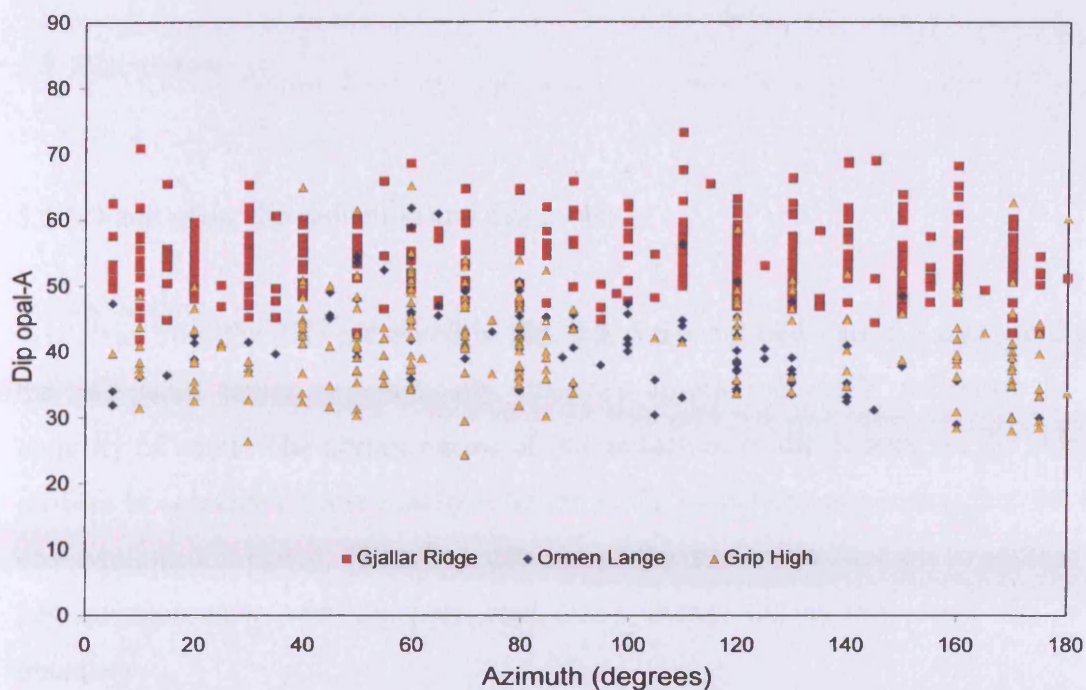
Fig. 5.9. Cross – plot of strike versus dip 'A' (dip opal – A) for all the measured faults showing that no correlation exists between the magnitude of the dip angle and orientation of the faults in the three survey area. Associated data are shown in Appendices A2.14 – A2.17.

5.5. Discussion

5.5.1. Fault plane dip reduction and diagenesis

It is clear from the data presented in Fig. 5.3, 5.6 – 5.8 and Tab. 5.3 that the dip of the polygonal faults systematically shallows across the A/CT reflection in the majority of cases. The abrupt nature of this reduction of dip is seen on the seismic profiles to coincide almost exactly with the A/CT reflection, suggesting that the two observations are related. Therefore, this part of the discussion attempts to address the key question as to why the polygonal faults change dip as they cross the A/CT boundary.

An abrupt change of dip could potentially be explained in two contrasting ways:

- due to some original lithological layering leading to propagation at originally different angles and refraction at the boundary (c.f. Peacock and Zhang, 1994; Schöpfer et al., 2007);
- due to a compactional flattening of the original fault plane dip (Jones and Addis, 1984).

The first explanation can be rejected for the simple reason that the diagenesis results in a denser, more cemented sedimentary lithology below the diagenetic front, in contrast with the unlithified, high porosity biosiliceous ooze prior to diagenesis. Sediments rich in opal – A have very low shear strength (e.g. Pittenger et al., 1989), whereas the cementation that occurs during opal – A to opal – CT transformation causes a distinct increase in the shear strength (Bjørlykke and Høeg, 1997).

In known examples of fault refraction (e.g. Schöpfer et al., 2007 and references therein), the fault traces observed in cross – section have steeper dipping segments in the strong layers and shallower dipping segments in the weak ones. This has either been attributed to different modes of fracturing (tensile versus shear) as a function of lithology (e.g. Ferrill and Morris, 2003) or to different friction coefficients within

114

the interbedded lithologies (e.g. Mandl, 2000). Thus, the observed reduction of dip at the A/CT boundary is the opposite of what would be predicted from a Mohr – Coulomb analysis.

The alternative interpretation for the reduction of dip is that the original fault plane dip has been substantially modified by later compaction. Strong support for this interpretation comes from the large body of porosity data from biosiliceous sediments that have undergone diagenesis obtained by the Ocean Drilling Program (ODP). From these data, and from field evidence, it is now well known that the opal – A to opal – CT diagenesis coincides with an important decrease in porosity (e.g. Compton, 1991; Chaika and Dvorkin, 2000; Meadows and Davies, 2008). It is common to find that porosity values in biosiliceous oozes are high at the time of deposition, and only gradually decrease with depth to the point where the sediment undergoes the diagenetic transformation, whereupon the porosity drops by 5 – 40 %, with a mean value of 18 %.

In the Gjallar Ridge case study area, it was possible to estimate the magnitude of the porosity reduction across the opal – A to opal – CT boundary from a combination of the density log from well 6704/12 – 1 located in the survey area and from physical property and lithological data from ODP site 642, located some 50 km from the survey area (Eldholm et al., 1987) (location in Fig. 5.1b).

At this location, the porosity of the opal – A rich sediments is 80 %, and that of the opal – CT rich interval is 70 %, based on data from ODP site 642. From the available density log of the well 6704/12 – 1 (Fig. 5.3a), the bulk density values of the opal – A and opal – CT sediments were extracted. The mean values are 1.3 and 1.55 g · cm^{-3}, respectively. This abrupt increase of bulk density is known from ODP drilling to correspond to a reduction in porosity.

A set of density values from ODP sources for boreholes that cross the A/CT boundary was compiled, including measured porosity differences above and below it (Fig. 5.10 and Tab. 5.4). This plot is highly scattered, but nonetheless shows a crude

A/CT boundary. From the trend line, it can be seen that a density difference of 0.25 g · cm^{-3}, observed locally in the well 6704/12 – 1, corresponds to a porosity change of 16 ± 6.8 %. This value is comparable to that recorded by direct measurement in Site 642. The porosity was not estimated based on the resistivity, density or neutron logs because of the lack of any data referring to the composition of the sediment matrix. Consequently, Archie or Wyllie equations (e.g. Hearst et al., 2000), could not be applied.

The compaction strain resulting from the diagenetic change can be calculated directly from the change in porosity across the A/CT boundary (Meadows and Davies, 2010a). The initial assumption is that all the porosity change is expressed in a 1 – D consolidation, and hence is expressed as a vertical strain. From this assumption, the compaction strain (E_z) is defined as the ratio of the final solid thickness to the original solid thickness of a column of sediments. Technically, E_z is equivalent to the stretch, which is one measure of strain (Twiss and Moores, 1992); however, in his chapter E_z will be referred to as compaction strain. E_z is also the inverse of the decompaction number (D) of Perrier and Quiblier (1974):

$$E_z = \frac{1}{D} = \frac{h_1}{h_0} = \frac{1-\phi_0}{1-\phi_1},$$ (Eq. 5.1)

where h_0 = the initial solid thickness; h_1 = the final solid thickness; ϕ_0 = initial porosity (porosity of the opal – A sediments or porosity 'A'); ϕ_1 = final porosity (porosity of the opal – CT sediments or porosity 'CT'). Xiao and Suppe (1989) also applied this relationship to growth normal faults from southern Louisiana, however, in their case, the values of initial porosity were unknown.

The porosity is expressed as a fraction of sediment that is made up of pore space:

$$\phi = \frac{h_v}{h_t},$$ (Eq. 5.2)

where h_v = the thickness of the pore spaces of a column of sediment and h_t = the total thickness of the sediment column.
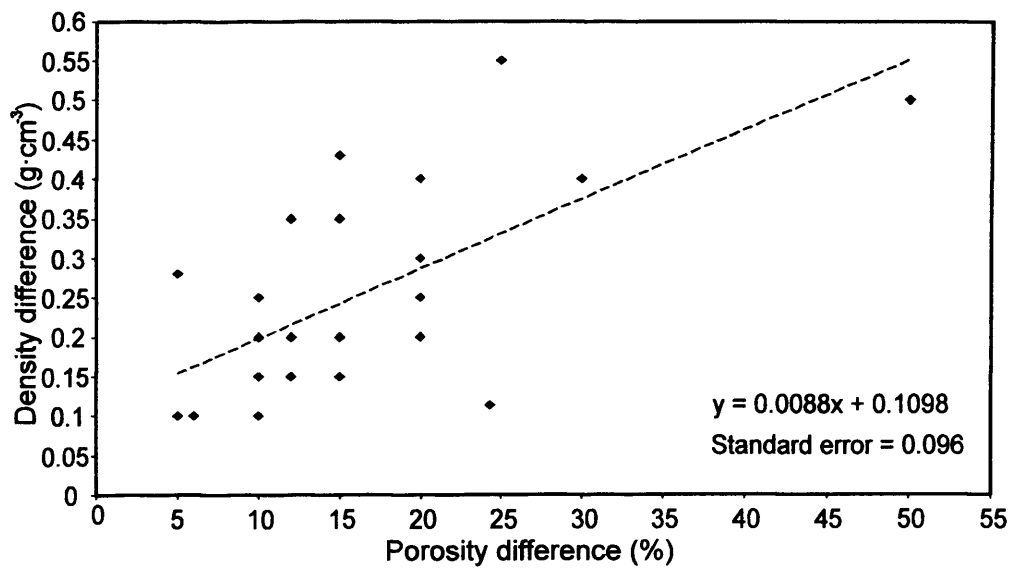
Fig. 5.10. Cross − plot of porosity difference versus density difference across the A/CT boundaries for the ODP sites listed in Tab. 5.4.

Tab. 5.4. Variation of the porosity (%) and bulk density (g · cm⁻³) of the opal – A ('A') and opal – CT ('CT') sediment for several ODP/DSDP sites that have drilled the A/CT diagenetic boundary. The porosity and bulk density values presented in this table are based on the data provided by the ODP/DSDP Initial Reports (http://www – odp.tamu.edu).

Leg	Site	Porosity 'A' (%)	Porosity 'CT' (%)	Bulk density 'A' (g · cm⁻³)	Bulk density 'CT' (g · cm⁻³)
ODP 128	799	77	57	1.5	1.8
ODP 127	794	85	70	1.27	1.7
ODP 127	795	80	55	1.75	1.85
ODP 127	796	70	55	1.55	1.9
ODP 127	797	85	65	1.4	1.8
ODP 128	798	65	55	1.7	1.85
ODP 113	696	70	45	1.45	2
ODP 105	647	75	63	1.45	1.8
ODP 201	1226	80	65	1.55	1.7
ODP 201	1225	80	70	1.45	1.55
ODP 198	1207	60	55	1.9	2.18
ODP 189	1170	62	50	1.65	1.8
ODP 188	1165	55	45	1.75	2
ODP 185	1149	70	20	1.5	2
ODP 178	1095	57	45	1.75	1.9
ODP 177	1090	83	77	1.25	1.35
ODP 189	1171	75	55	1.4	1.7
ODP 189	1172	65	53	1.55	1.75
ODP 150	903	65	45	1.6	1.9
ODP 150	904	60	50	1.7	1.95
ODP 138	846	70	60	1.55	1.7
ODP 104	642	80	60	1.4	1.8
ODP 105	643	80	60	1.4	1.65
ODP 186	1150	70	60	1.55	1.7
ODP 150	902	60	45	1.85	2.05
ODP 190	1173	65	50	1.6	1.8
ODP 167	1016	75	65	1.4	1.65
ODP 168	1010	77	67	1.5	1.7
ODP 143	869	60	40	1.3	1.5
ODP 159	959	60	30	1.5	1.9
DSDP 95	612	60	45	1.6	1.8
DSDP 96	613	55	45	1.65	1.75
DSDP 47	397	45	40	1.9	2

The thickness of a solid fraction (h_s) of the sediment is:

$$h_s = h_t - h_v$$ (Eq. 5.3)

After the substitution of Eq. 5.2 into Eq. 5.1, the thickness of the solid fraction becomes:

$$h_s = h_t(1 - \phi)$$ (Eq. 5.4)

During the diagenesis, the thickness of the solid fraction is assumed to remain constant, which is valid provided the phase change occurs only on a local scale (Perrier and Quiblier, 1974). In this case, the dissolution – precipitation reactions involved in converting opal – A to opal – C/T are generally considered to operate on a grain scale, without mass transfer over distances of more than a few millimetres (Hein et al., 1978; Davies, 2005), i.e. at a much smaller scale than the solid thicknesses considered (hundreds of metres). Thus, it can be considered that the final solid thickness equals the initial solid thickness (i.e. there is no significant mass transfer):

$$h_1(1 - \phi_1) = h_0(1 - \phi_0)$$ (Eq. 5.5.)

Using the values of porosity change from Site 642 (ϕ_0 = 80 %, ϕ_1 = 60 %), a compaction strain of 0.50 was obtained. Using the porosity change of 10 – 20 % from the density log response of well 6704/12 – 1, and a pre – diagenetic porosity of 80 %, the compaction strain falls within the range of 0.50 – 0.66. These values probably represent reasonable upper and lower bounds for the compaction strain in the Gjallar Ridge case study area, due to silica diagenesis, with the assumptions stated above.

5.5.2. Compaction strain from fault plane flattening

If a fault plane is considered as a linear marker that flattens with vertical compaction (e.g. Davison, 1987; Xiao and Suppe, 1989), its dip angle changes from θ_0 to θ_l as illustrated in Fig. 5.11. From simple trigonometry, the ratio of the final solid thickness to the initial solid thickness can be directly related to the change in dip angle:

$$\frac{h_1}{h_0} = \frac{\tan\theta_1}{\tan\theta_0},$$ (Eq. 5.6)

where θ_0 = initial dip angle and θ_l = final dip angle. If a case could be made that the polygonal faults in the study areas were planar prior to the diagenesis of the opal – A fraction of the biosiliceous sediment, then the compaction strain could be calculated from the change in fault dip using Eq 5.6. Polygonal faults are often described as being planar to gently listric (e.g. Cartwright and Lonergan, 1996; Lonergan et al., 1998; Stuevold et al., 2003). In order to quantify this geometry, the fault plane dips for a selection of faults that occur in the opal – A sediments in the Gjallar Ridge case study area were measured. These data show that polygonal fault planes are curvilinear with a dip variation of less than 20° for vertical distances of 300 to 500 m within the biosiliceous, opal – A rich, Brygge and Kai Formations (Fig. 5.12).
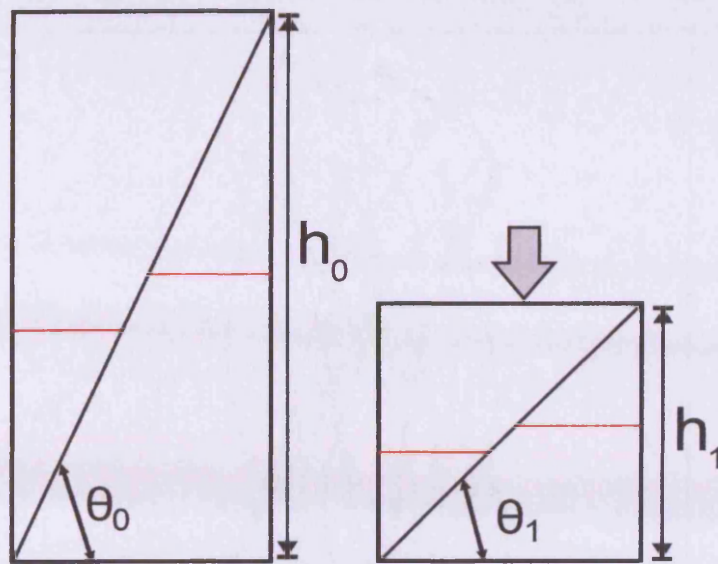
Fig. 5.11. Schematic representation of the flattening of a fault plane with vertical compaction. Note that the dip angle of the fault changes from θ_0 (initial dip angle) to θ_1 (final dip angle). h_0 and h_1 represent the initial and final solid thickness of a volume of sediments, respectively.
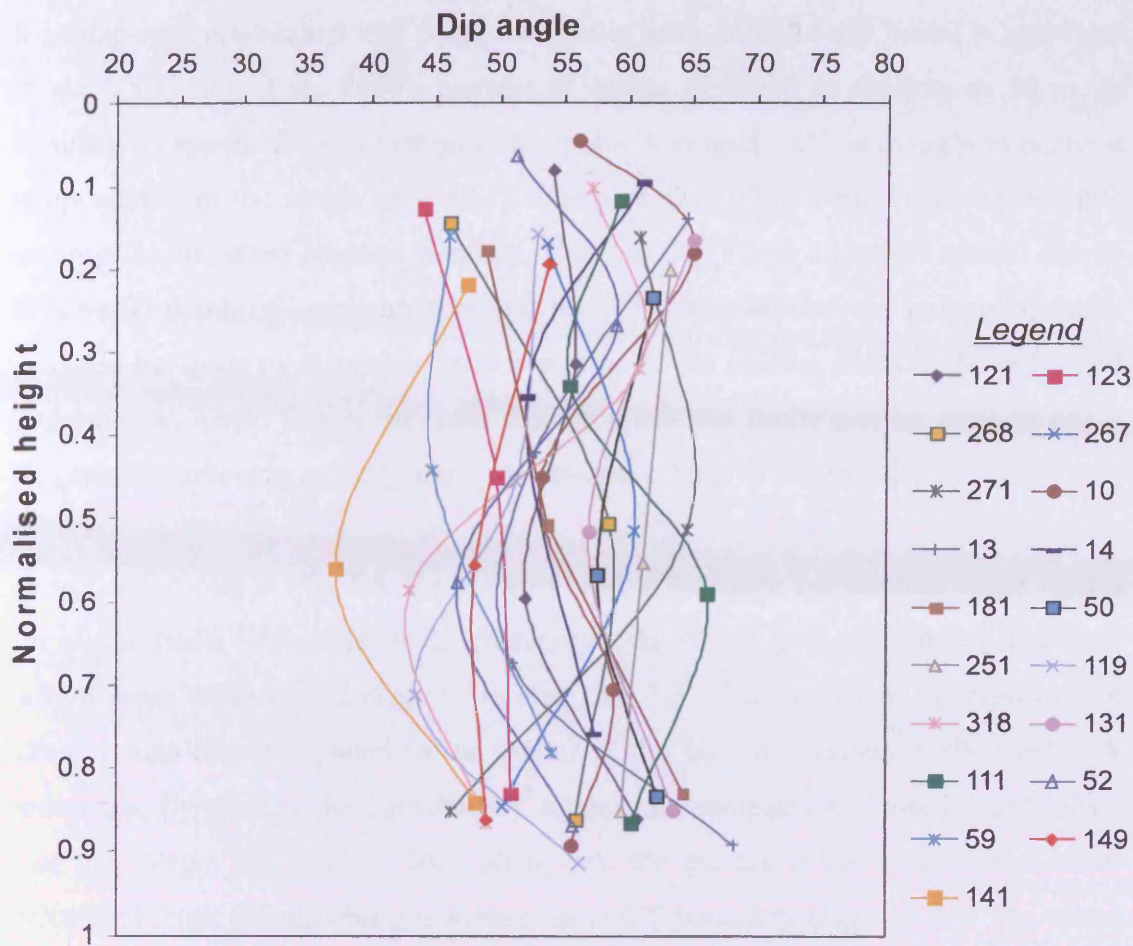
Fig. 5.12. Dip variation (abscissa) with normalised depth (ordinate) for a selection of faults that occur in the interval above the A/CT reflection in the Gjallar Ridge study area. The change in dips of up to 20° is not systematic over 300 to 500 m of the vertical height. Data used to build this plots are shown in Appendix A2.16.

It is also well established that polygonal faults form during early burial (Cartwright et al., 2003; Gay et al., 2004), perhaps at depths of burial as shallow as 50 m. In contrast, diagenetic transformation from opal – A to opal – CT is thought to occur at temperatures in the range 20 – 50 °C (Hein et al., 1978), which for a reasonable assumed temperature gradient (Brekke, 2000) of 50 °C per kilometre would equate to a burial depth of approximately 400 m. This suggests that the polygonal faults predated the onset of diagenetic transformation of the opaline silica in the deformed interval, and hence further supports the view that the faults can be used as pre – diagenetic markers to quantify the compactional effects of diagenesis.

Based on the data in Fig. 5.8, Eq. 5.1 was used to calculate compaction strain values for all the faults in the Gjallar Ridge survey area, which gave a normal distribution with a mean value of 0.7 (Fig. 5.13a and Tab. 5.5). The scatter in the compaction strain values can be equated to the scatter in the fault dip values in the opal – A sediments. By plotting the dip value 'A' against the compaction strain, it can be seen that the steeper the original fault plane dip, the greater is the compaction strain calculated from the dip changes across the A/CT boundary (Fig. 5.13b). The mean compaction strain calculated using this method (0.7) approximates the value bounds derived from the change in porosity and bulk density (0.50 – 0.66).

The comparable values for the compaction strain obtained from the porosity/density measurements and from the reduction in fault plane dip argues that silica diagenesis in this region offshore Norway resulted in a significant and abrupt vertical consolidation. Redwine (1981) suggested the consolidation could be triggered by loss of grain – to – grain contact stresses upon the dissolution of opal – A skeletal particles. There is no need to invoke significant lateral strains (e.g. Cartwright and Lonergan, 1996) simply because the two independent methods for vertical strain computation provide comparable values. If there was significant lateral (horizontal) strain at the grain scale due to the collapse of porosity, this would have resulted in a mismatch between the two sets of values, with a lesser degree of vertical consolidation implying the need for a smaller fault plane dip reduction.
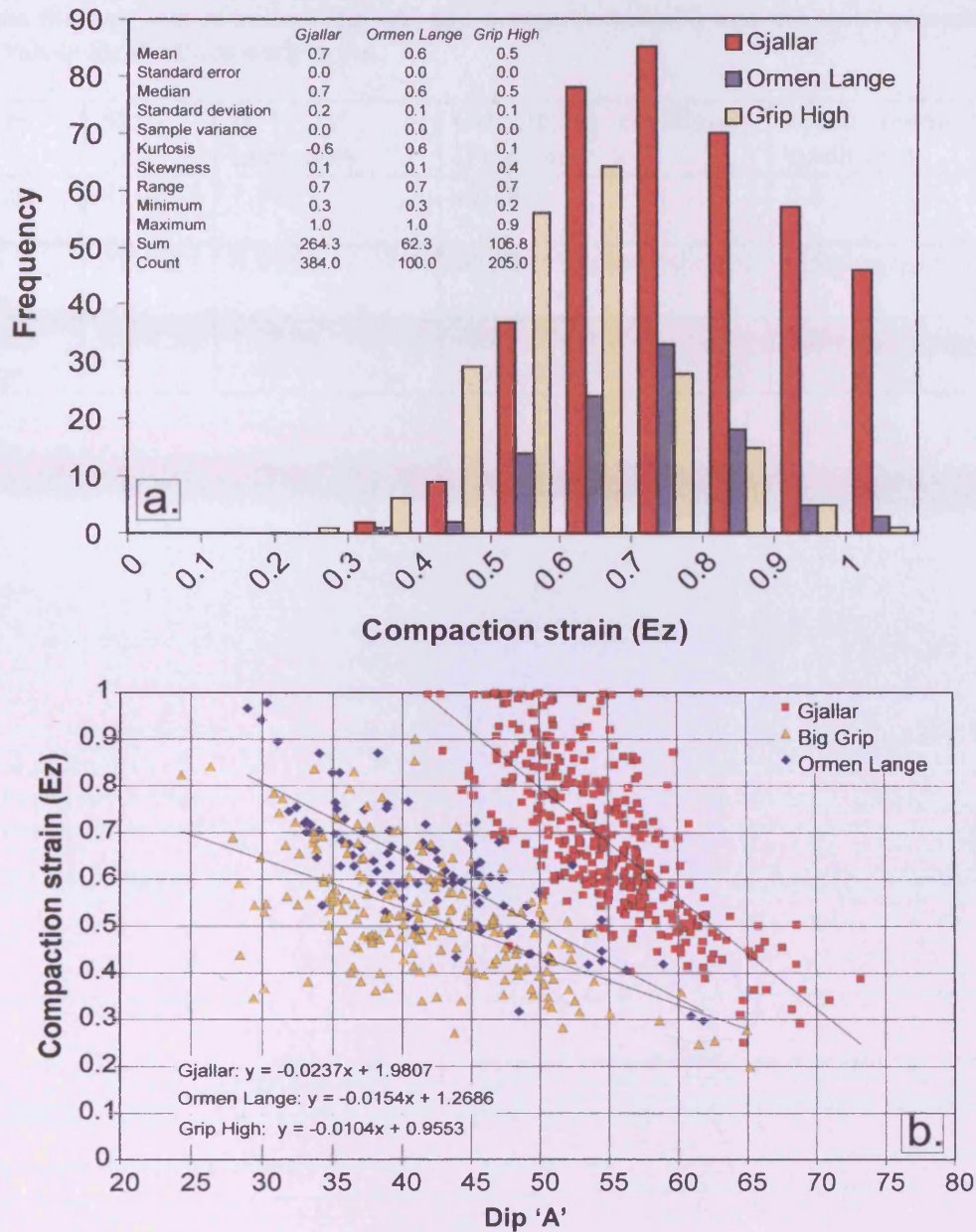
Fig. 5.13. (a) Histogram showing the frequency of the compaction strain values for the three surveys. Corresponding descriptive statistics are also shown. (b) Cross – plot of the compaction strain values versus dip 'A' values for the faults in the three surveys (symbols as in Fig. 5.8). The regression parameters and correlation coefficients for the two sets of values are presented in Tab. 5.5. Associated data are shown in Appendices A2.15 – A2.17.

124

Tab. 5.5. The parameters of the regression lines in Fig. 5.13. The correlation coefficients between the two sets of values (dip 'A' and compaction strain) and the mean compaction strain values for the three study areas.

Survey area	Slope (m)	B (y — intercept)	Correlation coefficient (Pearson)	Mean compaction strain (E_z)
Gjallar	-0.0237	1.9807	-0.74	0.7
Grip High	-0.0104	0.9553	-0.58	0.5
Ormen Lange	-0.0154	1.2686	-0.8	0.6

The results above demonstrate that the vertical compaction strain due to silica diagenesis can be predicted to reasonable accuracy in areas where there are no direct measurements of porosity or density, simply from the observation of reduction of fault plane dip. This technique can, potentially, be applied in many areas of the world where sedimentary layers that host polygonal fault systems have also been subject to silica diagenesis, such as offshore West Africa, the Blake Plateau, offshore Ireland and offshore NW Australia (Cartwright and Dewhurst, 1998). This technique does not yield absolute porosity value predictions, because similar compaction strains can be obtained for very different initial and final porosity values (Meadows and Davies, 2010a). Much further work is required for a direct prediction of porosity prior to and after this diagenetic transformation, because initial porosity and porosity reduction are likely to vary according to the specific concentration of silica in the original sediment, in addition to the presence of other minerals, such as clays and carbonates (Nobes et al. 1992).

5.5.3. Fault growth during silica diagenesis

The preceding discussion has argued the case that the transformation of opal – A to opal – CT results in a porosity collapse and a vertical consolidation that passively rotates dipping markers (fault planes) into shallower dip angles. The discussion can be concluded by considering what impact this dip reduction should have on continued fault growth, and what can be inferred regarding the actual growth of the polygonal faults in the three case study areas.

The dip measurements presented in Fig. 5.8ab show that reduction of dip across the A/CT boundary is typically 10 – 20°, but in many cases of steeper initial dip, this can exceed 25°. It was also noted above that diagenesis results in an increase in shear strength from the opal – A rich unconsolidated sediment to the opal – CT, cemented sediment (Pittenger et al., 1989; Bjørlykke and Høeg, 1997). There are few direct measurements of shear strength of opal – CT sediments, so this change is schematically represented in a Mohr construction in Fig. 5.14.

This construction suggests that the in situ stress state prior to diagenesis necessary to maintain active slip given a coefficient of friction appropriate for opal – A rich sediment (μ_{r-OpA}) would be insufficient to permit slip at the same burial depth for a material with a higher shear strength (μ_{r-OpCT}). When it is considered that the fault plane shallows by approximately 20° across the diagenetic front, it is even less likely that slip should occur after diagenesis. From this it follows that, in order to maintain active slip on a fault that has been rotated by this magnitude, a substantial reduction in friction coefficient and/or a substantial increase in differential effective stress (by reducing the minimum principal stress) are required.

Since silica diagenesis is known to result in the expulsion of large relative volumes of water (Jones and Segnit, 1971; Volpi et al., 2003; Davies and Cartwright, 2007), one possible mechanism for obtaining a reduced value for residual frictional strength of the fault zone is by dilation through pore fluid expulsion, similar to that invoked to explain fluid flow along thrust faults in accretionary prisms (e.g. Byrne et al., 1993; Cobbold and Rodrigues, 2007). Alternatively, it may be that the fault zone never becomes cemented by opal – CT, because of the different micromechanical conditions present on an active fault zone as opposed to those experienced by the intact sediment of the surrounding fault blocks.

Reduction in least confining stress would not, normally, be predicted by classical soil mechanics under confined loading, but in the situation prevalent here, where active dissolution was occurring during diagenesis, significant reductions in the least principal stress may be predicted (Shin et al., 2008). These speculative suggestions need further testing, but collectively argue that deviations from classical Mohr – Coulomb behaviour may be expected during the combined processes of diagenesis and porosity collapse, and may indeed be sufficient to promote continued fault growth.

There can be little doubt that diagenesis and porosity collapse leading to fault plane flattening did not adversely influence the continued accumulation of displacement on the polygonal faults in the study areas, and more generally in the Møre and Vøring Basins, offshore Norway. The plots of throw variation with depth measured

from the three case study areas show that displacement accumulated after the upward migration of the diagenetic front had effectively ceased (Fig. 5.4; Appendices A2.14 – A2.17), sometime in the Late Pliocene. This is consistent with the observation that the A/CT reflection is near parallel to the base of Naust Formation (Late Pliocene) in this area, supporting Brekke (2000) suggestion of an arrested development of the diagenesis of opal – A to opal – CT at about this time.

Cessation of the upward migration of the reaction front does not, of course, imply necessarily that all silica diagenesis ceased at this time, but given that opal – A is almost entirely converted at the reaction front, cessation of migration of the front is equivalent to a effective halt to any further porosity collapse mechanism or other substantial change in physical properties of the sediments. Therefore, the accumulation of further displacement after this point in time must have occurred under the conditions stipulated in the schematic Mohr construction of Fig. 5.14, but without the probable involvement of large pore fluid flux or dissolution – related change in confining stress.
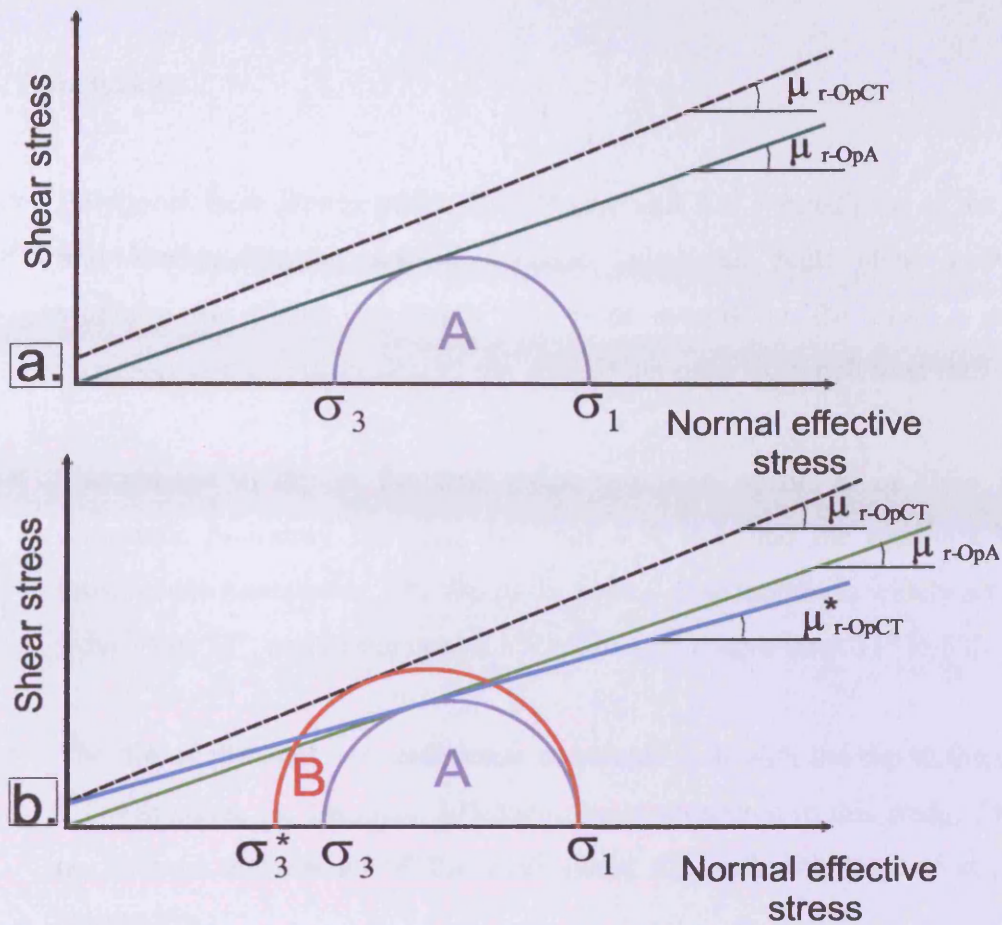
Fig. 5.14. (a) Mohr – Coulomb failure envelopes for the same sediment before diagenesis (continuous line) and after diagenesis (dashed line). μ_{r-OpA} is the coefficient of friction for opal – A rich sediment and μ_{r-OpCT} is the coefficient of friction for opal – CT rich sediment. σ_1 and σ_3 are the maximum and minimum principal stresses, respectively. The in situ stress state prior to diagenesis (circle A), necessary to maintain active slip, would be insufficient to permit slip at the same burial depth for a material with a higher shear strength (opal – CT). (b) Shear failure could occur by decreasing the friction angle to μ^*_{r-OpCT} (the shear failure envelope is represented by the dotted black line) while maintaining the same stress state (circle A) or by reducing the minimum normal stress to σ_3^* (stress circle B).

5.6. Conclusions

- Polygonal fault planes within the Brygge and Kai Formations, of the Møre and Vøring Basins, exhibit unusual segmented fault plane geometry, whereby the planar segments dip more steeply in the opal – A rich biosiliceous mudstones than in the underlying opal – CT rich interval.

- The change in dip in the fault plane segments occurs at or close to the diagenetic boundary between the opal – A rich and the opal – CT rich biosiliceous mudstones. The dip in the opal – A sediments is widely scattered from 24 to 73°, and in the opal – CT sediments ranges from 11° to 57°.

- The dip of the opal – A sediments correlates well with the dip in the opal – CT sediments, for the circa 700 fault planes measured in this study. There is no obvious correlation of the fault plane dip with lithology or structural parameters.

- The magnitude of the dip reduction across the opal – A to opal – CT reaction boundary is approximately 10° to 20°.

- Estimates of the compaction strain based on porosity and density measurements from calibration wells are 0.50 to 0.66. This equates with the mean vertical compaction strain calculated from the change of fault plane dip, assuming the fault planes were planar markers prior to diagenesis. This equivalence suggests that the fault planes were passively rotated into shallower dips as a result of diagenesis.

- The rotation of fault planes as a result of diagenesis offers a new method for estimating the porosity reduction due to silica diagenesis.

- The faults continued to grow after diagenesis had effectively ceased, and, as a result, the opal – A/CT reflection is systematically offset by a lesser

amount than the throw on the true stratal markers. Continued growth occurred in spite of changes in physical properties such as an increase in shear strength, in spite of the reduction in fault plane dip.

- Further work is required to understand this post – diagenetic phase of growth which cannot be explained mechanically at present.

Chapter 6.

FOSSILISATION OF A SILICA DIAGENESIS REACTION FRONT ON THE MID – NORWEGIAN MARGIN

6. FOSSILISATION OF A SILICA DIAGENESIS REACTION FRONT ON THE MID – NORWEGIAN MARGIN

6.1. Abstract

The diagenetic transformation of biogenic silica from opal – A to opal – CT was recognised on seismic reflection data over an area of 78 $\times 10^3$ km^2 on the mid – Norwegian margin. The opal – A/CT diagenetic boundary appears as a positive, high – amplitude reflection that generally crosscuts the hosting stratigraphy. It is demonstrated that it is not a sea – bottom simulating reflection (BSR) and that is not in thermal equilibrium with the present day isotherms. This chapter presents arguments that three styles of deformation associated with the opal – A/CT reflection (polygonal faulting, regional anticlines and synclines and differential compaction folding) indicate that the silica diagenesis reaction front is 'fossilised' at a regional scale. Isochore maps demonstrate the degree of conformity between the opal – A/CT reflection and three seismic horizons of Late Miocene to Early Pliocene age that potentially represent the paleo – seabed when 'fossilisation' of the reaction front took place. The seismic interpretational criteria for recognition of a 'fossilised' diagenetic front are evaluated and the results of this research are integrated with previous studies from other basins of the NE Atlantic in order to determine if the arrest of silica diagenesis was synchronous along this continental margin.

Keywords: opal – A, opal – CT, silica diagenesis, polygonal faulting, differential compaction, isochore maps, Vøring Basin, Møre Basin

6.2. Introduction

One of the most important outstanding questions in silica diagenetic research is the correct identification of active diagenetic fronts. The term 'active', refers to fronts that have recently been in motion relative to the sediment column, and where diagenetic reactions have been taking place at a recognisable rate. A few studies in the past two decades suggested that the A/CT reflection is not related to an active

diagenetic reaction front but is in fact 'fossilised' in its current position. The first to suggest this possibility were Rundberg (1989) and Roaldset and He (1995) who proposed that the opal – A to opal – CT reaction fronts in the North Sea and Barents Sea, respectively are 'fossilised', based on disequilibrium with present – day temperature relationships.

Brekke (2000) observed that the opal – A to opal – CT reaction front from the Vøring Basin and Vøring Marginal High in the Norwegian Sea is not parallel to the sea floor, but is generally concordant to the units occurring just below the Late Pliocene unconformity. He also noted that the opal – A to opal – CT reaction front was deformed by the latest phase of Late Miocene flexuring along this continental margin. From this, Brekke (2000) argues that the diagenesis took place in the Late Miocene to Early Pliocene and has been inactive thereafter. Importantly, he concluded that the 'fossilised' opal – A to opal – CT reaction front records a higher temperature gradient in Late Miocene – Early Pliocene than at present, possibly due to an event of increased heat flow in Mid – Miocene times caused by an unknown mechanism. Thus, Brekke (2000) was the first to propose that recognising 'fossilised' reaction fronts could be used to help constrain paleo – geothermal events.

Davies and Cartwright (2002) argued for a 'fossilised' A/CT transformation within the Faeroe – Shetland Basin, based on discordant structural and stratigraphic relationships between the A/CT reflection and its host sediments. They inferred that the opal – A to opal – CT transformation has been 'arrested' in its current stratigraphic position since the early Pliocene, and followed Brekke (2000) in linking the cause of the arrested diagenesis to changes in thermal regime, either due to the decreasing of the heat flow or to the cooling from the water column. The significance of discordant geometry has recently been challenged by Meadows and Davies (2008; 2010b) who suggested that the A/CT reflection within the Sea of Okhotsk, although generally discordant to the present seabed, is not 'fossilised', and has instead been subject to a significant decrease in the rate of conversion in the latest phase of basin evolution. Given the potential significance of recognising a truly 'fossilised' diagenetic front for a better understanding of the silica diagenetic

process and thermal evolution of basins in which the opal – A to opal – CT reaction front is developed, it is imperative to develop a set of interpretational criteria to allow a 'fossilised' reaction front to be distinguished from a currently active front. Therefore, the main aims of the research presented in this chapter are to: (a) critically evaluate seismic interpretational criteria for recognition of a 'fossilised' diagenetic front; and (b) to discuss the reasons for the arrested diagenesis in a wider context.

This research focuses on the examination of the evidence for a 'fossilised' opal – A to opal – CT reaction front on the mid – Norwegian margin, extending the work of Brekke (2000), by including a larger area of the Southern Vøring Basin and adjacent Møre Basin, and with the benefit of 2 – D and 3 – D reflection seismic data tied to over 20 hydrocarbon exploration and scientific boreholes (Fig. 6.1). The relationships between structural deformation of host sediments and the geometry of the diagenetic boundary are used to infer an arrested diagenesis. Isochore maps are used to evaluate the degree of conformity between the A/CT reflection and the host stratigraphy and to estimate the timing of 'fossilisation'. Finally, the results are integrated with previous studies from other basins of the NE Atlantic margin where the silica diagenesis front has been interpreted as 'fossilised', in an effort to establish if the arrest of silica diagenesis was synchronous or diachronous along the margin, and on what time and length scale.

6.3. Specific data and methodology

The data set used for this research is composed of a regional grid of multichannel 2 – D reflection seismic lines covering an area of 78 $\times 10^3$ km^2 of the Møre and southern Vøring Basins, on the mid – Norwegian continental margin (Fig. 6.1). The parameters of the surveys were presented in Tab. 2.1. of Chapter 2. Data from 19 exploration wells and Ocean Drilling Program Leg 104 were used for stratigraphic correlation (Fig. 6.1a and Tab. 6.1). The A/CT reflection was calibrated with all the available well data (Tab. 6.1), and mapped over an area of about 5 $\times 10^4$ km^2, comprising the Møre and Southern Vøring Basins (Figs. 6.1a and 6.2).
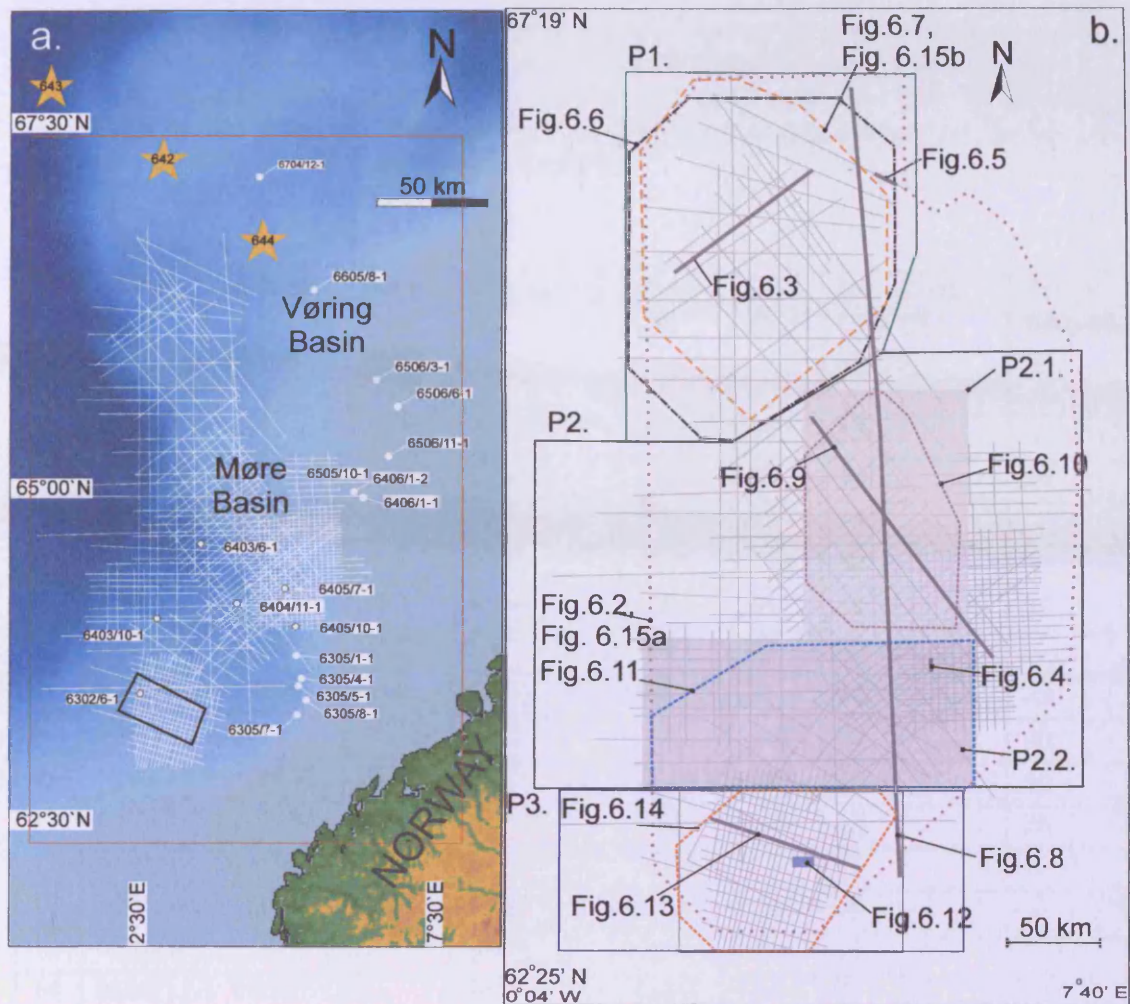
Fig. 6.1. (a) Location map of the study area. White dots mark the available exploration wells and yellow stars the nearby Ocean Drilling Program sites; (b) The regional grid of multichannel 2 – D seismic lines with the location of the subsequent figures. P1, P2 and P3 mark the three case study areas, and P2.1 and P2.2 mark the two sub – provinces of the central study area. A map of the seafloor reflection is shown in Appendix A3.4.

Tab. 6.1. The exploration wells in the study area. For every well the estimated geothermal gradient and the opal – A to opal – CT reaction front thickness are listed. The location of the wells is in Fig. 6.1a. TVD represents the total vertical depth relative to kelly bushing (KB). Metres below sea floor are abbreviated mbsf. BHT is the abbreviation for bottom hole temperature and G.G. means geothermal gradient.

No	Well	Water depth (m)	Sea – floor temp. (°C)	TVD (m)	KB (m)	Depth (m)	BHT (°C)	Estimated G.G. (°C · km-1)	TZ$_{A/CT}$ thickness (m)
1	6302/6-1	1261	-0.7	4234	25	2948	112	38	–
2	6403/10-1	1717	-1.5	3398	25	1656	80	49	20
3	6404/11-1	1495	-1	3650	25	2130	93	44	–
4	6403/6-1	1721	-1.5	4120	25	2374	118	50	–
5	6305/1-1	840	-0.3	4546	24	3682	141	38	25
6	6305/4-1	1004	-0.5	2974	25	1945	84	43	–
7	6305/5-1	886	-0.4	3053	26	2141	81	38	25
8	6305/7-1	857	-0.35	3377	26	2494	100	40	40
9	6405/10-1	928	-0.5	3182	24	2230.5	88	40	40
10	6405/7-1	1242	-0.7	4278	36	3000	126	42	25
11	6505/10-1	684	0	5026	23	4319	151	35	–
12	6406/1-2	383	5	4492	25	4084	164	39	–
13	6506/3-1	341	6	3662	25	3296	121	35	–
14	6506/11-1	246	7	4672	29	4397	143	31	–
15	6506/6-1	434	5	5474	18	5022	200	39	–
16	6704/12-1	1352	-0.8	4094	25	2717	142	53	35
17	6605/8-1	838	-0.35	4508	24	3646	158	43	–
18	6305/8-1	837	-0.35	3175	25	2313	–	–	41
19	6406/1-1	344	6	5057	24	4689	–	–	–
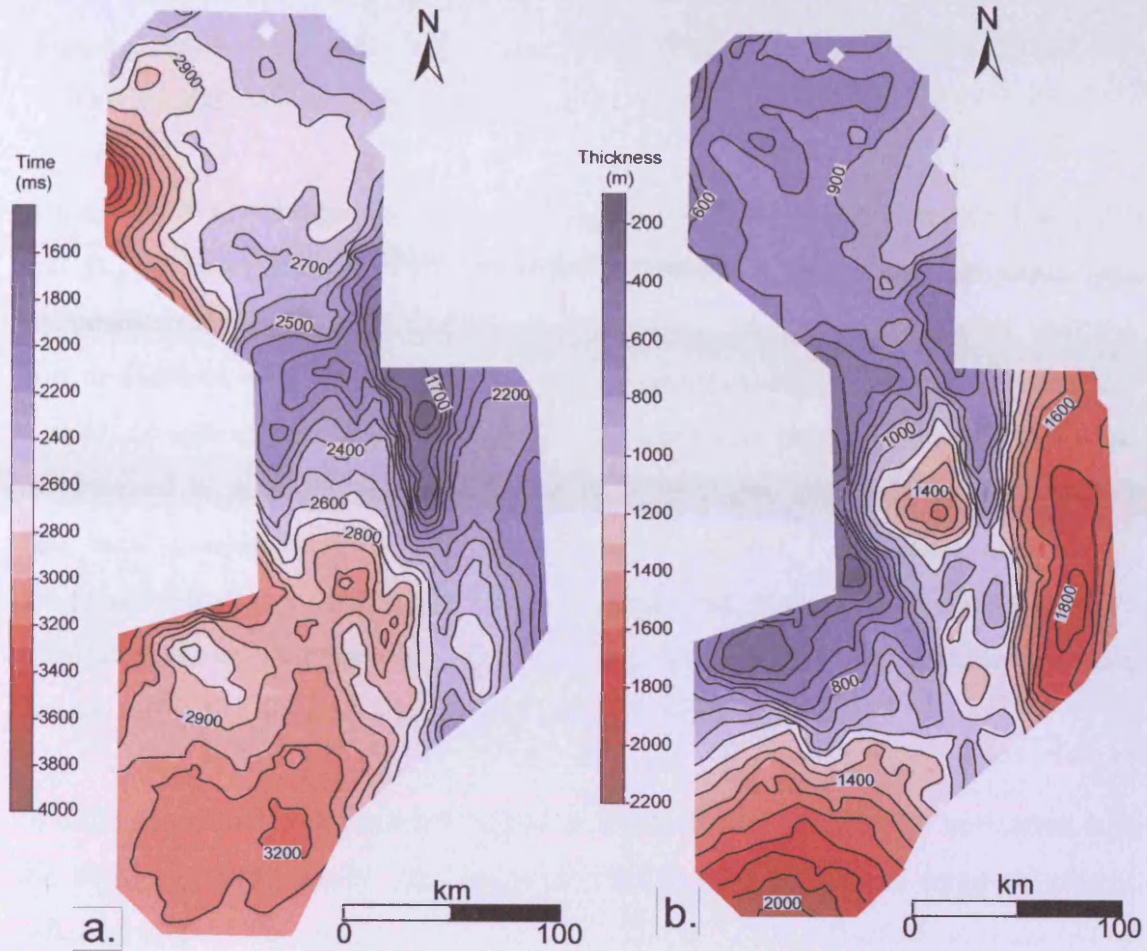
Fig. 6.2. Contour maps of the A/CT reflection. (a) Two – way travel time (TWT) map. The contour interval is 50 ms; (b) Isochore showing the thickness variation of the sediments bounded by the A/CT reflection and the present day seabed. The contour interval is 100 m. Interpolation parameters used for creating the grids are shown in Appendix A3.1.

The A/CT reflection is easily identified on the seismic data due to its high amplitude (Figs. 6.3 and 6.4) and commonly crosscutting relationship with the host stratigraphy (cf. Davies and Cartwright, 2002) (Fig. 6.3).

A number of key stratigraphic horizons through the interval of interest (Naust, Kai and Brygge Formations) were correlated and mapped throughout the study area (Appendices A3.3 – A3.19). One of the aims of this seismic – stratigraphic mapping was to evaluate whether the A/CT reflection was concordant with the present day seabed, or with any deeper horizon over any significant portion of the mapped area, as observed in previous studies (Davies and Cartwright, 2002). It is often the case that local concordance can be seen between the A/CT reflection and several shallower reflections on any one seismic profile, but inspection of several profiles invariably shows that the opal – A to opal – CT reaction front reflection is only concordant with a limited stratigraphic interval over a larger area.

In order to evaluate the regional degree of concordance of the A/CT reflection with the overlying stratigraphy, the isochore values between all the mapped seismic reflections up to the seafloor (e.g. Fig. 6.5) and the A/CT reflection were computed over the entire study area. The two – way travel time values of the seismic reflections were interpolated between the 2 – D seismic lines using the least squares method in order to generate two way – travel time (TWT) grids. The interpolation parameters (cell size of the grids, contour intervals) are presented in Appendix A3.1.

Based on the grids, TWT structure contour maps were generated (e.g. Fig. 6.6). The maps represent the vertical thickness of the sediments, thus greater deviation from true stratigraphic thickness occurs where the dips of the structures are higher, for example on the flanks of the anticlines (e.g. Helland Hansen Arch in Fig. 6.7). For simplification, a single interval velocity of 2000 m $\cdot$ s^{-1} was used for the depth conversion of the TWT maps. This value is based on the average interval velocity from the A/CT reflection to the interval of interest calculated from the well data (Tab. 6.2). The local variation of the average interval velocity is less than 10 % compared to the simplified value used (2000 m $\cdot$ s^{-1}).
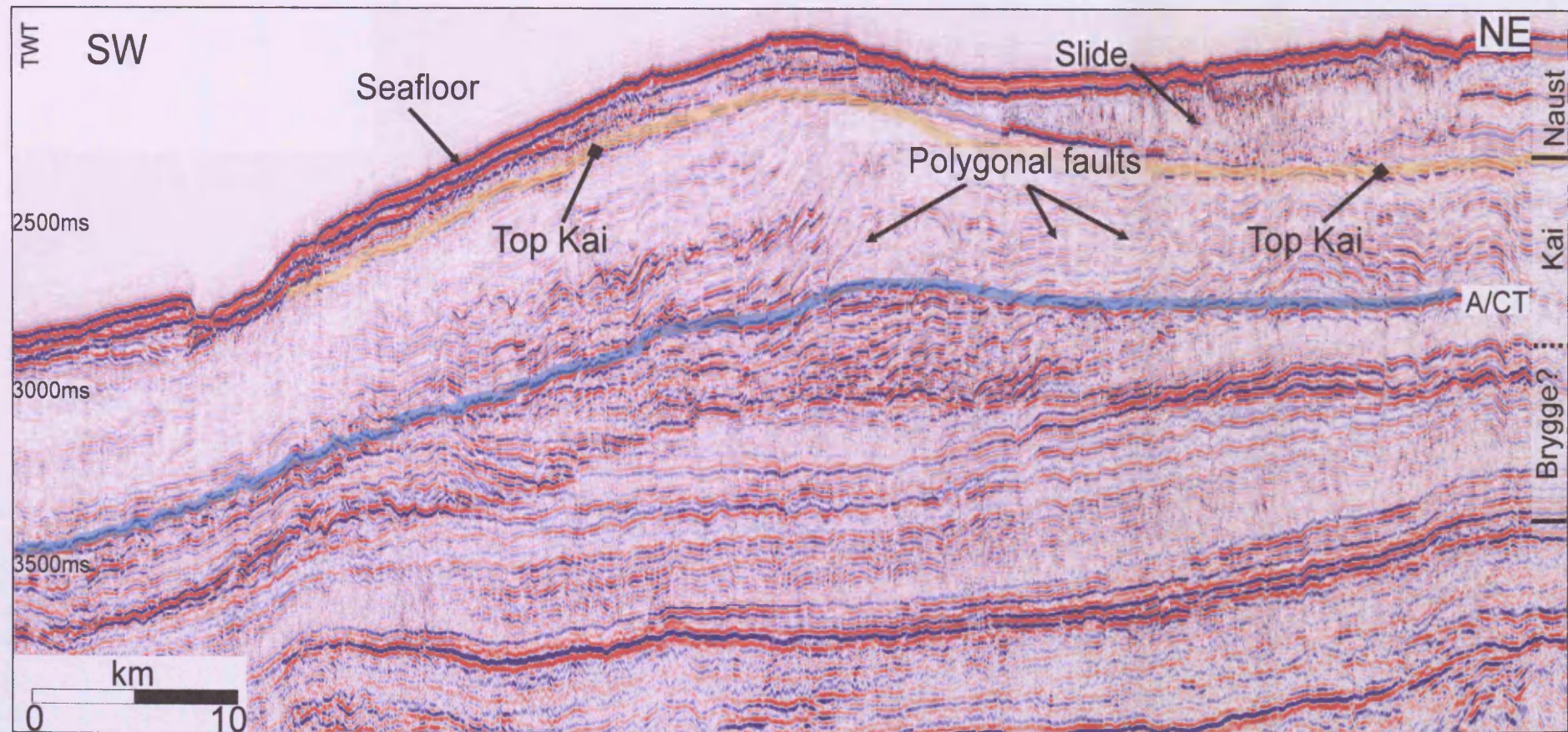
Fig. 6.3. Seismic cross – section from the northern study area illustrating the crosscutting relationship with the hosting stratigraphy of the A/CT reflection (highlighted in blue). Location of the profile is shown in Fig. 6.1b.
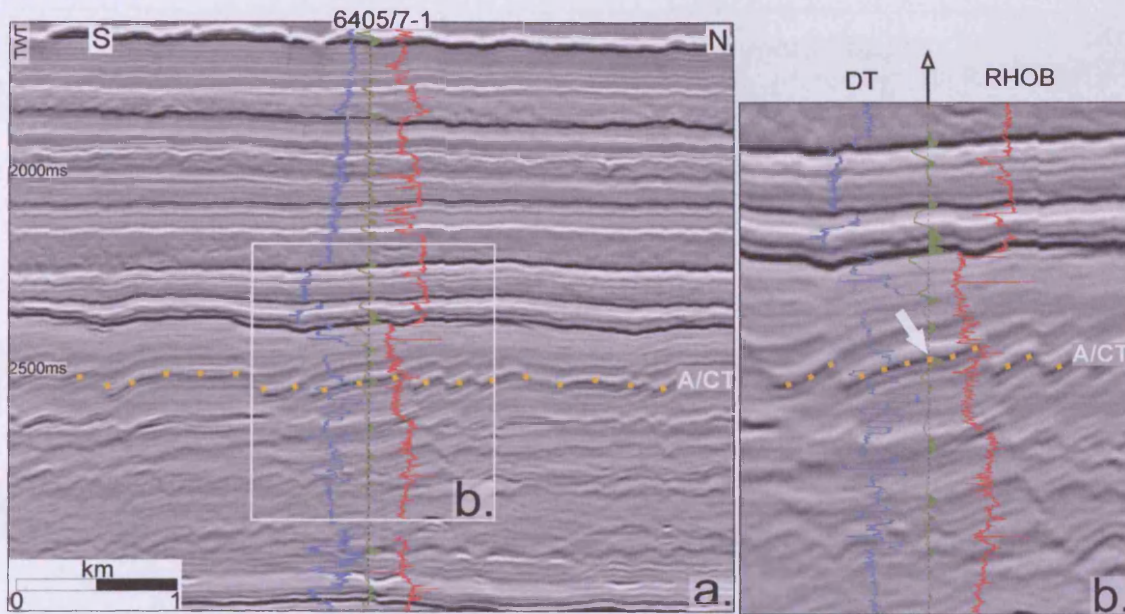
Fig. 6.4 (a) Seismic cross – section intersecting well 6405/7 – 1. Sonic (DT) and density (RHOB) logs are shown together with the synthetic seismogram (green curve). Note that the A/CT reflection is crosscut by polygonal faults. Location of the seismic profile is in Fig. 6.1b; (b) Close – up of the outlined area in Fig. 6.4a. The opal – A to opal – CT reaction front is marked by a positive amplitude reflection on the synthetic seismogram (indicated by the white arrow).
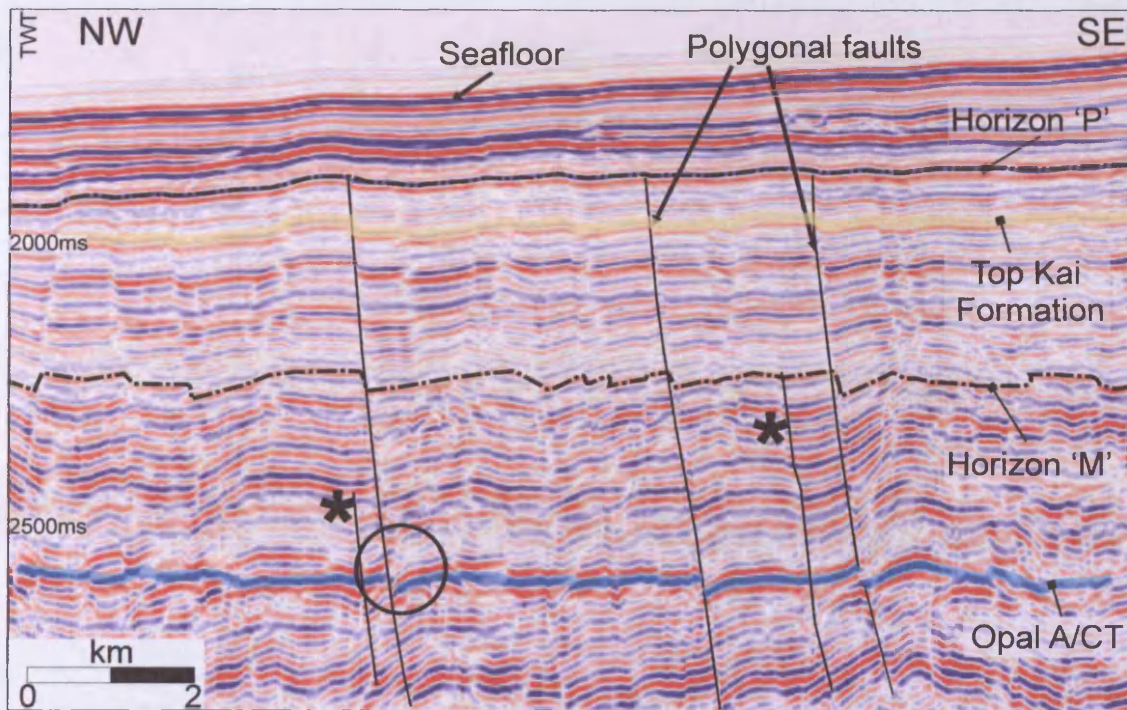
Fig. 6.5. Seismic cross – section from the northern study area (P1 in Fig. 6.1b. Location is shown in Fig. 6.1b. Top Kai Formation, horizon 'M' and the A/CT reflections are marked. Horizon 'P' represents the top of the polygonal fault tier. Note that the faults marked with * are shorter than the others. Also, the magnitude of throw at the A/CT reflection is less for the shorter faults compared to the throw at the A/CT reflection of the other polygonal faults (circled area). Other seismic profiles from the same area are presented in Appendices A3.5.2, A3.8.2, A3.11, A3.12.2, A3.14 and A3.19.
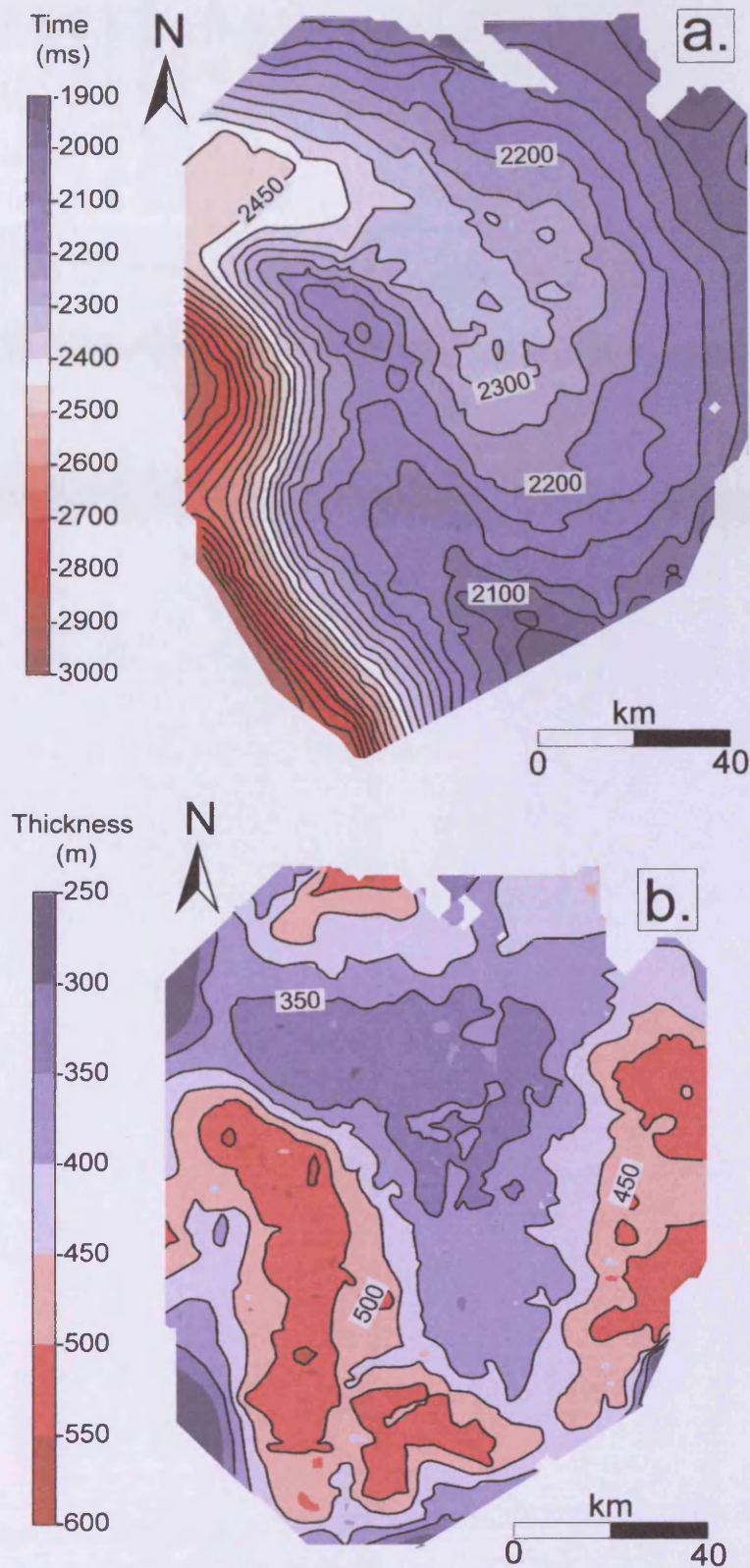
Fig. 6.6. Contour maps of the Top Kai horizon within the northern area (P1 in Fig 6.1b). (a) TWT of the Top Kai horizon. The contour interval is 50 ms; (b) Isochore map showing the thickness variation of the sedimentary section bounded by the Top Kai and the A/CT reflection. The contour interval is 50 m. Location of the maps is in Fig. 6.1b. Additional data are presented in Appendix A3.5
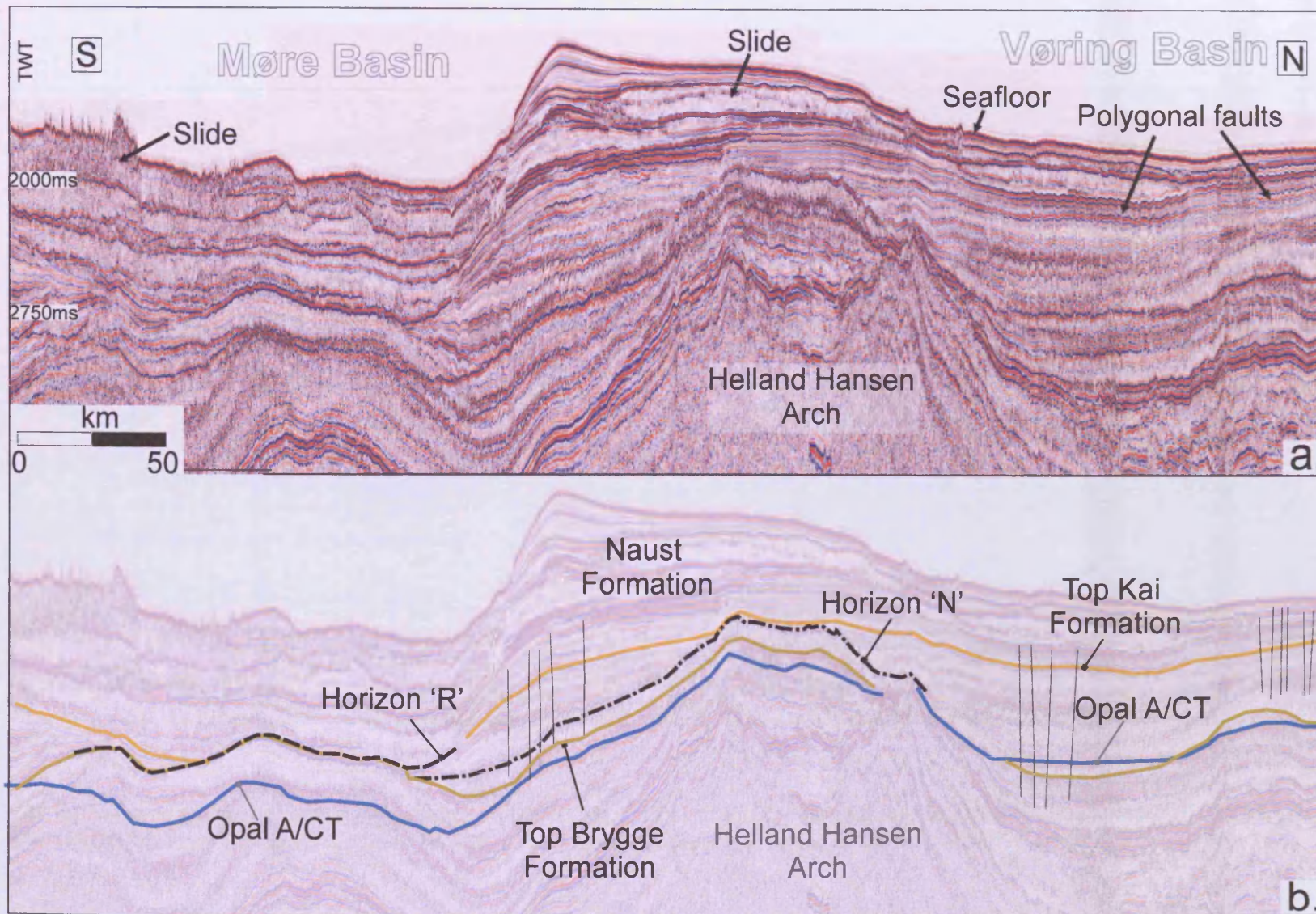
Fig. 6.7. (a) An example of a regional seismic profile oriented S – N; (b) The same seismic profile with the main interpreted seismic horizons superimposed. Location of the profile is in Fig. 6.1b.

144
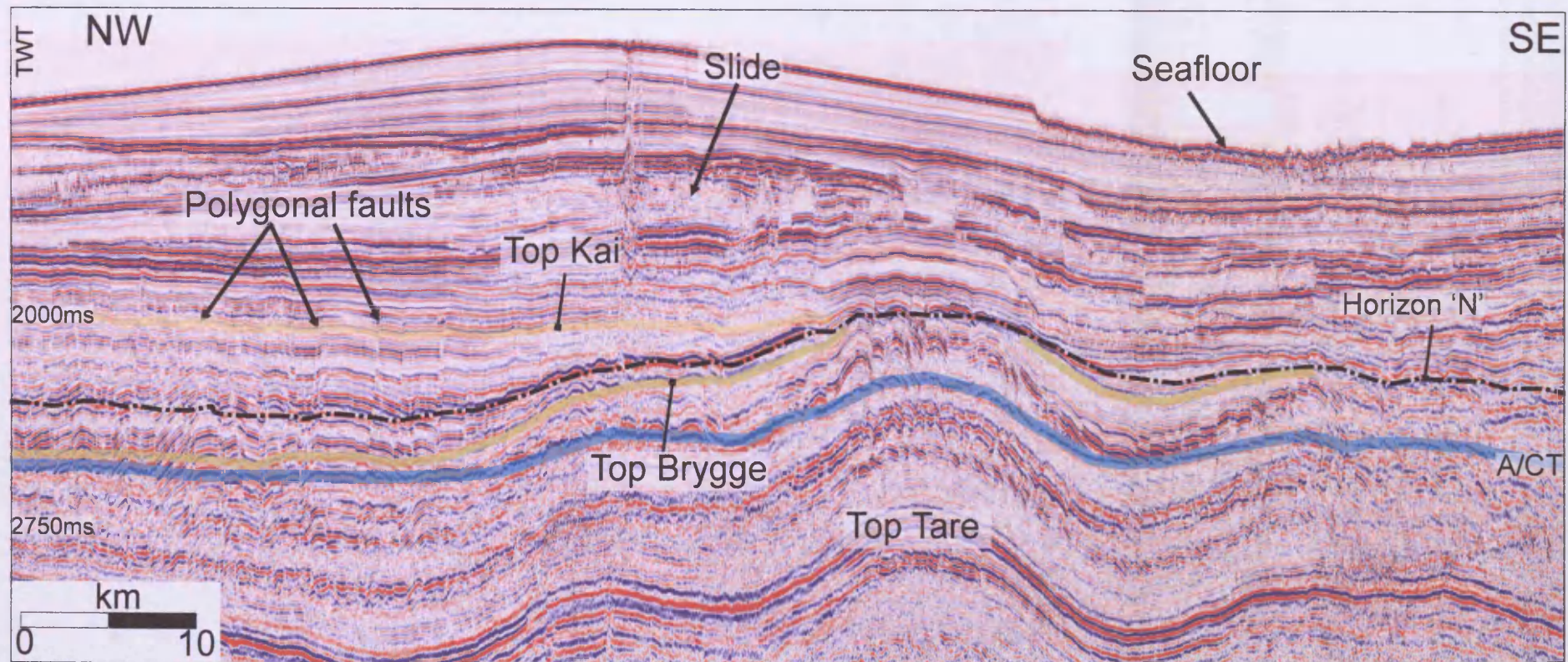
Fig. 6.8. Seismic profile from the central study area (P2 on Fig. 6.1a). Location of the profile is in Fig. 6.1b. The interpreted horizon 'N', A/CT reflection and Top Brygge, Kai and Tare Formations are marked. Note the A/CT reflection is folded in the central part of the profile.

145

Tab. 6.2. Interval velocities within the interval of interest for several wells in the study area. For simplification, an average velocity of 2000 m · s^{-1} was used for the conversion of isochore to isopach maps.

Well	Marker	TVD (m)	TWT (ms)	Interval velocities (m · s^{-1})
6305/5-1	Top Kai Opal – A/CT	1617 1920	1920 2220	1953
6305/1-1	Top Brygge Opal – A/CT	1720 1886	2065 2249	1804
6405/7-1	Top Naust Opal – A/CT	1242 2140	1644 2625	1830
6405/10-1	Top Brygge Opal – A/CT	1867 2118	2228 2493	1894

A synthetic seismogram was computed to illustrate the detailed acoustic response of the opal – A to opal – CT reaction front (Fig. 6.4). The synthetic seismogram was produced by the convolution of a wavelet with a reflection coefficient series estimated using the density and sonic logs.

A deterministic wavelet (i.e. extracts the frequency content and keeps the phase of the input data) was used. The wavelet was extracted from 50 traces of the inline closest to the well location, based on the energy spectrum. The wavelet has a length of 64 ms, a taper length of 32 ms and it contains 1 % white noise. This wavelet was convoluted with a reflection coefficient series obtained using the sonic and bulk density logs from well 6407/7 – 1 (Fig. 6.4). A time – depth function generated based on the sonic log data was used to re – locate and re – calibrate the well logs in time. The resultant synthetic seismogram was aligned to 10 seismic traces near the well location (5 traces on each side of the well location) and was manually calibrated to match the seismic data. Where the synthetic seismogram does not tie perfectly to the seismic, this can be due to the quality of the well logs and the seismic data, the wavelet extraction method and also to the fact that the two seismograms may not be sampling exactly the same subsurface volumes.

The synthetic seismogram is presented in Fig. 6.4. The opal – A to opal – CT reaction front is represented by a positive polarity (the same polarity as the seafloor reflection) and relatively high amplitude reflection (c.f. Hein et al., 1978; Bohrmann et al., 1992). At the location of the well, the A/CT reflection is relatively concordant to the host stratigraphy and is crosscut by numerous polygonal faults. The reflection is correlated to an increase in bulk density and a decrease in the sonic log interval transit time over a vertical zone 25 m thick (Fig.6.4).

6.4. Relationship of the A/CT reflection with the host stratigraphy and local structures

The study area has been divided into three regions (northern, central and southern) for ease of description (corresponding to P1, P2 and P3 in Fig. 6.1b). For every region, the description and analysis are based on representative seismic profiles (e.g.

Figs. 6.3, 6.7, 6.8), TWT contour maps of the A/CT reflection (e.g. Figs. 6a, 9a, 10a) and isochore maps between the A/CT reflection and shallower seismic horizons (e.g. Figs. 6b, 9b, 10b).

6.4.1. Northern region

This part of the study area represents the southern Vøring Basin (P1 in Fig. 6.1b). The focus of this research is the Neogene interval, which in this basin is mainly composed of contourite sediment drifts which developed largely free from any significant interaction with downslope processes (Bryn et al., 2005).

A representative seismic profile across the basin is presented in Fig. 6.3, and shows the typical stratal reflection configurations of the Cenozoic in this area. The A/CT reflection is seen as a high amplitude, positive polarity, discontinuous reflection that is discordant to the background stratal reflections of the host Kai and Brygge Formations, except at the south – western limit where it assumes an almost concordant geometry with respect to the adjacent reflections. The crosscutting relationship of the A/CT reflection with the host stratigraphy demonstrates there is sufficient biogenic silica in the overlying units to sustain the upward relative migration of the diagenetic front (Fig. 6.3).

Within most of this northern region, the opal – A to opal – CT reaction front has a similar seismic expression to that seen on Fig. 6.3, with differing degrees of concordance or discordance relative to the immediately underlying and overlying stratal reflections. The A/CT reflection was calibrated using petrophysical data and cores from well 6704/12 – 1 and ODP Site 642 (Fig. 6.1), where it is expressed by an increase in both bulk density and P – wave velocity over a 10 – 35 m thick zone.

Regionally, the A/CT reflection occurs mainly within the Miocene – Pliocene sediments of the Kai Formation. Throughout the basin it is crosscut and offset by a network of polygonal faults that are pervasively developed in this stratigraphic interval (Figs. 6.3, 6.5) (Cartwright and Dewhurst, 1998; Brekke, 2000; Berndt et al., 2004). Importantly, the magnitude of the throw of the polygonal faults measured at

the A/CT reflection is less than the true stratigraphic throw at that position (Fig. 6.5), similar to that observed previously in other areas along this margin of the NE Atlantic. This observation has been attributed to the arrest of the upward migration of the diagenetic front prior to the last period of movement on the polygonal faults (Cartwright, 2007). The majority of the faults in this area do not propagate above horizon 'P' (Fig. 5). Horizon 'P' corresponds to the top of Unit IC from ODP Site 644, which was dated as Pleistocene in age (Eldholm et al., 1987).

The A/CT reflection is highly discordant relative to recently deposited sediments in the northern region, occurring at a depth beneath the present day seafloor ranging from 300 m to 2000 m (Fig. 6.2b), therefore it cannot be considered as a sea bottom simulating reflection (BSR). The deepest position of the A/CT reflection is located in the eastern and southern parts of the basin (Fig. 6.2b), where the Pleistocene to Recent sediments are thickest. However, the A/CT reflection is relatively concordant with a set of reflections bounded by two important local marker reflections, horizon 'M' and the Top Kai Formation (Fig. 6.5). Of these, the reflection that is most consistently concordant with the A/CT reflection over this region is the Top Kai. This is a medium to high amplitude reflection that marks the base of the Naust Formation and was mapped over an area of 14×10^3 km^2 (Fig. 6.6a).

The Top Kai reflection corresponds to the top of Unit II in the nearby ODP Sites 644 and 642 (Eldholm et al., 1987) and is therefore dated as Pliocene. Due to its limited lateral continuity, it was not possible to correlate horizon 'M' to any of the nearby wells, however, it was estimated to be Late Miocene to Pliocene in age because it is confined within the upper part of the Miocene to Pliocene Kai Formation.

Isochore mapping shows that the thickness of the sediment package between Top Kai and the A/CT reflection is, in general, between 300 – 550 m for most of the study area (Fig. 6.6b). These variations in the isochore map demonstrate that the A/CT reflection is not strictly parallel to the Top Kai reflection. However, on the individual seismic profiles, the Top Kai reflection is the horizon most concordant to the A/CT reflection, when compared to the other overlying horizons.

6.4.2. Central region

The central region is located within the Møre Basin (P2 in Fig. 6.1b). Large submarine sliding events during deposition of the Plio – Pleistocene Naust Formation modified the margin. Slides have either cut through or cut down to the opal – A to opal – CT reaction front (Riis et al., 2005; Lawrence and Cartwright, 2009). In the eastern part of this area, there are several large domal anticlines which represent major inversion structures (e.g. Helland Hansen Arch) in this basin resulting from the Neogene phase of regional inversion tectonics (Doré and Lundin, 1996; Brekke, 2000; Løseth and Henriksen, 2005). Examples of inversion structures can be seen in Figs. 6.7 and 6.8.

The opal – A to opal – CT reaction front is sharply expressed on the seismic data as a high amplitude positive reflection, hosted within the sediments of the Kai and Brygge formations (Figs. 6.8 and 6.9). As with the northern region, both formations are pervasively deformed by a polygonal fault system, that is bounded above by the Top Kai Formation and below by the Top Tare Formation (Rogaland Group), which corresponds to the early Eocene (Stuevold et al., 2003).

The A/CT reflection was correlated to the exploration wells 6405/7 – 1 and 6405/10 – 1 (locations in Fig. 6.1) as a discrete increase in density and a decrease in the sonic log transit time over a vertical distance of 25 – 40 m (Fig. 6.4). Apart from the small offsets across most of the individual polygonal faults, the A/CT reflection is remarkably smooth and laterally continuous over the entire mapped area of 4×10^4 km^2. As seen on Fig. 6.8, for example, the geometry of the A/CT reflection is locally concordant and discordant relative to the immediately adjacent stratal reflections, but nevertheless maintains its continuity.

The A/CT reflection is highly discordant to the present seabed, which has itself been radically modified in form by the numerous slope failures of the Late Pleistocene to Holocene (Bryn et al., 2005). There is no evidence that the geometry of the A/CT reflection mirrors that of any of the major basal slide surfaces (e.g. Fig. 6.8). The depth of the A/CT reflection beneath the present day seabed varies considerably

from 300 m in the western part of the area to approximately 2000 m towards the east, beneath the rapidly prograding wedge of the Naust Formation (Figs. 6.2b, 6.7 and 6.8).

Regionally, the A/CT reflection is most discordant to the host stratigraphy where the Cenozoic section has been deformed into long wavelength domal anticlines and synclines (Figs. 6.7 and 6.8). Importantly, the A/CT reflection can be seen within these anticlines to have a structural relief that is clearly smaller than the maximum fold amplitude (Fig. 6.8). However, the shape of the fold at the level of the A/CT reflection is closely related in three dimensions to that exhibited by the folded Brygge Formation sediments, with a common fold axial plane. A similar geometrical relationship between folded stratigraphy and folded A/CT reflection was described from inversion anticlines in the Faeroe – Shetland Basin by Davies and Cartwright (2002).

Unlike the northern region, where there has been relatively little slope failure within the past few million years, the frequent occurrence of large volume mass transport deposits and their associated slide scars in the central region present significant obstacles to the challenge of evaluating whether the A/CT reflection is concordant with any overlying stratal surface. Nevertheless, it was possible to interpret the two reflections in two different parts of the central region that most closely parallel the A/CT reflection, referred to here as horizons 'N' and 'R' (Figs. 6.7 and 6. 8).

Horizon 'N' is mapped as a high – amplitude reflection, with high lateral continuity over an area of 9×10^3 km^2 throughout the central region. The degree of parallelism with the A/CT reflection is highest in the eastern part of the region where the isochore values range between 100 – 300 m (Fig. 6.9). Over most of the mapped area the local variations in isochore values are less than 50 m. Horizon 'N' is confined within the sediments of the Kai Formation and occurs stratigraphically in the upper part of the syn – compressional packages that are most thickly developed within the synclinal structures (Figs. 6.7 and 6.8).

Based on a long – range seismic tie to well 6302/6 – 1, horizon 'N' is tentatively dated at some time within the Late Miocene to Early Pliocene interval. Most wells in this area targeted the crests of domal structures where the Kai Formation is either missing or is very thin (e.g. 20 m in the 6405/7 – 1 well), and hence cannot be used to date horizon 'N' more precisely.

Further west in the central region, horizon 'R' exhibits a parallel relationship with the A/CT reflection over a mapped area of 8×10^3 km² (Fig. 6.10). Isochore values between the two horizons range from 150 – 250 m, but local variations can be of the order of 50 m (Fig. 6.10b). Over most of the western flank of the central region, horizon 'R' represents an erosional unconformity at the base of the earliest major sliding event to affect the Naust Formation. This unconformity cannot be dated with precision (Lawrence and Cartwright, 2009), but long – range correlation to well 6302/6 – 1 suggests it is the equivalent time period to the Upper Kai Formation and horizon 'R' is therefore likely to be Late Miocene to Early Pliocene in age.
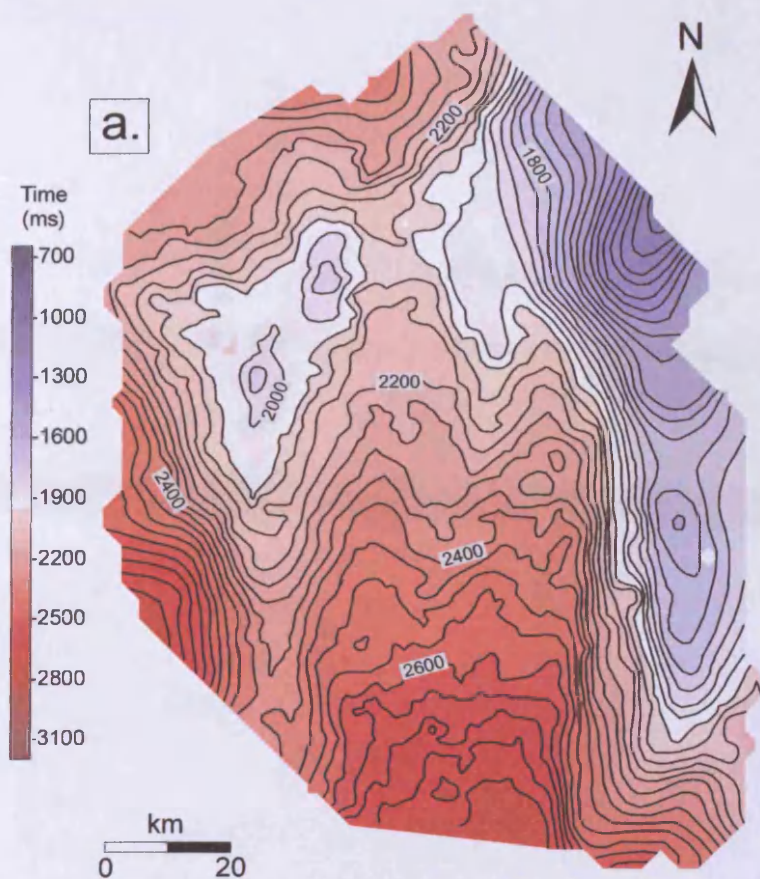
Fig. 6.9. Contour maps of the Horizon 'N' within the central study area (P2.1 on Fig. 6.1b). a. TWT. The contour interval is 50 ms; b. Isochore map showing the thickness variation of the sediment package bounded by the A/CT reflection and horizon 'N'. The contour interval is 50 m. The location of the maps is marked in Fig. 6.1b. Additional data are presented in Appendix A3.9.
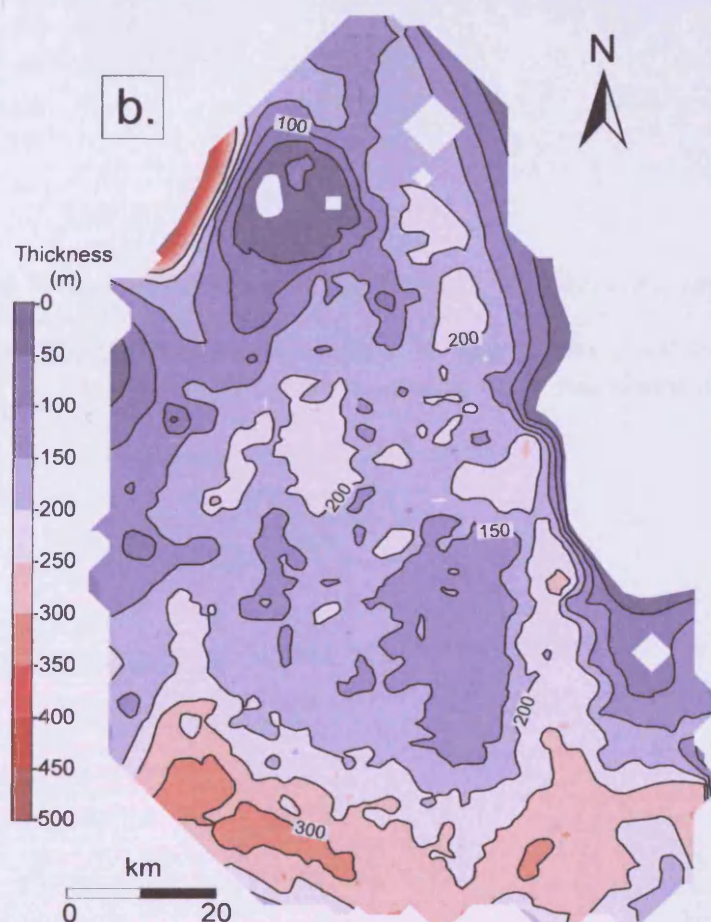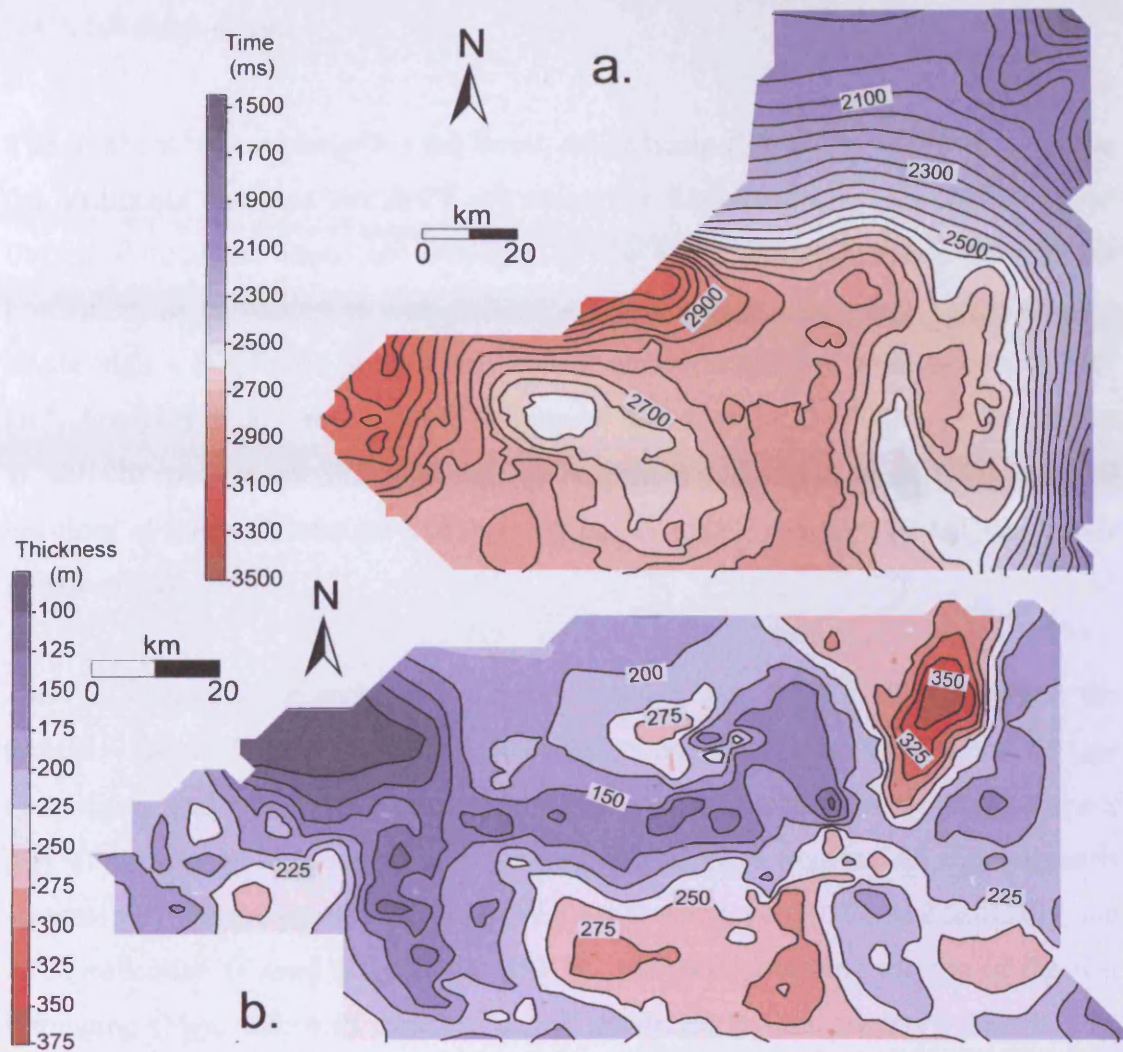
Fig. 6.10. Contour maps of the Horizon 'R' within the central study area (P 2.2 on Fig. 6.1b). (a) TWT map. The contour interval is 50 ms; (b) Isochore showing the thickness of the sediments bounded by horizon 'R' and the A/CT reflection. The contour interval is 25 m. The location of the maps is in Fig. 6.1b. Additional data are presented in Appendix A3.15.

6.4.3. Southern region

The southern region comprises the South Møre Basin (P3 in Fig. 6.1b). In this area, the sediments that host the A/CT reflection are the biosiliceous mudstones of the Brygge Formation. These are overlain by the Kai Formation and a thick Naust Formation, as correlated to well 6302/6 – 1 (Fig. 6.11). The A/CT reflection is a single high – amplitude positive reflection, which is mapped over an area of 10^4 km^2. Analyses of X – ray powder diffraction data from well 6302/6 – 1 (Ireland et al., 2010b) confirm that this high amplitude reflection found at about 1500 m below sea floor at the well location corresponds to the opal – A to opal – CT diagenetic transformation.

The A/CT reflection is mapped at a depth ranging from 1000 to 2000 m below the present – day seafloor (Fig. 6.2b). It is roughly concordant with the Kai and Brygge Formations, and is generally discordant to the irregular reflections within the upper part of the Naust Formation, which comprises a large number of slide deposits separated by thinner contouritic units (Fig. 6.11) (Bryn et al., 2005). Regionally, the A/CT reflection is most concordant with the reflection marking the top of the Kai Formation (Figs. 6.7, 6.11 and 6.12a), as illustrated by the isochore map in Fig. 6.12b. Over most of the area the interval between the A/CT reflection and Top Kai reflections is approximately 350 ± 50 m thick. The Top Kai reflection was identified as Early Pliocene using the data from well 6302/6 – 1.

In contrast to the other two regions, the A/CT reflection exhibits an irregular morphology with a cellular geometry (Figs. 6.11, 6.13a,b). The cellular pattern of the reaction front in this area was investigated by Davies and Cartwright (2007). They described the cells as localized areas, generally circular in shape, that form elevations on the front and which they interpreted to have resulted from differential advance of the front. They suggested that regions of enhanced diagenesis may be related to focusing of fluids from the underlying polygonal fault system that affects the deeper parts of the Brygge Formation oozes.
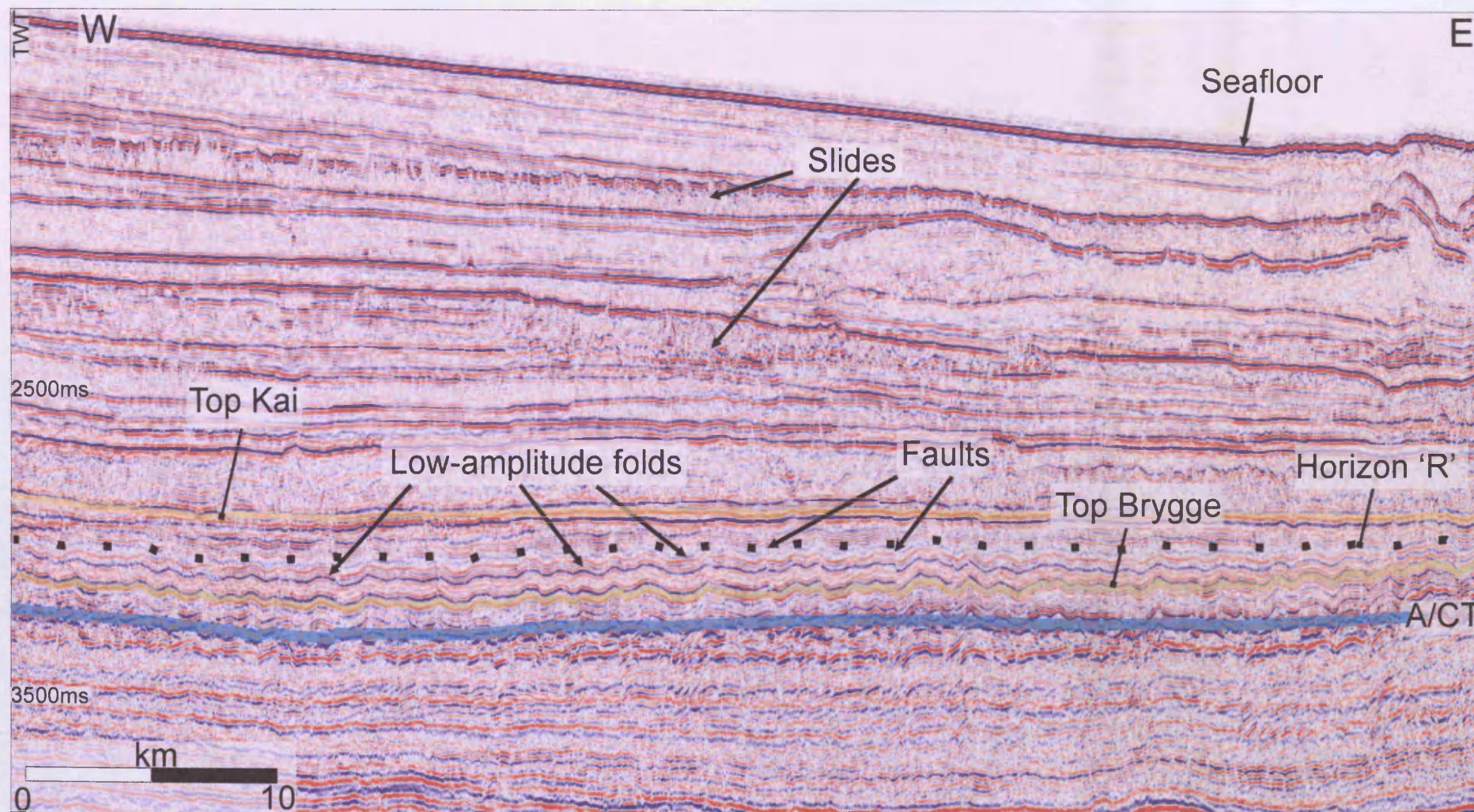
Fig. 6.11. Seismic profile from the southern study area (P3 in Fig. 6.1b) showing the low – amplitude folds above the A/CT reflection. Horizon 'R', Top Kai and Top Brygge Formations are marked. Location of the profile is in Fig. 6.1b.

156
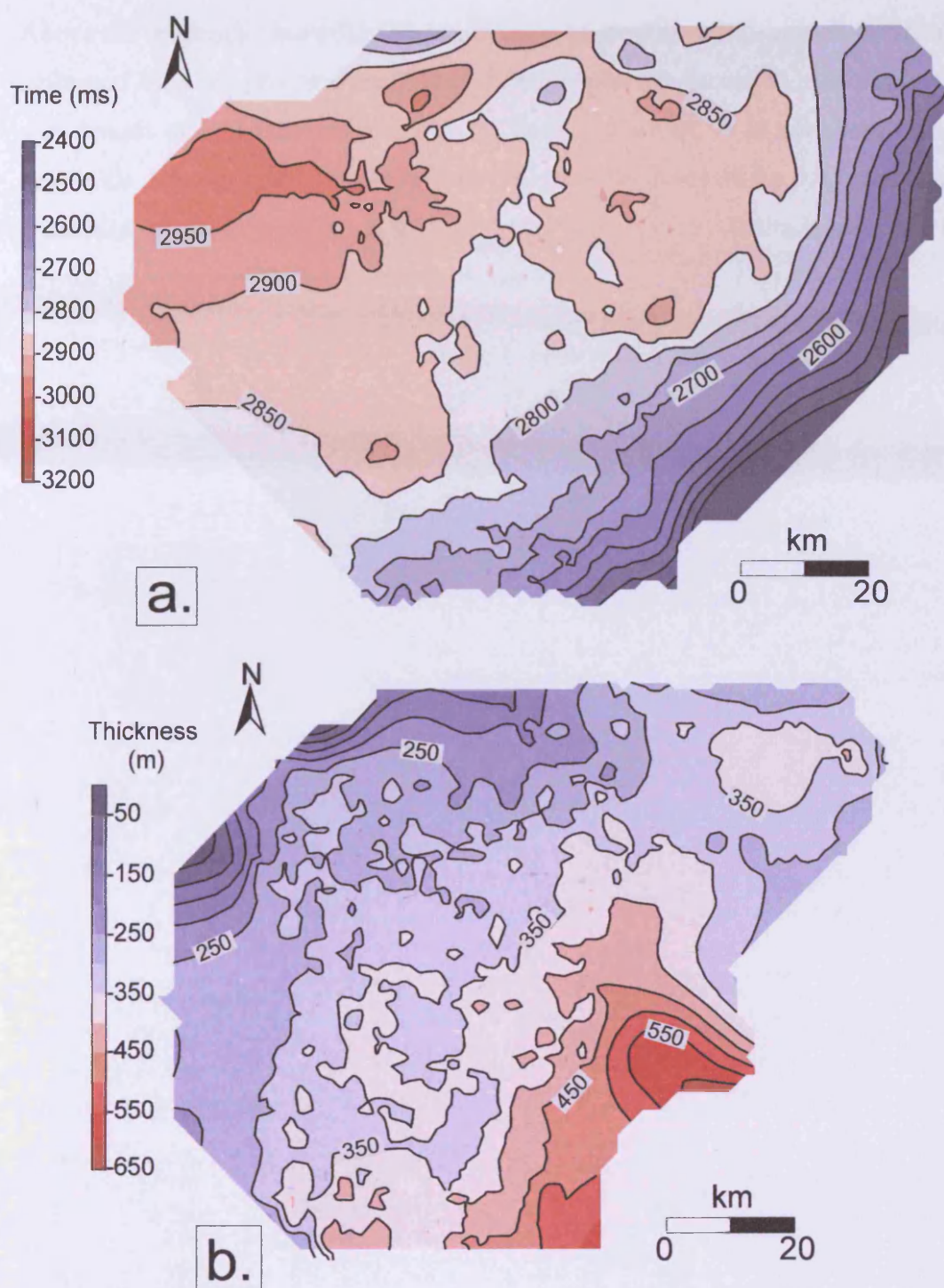
Fig. 6.12. Contour maps of the Top Kai reflection within the southern study area (P3 in Fig. 6.1b). (a) TWT. The contour interval is 50 ms; (b) Isochore showing the thickness of the sediments bounded by the Top Kai and the A/CT reflection. The contour interval is 50 m. Location of the maps in Fig. 6.1b. Additional data are presented in Appendix A3.6.

Above the diagenetic boundary, the sediments of the Kai and Brygge Formations are deformed by a set of low – amplitude folds. These are domal in plan view, with a wavelength of approximately 1 km. In cross – section, it is observed that their amplitude decreases systematically upwards from the level of the A/CT reflection to a position at the top of the Kai Formation (Fig. 6.13c). Sediments of the Naust Formation are completely unaffected by this style of folding (Fig. 6.13c).
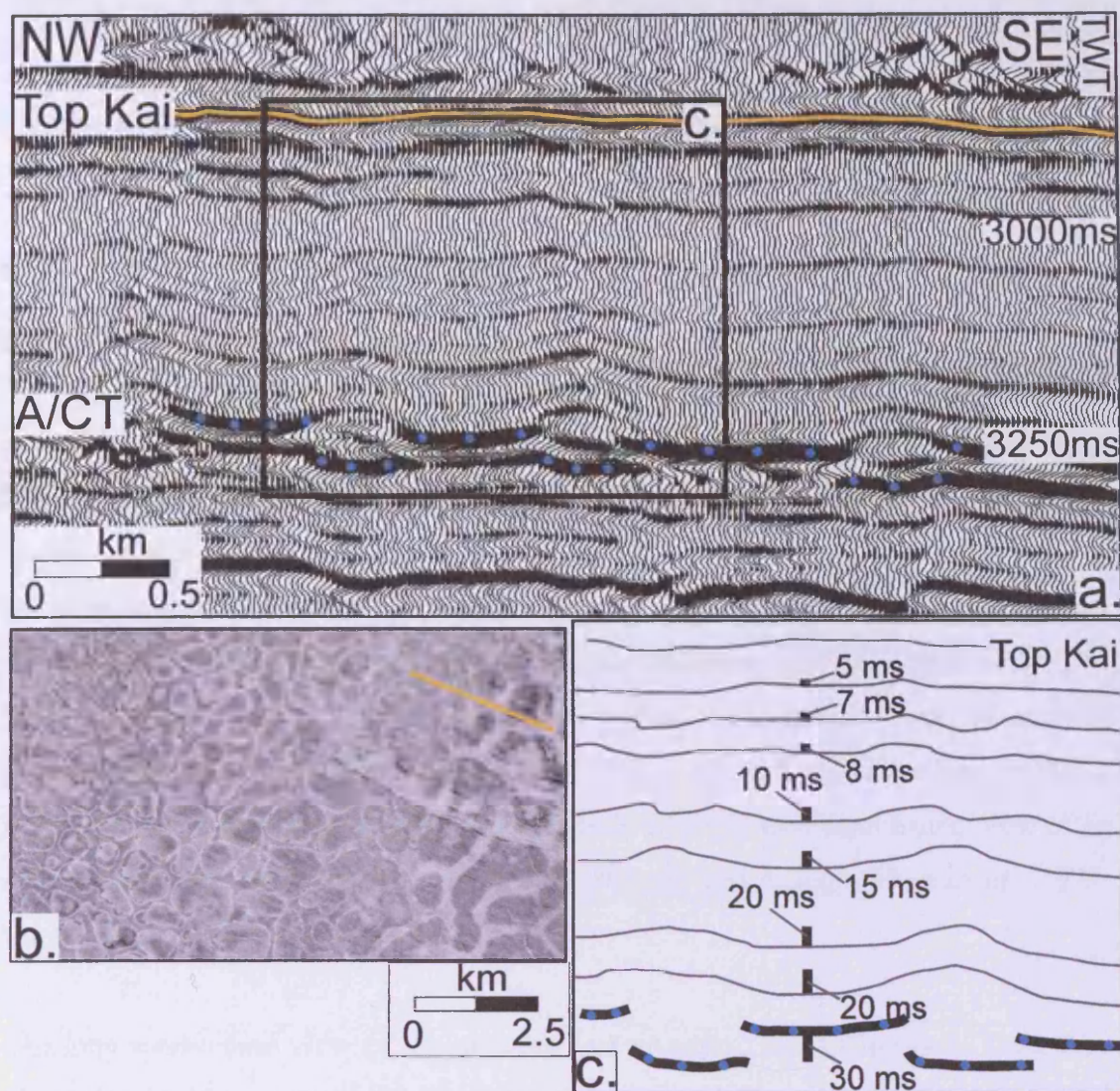
Fig. 6.13. (a) Seismic cross – section from the southern study area (P3 in Fig. 6.1b) showing the folds above the A/CT reflection; (b) Seismic amplitude map of the A/CT reflection highlighting its cellular morphology. Location in Fig. 6.1b; (c) Line drawing based on the profile in Fig. 6.11a showing that the amplitude of the folds decreases progressively upwards from the A/CT reflection up to the Top Kai reflection.

6.5. Discussion

6.5.1. Controls on the reaction front geometry

In the previous sections it has been shown that in all the regions of the study area, the A/CT reflection is only parallel to the present day seafloor over a local scale (e.g. SW end of the profile in Fig. 6.3). Regionally, the A/CT reflection is buried at a highly variable depth beneath the present seafloor (Fig. 6.2b). This simple view of isochore variations between the seafloor and the A/CT reflection is complicated by the frequent and large scale occurrence of Late Pleistocene to Holocene slides and their associated scars, which have re – shaped the seafloor from its smooth progradational geometry (Bryn et al., 2005). Nevertheless, it is evident that the A/CT reflection is at a present day depth that conflicts with the well established view of an active diagenetic front being close to 'sea bottom simulating' (Hein et al., 1978; Lonsdale, 1990; Kuramoto et al., 1992).

The long established view of the geometry of an active silica diagenetic front (see discussion in Meadows and Davies, 2008) originated from the theoretically based reasoning that temperature is the dominant controlling factor determining the rate of advance of the front through biogenic sediments (Kastner et al., 1977; Williams and Crerar, 1985). Other subordinate controlling parameters include the composition of the host sediment, in particular the presence or absence of clays and carbonate, pore fluid chemistry, pH and sediment age (Hein et al,. 1978; Behl and Garrison, 1994; Meadows and Davies, 2008).

In the study area, the observation that the A/CT reflection is smooth and continuous over a large area (approximately 4×10^4 km^2) strongly supports the view that there is a first – order control by temperature on the diagenetic reaction, and the other factors cited above have only local effects. If lithology played a dominant role, a smooth geometry of the A/CT reflection where cutting across the host stratal surfaces occurs (Figs. 6.3, 6.7 and 6.8) would not be observed. Instead, a more serrated boundary

should be observed on the seismic data, similar to that described by Meadows and Davies (2008) from the Sea of Okhotsk.

It is also notable that, in all the wells used for this research, the opal – A to opal – CT reaction occurs over a very narrow depth interval of 20 – 40 m, regardless of the local stratigraphy and lithology of the host sediments (Kai or Brygge Formations) (Tab. 6.1). This also suggests a dominance of the first order control of temperature. Moreover, the crosscutting relationship of the A/CT reflection with host stratigraphy demonstrates that the geometry of the boundary is not delimited by the availability of sufficient proportions of biogenic silica in the units above the reaction front (e.g. Figs. 6.3 and 6.7). This has also been noted by Meadows and Davies (2008) for the silica diagenesis front from the Sea of Okhotsk. Where the boundary is concordant to the local stratigraphy, the lack of sufficient biogenic silica above the front is one possible explanation of the concordant geometry, but this can be excluded here because of the high degree of local discordance (e.g. Fig. 6.7).

If the temperature is the dominant control, as previous studies suggest, then it is reasonable to expect an active reaction front to mimic closely the geometry of the isotherms within the shallower part of the basin. This is particularly valid for a marine basin with a simple structure and laterally continuous sequences with homogeneity of sedimentation rates typical of basin floor regions or deeper slopes, where isotherms are likely to closely parallel the seafloor (Gretener, 1981). This argument supports one of the implicit assumptions in previous studies of the geometry of the opal – A to opal – CT reaction front that an active reaction front is likely to simulate sea bottom morphology. However, it was noted that such a simple view of a 'sea bottom simulating' reaction front geometry is unlikely to apply in more highly structured basins where local variations in heat flow and thermal conductivity result in a more complex shallow thermal structure (e.g. Meadows and Davies, 2008; 2010b). This idea was introduced by Mizutani (1977) who proposed that, where deformation occurred shortly after sedimentation, the diagenetic isopleths (lines of equal maturation of cristobalite) are likely cross the stratigraphic boundaries. This is because the parts of the deformed strata experienced different thermal histories.

The primary objective of this research is to evaluate whether the opal – A to opal – CT reaction front is 'fossilised' on the mid – Norwegian margin, and if so, to attempt to date this end of the active diagenetic advance. Based solely on large variations in the present day burial depth of the A/CT reflection, a strong case can be made that it has been 'fossilised' and subsequently buried. An alternative explanation of the present burial depth data is that the reaction front is indeed currently active, but that the opal – A to opal – CT reaction is not controlled primarily by temperature. Arguments against this second explanation are presented next, after the evaluation of the present day temperature distribution in the study area.

6.5.2. Temperature as the controlling factor of silica diagenesis?

To evaluate the role of temperature in the stratigraphic position of the opal – A to opal – CT reaction front, a database of bottom – hole temperature data for all the boreholes within and in close proximity of the study area was compiled. The geothermal gradient of the study area was roughly estimated using the bottom – hole temperatures from the exploration wells (Fig. 6.1 and Tab. 6.1) and sea bottom temperatures from Mienert et al. (2005).

The temperature at the A/CT reflection (Fig. 6.14) was estimated based on its present burial depth, using the mean value of the geothermal gradient of 41 °C · km^{-1} (Tab. 6.1). The temperatures range from approximately 20 to 80 °C for the entire study area, these large variations being a function of burial depth, rather than the result of the lateral variation in geothermal gradient (Fig. 6.14b and Tab. 6.1). In particular, for the northern part of the study area the temperature is within the range of 20 – 40 °C, for the central part 20 – 70 °C, and for the southern part 40 – 80 °C. For the lower end of the temperature range (less than 40 °C), it is plausible that these are not maximum temperatures encountered during burial because of elevated geothermal gradients in the past few million years and the complicated temperature history of the basin (Brekke et al., 1999). The areas where the opal – A to opal – CT temperature is less than 40 °C are characterised by the presence of numerous slope failures in the Naust Formation (e.g. Fig. 6.8).
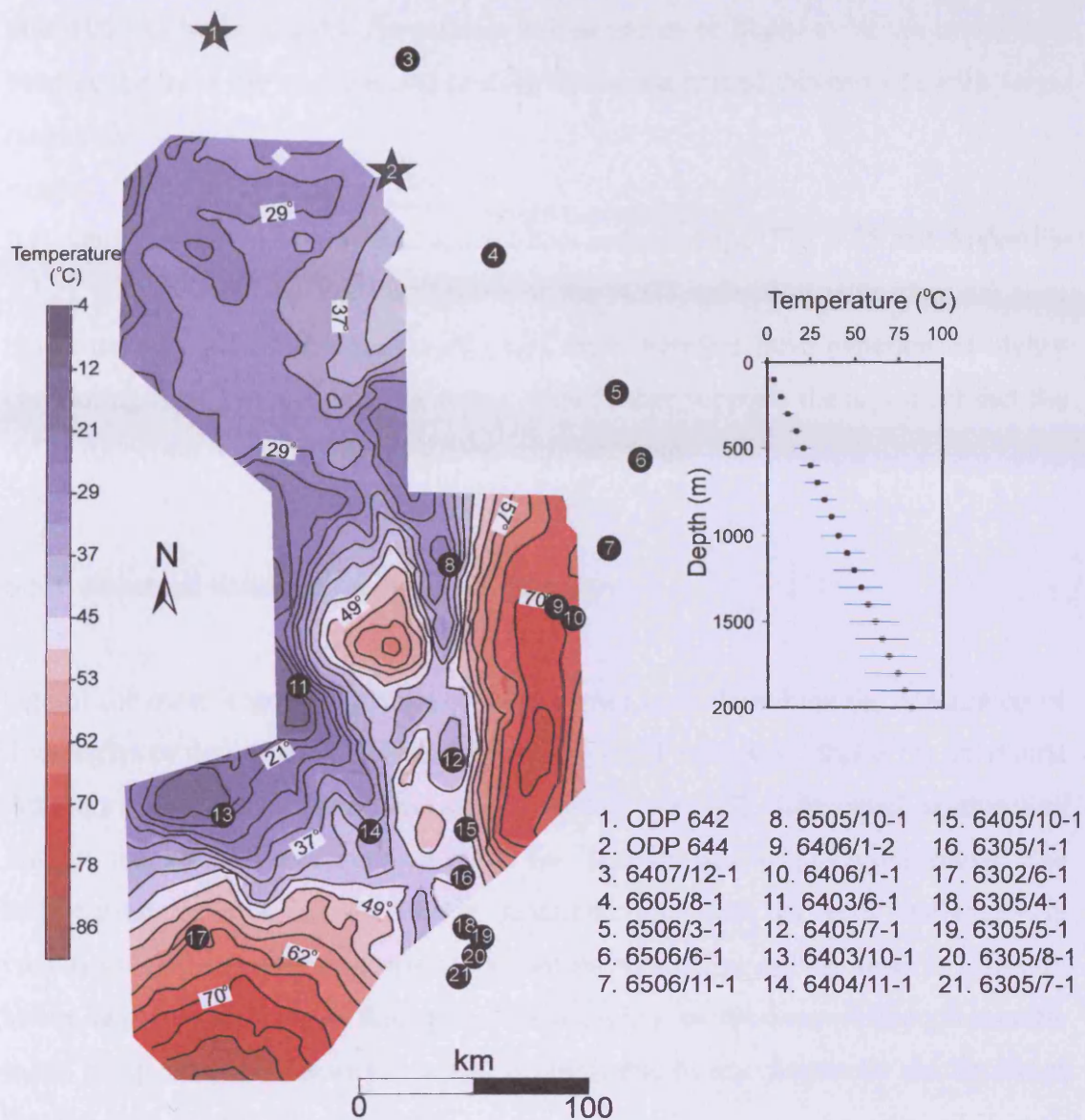
Fig. 6.14. (a) Contour map showing the temperatures at the depth of the A/CT reflector. The temperatures were estimated using an average geothermal gradient of 41 °C · km^{-1}. (b) The temperatures plotted as a function of depth. The error bars correspond to a variation of the geothermal gradient between 30 °C and 50 °C · km^{-1}.

1. ODP 642	8. 6505/10-1	15. 6405/10-1
2. ODP 644	9. 6406/1-2	16. 6305/1-1
3. 6407/12-1	10. 6406/1-1	17. 6302/6-1
4. 6605/8-1	11. 6403/6-1	18. 6305/4-1
5. 6506/3-1	12. 6405/7-1	19. 6305/5-1
6. 6506/6-1	13. 6403/10-1	20. 6305/8-1
7. 6506/11-1	14. 6404/11-1	21. 6305/7-1

However, for areas where the temperature exceeds 40 °C (corresponding to more than 1000 m burial depth), the present values are most likely to be the maximum because the latest burial phase and heating that accompanied this was of such a large magnitude.

It is significant that when plotted against host sediment age (Fig. 6.15 and Appendix A3.2), it is evident that host sediments at the A/CT reflection with identical ages have markedly different temperatures, and must therefore have experienced highly contrasting time – temperature histories. This further supports the argument that the A/CT reflection represents a 'fossilised' reaction front.

6.5.3. Structural deformation of the reaction front

One of the most important results of this chapter is to show how the description of three styles of deformation associated with the A/CT reflection, that is (1) polygonal faulting; (2) regional anticlines and synclines; and (3) differential compaction folding, can be used as criteria to argue for 'fossilisation' of silica diagenesis. The deformation of a silica diagenetic reaction front and its host sediments in conjunction offers another means of evaluating whether or not the front is currently active, and also a means of dating the 'fossilisation' of the front. Although specific to the study area, the discussion below is applicable to any diagenetic reaction front that has been structurally deformed.

6.5.3.1. Polygonal Faulting

In all three regions of the study area, an extensive developed polygonal fault system deforming the Brygge and Kai Formations is responsible for minor offsets of the A/CT reflection (Figs. 6.3 – 6.5, 6.7, 6.8 and 6.11). Occasionally, faults with no offset of the A/CT reflection are encountered close to those with a 10 – 20 m offset of the A/CT reflection. However, in these cases, the faults with no offset have upper tips that occur at older horizons than those with significant offsets (e.g. Fig. 6.5). The magnitude of the offsets at the A/CT reflection is typically less than 20 % of the

total stratigraphic throw at the same position on the fault (Chapter 5). These relationships between offset, throw and upper tip positions have been explained previously (Cartwright, 2007) as resulting from the upward ascent of a smooth diagenetic reaction front across the fault, the arrest of the upward migration of the front and subsequent continuation of displacement across the fault. Therefore, by careful restoration of the displacement history of a set of polygonal faults, it would be possible to define an interval when the diagenetic arrest took place.
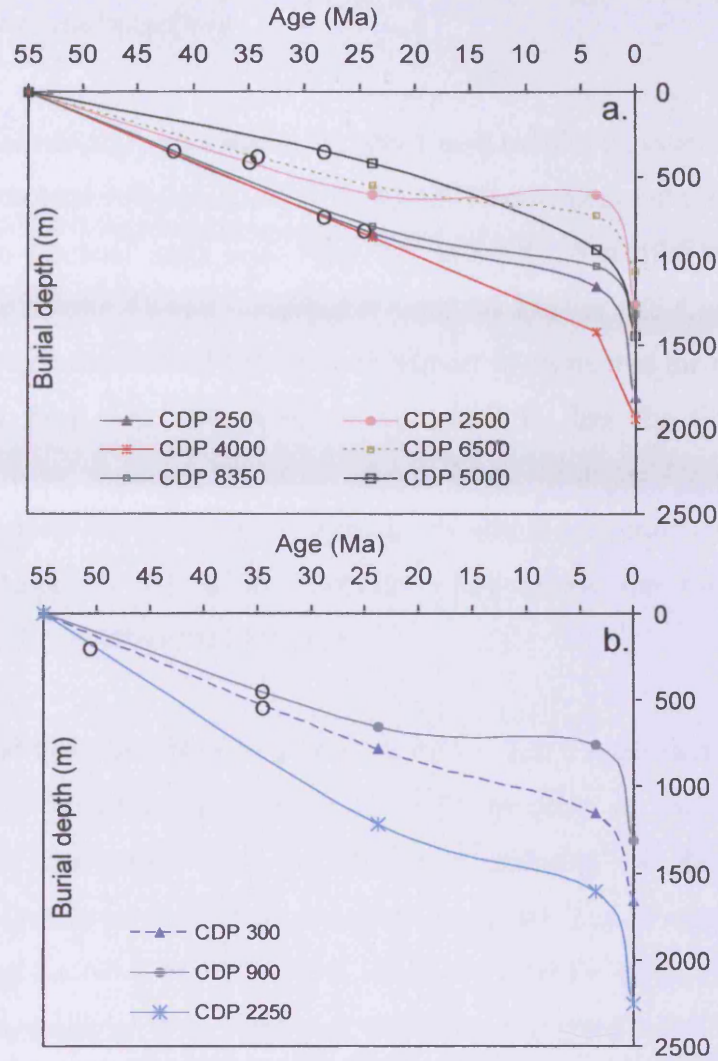
Fig. 6.15. (a) Burial history plots based on the interpretation of the seismic profile in Fig. 6.7. Associated data are presented in Appendix A3.2; (b) a representative seismic profile oriented W – E within the central case study area. Black circles mark the present – day location of the opal – A/CT diagenetic boundaries. Associated data are presented in Appendix A3.3.

6.5.3.2. Anticlines and synclines

The major anticlines and synclines in the study area exhibit a systematic relationship between the structural relief as defined at the A/CT reflection and the adjacent stratal surfaces within the host units (e.g. Figs. 6.7 and 6.8). A similar relationship was observed in the nearby Faeroe – Shetland Basin by Davies and Cartwright (2002), who used the reconstruction of fold growth history to argue that the opal – A to opal – CT reaction front was 'fossilised' in situ, and to date the time when arrest occurred. A similar approach has been adopted here to argue for a Late Miocene timing for the arrest based on the recognition of stratal reflections within the syn – kinematic packages in the growth synclines that mimic the fold shape of the underlying A/CT reflection (Section 4.2).

It can be argued that the folded morphology of the A/CT reflection could be due to different thermal histories experienced by different parts of the deformed strata. Mizutani (1977) proposed that the structural ordering of the cristobalite is comparatively less in a rock at the crest of an anticline than in a syncline, with the isopleths having the same shape, but less curvature than the folded strata. However, the reaction front should have continued to advance upwards after the cessation of folding, given the availability of biogenic silica. In this case, the folded morphology of the front would have been replaced by a geometry that was more highly influenced by overburden architecture, and this is clearly not the case anywhere in the study area.

6.5.3.3. Differential Compaction Folds

The unusual domal folds described from the southern region (Figs. 6.11 and 6.13) were interpreted as being a result of the differential advance of the silica diagenetic reaction front (represented by the A/CT reflection), and to the differential compaction that this would necessarily involve (Davies, 2005). Most significant for this research, if this interpretation of fold genesis is correct, it implies that active growth of the folds must have occurred as the reaction front was differentially

advancing through the biogenic sediments of the Brygge Formation. It follows that this advance occurred during the deposition of the Kai Formation, since by the end of this period of deposition, all growth of the folds had ceased. The systematic upward reduction of structural relief is consistent with a mechanism based on differential porosity collapse (Davies, 2005) and hence strongly suggests that all active differential advance of the reaction front had ceased prior to deposition of the Naust Formation (Figs. 6.11 and 6.13). Interestingly, this time coincides with the initiation of the major submarine sliding events that characterise the Naust Formation.

In summary, these three modes of deformation independently provide strong supporting evidence to the arguments already advanced using differential burial depth and large range of present – day temperature that the A/CT reflection is a 'fossilised' reaction front. Therefore, the final part of the discussion is focused on the timing of this event in a regional context.

6.5.4. The timing of the 'fossilisation' event

The approach taken here to date the 'fossilisation' event is to identify the stratal surface that is most concordant to the A/CT reflection. Implicitly, this approach assumes that the position of the boundary at the time of 'fossilisation' roughly mimicked the seabed at that time, i.e. it was sea bottom simulating. This assumption is most likely valid for areas with uniform sedimentation rates and facies, low to moderate sedimentation rates preceding the arrest (i.e. shallow burial depth of the reaction front at the time of arrest), and where there was only limited lateral variation in thermal conductivity of the shallow sedimentary succession. These conditions apply to most of the study area. Because of structural complexity and the slope failures in the Naust Formation, it was not possible to correlate at a regional scale the locally interpreted marker reflections that were identified as being most continuously parallel to the A/CT reflection. Hence, the approach taken was to date the candidate 'fossilisation' event horizons locally in three regions, and to use nearby wells to date these markers.

In the northern and central regions, the 'fossilisation' took place within the Late Miocene to Early Pliocene interval (Section 4.1.1.), and in the southern region in the Early Pliocene. Uncertainties in the unique identification of a presumed paleo – seabed marker combined with problems of accurately dating specific seismic markers within the Kai Formation imply that an accurate estimation of the timing of the 'fossilisation' is not possible. Both horizons ('N' and 'R') have been tentatively dated at some time within Late Miocene to Early Pliocene. Since horizon 'R' is an erosional unconformity, it is possibly younger than horizon 'N' (Fig. 6.7). Therefore, at a regional scale (about 1000 km), the 'fossilisation' occurred at some time within the Late Miocene to Early Pliocene. Significantly, this matches the estimated timing of 'fossilisation' of silica diagenesis in the Faeroe Shetland Basin (Early Pliocene) (Davies and Cartwright, 2002), and coincides with earlier estimates of the timing of 'fossilisation' in the Norwegian Sea by Brekke (2000). It has not been possible to establish whether the 'fossilisation' was synchronous or diachronous over the length of the study area, simply because of the problems in regional seismic correlation. However, the evidence from the relationships with polygonal faults and sets of anticlines and synclines strongly suggests that 'fossilisation' occurred rapidly.

6.5.5. Wider recognition of 'fossilisation' and possible causes

One of the most puzzling aspects of the 'fossilisation' of the silica diagenesis in the Norwegian Sea is that over a large part of the area, the present day temperatures at the position of the A/CT reflection are most likely the maximum temperatures that have occurred at this depth (Fig. 6.15). The isochore data show that the A/CT reflection is typically at a depth of 300 – 400 m below the respective paleo – seabed markers at the time of arrest. Even for an extreme paleo – geothermal gradient of 100 °C · km^{-1}, this amounts to a likely temperature of only 35 – 45 °C (for a sea bottom temperature of 5 °C) at the reaction front as it reached its point of arrest. This value is consistent with conversion temperatures based on oxygen isotope ratios of silica (Isaacs et al., 1983 and references therein) of 18 – 56 °C for the opal – A to opal – CT. But a value even as high as 45 °C is still much lower than present day temperatures along most of the eastern part of the study area, where deposition of 1500 – 2000 m of Naust formation has resulted in temperature at the A/CT reflection

169

being 60 – 75 °C along a zone of approximately 10^4 km^2. This region would have exceeded the earlier 'arrest' temperature of about 40 °C at least a million years ago, which is a long enough period (Tada, 1991) for the reaction to have once again advanced upwards through the biogenic rich intervals of unconverted Kai Formation oozes.

Previous studies that have recognised the 'fossilisation' have mainly appealed to changes in geothermal gradient as an explanation (Roaldset and He, 1995; Brekke et al., 1999; Brekke 2000; Davies and Cartwright, 2002). However, as noted above, even an extreme paleo – geothermal gradient followed by a cooling to a modern value does not account for the discrepancy in the estimated temperatures at the time of 'fossilisation' versus present day temperatures at the inactive opal – A to opal – CT reaction front.

Opal – A to opal – CT reaction fronts are widely developed at their maximum burial depth in many continental margin sedimentary basins, and have been penetrated in over 100 separate boreholes drilled by the ODP and DSDP. However, with the exception of those described along the NE Atlantic margin, and in the Sea of Okhotsk (Meadows and Davies, 2008; 2010b), all these fronts have been assumed to be active, rather than 'fossilised'. This assumption may be due to the fact that these fronts are often apparently 'sea bottom simulating' on the few seismic profiles used to characterise their geometry. However, as evident from the research presented in this chapter, in areas where the front is generally concordant with the host stratigraphy, it is extremely difficult to make a case that it is 'fossilised' at all. It is only where the front crosscuts stratigraphy, or where there are large variations in burial depth, or contemporaneous deformation of the front during its 'fossilisation' that the seismic stratal geometry reveals the true nature of the arrested diagenesis.

6.6. Conclusions

- In this chapter, the evidence for a 'fossilised' opal – A to opal – CT reaction front on the mid – Norwegian margin was examined. It was demonstrated that the A/CT reflection is not a sea bottom simulating reflector, therefore not in thermal equilibrium with the local isotherms. The deformation of a silica diagenetic reaction front offers another means of evaluating whether or not the front is currently active. Based on the analysis of three styles of deformation associated with the A/CT reflection, that is polygonal faulting, regional anticlines and synclines and differential compaction folding, the 'fossilisation' of the silica diagenesis reaction front at a regional scale was demonstrated.

- Dating the 'fossilisation' time was attempted by the means of identifying the stratal surface that is most concordant to the A/CT reflection. At a regional scale, the 'fossilisation' occurred at some time within the Late Miocene to Early Pliocene. An accurate estimation of the timing is not possible due to uncertainties in the unique identification and accurate dating of a presumed paleo – seabed marker.

- Given the available data, it was not possible to establish whether the 'fossilisation' was synchronous or diachronous over the study area because of the problems in regional seismic correlation. However, the evidence from the relationships with polygonal faults and anticlines and synclines strongly suggests that 'fossilisation' occurred rapidly over a geological time scale.

- It seems likely that 'fossilisation' of the silica diagenetic reaction front in other basins is much more common than currently appreciated. Further progress on the cause of arrested diagenesis is unlikely until a fuller inventory of active versus 'fossilised' fronts and their geological contexts has been undertaken, which is therefore considered a priority for future research in this field.

Chapter 7.

SUMMARY AND

DISCUSSION

7. SUMMARY AND DISCUSSION

7.1. Introduction

By integrating seismic and well data, two principal aspects of biogenic silica diagenesis were investigated in this thesis: (1) its role on the evolution of the physical properties of the sediments during burial and deformation and (2) the temperature as a controlling factor of diagenesis. In this chapter, the main results of this research are integrated into a comprehensive discussion aimed at highlighting their implications for different aspects of basin analysis, such as sediment compaction, thermal evolution of sedimentary basins, overpressure and fluid flow (Fig. 7.1).

The aims of this chapter are:

- to summarise the main scientific results of the research presented in Chapters 4 – 6;

- to integrate the scientific results in order to evaluate the implications on different aspects of sedimentary basins;

- to discuss the applicability and significance of this research in a wider context;

- to outline the limitations of the methodology used in this research;

- to present recommendations for further research in this field based on the questions raised by this research.

7.2. Summary of results

7.2.1. Results from 'Biogenic silica diagenesis transition zones – a physical and chemical characterisation using Ocean Drilling Program data' (Chapter 4)

The results from 33 scientific boreholes from various locations were analysed in order to identify the silica diagenesis transition zones. These data allowed the definition and the physical and chemical characterisation of the opal – A to opal – CT transition zones (TZ$_{A/CT}$). Based on these properties, the criteria for identifying the presence of a silica diagenesis transition zone were proposed. In addition, it was demonstrated that the TZ$_{A/CT}$ represent narrow depth ranges (usually between 10 and 40 m) where the opal – A and opal – CT phases coexist. Importantly, the physical properties of the sediments change sharply across the TZ$_{A/CT}$, which has important implications on sediment compaction in sedimentary basins. Temperature was identified as the main factor determining the thickness of the TZ$_{A/CT}$, other factors like lithology, pore – water chemistry etc having a secondary role. Updating the temperature versus age plot of Hein et al. (1978) allowed a re – evaluation of the silica diagenesis time – temperature stability field. The idea that some of the diagenetic transition zones were formed as a response to higher paleo – geothermal gradients and are presently 'fossilised' was presented.

7.2.2. Results from 'Measurement of diagenetic compaction strain from quantitative analysis of fault plane dip' (Chapter 5)

In Chapter 5, the remarkable segmented fault plane geometry of the widespread system of polygonal faults in the Møre and Vøring Basins was interpreted as being related to the diagenesis of biosiliceous sediments of the Kai and Brygge Formations. The planar segments dip more steeply in the opal – A rich biosiliceous mudstones than in the underlying opal – CT rich interval. The compaction strain due to diagenesis was estimated from the change in dip of the fault planes. It was concluded that the fault planes were passively rotated into shallower dips as a result of diagenesis, assuming they were planar markers prior to diagenesis. This interpretation offers a new method for the estimation of the porosity reduction due to silica diagenesis. It should be noted that this method does not give absolute porosity values since the same value of the compaction strain can be obtained from different initial and final porosity values.

An important observation made in Chapter 5 was that the faults continued to grow after the diagenesis had effectively ceased, despite of changes in physical properties, such as the increase of the shear strength. The reasons for this post – diagenetic phase of fault growth cannot be explained mechanically at present, and should make the object of a future study.

7.2.3. Results from 'Fossilisation of a silica diagenesis reaction front on the mid – Norwegian margin' (Chapter 6)

It was demonstrated that the A/CT reaction front is not in thermal equilibrium with the present isotherms, implying it is related to a 'fossilised' reaction. In addition, three styles of deformation associated with the opal – A/CT reflection (polygonal faulting, regional anticlines and synclines and differential compaction folding), were used to demonstrate that the opal – A to opal – CT reaction front in Norwegian Sea is 'fossilised'. Identifying the 'fossilisation' time was attempted by the means of recognising the stratal surface that is concordant to the A/CT reflection, presumably the paleo – seabed when the reaction became inactive. At a regional scale, the 'fossilisation' occurred at some time within the Late Miocene to Early Pliocene. The causes of 'fossilisation' were proposed to be related to the change in the geothermal gradient.

7.3. Implications of the research

In Chapter 4, the definition and criteria for identification of silica diagenesis transition zones were presented. This is the first time that the physical and chemical characterisation of opal – A to opal – CT transition zones from different ODP locations is attempted. The implications of these results on sediment compaction and overpressure will be examined in the current chapter.

Chapter 5 focused on the analysis of a specific physical property (i.e. the porosity) of the sediments undergoing silica diagenesis using three case studies from the Norwegian Sea. Chapter 5 also considered the effects of silica diagenesis on the

shear strength of the sediments and fault growth. In this chapter, additional implications of diagenesis on fluid flow in sedimentary basins are examined.

In Chapter 6, the proposed reason for 'fossilisation' of the silica diagenetic boundary in the Norwegian Sea was the change in the geothermal gradient. In this chapter, the opal – A to opal – CT reaction is compared to other diagenetic reactions (i.e. the smectite to illite diagenetic reaction and organic matter maturation) in an attempt to provide an alternative explanation for the 'fossilisation' of the biogenic silica diagenetic reaction.

7.3.1. Silica diagenesis and overpressure

In this section, the relationship between silica diagenesis and overpressure is investigated. Firstly, the mechanisms for generating overpressure in the Norwegian Sea Cenozoic sediments are considered, including a discussion of silica diagenesis as one of the possible mechanisms. Secondly, the relationships between overpressure and two different aspects of silica diagenesis, physical properties changes and the 'fossilisation' of the reaction front, are discussed.

7.3.1.1. Overpressure in the Cenozoic sediments of the Norwegian Sea

Disequilibrium compaction

A pore fluid is overpressured if its pressure is higher than the hydrostatic gradient at a specific depth (Osborne and Swarbrick, 1997). The hydrostatic gradient is the pressure that would be exerted by a continuous column of static fluid.

Overpressure can develop in a sedimentary basin by several mechanisms: compaction disequilibrium and tectonic stress; changes in the volume of a fluid or rock matrix (e.g. clay diagenesis and hydrocarbon generation); fluid movement and buoyancy (Osborne and Swarbrick, 1997). Significantly for this study, documented causes for overpressure are rapid sediment loading (> 1 mm $\cdot$ year^{-1}) (Dugan and Flemings, 2000) and the presence of low – permeability sediments, such as clays

(Osborne and Swarbrick, 1997; Bjørlykke, 1999), which create compaction disequilibrium.

At least two of the factors leading to the development of overpressure are present in the Cenozoic sediments of the Møre and Vøring Basins (Norwegian Sea), the case study area for the research presented in Chapters 5 and 6 of this thesis: the presence of clays and high sedimentation rates. Firstly, the dominant type of sediment is represented by low permeability clays of the Kai and Brygge Formations (Dalland, 1988; Brekke, 2000). The biosiliceous fraction of the sediments has a high permeability (Spinelli et al., 2004), however, in the case study area, the sediments contain only 30 – 40 % diatoms (Eldholm et al., 1987), the main component of the sediments being clay. This has low permeability and restricts the water flow, influencing the development of overpressure (e.g. Bjørlykke and Høeg, 1997; Aplin et al., 1999). High pore pressures have been reported to occur in the Cenozoic mudstones from the northern North Sea (Evans et al., 2002).

In the Vøring Basin, the fast deposition of a Plio – Pleistocene sediment wedge resulting from the glaciation of the uplifted mainland and the cyclic advancement of glaciers over the shelf might have led to the development of overpressure in the underlying sediments (Reemst et al., 1996). In addition, it was proposed that a possible base Pliocene shale layer acted as an effective seal for water drainage from the underlying sediments (i.e. the biosiliceous mudstones of the Kai Formation). However, such a shale layer has not been observed in most of the wells in the area.

Importantly, drilling of the biosiliceous ooze in the Møre Basin, more specifically in the wells in the Storegga Slide area, confirmed the existence of pore pressures higher than hydrostatic (Riis et al., 2005). The data suggest a build-up of overpressure in the ooze sediments which were buried under the prograding Naust Formation (Riis et al., 2005). In conclusion, it is possible that the biosiliceous oozes in the Norwegian Sea are overpressured.
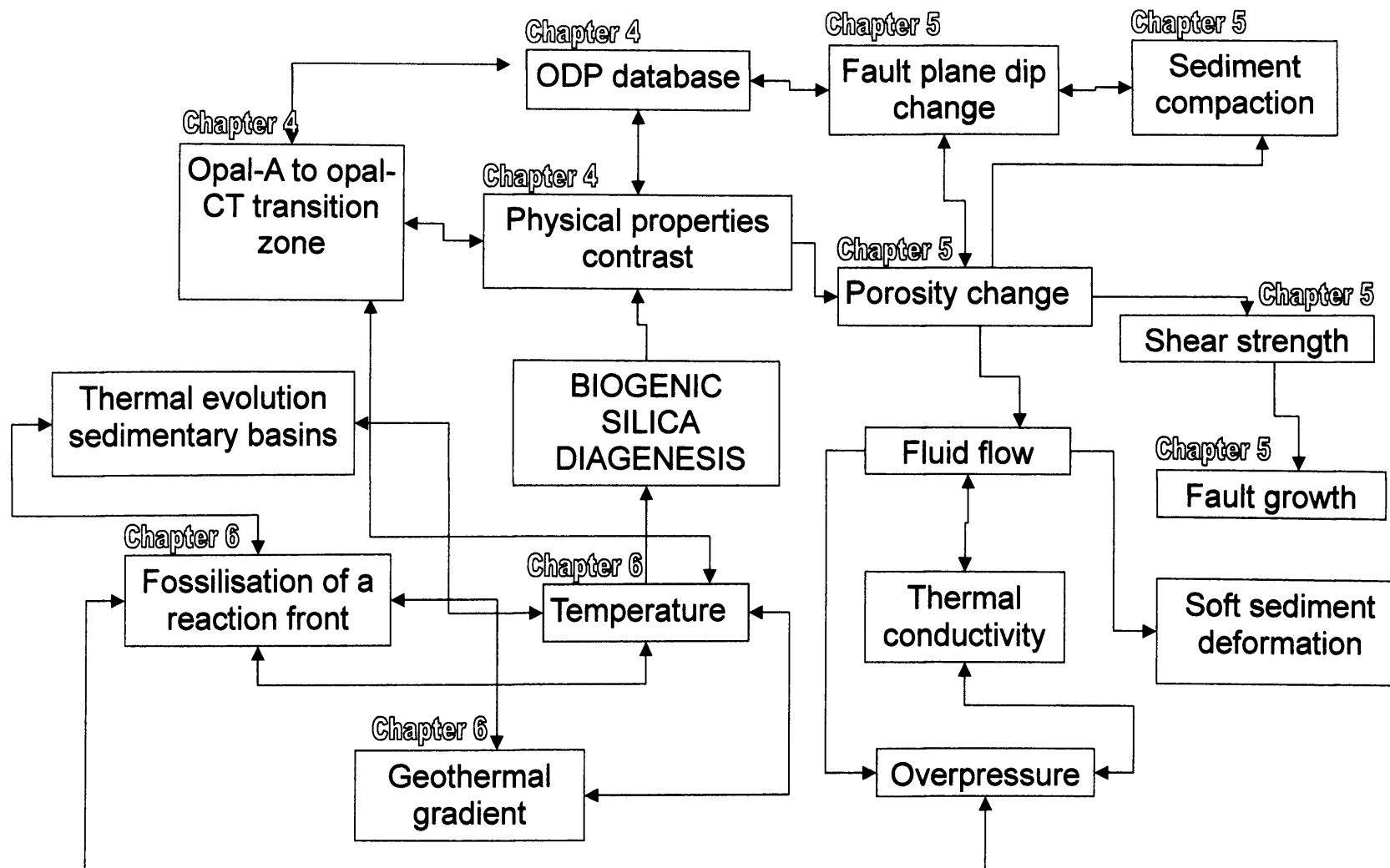
Fig. 7.1. Scheme illustrating the connections between the main topics of Chapters 4 – 6 and various implications discussed in the current chapter.

Overpressure generation by silica diagenesis?

In addition to the high sedimentation rate and the predominance of clay in the sediments of the Møre and Vøring basins, the diagenetic reactions are an important element that needs to be considered as contributing to the development of overpressure (Bjørlykke and Høeg, 1997).

Diagenetic reactions lead to the expulsion of pore fluid due to chemical and physical compaction, and if the fluid is prevented from being expelled from the sediments by the presence of low permeability sediments, overpressure might develop. However, there are a limited number of quantitative data to constrain the impact of the diagenetic reactions on sediment permeability and overpressure development (Aplin et al., 1999).

It was proposed that the smectite to illite transformation has a strong influence on the build – up of overpressure (Bruce, 1984; Dutta, 1986; Colten – Bradley, 1987; Nadeau et al., 2002). In the Møre Basin, Peltonen et al. (2008, 2009) established that the smectite to illite transformation is confined within Cretaceous sediments, based on geochemical analyses of well data. As the focus of this research is limited to the Cenozoic sediments of the Norwegian Sea, this diagenetic reaction will not be considered further as having a possible effect on overpressure in the interval of interest.

Nevertheless, another diagenetic reaction, i.e. the opal – A to opal – CT conversion, affects the Cenozoic sediments over most of the Norwegian Sea continental margin, according to the observations presented in Chapter 6. The effect of this diagenetic transformation on the overpressure development has been previously discussed by several authors (Hesse, 1988; Eichhubl and Behl, 1998; Volpi et al., 2003; Davies et al., 2008).

It was shown in Chapter 4 that opal – A to opal – CT reaction frequently results in an important reduction in porosity of the sediment, of up to 50 %, over a narrow transition zone (usually less than 40 m). In turn, the release of significant volumes of pore water might contribute to overpressure in the overburden (i.e. opal – A

sediments) if the sediments have low permeability (Brekke et al., 1999). As silica diagenesis is a process affecting the sediments at the scale of a sedimentary basin (Chapter 6), it is inferred that the release of pore water could lead to large – scale overpressure.

Hesse (1988) proposed that the opal – A to opal – CT reaction could generate excess pore pressure in the strata above the diagenetic fronts. However, no strong evidence supports the hypothesis that diagenesis in general is a direct cause for overpressure (Osborne and Swarbrick, 1997), even though it has an important effect on sediment permeability due to cementation. This, in turn, would delay the release of overpressured pore fluid generated by other mechanisms, such as disequilibrium compaction.

In conclusion, it is likely that silica diagenesis reduces sediment permeability or enhances the overpressure in the overburden due to the release of significant volumes of pore water. These processes might enhance the magnitude of the overpressure generated by other mechanisms, such as disequilibrium compaction.

7.3.1.2. Effect of overpressure on the fault plane dips

In the previous section it was demonstrated that conditions for overpressure are present in the Cenozoic sediments of the Norwegian Sea continental margin. In this section, the relationship between overpressure and the change in dip of the fault planes will be discussed.

In Chapter 5, the systematic flattening of fault plane dips occurring at the opal – A to opal – CT diagenetic boundary was interpreted as an effect of the compaction due to silica diagenesis. In other words, the fault planes were passively rotated into shallower dips as a result of diagenesis, and this allowed the estimation of the porosity reduction due to silica diagenesis for three case studies from the Norwegian Sea.

Similar observations have been made about listric faults from the Gulf Coast basin. Bruce (1984) observed that the dips of listric faults decrease rapidly from 60° to 15° within the interval of smectite to illite transformation, suggesting a causal relationship between the development of listric normal faults and overpressured shales. This interpretation was re – evaluated by Bradshaw and Zoback (1988) who proposed that the low – angle normal faults form because of a rotation of the maximum principal stress away from vertical with depth due to a significant viscosity contrast between two adjacent strata, such as normally pressured sandstone and overpressured shale.

Similarly, an alternative explanation of the fault plane dip change due to overpressure in the opal – CT interval needs to be considered. However, due to the lack of any data that could confirm the presence of higher pore fluid pressures in the opal – CT sediments with respect to the opal – A sediments, this alternative interpretation remains only a speculation. Assuming this interpretation is valid, the presence of the polygonal fault system itself should be taken into account when discussing overpressure. It is known that faults can be fluid barriers but also fluid conduits (Hooper, 1991; Sibson, 2000) and, in the presence of overpressure, fractures in shales can remain open due to the decrease of the effective normal stress normal to the fracture walls (Bjørlykke and Høeg, 1997; Giles, 1992). Consequently, overpressure could be dissipated due to expulsion of the pore fluids through the open fractures. In conclusion, this alternative explanation for the fault plane dip change remains speculative, and the interpretation presented in Chapter 5 is considered more reliable.

7.3.1.3. Overpressure and the 'fossilisation' of the silica reaction on the mid – Norwegian continental margin

In Chapter 6, arguments have been presented to demonstrate that the silica diagenesis reaction in the Norwegian Sea is 'fossilised'. It was proposed that the reason for the 'fossilisation' of the reaction is related to change in the geothermal gradient (Brekke, 2000; Davies and Cartwright, 2002). However, as mentioned in Chapter 6, even an extreme paleo – geothermal gradient followed by a cooling to the

present value does not account for the discrepancy in the estimated temperatures at the time of 'fossilisation' and the current temperatures at the inactive opal – A to opal – CT reaction front. As an alternative explanation, the hypothesis that the silica diagenesis reaction is inhibited and/or stopped by overpressure is considered next.

Several authors have proposed that some diagenetic reactions, such as the smectite to illite transformation (Dutta, 1986; Colten – Bradley, 1987; Osborne and Swarbrick, 1997 and references therein) and organic matter maturation (Carr 2000 and references therein) can be inhibited or retarded by overpressure. In other words, the reaction rates of these diagenetic processes are reduced due to the effects of overpressure in a sedimentary basin (Carr, 2000). Colten – Bradley (1978) demonstrated that the release of water in low permeability shales due to smectite – illite transformation results in overpressure and also inhibits any further transformation. This hypothesis is discussed next as the explanation for the arrest of the silica diagenetic reaction in the Norwegian Sea.

Pressure is not considered one of the controlling factors of silica diagenesis, the dominant controls being temperature and time (Kastner et al., 1977; Williams and Crerar, 1985). Subordinate controls include the composition of the host sediment, pore fluid chemistry and pH (Hein et al., 1978; Behl and Garrison, 1994). In Chapter 4, it was demonstrated that the temperature is the main control of the TZ$_{ACT}$ thickness, with secondary influence from lithology (clay or carbonates). No correlation was found between the TZ$_{ACT}$ thickness and the overburden pressure. However, McTavish (1988) highlighted the fact that the type of pressure is important when investigating its effect on diagenetic reactions. Even though lithostatic pressures do not have any effect on hydrocarbon generation or the rank of coal, high pore pressures will retard these processes.

It is known that overpressure lowers the effective stress (Giles, 1992), reducing grain contacts, therefore it is likely that this will have an effect on chemical reactions, such as the opal – A to opal – CT transformation, which involves dissolution of opal – A and reprecipitation of opal – CT. If overpressure is not dissipated, the reaction might be impeded to advance, leading to its 'fossilisation', as demonstrated in Chapter 6.

Conversely, if overpressure is dissipated, for example through faults acting as fluid conduits, the diagenetic reaction should continue.

Assuming this hypothesis is correct, the regions where silica diagenesis is taking place actively in the Norwegian Sea should coincide with areas with evidences for fluid flow. These are present in a limited area in the NW of the Gjallar Ridge 3D survey and over the entire area of the pl251 survey in the Møre Basin (Appendices A4.1 – A4.3). These two areas have received particular attention in the last few years, due to the atypical morphology of the opal – A to opal – CT reaction front, i.e. vertical relief with cylindrical promontories, named 'cells', separated by troughs (c.f. Davies and Cartwright, 2007).

The authors who studied the silica diagenesis in these areas (Davies and Cartwright, 2007; Ireland et al., 2010 a; b) proposed that the atypical morphology of the diagenetic front is related to the enhanced diagenetic reaction due to water circulation through faults. Davies and Cartwright (2007) suggested that the transport of fluid that is anomalously hot into sediment rich in unconverted opal – A enhances diagenesis. Ireland et al. (2010b) proposed that the magnesium transported by the fluid along the faults acts like a catalyst, promoting opal – CT formation.

An alternative interpretation is that the atypical morphology of the diagenetic boundary represents a 'snapshot' of an active diagenetic boundary, zones where a digenetic reaction has advanced due to the release of overpressured fluids through the network of polygonal faults. This does not undermine the interpretation of Davies and Cartwright (2009) or Ireland et al. (2010b), since the cause for the advancement of the diagenetic front is ultimately related to the expulsion of pore fluid.

In Chapter 6, the differential compaction folds above the 'cells' in the Møre Basin have been used to demonstrate that diagenesis is arrested, since no compaction folds were observed shallower than the Top Kai horizon. This seems to conflict with the interpretation proposed in this chapter. However, the release of overpressure which allows diagenesis to continue, illustrated by the development of the 'cellular' morphology of the diagenetic boundary does not imply the diagenesis is presently

active. It only implies that the diagenetic front was able to advance in the areas where overpressure was released. Based on the observation that the compaction folds die out at the level of the Top Kai Horizon, it was interpreted that diagenesis has been inactive since Late Miocene to Early Pliocene in the Møre Basin. No fluid features such as pockmarks or pipes have been identified at the seabed in the study area (i.e. pl251), suggesting that, if overpressure was indeed released by the fluid circulation along faults, allowing diagenesis to continue, this circulation stopped before or at the time corresponding to Top Kai horizon.

Overpressure conditions might be present in some of the sedimentary basins investigated by the ODP sites presented in Chapter 4, and, if the hypothesis presented here is correct, the fossilisation of the silica diagenesis reactions might be more common than currently estimated. The silica diagenetic fronts likely to be fossilised are those hosted by overpressured sediments, and potential candidates are the reaction fronts embedded in clay – rich sediments in basins with high sedimentation rates. Classifying a reaction front as 'fossilised' has been so far done based on seismic data (e.g. Davies and Cartwright, 2002). Hence, where these are not available, it is difficult to demonstrate a reaction is 'fossilised' based on other types of data, such as pore water chemistry or present – day temperature estimation. In conclusion, the relationship between overpressure and the 'fossilisation' of silica diagenesis proposed here remains only a hypothesis until additional data will confirm or invalidate it.

7.3.2. Silica diagenesis transition zones and sediment compaction

In the shallow part of sedimentary basins, the sediment compaction is described as being primarily mechanical, which is a function of the effective overburden stress and stress history (Bjørlykke and Høeg, 1997). At burial depths of 2 – 3 km, chemical compaction related to the dissolution and precipitation of minerals is taken into account in basin modelling. An important diagenetic reaction in mudstone compaction, for example, is the dissolution of smectite and the precipitation of illite, which occurs at temperatures from 80 – 120 °C. In this section, it will be highlighted

that the chemical compaction associated with the early diagenesis of biogenic silica needs to be also taken into consideration in compaction models.

The results of Chapter 4 showed that diagenesis of biogenic silica results in important physical properties changes of the sediments at burial depths of less than 1 km, in the realm dominated by mechanical compaction. Silica diagenesis transition zones are characterised by a significant decrease in sediment porosity over a narrow depth interval (10 to 40 m thick, generally). The porosity contrast across the analysed transition zones varies between 5 and 40 %, with a mean value of 15 %. For the ODP sites with a clay – dominated lithology, a good correlation was found between the opal – A content of the sediments and the porosity contrast across the transition zone. Explicitly, the higher the opal – A content of the sediments, the higher the porosity contrast resulting from diagenesis, due to the higher mass available for dissolution.

The porosity 'collapse' of the sediments subjected to diagenesis results from chemical compaction, which leads to the dissolution of load supporting framework minerals. If the subsequent permeability decrease of the opal – CT sediments results in the prevention of the expulsion of pore fluids, overpressure conditions might develop, as discussed in Section 7.3.1.1. High fluid pressures might lead to the generation of extension fractures by hydraulic fracturing or the reactivation of faults, as discussed by Eichhubl and Behl (1998) and Davies et al. (2008).

Silica diagenesis transition zones are present in all the world's oceans and, as demonstrated in Chapter 6, the seismic reflection from the opal – A to opal – CT diagenetic transition zone can be a laterally continuous feature over the scale of an entire sedimentary basin. Therefore, as also mentioned by Bjørlykke and Høeg (1997) and Spinelli et al. (2004), the porosity reduction due to silica diagenesis needs to be taken into account in compaction models for the shallow sedimentary section.

Are thin silica diagenesis transition zones the rule or the exception?

In Chapter 4, it was shown that all the silica diagenesis transition zones are thin (i.e. less than 40 m thick), and it was proposed that some of them are related to 'fossilised' diagenetic reactions. In particular, the transition zone in the Norwegian Sea studied in Chapter 6 is a narrow depth interval (20 – 40 m thick) related to a 'fossilised' reaction. The question that needs to be addressed now is: Are thin diagenetic transition zones related to 'active' or 'fossilised' reactions?

As proposed in Chapter 4, only some diagenetic transition zones are related to 'fossilised' reactions. The likely candidates are the silica diagenetic fronts embedded in young sediments (Miocene or younger) and characterised by low sedimentation rates and geothermal gradients (the sites in data cluster 'c' in Fig. 4.15b). The rest of the sites can be considered to represent 'active' reactions, based on the fact that temperature history is the main controlling factor of silica diagenesis.

In comparison, the opal – A to opal – CT transition zone from the Monterey Formation, California, is hundreds of meters in thickness (Keller and Isaacs, 1985). This was proposed to be related to the heterogeneous lithology: clay – rich strata convert to opal – CT slower than carbonate – rich layers. From the analysis of the ODP sites in Chapter 4, it was concluded that, indeed, the silica diagenesis transition zones in clay – rich sediments are thicker than those embedded in carbonate – rich sediments. However, all the analysed transition zones are thin depth intervals, representing variations in temperature of 0.12 – 5.50 °C. Moreover, the transition zone in the Monterey Formation, reported as being reported hundreds of metres thick, is evidently related to a 'fossilised' reaction front. This is because the entire sequence has been uplifted and, therefore, 'fossilised', since the reaction cannot continue to advance.

It is concluded that the thin transition zones are likely to represent 'active' silica diagenesis reactions. This is important for basin modelling, fluid – flow modelling and seismic interpretation, since the increase in compressional velocity associated with opal – A to opal – CT transformation will affect velocity analysis and depth conversion of the seismic data.

7.3.3. The relationship between silica diagenesis reaction front and the thermal evolution of sedimentary basins

One of the most important results of Chapters 6 is that the silica diagenesis reaction fronts cannot be considered typical bottom simulating reflectors or BSRs. It was proved that the reflection from the opal – A to opal – CT reaction in Norwegian Sea is not parallel to the present – day seafloor and not in equilibrium with the present – day temperature. Hence, in agreement with recent studies (Meadows and Davies, 2010b), it is concluded that the opal – A to opal – CT reaction fronts are not isothermal markers, and cannot help constrain the temperature distribution of a sedimentary basin.

Moreover, as shown in Chapter 4, in various locations worldwide, the opal – A to opal – CT transition zones can be found at a depth varying from 90 to 1050 mbsf. Accordingly, their present – day temperatures vary between 2 and 60 °C, one explanation for this wide range of values being that not all of them represent the temperature of active silica diagenesis. It was shown (Fig. 4.15) that the diagenetic fronts most likely to be 'fossilised' are hosted by sediments with a low temperature (< 25 °C) and relatively young age (e.g. Miocene).

The criteria for recognising 'fossilised' diagenetic fronts from currently active fronts were presented in Chapter 6 and are based on seismic data. The causes for 'fossilisation' remain speculative for the moment. Until these are understood, it is not possible to use 'fossilised' silica diagenetic fronts to constrain the thermal evolution of sedimentary basins. The use of active diagenetic fronts for understanding the present – day thermal structure of a sedimentary basin is not recommended, until the impact of all the other controls of the diagenetic reactions (e.g. sediment age and composition, pore – water lithology etc) is investigated in the respective context of the sedimentary basin.

7.4. Limitations of the research

The research presented in this thesis is based on a combination of seismic and well data, which allowed the investigation of several aspects of silica diagenesis at a regional scale. Beyond the purpose of this study was the examination of silica diagenesis at outcrop scale or the design of experimental studies focused on the reaction kinetics. The motivation was that, while 'seismic diagenesis' (c.f. Davies and Cartwright, 2007) is a new discipline, most of the research on silica diagenesis in the last four decades is based on core samples, field or experimental data. This allowed the integration of these results in this thesis, mainly in the development of working hypotheses (e.g. kinetic controls of the silica diagenesis reaction), supporting arguments and comparisons (e.g. thickness of the transition zone of the Monterey Formation at outcrops versus the thickness estimated based on ODP data).

In addition, for every chapter, there are specific limitations mainly related to the typology of data used for the research. These will be described in the subsequent paragraphs.

Chapter 4 is based on the study of a restricted number of scientific boreholes (i.e. 33), despite the fact that the silica diagenesis transition zones have been drilled in a higher number of locations. This is because the relevant data needed for the physical and chemical characterisation of the diagenetic transition zones were only available for a limited number of boreholes. However, it was considered that these sites are representative for the diagenetic transition zones worldwide. Another drawback of Chapter 4 relates to the age of the sediments in which the opal – A to opal – CT transition zones are embedded. In general, the exact age determination was not available from the ODP reports, so most of the data points have large associated error bars (e.g. Fig. 4.12) which did not permit an unbiased interpretation of the relationship between sediment age and temperature of the $TZ_{A/CT}$.

One of the factors limiting the research in Chapter 5 was that no information related to the composition of the sediment matrix was available from the exploration wells

in the study area. The resistivity logs were available for some of the exploration wells, and knowing the composition of the matrix would have allowed the determination of sediment porosity using the Wyllie or the Archie equations (e.g. Hearst et al., 2000). Instead, the average porosity values and biogenic silica content of the sediments were extracted from the ODP site 642, located some 50 km outside the study area, assuming little or no facies lateral variation. In addition, the research presented in Chapter 5 would have benefited from shear strength measurements of the opal – A and opal – CT sediments from the study area. Since these were lacking, qualitative information from literature had to be used as an alternative.

The limitations of the study presented in Chapter 6 relate to several issues. Firstly, the value of the temperature at which opal – A converts into opal – CT was estimated, based on literature data. Secondly, until a classification of 'active' versus 'fossilised' reaction fronts from several sedimentary basins is completed, it is only possible to speculate on the factors that led to the 'fossilisation'. Also, the limited availability of well data impeded the regional correlation and dating of some seismic horizons. Moreover, the paleo – isotherms at the time of 'fossilisation' were assumed to be parallel to the paleo – seabed. No vitrinite reflectance data needed to constrain paleo – temperatures were available, and also the variations in thermal conductivity of the sediments are unknown, therefore the model used is clearly over – simplified and, hence, prone to lack accuracy. Finally, the criteria used to classify a diagenetic front as 'fossilised' are based on seismic evidence of structural deformation. This limits their applicability, hence where no seismic data are available or no deformation of the reaction front is present, it is difficult to make a case that the reaction is 'fossilised' at all.

7.5. Suggestions for further work

This project was not aimed to be an exhaustive study of silica diagenesis process, due the complexity of the subject and data limitations. The purpose of the research presented here is to expand the knowledge of two important aspects of silica diagenesis: the physical properties changes and the diagenetic transition zones. A

combination of seismic reflection and well data was the selected tool for the investigation of these aspects at a regional scale. Consequently, the results of this project complement previous studies on diagenesis based on experimental and outcrop data, and, in turn, are to be a step for future research aimed at understanding the complex process of silica diagenesis at the scale of sedimentary basins. The purpose of the following section is to make some suggestions for future work.

7.5.1. Opal – CT to quartz transformation

Beyond the purpose of this research was the study of the opal – CT to quartz transformation. There were several reasons for this choice. Firstly, this diagenetic transformation does not result in dramatic changes of the physical properties of the sediments; therefore its study is not as important for the compaction of sediments as the opal – A to opal – CT transformation. Secondly, the CT to quartz transformation, being associated with higher temperatures, takes place at a higher burial depth, and, consequently has only been drilled by few ODP sites. Finally, even if this silica phase boundary can create a seismic reflection, as demonstrated by Mayerson and Crouch (1994), Pegrum et al. (2001) and Meadows and Davies (2008), its identification has not been confirmed by the available drilling data in the Norwegian Sea.

Interestingly, in the Southern Vøring Basin, I have mapped a reflection parallel to the opal – A to opal – CT front, located about 200 ms deeper in the seismic section (Appendices A3.13 – A3.14). The reflection is continuous over the area of Province 1 in Fig. 6.1b and had been identified by another study; it was called 'BSR 2' by Berndt et al. (2004). They interpreted it as related to the smectite to illite transformation. However, recent work of Peltonen et al. (2008, 2009) established, based on geochemical analyses of well data, that the smectite to illite transformation is confined within Cretaceous sediments within the study area. Since 'BSR2' is hosted by younger sediments, Oligocene to Miocene, its origin cannot be related to the smectite to illite transformation. It is possible that this reflection is related to the

opal – CT to quartz transformation, however, until a well calibration will confirm it, this remains only a supposition.

7.5.2. The relationship between silica diagenesis and overpressure

In this thesis, the prospect of overpressure generation by silica diagenesis in sediments with low permeability was discussed. Investigating the effect of opal – A to opal – CT dehydration to the build – up of overpressure could benefit from numerical modelling. It is expected that sediments with varying opal – A contents, hence with varying porosity, when subjected to different temperatures, will have different reaction rates. These, in turn, would be correlated to the rate of expulsion of pore fluids, which could be either the mechanism leading to or the factor enhancing overpressure in sedimentary basins. Understanding this process and knowing silica diagenesis can be a basin – wide process would then lead to the incorporation of the effect of silica diagenesis dehydration in overpressure models focused on shale compaction.

In section 7.3.1.3 of the thesis it was proposed that overpressure inhibits the rate of opal – A to opal – CT transformation and could be a reason for the 'fossilisation' of the reaction front at the scale of a sedimentary basin. The hypothesis of overpressure inhibiting silica diagenesis could only be proven by experimental work focused on the reaction kinetics.

7.5.3. The relationship between silica diagenesis and polygonal faults

Further work is required to understand the post – diagenetic phase of fault growth presented in Chapter 5. It was demonstrated that the polygonal faults continued to grow after diagenesis had effectively ceased, and this occurred despite the increase in the shear strength of the sediments. Since the results of this thesis have been unable to explain this, it is proposed that an accurate restoration of the displacement history of a set of polygonal faults would define the time interval when diagenesis

ceased. The causes of the continued growth of the polygonal faults after this exact time might then be easier to understand.

Outside the purpose of this thesis was the investigation of the genesis of the extensive polygonal fault system present within the same sedimentary sequence affected by silica diagenesis in the Norwegian Sea. A recent study (Davies et al., 2009) proposed that silica diagenesis is a new mechanism for fault propagation and could explain how some polygonal faults are generated. Additionally, the result of a numerical modelling study (Shin et al., 2008), investigating shear failure initiation in uncemented materials, suggested that dissolution due to diagenesis could promote shear failures, possibly leading to the formation of polygonal faults. It is proposed that these studies, together with other research on the relationship between silica diagenesis and fractures based on outcrop data (e.g. Eichhubl and Boles, 2000; Eichhubl et al., 2001), could represent the foundation of a future study aimed at demonstrating the impact of diagenesis on initiation and propagation of polygonal faults.

Chapter 8.

CONCLUSIONS

8. CONCLUSIONS

To the author's knowledge, this research involves several novel aspects of the study of silica diagenesis. Firstly, this thesis represents the first published synthesis of scientific drilling data used for the characterisation of the silica diagenesis transition zones. Secondly, a new methodology for estimating the compaction strain due to diagenesis based on seismic and well data was proposed. Finally, the approach based on the use of isochore maps to demonstrate the silica diagenesis reaction is 'fossilised' and to estimate the time of 'arrest' has not been used previously. In general, the integration of seismic reflection and well data (exploration and scientific drilling) to investigate the physical properties contrast across silica diagenesis transition zones (Chapter 4), with a focus on the porosity change and related compaction strain (Chapter 5) and the potential 'fossilisation' of the reaction fronts (Chapter 6) represents a new approach on the study of silica diagenesis. The conclusions of this research are presented next, followed by a commentary on their general applicability.

8.1. Conclusions of Chapter 4

- A representative number of ODP sites from various locations allowed the identification of the silica diagenesis transition zones ($TZ_{A/CT}$).

- The $TZ_{A/CT}$ represent narrow depth ranges (< 40 m) where the opal – A and opal – CT phases coexist.

- There is an important contrast in the physical properties of the sediments across the $TZ_{A/CT}$.

- Criteria for identifying the presence of a $TZ_{A/CT}$ were defined based on the physical properties contrast and the chemistry of interstitial water.

- Temperature was proposed to be the main factor controlling the thickness of the $TZ_{A/CT}$.

- It is possible that some of the $TZ_{A/CT}$ formed as a response to higher paleo – geothermal gradients and are presently 'fossilised'. The likely candidates are

the diagenetic fronts at sites with a low present – day temperature and relatively young age (Miocene or younger).

- Due to the widespread occurrence of the silica diagenesis transition zones and the associated physical properties contrast, they should be considered an important element for the evaluation of sediment compaction in basin analysis.

8.2. Conclusions of Chapter 5

- Polygonal faults from the biosiliceous sediments of the Møre and Vøring Basins exhibit unusual segmented fault plane geometry.
- The planar segments dip more steeply in the opal – A rich biosiliceous mudstones than in the underlying opal – CT sediments.
- The change in dip in the fault plane segments systematically occurs at or close to the opal – A to opal – CT diagenetic boundary.
- Assuming the fault planes were planar markers prior to diagenesis, they were used to quantify the vertical compaction strain due to diagenesis.
- The rotation of fault planes as a result of diagenesis offers a new method for estimating the porosity reduction due to silica diagenesis.
- The faults continued to grow after the diagenesis had effectively ceased, despite of changes in physical properties such as an increase in shear strength.
- This post – diagenetic phase of growth cannot be explained mechanically at present.

8.3. Conclusions of Chapter 6

- Evidence for a 'fossilised' opal – A to opal – CT reaction front on the mid – Norwegian margin was examined.
- Using isochore maps, it was demonstrated that the A/CT reflection is not a sea bottom simulating reflector (BSR), therefore not in thermal equilibrium with the local isotherms.

- The 'fossilisation' of the silica diagenesis reaction front at a regional scale was demonstrated based on the analysis of three styles of deformation associated with the A/CT reflection: polygonal faulting, regional anticlines and synclines and differential compaction folding.

- Identifying the 'fossilisation' time was attempted by the means of recognising the stratal surface concordant to the A/CT reflection.

- It was found that, at a regional scale, the 'fossilisation' occurred at some time within the Late Miocene to Early Pliocene.

- An accurate estimation of the timing of 'fossilisation' is not possible due to uncertainties associated with the unique identification and accurate dating of a presumed paleo – seabed marker.

- Establishing whether the 'fossilisation' was synchronous or diachronous over the study area was prevented by the problems in regional seismic correlation. However, the evidence from the relationships with polygonal faults and anticlines and synclines strongly suggests that 'fossilisation' occurred rapidly over a geological time scale.

- The A/CT reflection is not a typical BSR and cannot be used to constrain temperature in sedimentary basins.

- It seems likely that 'fossilisation' of the silica diagenetic reaction front in other basins is much more common than currently appreciated.

8.4. General applicability

From an economic perspective, the study of biogenic silica diagenesis is relevant because biosiliceous mudstones, porcelanites and cherts can represent significant hydrocarbon reservoirs (e.g. Monterey Formation, California) or shale – gas systems (e.g. Barnett Formation, Texas).

Investigating the role of silica diagenesis on the evolution of sediment physical properties during burial and deformation is important for understanding sediment compaction, the relationship with fluid flow and possibly the generation of overpressure. Moreover, if 'fossilised' or 'relict', silica diagenetic zones are not

isothermal boundaries, so they cannot be used to constrain the temperature distribution in sedimentary basins.

Silica diagenesis transition zones are present in all the world's oceans and can extend to the area of an entire sedimentary basin and, due to the important associated porosity reduction and associated water expulsion, they need to be taken into account in compaction models for the shallow (< 1 – 1.5 km) sedimentary section, where normally only mechanical compaction is considered.

REFERENCES

A

Amante, C. and Eakins, B.W. 2008. ETOPO1 1 Arc – Minute Global Relief Model: Procedures, Data Sources and Analysis, National Geophysical Data Center, NESDIS, NOAA, U.S. Department of Commerce, Boulder, CO.

Aplin, A.C., Fleet, A.J. and Macquaker, J.H.S. 1999. Muds and mudstones: physical and fluid – flow properties. In: Aplin, A.C., Fleet, A.J. and Macquaker, J.H.S. (eds). Muds and Mudstones. Physical and Fluid Flow Properties. Geological Society, London, Special Publications 158, 1 – 8.

Atkins, P. and de Paola, J. 2006. Physical Chemistry, Oxford University Press, 1149 p.

Audet, D.M,. and Fowler, A.C. 1992. A mathematical model for compaction in sedimentary basins. Geophysical Journal International 110 (3), 577 – 590.

B

Baudon, C., Cartwright, J. 2008. The kinematics of reactivation of normal faults using high resolution throw mapping. Journal of Structural Geology 30 (8), 1072 – 1084.

Bayer, U. and Wetzel, A. 1989. Compactional behavior of fine – grained sediments – examples from Deep Sea Drilling Project cores. International Journal of Earth Sciences 78 (3), 807 – 819.

Behl, R.J. 1999. Since Bramlette (1946): The Miocene Monterey Formation of California revisited. In Moores, E.M., Sloan, D. and Stout, D.L. (eds.). Classic Cordilleran Concepts: A View from California: Boulder, Colorado, Geological Society of America Special Paper 338.

Behl, R.J. and Garrison, R.E. 1994. The origin of chert in the Monterey Formation of California (USA), in Iijima, A., Abed, A., and Garrison, R. (Eds.). Siliceous, phosphatic and glauconitic sediments of the Tertiary and Mesozoic: Utrecht, International Geological Congress Proceedings, Part C: 101 – 132.

Berg, K., Solheim, A., Bryn, P. 2005. The Pleistocene to Recent geological development of the Ormen Lange area. Marine and Petroleum Geology 22, 45 – 56.

Berndt, C., Bünz, S., Clayton, T., Mienert, J., Saunders, M. 2004. Seismic character of bottom simulating reflectors: Examples from the mid – Norwegian margin. Marine and Petroleum Geology 21 (6), 723 – 733.

Berndt, C., Bünz, S., Mienert, J. 2003. Polygonal fault systems on the mid – Norwegian margin: A long – term source for fluid flow. Geological Society Special Publication 216, 283 – 290.

Berndt, C., Mjelde, R., Planke, S., Shimamura, H. and Faleide, J. I. 2001. Controls on the tectono – magmatic evolution of a volcanic transform margin: the Vøring Transform Margin, NE – Atlantic. Marine Geophysical Researches 22 (3), 133 – 152.

Bethke, C.M. and Corbet, T.F. 1988. Linear and nonlinear solutions for one – dimensional compaction flow in sedimentary basins. Water Resources Research 24 (3), 461 – 467.

Bjørlykke, K. 1999. Principal aspects of compaction and fluid flow in mudstones. In: Aplin, A.C., Fleet, A. J. and Macquaker, J.H.S. (eds). Muds and Mudstones. Physical and Fluid Flow Properties. Geological Society, London, Special Publications 158, 73 – 78.

Bjørlykke, K. and Høeg, K. 1997. Effects of burial diagenesis on stresses, compaction and fluid flow in sedimentary basins. Marine and Petroleum Geology 14 (3), 267 – 276.

Blum, P. 1997. Physical properties handbook. ODP Tech. Note, 26. doi:10.2973/odp.tn.26.1997.

Blystad, P., Brekke, H., Færseth, R.B., Larsen, B.T., Skogseid, J. and Tørudbakken, B. 1995. Structural elements of the Norwegian continental shelf. Part II: The Norwegian Sea region. Norwegian. Petroleum Directory Bulletin 6.

Bohrmann, G., Abelmann, A., Gersonde, R., Hubberten, H., Kuhn, G. 1994. Pure siliceous ooze, a diagenetic environment for early chert formation. Geology 22 (3), 207 – 210.

Bohrmann, G., Spieß, V., Hinze, H., Kuhn, G. 1992. Reflector 'Pc' a prominent feature in the Maud Rise sediment sequence (eastern Weddell Sea): occurrence, regional distribution and implications to silica diagenesis. Marine Geology 106 (1 – 2), 69 – 87.

Bohrmann, G. and Stein, R. 1989. Biogenic silica at ODP Site 647 in the Southern Labrador Sea: occurrence, diagenesis, and paleoceanographic implications. In: Srivastava, S. P., Arthur, M., Clement, B., et al. 1989. Proceedings of the Ocean Drilling Program, Scientific Results, Vol. 105

Bradshaw, G.A. and Zoback, M.D. 1988. Listric normal faulting, stress refraction and the state of stress in the Gulf Coast basin. Geology 16, 271 – 274.

Bramlette, M.N. 1946. The Monterey Formation of California and the origin of its siliceous rocks, U.S. Geological Survey Professional Paper 212, 57 p.

Brekke, H. 2000. The Tectonic Evolution of the Norwegian Sea Continental Margin with Emphasis on the Vøring and Møre Basins. In: Geological Society Special Publications167, 327 – 378.

Brekke, H., Dahlgren, S., Nyland, B., Magnus, C. 1999. The prospectivity of the Vøring and Møre basins on the Norwegian Sea continental margin. In: Fleet, A.J., and Boldy, S.A.R. (eds) Petroleum Geology of Northwest Europe: Proceedings of the 5th Conference, 261 – 274. Petroleum Geology '86 Ltd. Geological Society, London.

Brekke, H. and Riis, F. 1987. Tectonics and basin evolution of the Norwegian shelf between 62°N and 72°N. Norsk Geologisk Tidsskrift 67, 295 – 322.

Brown, A. 2004. Interpretation of Three – Dimensional Seismic Data, sixth ed. American Association of Petroleum Geologists Memoir.

Bruce, C. H. 1984. Smectite Dehydration – Its Relation to Structural Development and Hydrocarbon Accumulation in Northern Gulf of Mexico Basin. AAPG Bulletin 68 (6), 673 – 683.

Bryn, P., Berg, K., Stoker, M., Haflidason, H., Solheim, A. 2005. Contourites and their relevance for mass wasting along the Mid – Norwegian Margin. Marine and Petroleum Geology 22 (1 – 2), 85 – 96.

Bull, S., Cartwright, J., Huuse, M. 2009. A subsurface evacuation model for submarine slope failure. Basin Research 21 (4), 433 – 443.

Bünz, S., Mienert, J., Berndt, C. (2003) Geological controls on the Storegga gas-hydrate system of the mid-Norwegian margin. Earth and Planetary Science Letters 209 (3–4), 291–307.

Byrne, T., Maltman, A., Stephenson, E., Soh, W., and Knipe, R. 1993. Deformation structures and fluid flow in the toe region of the Nankai accretionary prism. In Hill,

I.A., Taira, A., Firth, J.V., et al. Proceeding of the ODP, Scientific Results, 131: College Station, TX.

C

Carr, A.D. 2000. Suppression and retardation of vitrinite reflectance, Part 1. Formation and significance for hydrocarbon generation. Journal of Petroleum Geology 23 (3), 313 – 343.

Cartwright, J.A. 1994. Episodic basin – wide fluid expulsion from geopressured shale sequences in the North Sea Basin. Geology 22 (5), 447 – 450.

Cartwright, J.A. 1996. Polygonal fault systems: A new type of fault structure revealed by 3D seismic data from the North Sea Basin: American Association of Petroleum Geologists Studies in Geology 42, 225 – 230.

Cartwright, J.A. 2007. The impact of 3D seismic data on the understanding of compaction, fluid flow and diagenesis in sedimentary basins. Journal of the Geological Society 164, 881 – 893.

Cartwright, J.A., Bouroullec, R., James, D., Johnson, H.D. 1998. Polycyclic motion history of some Gulf Coast growth faults from high – resolution displacement analysis. Geology 26 (9), 819 – 822.

Cartwright, J.A., Dewhurst, D.N. 1998. Layer – bound compaction faults in fine – grained sediments. Bulletin of the Geological. Society of America 110 (10), 1242 – 1257.

Cartwright, J.A., James, D., Bolton, A. 2003. The genesis of polygonal fault systems: A review. In: Van Rensbergen, P., Hillis, R.R., Maltman, A.J., Morley, C.K. (Eds.) Subsurface Sediment Mobilization, Geological Society, London, Special Publications 216, 223 – 243.

Cartwright, J. A., Lonergan, L. 1996. Volumetric contraction during the compaction of mudrocks: A mechanism for the development of regional – scale polygonal fault systems. Basin Research 8 (2), 183 – 193.

Cartwright, J., Wattrus, N., Rausch, D. and Bolton, A. 2004. Recognition of an early Holocene polygonal fault system in Lake Superior: implications for the compaction of fine – grained sediments. Geology 32, 253 – 256.

Chaika, C. and Dvorkin, J. 1997. Ultrasonic velocities of opaline rocks undergoing silica diagenesis. Geophysics Research Letters 24 (16), 2039 – 2042.

Chaika, C. and Dvorkin, J. 2000. Porosity reduction during diagenesis of diatomaceous rocks. American Association of Petroleum Geologists Bulletin 84 (8), 1173 – 1184.

Chaika, C. and Williams, L.A. 2001. Density and mineralogy variations as a function of porosity in Miocene Monterey Formation oil and gas reservoirs in California. AAPG Bulletin 85 (1), 149 – 167.

Chopra, S. and Marfurt, K.J. 2005. Seismic attributes – A historical perspective. Geophysics 70 (5), 3SO – 28SO.

Clausen, J.A., Gabrielsen, R.H., Reksnes, P.A. and Nysether. E. 1999. Development of intraformational faults in the northern North Sea: influence of remote stresses and doming of Fennoscandia. Journal of Structural Geology 21, 1457 – 1475.

Cobbold P.R. and Rodrigues, N. 2007. Seepage forces, important factors in the formation of horizontal hydraulic fractures and bedding – parallel fibrous veins ('beef' and 'cone – in – cone'). Geofluids 7 (3), 313 – 322.

Colten – Bradley, V.W.A. 1987. Role of Pressure in Smectite Dehydration – Effects on Geopressure and Smectite – to – Illite Transformation. AAPG Bulletin 71 (11), 1414 – 1427.

Compton, J.S. 1991. Porosity reduction and burial history of siliceous rocks from the Monterey and Sisquoc Formations, Point Pedernales area, California. Geological Society of America Bulletin 103 (5), 625 – 636.

Corfield, S.M., Wheeler, W., Karpuz, R., Wilson, M. and Helland, R. 2004. Exploration 3D seismic over the Gjallar Ridge, Mid – Norway: visualization of structures on the Norwegian volcanic margin from Moho to seafloor. In: Davies, R.J., Cartwright, J.A., Stewart, S.A., Lappin, M. & Underhill, J.R. (eds.). 2004. 3D Seismic Technology: Application to the Exploration of Sedimentary Basins. Geological Society London, Memoirs 29, 177 – 185.

Craig, J. 1987. The structure of the Llangranog Lineament, West Wales: A Caledonian transpression zone. Geological Journal 22 (S1), 167 – 181.

D

Dalland, A., Worsley, D., Ofstad, K. (Eds.). 1988. A Lithostratigraphic Scheme for the Mesozoic and Cenozoic Succession Offshore Mid – and Northern – Norway. NPD Bulletin 4.

Davies, R.J. 2005. Differential compaction and subsidence in sedimentary basins due to silica diagenesis: A case study. Bulletin of the Geological Society of America 117 (9 – 10), 1146 – 1155.

Davies, R.J. and Cartwright, J. 2002. A fossilized Opal – A to Opal C/T transformation on the northeast Atlantic margin: Support for a significantly elevated palaeogeothermal gradient during the Neogene? Basin Research 14 (4), 467 – 486.

Davies, R.J. and Cartwright, J.A. 2007. Kilometer – scale chemical reaction boundary patterns and deformation in sedimentary rocks. Earth and Planetary Science Letters 262 (1 – 2), 125 – 137.

Davies, R., Cartwright, J., Rana, J. 1999. Giant hummocks in deep – water marine sediments: Evidence for large scale differential compaction and density inversion during early burial. Geology 27 (10), 907 – 910.

Davies, R.J., Goulty, N.R., Meadows, D. 2008. Fluid flow due to the advance of basin – scale silica reaction zones. Bulletin of the Geological Society of America 120 (1 – 2), 195 – 206.

Davies, R.J., Ireland, M. and Cartwright, J. 2009. Differential compaction due to the irregular topology of a diagenetic reaction boundary: a new mechanism for the formation of polygonal faults. Basin Research 21(3), 354 – 359.

Davison, I. 1987. Normal fault geometry related to sediment compaction and burial. Journal of Structural Geology 9 (4), 393 – 401.

Dewhurst, D.N., Cartwright, J.A., Lonergan, L. 1999. The development of polygonal fault systems by syneresis of colloidal sediments. Marine and Petroleum Geology 16 (8), 793 – 810.

D'Hondt, S.L., Jørgensen, B.B., Miller, D.J., et al. 2003. Proceedings of the Ocean Drilling Program, Initial Reports 201, doi:10.2973/odp.proc.ir.201.107.2003.

Doré, A.G. and Lundin, E.R. 1996. Cenozoic compressional structures of the NE Atlantic margin: nature, origin and potential significance for hydrocarbon exploration. Petroleum Geoscience 2, 299 – 311.

Dugan, B. and Flemings, P.B. 2000. Overpressure and Fluid Flow in the New Jersey Continental Slope: Implications for Slope Failure and Cold Seeps. Science 289, 288 – 291.

Dutta, N.C. 1986. Shale compaction, burial diagenesis, and geopressures: A dynamic model, solution, and some results. In: Burrus, J (editor). Thermal Modeling in Sedimentary Basins, 1st IFP Exploration Research Conference, Carcans, France, June 3 – 7, 1985, Editions Technip, Paris.

E

Eichhubl, P., Aydin, A., and Lore, J. 2001. Opening – mode fracture in siliceous mudstone at high homologous temperature – Effect of surface forces: Geophysical Research Letters 28, 1299 – 1302.

Eichhubl, P. and Behl, R.J. 1998. Diagenesis, deformation and fluid flow in the Miocene Monterey Formation. In Eichhubl, P. et al. (eds.) Diagenesis, deformation and fluid flow in the Miocene Monterey Formation: Pacific Section SEPM Special Publication, Book 83.

Eichhubl, P. and Boles, J.R. 2000. Focused fluid flow along faults in the Monterey Formation, coastal California. Bulletin of the Geological Society of America 112 (11), 1667 – 1679.

Eidvin, T., Eystein, J., Rundberg, Y., Brekke, H., Grogan, P. 2000. The upper Cainozoic of the Norwegian continental shelf correlated with the deep sea record of the Norwegian Sea and the North Atlantic. Marine and Petroleum Geology 17, 579 – 600.

Eldholm, O. 1991. Magmatic – tectonic evolution of a volcanic rifted margin. Marine Geology 102, 42 – 61.

Eldholm, O., Thiede, J., Taylor, E., et al. 1987. Proceedings of ODP, Initial Reports, 104: College Station, TX.

Evans, D., King, E.L., Kenyon, N.H., Brett, C., Wallis, D. 1996. Evidence for long – term instability in the Storegga Slide region off western Norway. Marine Geology 130, 281 – 292.

Evans, D., McGiveron, S., Harrison, Z., Bryn, P.Graham, C., Armour, A. and Berg, K. 2002. Along – slope variation in the late Neogene evolution of the mid –

Norwegian margin in response to uplift and tectonism. In: Exhumation of the North Atlantic Margin: Timing, Mechanisms and Implications for Petroleum Exploration (Ed. by Doré, A.G. Cartwright, J.A. and Stoker, S.J.PBathurst, P. 2003. The Millenium Atlas: Petroleum Geology of the Central and Northern North Sea. The Geological Society, London, 390 p.

Exon, N.F., Lafoy, Y., Hill, P.J., Dickens, G.R. and Pecher, I. 2007. Geology and petroleum potential of the Fairway Basin in the Tasman Sea. Australian Journal of Earth Sciences 54, 629 – 645.

F

Ferrill, D. and Morris, A. 2003. Dilational normal faults. Journal of Structural Geology 25 (2), 183 – 196.

Fisher, A.T. and Becker, K. 1988. A guide to ODP tools for downhole measurements. ODP Tech. Note, 10. doi:10.2973/odp.tn.10.1988.

Fütterer, D.K. 2000. The Solid Phase of Marine Sediments. In: Schulz, H. D., Zabel, M. (Eds.). Marine Geochemistry. Springer – Verlag Berlin. p. 455.

G

Gay, A. and Berndt, C. 2007. Cessation/reactivation of polygonal faulting and effects on fluid flow in the Vøring Basin, Norwegian Margin. Journal of the Geological Society 164 (1), 129 – 141.

Gay, A., Lopez, M., Cochonat, P., Sermondadaz, G. 2004. Polygonal faults – furrows system related to early stages of compaction – upper Miocene to recent sediments of the Lower Congo Basin. Basin Research 16 (1), 101 – 116.

Gerland, S., Kuhn, G. and Bohrmann, G. 1997. Physical properties of a porcellanite layer (Southwest Indian Ridge) constrained by geophysical logging. Marine Geology 140 (3 – 4), 415 – 426.

Gieskes, J.M., Gamo, T. and Brumsack, H. 1991. Chemical methods for interstitial water analysis aboard JOIDES Resolution, ODP Tech. Note 15. doi:10.2973/odp.tn.15.1991.

Giles, M.R. 1997. Diagenesis: A Quantitative Perspective, Kluwer Academic Publishers, Dordrecht, The Netherlands, p. 526.

Goulty, N.R. 2001. Polygonal fault networks in fine – grained sediments: an alternative to the syneresis mechanism. First Break 19 (2), 69 – 73.

Goulty, N.R. 2002. Mechanics of layer – bound polygonal faulting in fine – grained sediments. Journal of the Geological Society 159 (3), 239 – 246.

Goulty, N.R. 2008. Geomechanics of polygonal fault systems: a review. Petroleum Geoscience 14: 389 – 397.

Goulty, N. and Swarbrick, R. 2005. Development of polygonal fault systems: a test of hypotheses. Journal of the Geological Society 162 (4), 587 – 590.

Gómez M. and Vergés J. 2005. Quantifying the contribution of tectonics vs. differential compaction in the development of domes along the Mid – Norwegian Atlantic margin. Basin Research 17, 289 – 310.

Gretener, P.E. 1981. Geothermics: Using Temperature for Hydrocarbon Exploration. In: Education Course Note Series #17. American Association of Petroleum Geologists, Tulsa, Oklahoma, USA, 170 p.

Guerin, G. and Goldberg, D. 1996. Acoustic and elastic properties of calcareous sediments across a siliceous diagenetic front on the eastern U.S. continental slope. Geophysical Research Letters 23 (19), 2697 – 2700.

H

Hamilton, E.L. 1976. Shear – wave velocity versus depth in marine sediments: a review. Geophysics 41 (5), 985 – 996.

Hammond, R.D., Gaither, J.R. 1983. Anomalous seismic character e Bering Sea Shelf. Geophysics 48 (5), 590 – 605.

Hansen, J.P. V., Cartwright, J.A., Huuse, M., Clausen, O. R. 2005. 3D seismic expression of fluid migration and mud remobilization on the Gjallar Ridge, offshore mid – Norway. Basin Research 17 (1), 123 – 139.

Hay, W. W., Sloan, J. L., and Wold, C. N. 1988. Mass/age distribution and composition of sediments on the ocean floor and the global rate of sediment subduction. Journal of Geophysical Research 93, 14933 – 14940.

Hearst, J.R., Nelson, P.H. and Frederik, L.P. 2000. Well Logging for Physical Properties: A Handbook for Geophysicists, Geologists, and Engineers. John Wiley & Sons Ltd, Chichester, p. 483.

Hein, J.R., Scholl, D.W., Barron, J.A., Jones, M.G., Miller, J. 1978. Diagenesis of late Cenozoic diatomaceous deposits and formation of the bottom simulating reflector in the southern Bering Sea. Sedimentology 25, 155 – 181.

Henrich, R., Eldholm, O., Thiede, J. 1989. Diagenetic environments of authigenic carbonates and opal – CT crystallization in lower Miocene to upper Oligocene deposits of the Norwegian Sea (ODP Site 643, Leg 104). Proc., scientific results, ODP, Leg 104, Norwegian Sea, 233 – 247.

Henriet, J.P., De Batist, M., Verschuren, M. 1989. Seismic facies and clay tectonic features in the southern North Sea. Bulletin of the Belgian Geological Society, 97, 457-472.

Henriet, J.P., De Batist, M., Verschuren, M. 1991. Early fracturing of Palaeogene clays, southernmost North Sea: relevance to mechanisms of primary hydrocarbon migration. Generation, accumulation, and production of Europe's hydrocarbons, 217 – 227.

Hesse, R. 1988. Diagenesis #13. Origin of Chert: diagenesis of biogenic siliceous sediments. Journal of the Geological Association of Canada 15 (3), 171 – 192.

Hillier, R.D. and Cosgrove, J.W. 2002. Core and seismic observations of overpressure related deformation within Eocene sediments of the Outer Moray Firth, UKCS: Petroleum Geoscience 8, 141 – 149.

Hinman, N.W., 1990. Chemical factors influencing the rates and sequences of silica phase transitions: effects of organic constituents. Geochimica et Cosmochimica Acta 54 (6), 1563 – 1574.

Hjelstuen, B. 1997. Vøring Plateau diapir fields and their structural and depositional settings. Marine Geology 144 (1 – 3), 33 – 57.

Hjelstuen, B.O., Sejrup, H.P., Haflidason, H., Berg, K. and Bryn, P. 2004. Neogene and Quaternary depositional environments on the Norwegian continental margin, 62°N – 68°N. Marine Geology 213, 257 – 276.

Hooper, E.C.D. 1991. Fluid migration along growth faults in compacting sediments. Journal of Petroleum Geology 14 (S1), 161 – 180.

Hovland, M., Nygaard, E. and Thorbjørnsen. 1998. Piercement shale diapirism in the deep – water Vema Dome area, Vøring basin, offshore Norway. Marine and Petroleum Geology 15, 191 – 201.

Hustoft, S., Mienert, J., Bünz, S., Nouzé, H. 2007. High – resolution 3D – seismic data indicate focussed fluid migration pathways above polygonal fault systems of the mid – Norwegian margin. Marine Geology 245, 89 – 106.

I

Ireland, M.T., Davies, R.J., Goulty, N.R., Carruthers, D. 2010a. Structure of a silica diagenetic transformation zone: the Gjallar Ridge, offshore Norway. Sedimentology. doi:10.1111/j.1365 – 3091.2010.01170.x 58 (2), 424 – 441.

Ireland, M.T., Goulty, N.R. & Davies, R.J. 2010b. Influence of pore water chemistry on silica diagenesis: evidence from the interaction of diagenetic reaction zones with polygonal fault systems. Journal of the Geological Society 167: 273 – 279

Ireland, M.T., Goulty, N.R. & Davies, R.J. 2010c. Influence of stratigraphic setting and simple shear on layer – bound compaction faults offshore Mauritania. Journal of Structural Geology. *In press.*

Isaacs, C.M., 1981. Porosity reduction during diagenesis of the Monterey Formation, Santa Barbara coastal area, California. In: Garrison, R.E., Douglas, R.G., Pisciotto, K.E., Isaacs, Caroline M., Ingle, James C. (Eds.), The Monterey Formation and Related Siliceous Rocks of California, SEPM Research Symposium (San Francisco, California), 257 – 271.

Isaacs, C.M. 1982. Influence of rock composition on kinetics of silica phase changes in the Monterey formation, Santa Barbara area, California. Geology 10 (6), 304 – 308.

Isaacs, C.M., Pisciotto, K.A., Garrison, R.E. 1983. Facies and diagenesis of the Monterey Formation, California: a summary. In: Iijima, A., Hein, J.R., Siever, R. (Eds.), Siliceous Deposition in the Pacific Region. Elsevier, Amsterdam, 247 – 281.

J

Jones, J.B., Segnit, E.R. 1971. The nature of opal. I. Nomenclature and constituent phases. Geological Society of Australia Journal 68, 56 – 68.

Jones, M.E. and Addis, M.A. 1984. Volume change during sediment diagenesis and the development of growth faults. Marine and Petroleum Geology 1 (2), 118 122.

K

Kastner, M. 1981. Authigenic silicates in deep – sea sediments: formation and diagenesis. In Emiliani, C. (editor). The Oceanic Lithosphere, New York: Wiley, 915 – 980.

Kastner, M., Keene, J.B. and Gieskes, J.M. 1977. Diagenesis of siliceous oozes – I. Chemical controls on the rate of opal – A to opal – CT transformation – an experimental study. Geochimica et Cosmochimica Acta, 41 (8), 1041 – 1059.

Keller, M.A., Isaacs, C.M. 1985. An evaluation of temperature scales for silica diagenesis in diatomaceous sequences including a new approach based on the Miocene Monterey Formation, California, Geo – Marine Letters 5 (1), 31 – 35.

Kim, G., Yoo, D., Lee, H., Lee, Y., Kim, D. 2007. The relationship between silica diagenesis and physical properties in the East/Japan Sea: ODP Legs 127/128 Journal of Asian Earth Sciences 30 (3 – 4), 448 – 456.

Kinoshita, M., Tobin, H., Ashi, J., Kimura, G., Lallemant, S., Screaton, E.J., Curewitz, D., Masago, H., Moe, K.T. and the Expedition 314/315/316 Scientists. 2001. Proc. IODP, 314/315/316: Washington, DC.

Kuramoto, S., Tamaki, K., Langseth, M.G., Nobes, D.C., Toluyama, H., Pisciotto, K.A., Taira, A 1992. Can opal – A/opal – CT BSR be an indicator of the thermal structure of the Yamato Basin, Japan Sea. Proceedings, Scientific Results, ODP, Legs 127/128, Japan Sea, 1145 – 1156.

L

Laberg, J.S., Dahlgren, K.I.T., Vorren, T.O. 2005. The Eocene – late Pliocene paleoenvironment in the Vøring Plateau area, Norwegian Sea – paleoceanographic implications. Marine Geology 214, 269 – 285.

Larue, D.K., Gortner, C.W., Torrini, R. 1987. Silica diagenesis in accreted Eocene siliceous rocks (Horizon Ac) on Barbados. Journal of Sedimentary Research 57 (6), 1033 – 1039.

Lawrence, G.M.W., Cartwright, J.A. 2009. The initiation of sliding on the mid Norway margin in the Møre Basin. Marine Geology 259, 21 – 35.

Lee, G.H., Kim, H. J., Jou, H.T., Cho, H.M. 2003. Opal – A/opal – CT phase boundary inferred from bottom – simulating reflectors in the southern South Korea Plateau, East Sea (Sea of Japan). Geophysics Research Letters 30 (24).

Littke, R., Fourtanier, E., Thurow, J., Taylor, E. 1991. Silica diagenesis and its effects on lithification of Broken Ridge deposits, Central Indian Ocean. Proceedings of the Ocean Drilling Program, Scientific Results 121.

Lonergan, L., Cartwright, J., Jolly, R. 1998. The geometry of polygonal fault systems in Tertiary mudrocks of the North Sea. Journal of Structural Geology 20 (5), 529 – 548.

Lonsdale, M. 1990. The relationship between silica diagenesis, methane, and seismic reflections on the South Orkney Microcontinent. In: Proceedings of the Ocean Drilling Program. Scientific Results, vol. 113, 27 – 37. College Station, TX.

Løseth, H., Henriksen, S. 2005. A Middle to Late Miocene compression phase along the Norwegian passive margin. Petroleum Geology Conference Series 6, 745 – 859.

M

Mandl, G. 2000. Faulting in Brittle Rocks: An Introduction to the Mechanics of Tectonic Faults., Springer – Verlag, New York, 434 p.

Mansfield, C.S. and Cartwright, J. A. 1996. High resolution fault displacement mapping from three – dimensional seismic data: Evidence for dip linkage during fault growth. Journal of Structural Geology 18 (2 – 3), 249 – 263.

Mayer, L., Pisias, N., Janecek, T., et al. 1992. Proc. ODP, Init. Repts., 138: College Station, TX (Ocean Drilling Program). doi:10.2973/odp.proc.ir.138.1992

Mayerson, D. and Crouch, J. 1994. The Opal-CT/Quartz Diagenetic Boundary Within the Monterey Formation of the California Offshore Santa Maria Basin: An Untapped Exploration Target. AAPG Search and Discovery Article #90981©1994 AAPG Pacific Section Meeting, Ventura, California, April 27-29, 1994.

Mayerson, D. A., C. A. Dunkel, K. A. Piper, and H. L. Cousminer. 1995. Identification and correlation of the opal-CT/quartz phase transition in offshore central California (abs.): AAPG Bulletin 79 (4), 592.

Matheney, R.K. and Knauth, L.P. 1993. New isotopic temperature estimates for early silica diagenesis in early cherts. Geology 21, 519 – 522.

Mazzullo, J.M., and Graham, A.G. (Eds.). 1988. Handbook for shipboard sedimentologists. ODP Tech. Note, 8: 45 – 67. doi:10.2973/odp.tn.8.1988.

McGuire, M. D., J. R. Bowersox, and L. J. Earnest. 1983. Diagenetically enhanced entrapment of hydrocarbons—southeastern Lost Hills fractured shale pool, Kern County, California, in C. M. Isaacs and R. E. Garrison, eds., Petroleum generation and

occurrence in the Miocene Monterey Formation, California: Pacific Section SEPM, 171–183.

McManus, J., Hammond, D.E., Berelson, W.M. et al. 1995. Early diagenesis of biogenic opal: Dissolution rates, kinetics, and paleoceanographic implications. Deep – Sea Research II 42 (2 – 3), 871 – 903.

McTavish, R.A. 1988. The Role of Overpressure in the Retardation of Organic Matter Maturation. Journal of Petroleum Geology 21 (2), 153 – 186.

Meadows, D. and Davies, R.J. 2008. Morphological development of basin – scale silica diagenetic fronts revealed with 2 – D seismic reflection data: offshore Sakhalin, Russian Far East. Journal of the Geological Society 164 (6), 1193 – 1206.

Meadows, D. and Davies, R.J. 2010a. Predicting porosity reduction due to silica diagenesis using seismic reflection data. Marine and Petroleum Geology 26 (8), 1543 – 1553.

Meadows, D. and Davies, R.J. 2010b. The limited suitability of silica diagenetic boundaries as isothermal markers: Insights from seismic reflection imaging, Offshore Sakhalin, Russian Far East. Marine and Petroleum Geology 27 (95),

1028 – 1039.

Mienert, J., Vanneste, M., Bünz, S., Andreassen, K., Haflidason, H., Sejrup, H.P. 2005. Ocean warming and gas hydrate stability on the mid – Norwegian margin at the Storegga Slide. Marine and Petroleum Geology 22, 233 – 244.

Mienert, J., Vanneste, M., Haflidason, H. and Bünz, S. 2010. Norwegian margin outer shelf cracking: a consequence of climate – induced gas hydrate dissociation? Int. J. Earth S. 99 (Suppl. 1), S207 – S225.

Mizutani, S. 1970. Silica minerals in the early stage of diagenesis. Sedimentology 15, 419 – 436.

Mizutani, S. 1977. Progressive ordering of cristobalitic silica in the early stage of diagenesis. Contrib. Mineral. Petrol 61, 129 – 140.

Mountain, G.S., Miller, K.G., Blum, P., et al. 1994. Proc. ODP, Init. Repts., 150: College Station, TX (Ocean Drilling Program). doi:10.2973/odp.proc.ir.150.1994

Muraoka, H. and Kamata, H. 1983. Displacement distribution along minor fault traces. Journal of Structural Geology 5 (5), 483 – 495.

Murata, K.J. and Larson, R.R. 1975. Diagenesis of Miocene Siliceous Shales, Temblor Range, California. J Res US Geological Survey 3 (5), 553 – 566.

Murray, R.W. 1994. Chemical criteria to identify the depositional environment of chert: general principles and applications. Sedimentary Geology 90 (3 – 4), 213 – 232.

Murray, R.W., Brumsack, H.J., von Breymann, M.T., Sturz, A.A., Dunbar, R.B., Gieskes, J.M. 1992a. Diagenetic reactions in deeply – buried sediments of the Japan Sea: a synthesis of interstitial water chemistry results from Leg 127 and Leg 128. In: Proceedings of the Ocean Drilling Program. Scientific Results, 127/128, 1261 – 1274.

Murray, R.W., Buchholtz ten Brink, M.R., Gerlach, D.C., Russ III, G.P., Jones, D.L. 1992b. Rare – earth, major, and trace element composition of Monterey and DSDP chert and associated host sediment, assessing the influence of chemical fractionation during diagenesis. Geochimica et Cosmochimica Acta 56, 2657 – 2671.

N

Nadeau, P.H., Peacor, D.R., Yan, J. and Hillier, S. 2002. I – S precipitation in pore space as the cause of geopressuring in Mesozoic mudstone, Egersund Basin, Norwegian continental shelf. American Mineralogist 87, 1850 – 1859.

Neagu, R.C., Cartwright, J., Davies, R. 2010a. Measurement of diagenetic compaction strain from quantitative analysis of fault plane dip. Journal of Structural Geology 32, 641 – 655.

Neagu, R.C., Cartwright, J., Davies, R. and Jensen, L. 2010b. Fossilisation of a silica diagenesis reaction front on the mid – Norwegian margin. Marine and Petroleum Geology 27, 2141–2155.

Neagu, R.C., Volpi, V., Tinivella, U., Rebesco, M. and Camerlenghi, A. 2008. Estimation of biogenic silica contents in marine sediments using seismic and well log data: Sediment Drift 7, Antarctica. International Journal of Earth Sciences 98 (4), 839 – 848.

Neves, F.A., Zahrani, M.S. and Bremkamp, S.W. 2004. Detection of potential fractures and small faults using seismic attributes. The Leading Edge 23 (9), 903 – 906.

Nobes, D.C., Murray, R.W., Kuramoto, S., Pisciotto, K.A., and Holler, P. 1992. Impact of silica diagenesis on physical property variations. In Pisciotto, K.A., Ingle, J.C., Jr., von Breymann, M.T., Barron, J., et al., Proceedings of ODP, Scientific Results, 127/128 (Pt. 1): College Station, TX.

Nouzé, H., Cosquer, E., Collot, J., Foucher, J.P., Klingelhoefer, F., Lafoy, Y., Geli, L. 2009. Geophysical characterization of bottom simulating reflectors in the Fairway Basin (off New Caledonia, Southwest Pacific), based on high resolution seismic profiles and heat flow data. Marine Geology 266 (1 – 4), 80 – 90.

O

O'Brien, D.K., Manghnani, M. H., Schoonmaker – Tribble, J. 1989. Irregular trends of physical properties in homogeneous clay – rich sediments of DSDP Leg 87 Hole 584, midslope terrace in the Japan Trench. Marine Geology 87 (2 – 4), 183 – 194.

Osborne, M.J. and Swarbrick, R.E. 1997. Mechanisms for Generating Overpressure in Sedimentary Basins: A Reevaluation. AAPG Bulletin 81 (6), 1023 – 1041.

P

Parize, O. and Beaudoin, B. 1988. Clastic dykes and sills from Numidian flysch (Sicily and Tunisia): Sandy injection related to a high – density turbidity deposit. AAPG Bulletin 72 (8), 1018.

Peacock, D.C.P. and Zhang, X. 1994. Field examples and numerical modeling of oversteps and bends along normal faults in cross – section. Tectonophysics 234, 147 – 167.

Pearson. F.J. 1999. What is the porosity of a mudrock? In: Aplin, A.C., Fleet, A.J. & Macquaker, J.H.S. (eds) Muds and Mudstones: Physical and Fluid Flow Properties. Geological Society, London, Special Publications 158, 9 – 21.

Pegrum, R.M., Ødegård, T., Bonde, K. and Hamann, N.E. 2001. Exploration in the Fylla Area, SW Greenland. AAPG Regional Conference, St. Petersburg, Russia, July 15 – 18, 2001.

Peltonen, C., Marcussen, Ø., Bjørlykke, K. and Jahren, J. 2008. Mineralogical control on mudstone compaction: a study of Late Cretaceous to Early Tertiary mudstones of the Vøring and Møre basins, Norwegian Sea. Petroleum Geoscience 14(2), 127 – 138.

Peltonen, C., Marcussen, Ø., Bjørlykke, K. and Jahren, J. 2009. Clay mineral diagenesis and quartz cementation in mudstones: The effects of smectite to illite reaction on rock properties, Marine and Petroleum Geology 26 (6), 887 – 898.

Perrier R., Quiblier J. 1974. Thickness changes in sedimentary layers during compaction history: methods for quantitative evaluation, AAPG Bulletin 58 (3), 507 – 520.

Pisciotto, K.A. 1981. Distribution, thermal histories, isotopic compositions, and reflection characteristics of siliceous rocks recovered by the Deep Sea Drilling Project. In: Warme, J.E., Douglas, R.G., Winterer, E.L. (Eds.), The Deep Sea Drilling Project: A Decade of Progress. Society of Economic Paleontologists and Mineralogists Special Publication No. 32, 129 – 148.

Pisciotto, K.A., Murray, R.W., Brumsack, H.J., Tamaki, K., Ingle, J.C. 1992. Thermal History of Japan Sea Sediments from Isotopic Studies of Diagenetic Silica and Associated Pore Waters. In: Proc., Scientific Results, ODP, Legs 127/128, Japan – Sea, 49 – 56.

Pittenger, A., Taylor, E., and Bryant, W.R. 1989. The influence of biogenic silica on the geotechnical stratigraphy of the Vøring Plateau, Norwegian Sea. In: Eldholm, O., Thiede, J., Taylor, E., et al., Proceedings of. ODP, Scientific Results, 104: College Station, TX (Ocean Drilling Program), 923 – 940.

R

Redwine, L. 1981. Hypothesis combining dilation, natural hydraulic fracturing, and dolomitization to explain petroleum reservoirs in Monterey shale, Santa Maria area, California. In: Garrison, R.E and Douglas, R.G. (Eds.), The Monterey Formation and related siliceous rocks of California: Los Angeles, Pacific Section, Society of Economic Paleontologists and Mineralogists, 221 – 248.

Reemst, P., Skogseid, J. and Larsen, B.T. 1996. Base Pliocene velocity inversion on the eastern Vøring Margin – causes and implications. Global and Planetary Change 12, 201 – 211.

Rice, S.B., Freund, H., Huang, W.L., Clouse, J.A. and Isaacs, C.M. 1995. Application of Fourier Transform Infrared Spectroscopy to silica diagenesis: The opal – A to opal – CT transformation. Journal of Sedimentary Research A65, 639 – 647.

Riech, V. and von Rad, U. 1979. Silica diagenesis in the Atlantic Ocean: diagenetic potential and transformations. In: Talwani, M., Hay, W. and Ryan, W.B.F. (Eds.). Deep Drilling Results in the Atlantic Ocean: Continental Margins and Paleoenvironment, Maurice Ewing Series 3, American Geophysical Union, Washington, D.C., 315 – 340.

Rieke, H.H. and Chilingarian, C.V. 1974. Compaction of argillaceous sediments. Developments in Sedimentology 16, Elsevier, Amsterdam, p. 424.

Riis, F., Berg, K., Cartwright, J., Eidvin, T., Hansch, K. 2005. Formation of large, craterlike evacuation structures in ooze sediments in the Norwegian Sea. Possible

implications or the development of the Storegga Slide. Marine and Petroleum Geology 22, 257 – 273.

Roaldset, E. and He, W. 1995. Silica – phase Transformation of Opal – A to Opal – CT to Quartz – an Experimental Approach. Report. Department of Geology and Mineral Resources Engineering, Norwegian Institute of Technology, Trondheim.

Rokoengen, K. 1995. Upper Cenozoic stratigraphy on the mid – Norwegian continental shelf. Norsk Geologisk Tidsskrift 75 (2e3), 88 – 104.

Rundberg, Y. 1989. Tertiary and Sedimentary History and Basin Evolution of the Norwegian North Sea between 60°N and 62°N. An Integrated Approach. PhD thesis, Norwegian Institute of Technology, Trondheim.

S

Scheck – Wenderoth, M., Raum, T., Faleide, J.I., Mjelde, R., Horsfield, B. 2007. The transition from the continent to the ocean: a deeper view on the Norwegian margin. Journal of the Geological Society, London, 164, 855 – 868.

Schöpfer M.P.J., Childs, C., Walsh J., Manzocchi, T., Koyi, H. 2007. Geometrical analysis of the refraction and segmentation of normal faults in periodically layered sequences. Journal of Structural Geology 29, 318 – 335.

Shelton, J. W. 1984. Listric normal faults: an illustrated summary. AAPG Bulletin 68 (7), 801 – 815.

Sheriff, R.E. and Geldart, L.P. 1995. Exploration Seismology, Vol. 2, Cambridge University Press, Great Britain, 628 p.

Shin, H., Santamarina, J.C., Cartwright, J. A. 2008. Contraction – driven shear failure in compacting uncemented sediments, Geology 36, 931 – 934.

Sibson, R.H. 2000. Fluid involvement in normal faulting. Journal of Geodynamics 29, 469 – 499.

Skempton, A. 1981. Landmarks in early soil mechanics', Proceedings of the 7th European Conference on Soil Mechanics and Foundation Engineering 5, 1 – 26.

Skogseid, J., Eldholm, O. 1989. Vøring Plateau Continental Margin: seismic interpretation, stratigraphy, and vertical movements. In: Proceedings of the Ocean Drilling Program, Scientific Results, Vol. 104, 993 – 1030.

Skogseid, J., Pedersen, T. and Larsen, V.B. 1992. Vøring Basin: subsidence and tectonic evolution. In: Larsen, R., Brekke, M., Larsen, B.T. and Talleraas, E., Editors, 1992. Structural and Tectonic Modelling and its Application to Petroleum Geology. Norway Petroleum Society Vol. 1, Elsevier, Amsterdam, 55 – 82.

Spencer, A.M., Birkeland, Ø., Knag, G. Ø. et al. 1999. Petroleum systems of the Atlantic margin of northwest Europe. Petroleum Geology Conference series 5, 231 – 246.

Spinelli, G.A., Giambalvo, E.R. and Fisher, A.T. 2004. Sediment permeability, distribution, and influence on fluxes in oceanic basement. In Hydrogeology of the Oceanic Lithosphere. Davis, E.E. and Elderfield, H (eds.). Cambridge University Press, 151 – 188.

Stuevold, L.M., Faerseth, R.B., Arnesen, L., Cartwright, J., Möller, N. 2003. Polygonal faults in the Ormen Lange Field, Møre Basin, offshore Mid Norway. Geological Society Special Publications 216, 263 – 281.

T

Tada, R. 1991. Compaction and cementation in siliceous rocks and their possible effect on bedding enhancement. Cycles and Events in Stratigraphy, 480 – 491.

Tamaki, K., Pisciotto, K., Allen, J., et al. 1990. Proceedings of the Ocean Drilling Program, Initial Reports, Vol. 127. College Station, TX (Ocean Drilling Program). doi:10.2973/odp.proc.ir.127.1990

Terzaghi, K., and Peck, R.B. 1948. Soil Mechanics in Engineering Practice, John Wiley and Sons, New York.

Thein, J. and von Rad, U. 1987. Silica Diagenesis in Continental Slope and Rise Sediments off Eastern North America (Sites 603 and 605, Leg 93; Sites 612 and 613, Leg 95). In: Poag, C.W., Watts, A.B. et al. Init. Rep. DSDP, 95, 501 – 525.

Twiss, R. J. and Moores, E. M. 1992. Structural Geology. W. H. Freeman and Company, New York, 532 p.

V

Velde, B. 1996. Compaction trends of clay – rich deep sea sediments. Marine Geology 133, 193 – 201.

Volpi, V., Camerlenghi, A., Hillenbrand, C.D., Rebesco, M., Ivaldi, R. 2003. Effects of biogenic silica on sediment compaction and slope stability on the Pacific margin of the Antarctic Peninsula. Basin Research 15 (3), 339 – 363.

von Rad, U., Riech, V. and Rösch, H. 1978. Silica diagenesis in continental margin sediments off Northwest Africa. DSDP Initial Reports, Vol. 41.

W

Walsh, J. and Watterson, J. 1987. Displacement Efficiency of Faults and Fractures: Discussion. Journal of Structural Geology 9 (8), 1051 – 1052.

Warme, J.E., Douglas, R.G. and Winterer, E.L. (eds.). 1981. The Deep Sea Drilling Project: A Decade of Progress. Society of Economic Paleontologists and Mineralogists Special Publication No. 32. Tulsa, Oklahoma, U.S.A.

Watterson, J., Walsh, J., Nicol, A., Nell, P.A.R., Bretan, P. G. 2000. Geometry and origin of a polygonal fault system. Journal of the Geological Society 157 (1), 151 – 162.

Williams, L.A. and Crerar, D.A. 1985. Silica diagenesis: II. General mechanisms. Journal of Sedimentary Petrology 55 (3), 312 – 321.

Williams, L.A., Parks, G.A., Crerar, D.A. 1985. Silica diagenesis: I. Solubility controls. Journal of Sedimentary Petrology 55 (3), 301 – 311.

X

Xiao, H.B. and Suppe, J. 1989. Role of Compaction in Listric Shape of Growth Normal Faults, AAPG Bulletin 73 (6), 777 – 786.

Y

Yeats, R.S., Haq, B.U. and Pisciotto, K.A. 1981. Deep Sea Drilling Project 63 Initial Reports.

Yilmaz, O. 2001. Seismic Data Analysis (Investigations in Geophysics No. 10), Society Of Exploration Geophysicists (2 volumes), p. 2027.

Z

Zimmerman, H.B., Supko, P.R., McCoy, F.W. 1979. Acoustic horizons in the Argentine Basin, southwestern Atlantic Ocean: new evidence from deep – sea drilling. Geology 7 (1): 45 – 48.

APPENDICES

Appendix A1 (additional data – Chapter 4)

A1.1. Summary statistics for the data presented in Fig. 4.3.

a. Bulk density - Clay

	opal-A	opal-CT
Mean	1.57	1.84
Standard Error	0.04	0.03
Median	1.55	1.80
Mode	1.70	1.80
Standard Deviation	0.16	0.12
Sample Variance	0.03	0.02
Kurtosis	-0.74	-0.92
Skewness	0.20	0.37
Range	0.58	0.40
Minimum	1.27	1.65
Maximum	1.85	2.05
Sum	31.42	36.75
Count	20.00	20.00

e. Bulk density - Carbonates

	opal-A	opal-CT
Mean	1.53	1.75
Standard Error	0.05	0.07
Median	1.55	1.73
Mode	1.55	1.70
Standard Deviation	0.18	0.23
Sample Variance	0.03	0.05
Kurtosis	0.56	0.16
Skewness	0.46	0.09
Range	0.65	0.83
Minimum	1.25	1.35
Maximum	1.90	2.18
Sum	19.90	21.03
Count	13.00	12.00

b. Porosity - Clay

	opal-A	opal-CT
Mean	70.58	54.83
Standard Error	2.54	2.73
Median	70.00	56.00
Mode	70.00	55.00
Standard Deviation	11.08	11.60
Sample Variance	122.81	134.50
Kurtosis	1.83	3.82
Skewness	-1.12	-1.57
Range	45.00	50.00
Minimum	40.00	20.00
Maximum	85.00	70.00
Sum	1341.00	987.00
Count	19.00	18.00

f. Porosity - Carbonates

	opal-A	opal-CT
Mean	67.92	53.75
Standard Error	2.73	3.79
Median	65.00	54.00
Mode	60.00	55.00
Standard Deviation	9.44	13.12
Sample Variance	89.17	172.20
Kurtosis	-1.30	-0.07
Skewness	0.44	0.06
Range	28.00	47.00
Minimum	55.00	30.00
Maximum	83.00	77.00
Sum	815.00	645.00
Count	12.00	12.00

c. Velocity - Clay

	opal-A	opal-CT
Mean	1.79	1.94
Standard Error	0.05	0.06
Median	1.73	1.90
Mode	1.70	1.90
Standard Deviation	0.19	0.24
Sample Variance	0.03	0.06
Kurtosis	3.94	0.83
Skewness	1.82	1.05
Range	0.70	0.85
Minimum	1.60	1.65
Maximum	2.30	2.50
Sum	25.00	29.15
Count	14.00	15.00

g. Velocity - Carbonates

	opal-A	opal-CT
Mean	1.66	1.79
Standard Error	0.04	0.04
Median	1.70	1.85
Mode	1.75	1.90
Standard Deviation	0.13	0.13
Sample Variance	0.02	0.02
Kurtosis	-1.58	-0.23
Skewness	0.03	-1.04
Range	0.35	0.35
Minimum	1.50	1.55
Maximum	1.85	1.90
Sum	18.22	19.65
Count	11.00	11.00

d. Resistivity - Clay

	opal-A	opal-CT
Mean	0.59	0.87
Standard Error	0.08	0.15
Median	0.55	0.70
Mode	0.40	0.60
Standard Deviation	0.28	0.49
Sample Variance	0.08	0.24
Kurtosis	-0.93	-0.11
Skewness	0.33	0.83
Range	0.83	1.63
Minimum	0.17	0.17
Maximum	1.00	1.80
Sum	6.47	9.52
Count	11.00	11.00

h. Resistivity - Carbonates

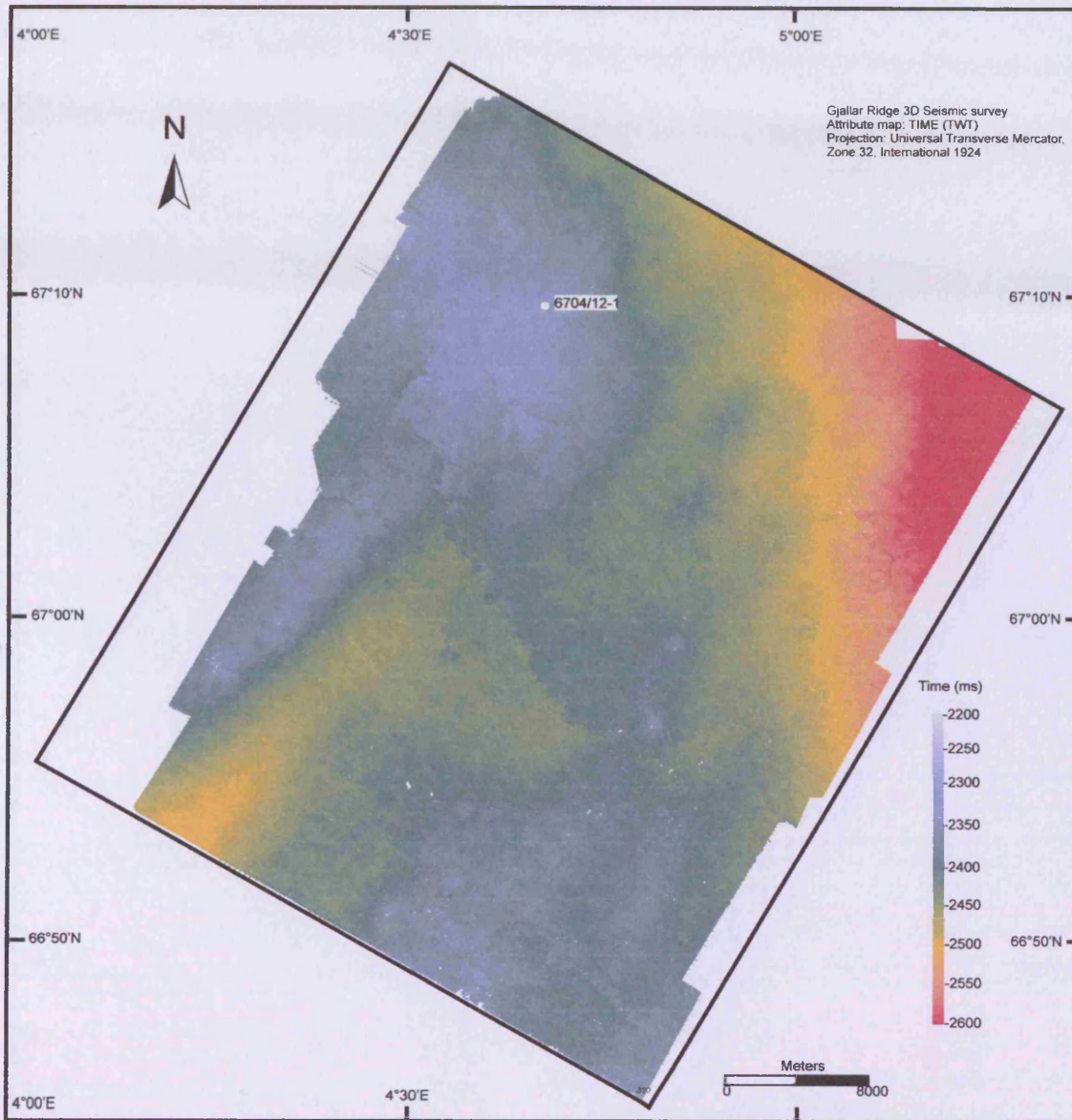|	opal-A	opal-CT
Mean	0.62	0.92
Standard Error	0.06	0.15
Median	0.55	0.80
Mode	0.55	0.90
Standard Deviation	0.19	0.45
Sample Variance	0.03	0.20
Kurtosis	1.03	4.80
Skewness	1.08	2.05
Range	0.60	1.50
Minimum	0.40	0.50
Maximum	1.00	2.00
Sum	5.60	8.25
Count	9.00	9.00

Appendix A1 Digital Files

Located on the attached CD:

A1.1. Spreadsheet with data used for the analysis in Chapter 4. The file also contains digital plots, some previously shown in Chapter 4.

A.1.2. Additional spreadsheet with data used for the analysis in Chapter 4. The ODP sites have been classified according to their dominant lithological type (either clay or carbonates). The file also contains digital plots, some shown in Chapter 4.
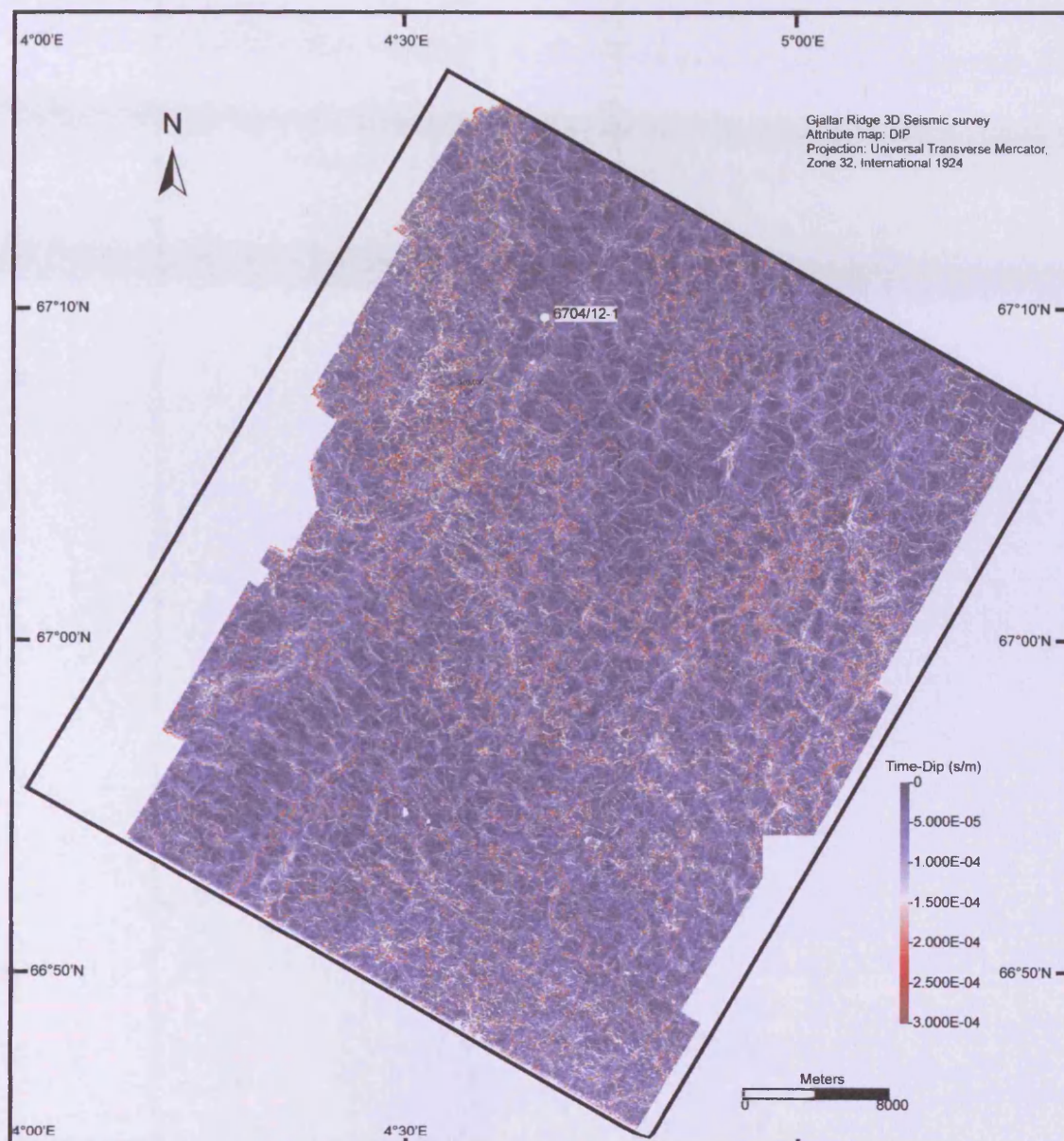
Appendix A2 (additional data – Chapter 5)

A2.1. Two — way travel time map (ms) of the opal — A to opal — CT horizon in the Gjallar 3 — D survey. Location of the survey is shown in Fig. 2.1. Exploration well 6704/12-1 is also shown.
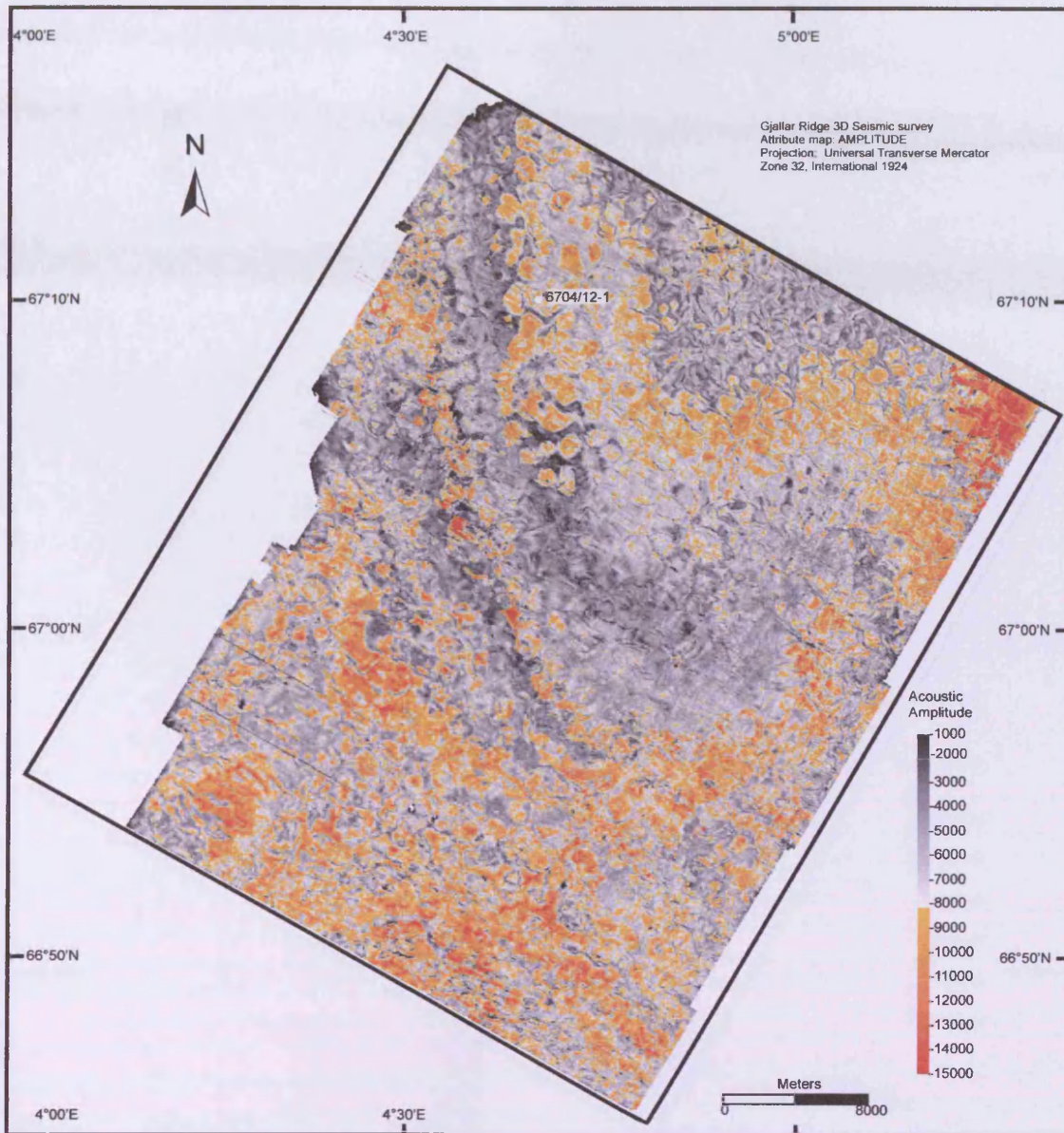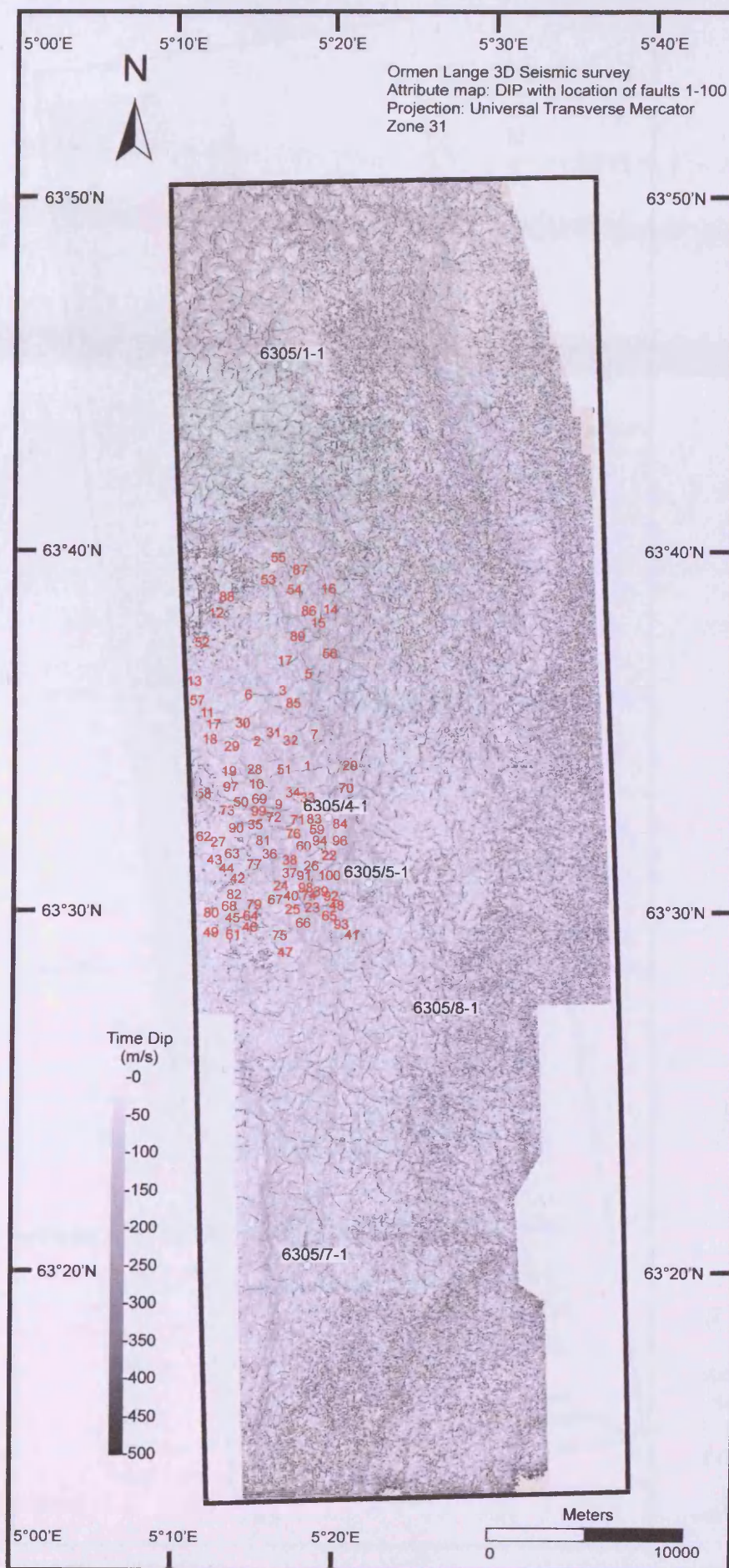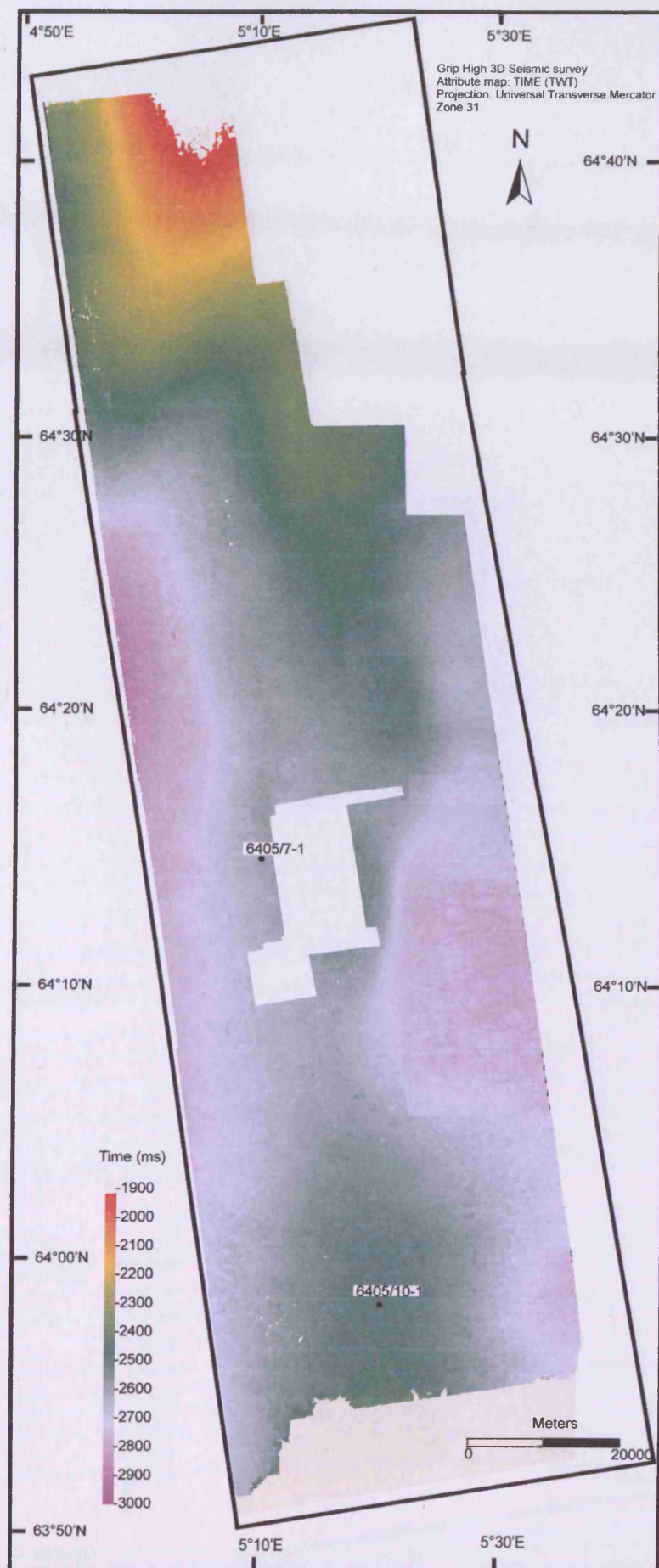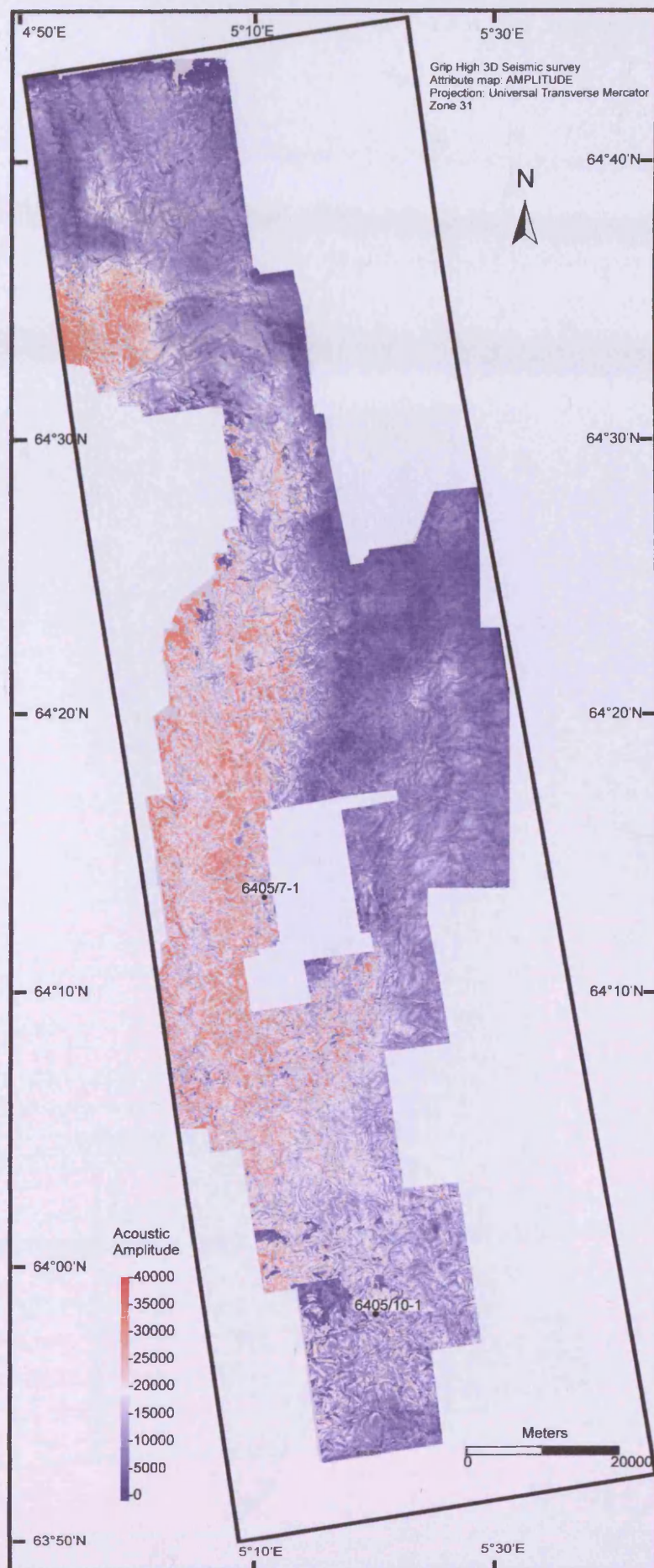
A2.2. Acoustic amplitude map of the opal — A to opal — CT horizon in the Gjallar 3 — D survey. Location of the survey is shown in Fig. 2.1. Exploration well 6704/12-1 is also shown.

A2.3. Dip map of the opal — A to opal — CT horizon in the Gjallar 3 — D survey. Location of the survey is shown in Fig. 2.1. Exploration well 6704/12-1 is also shown.
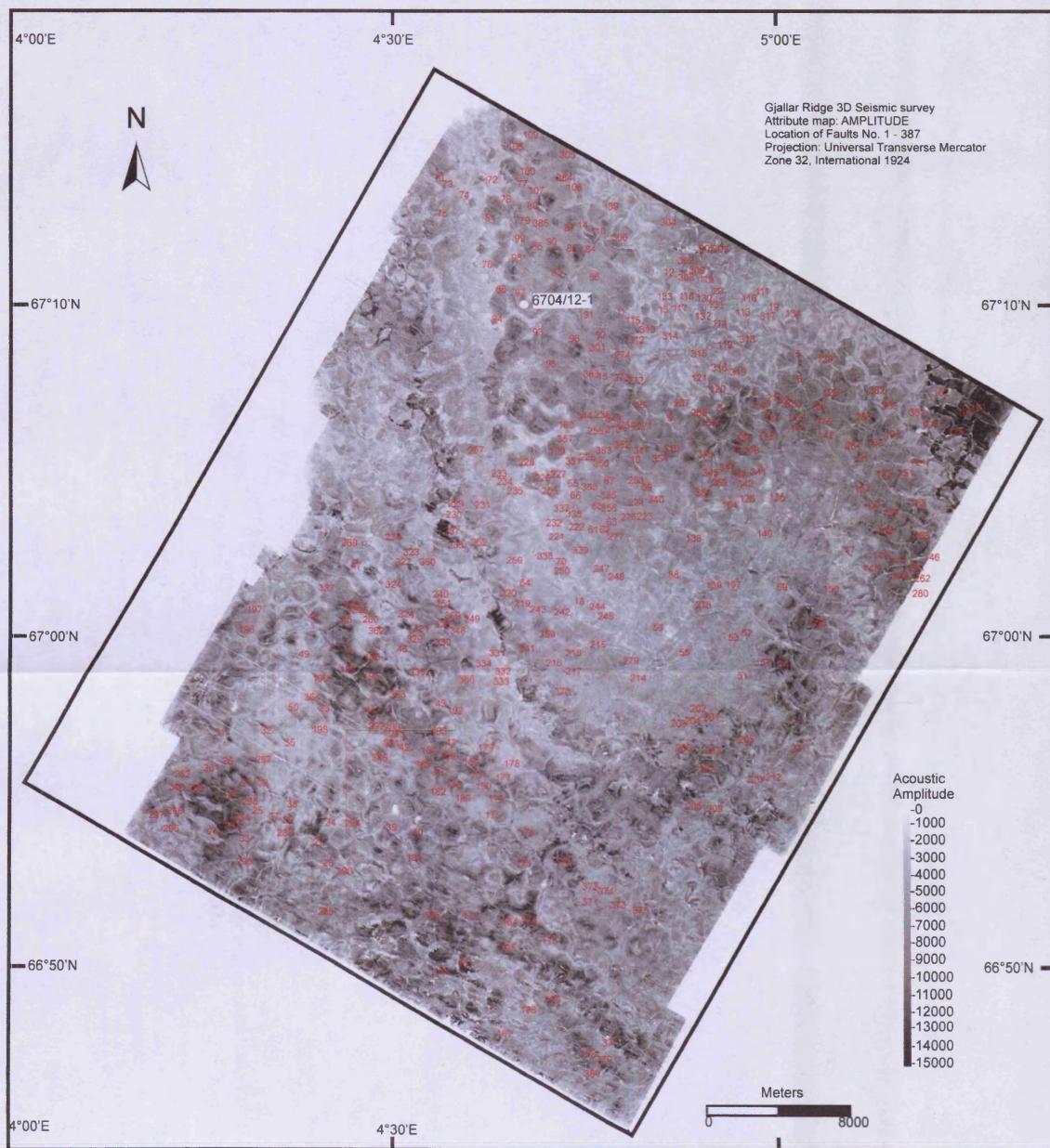
A2.4. Amplitude map of the opal — A to opal — CT horizon in the Gjallar 3 — D survey with the location of faults 1 to 387. Location of the survey is shown in Fig. 2.1. Exploration well 6704/12-1 is also shown.

Ormen Lange 3D Seismic survey
Attribute map: TIME (TWT)
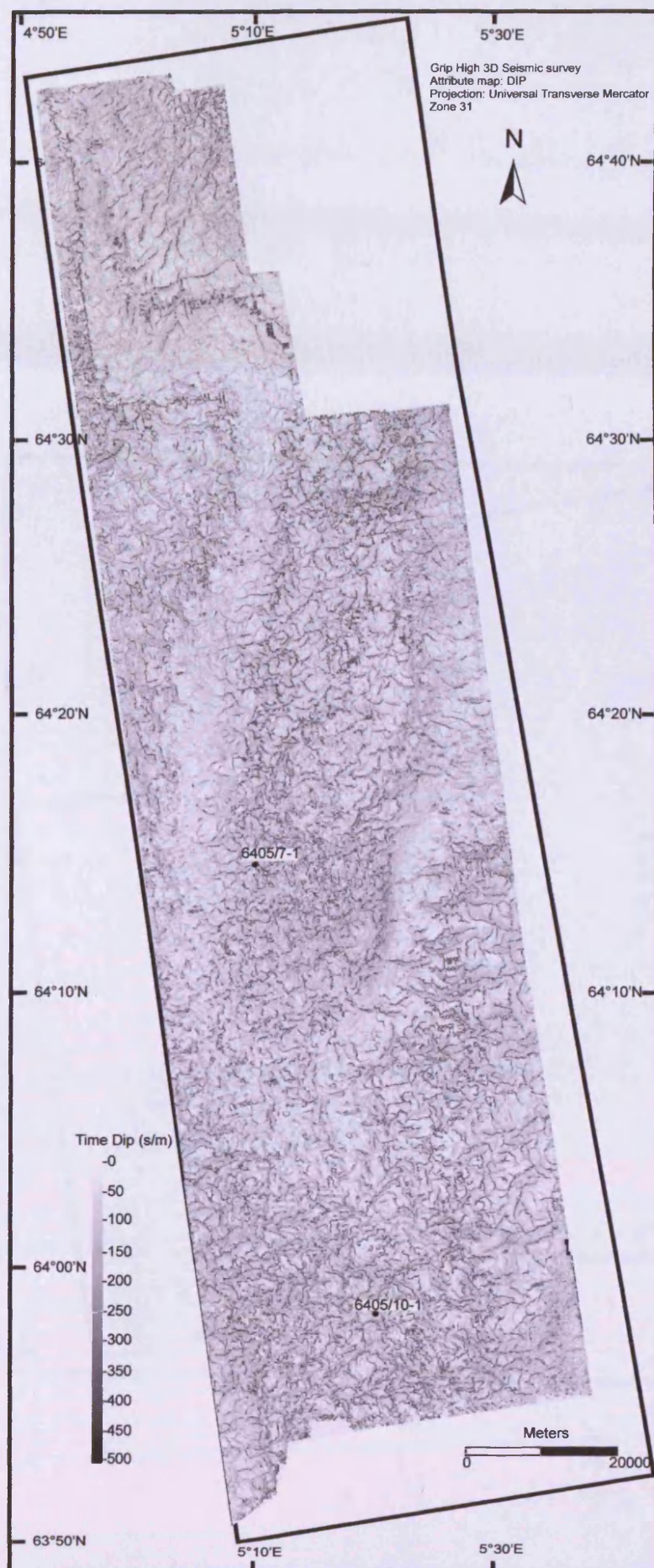Projection: Universal Transverse Mercator
Zone 31
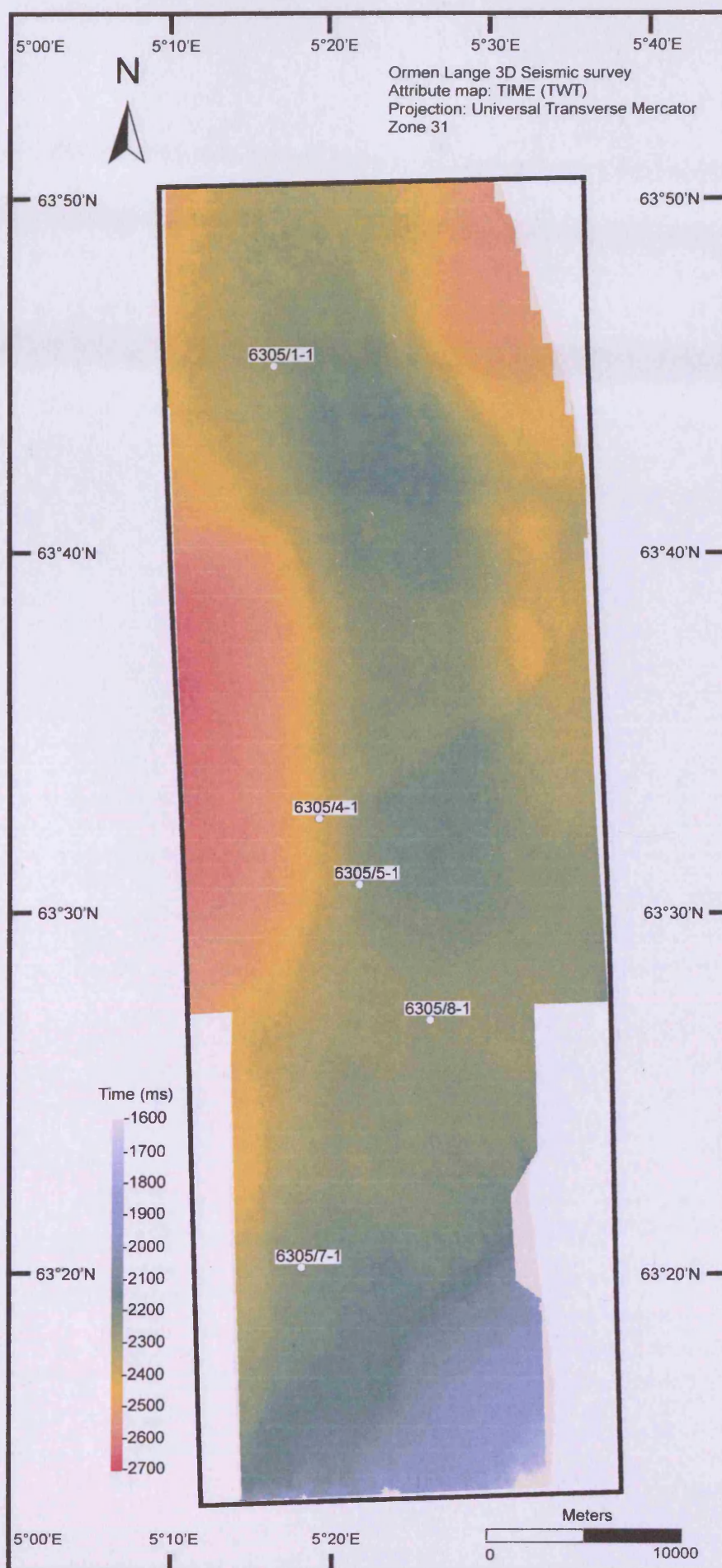
A2.5. Two — way travel time (ms) of the opal — A to opal — CT horizon in the Ormen Lange 3 — D survey. Location of the survey is shown in Fig. 2.1. Exploration wells in the area are also shown.
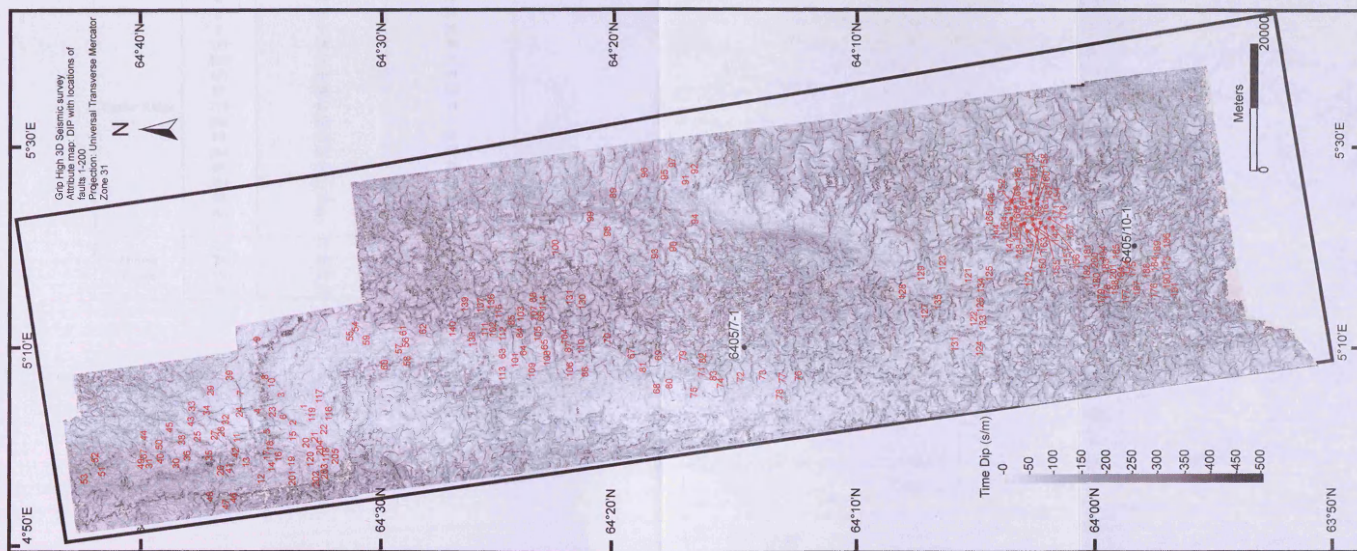
Ormen Lange 3D Seismic survey
Attribute map: AMPLITUDE
Projection: Universal Transverse Mercator
Zone 31

A2.6. Seismic amplitude map of the opal — A to opal — CT horizon in the Ormen Lange 3— D survey. Location of the survey is shown in Fig. 2.1. Exploration wells in the area are also shown.

Ormen Lange 3D Seismic survey
Attribute map: DIP
Projection: Universal Transverse Mercator
Zone 31

A2.7. Dip map of the opal — A to opal — CT horizon in the Ormen Lange 3 — D survey. Location of the survey is shown in Fig. 2.1. Exploration wells in the area are also shown.

230
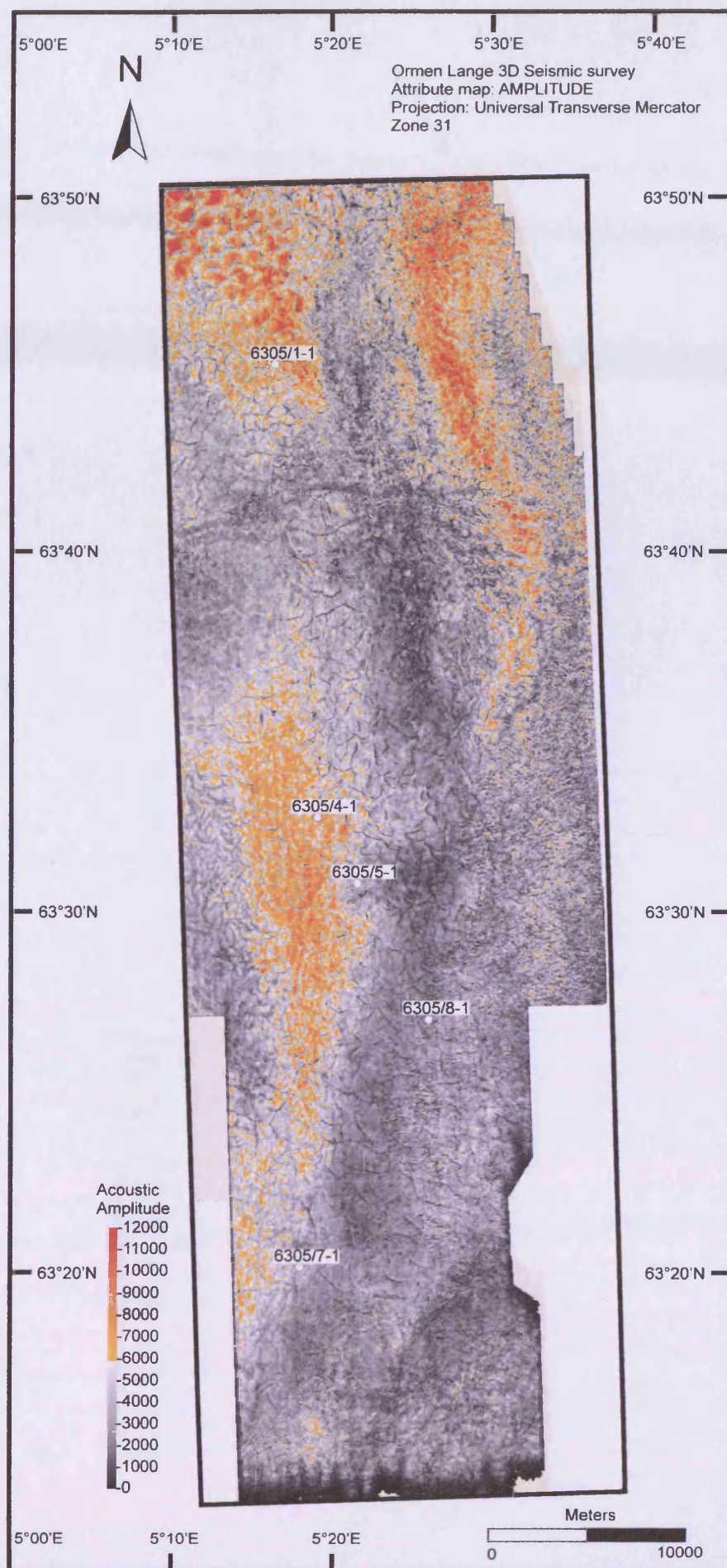
Ormen Lange 3D Seismic survey
Attribute map: DIP with location of faults 1-100
Projection: Universal Transverse Mercator
Zone 31
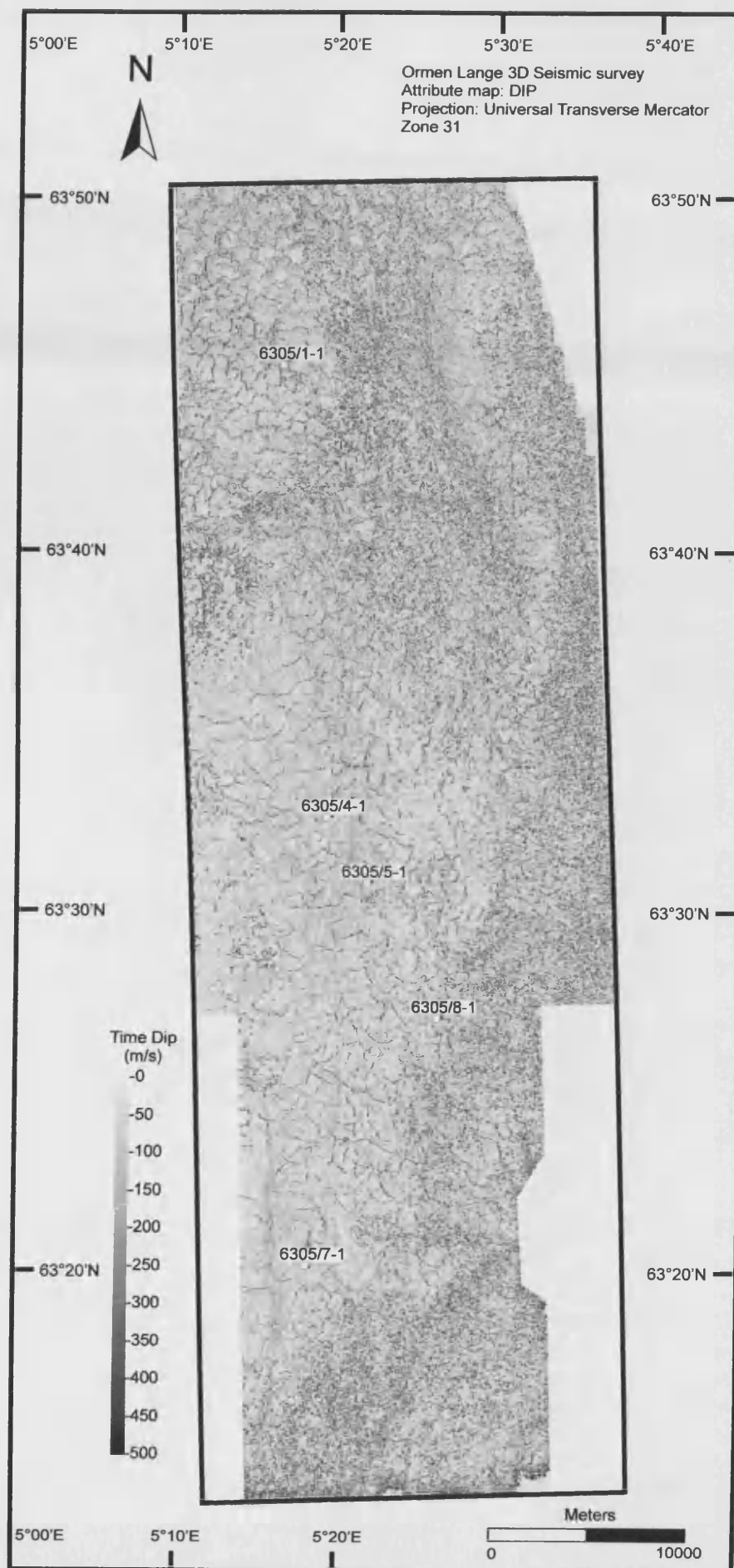
A2.8. Dip map of the opal — A to opal — CT horizon in the Ormen Lange 3 — D survey with the location of faults 1 to 100. Location of the survey is shown in Fig. 2.1. Exploration wells in the area are also shown.

Grip High 3D Seismic survey
Attribute map: TIME (TWT)
Projection: Universal Transverse Mercator
Zone 31

N

6405/7-1

Time (ms)

-1900
-2000
-2100
-2200
-2300
-2400
-2500
-2600
-2700
-2800
-2900
-3000

6405/10-

Meters
0   20000

A2.9. Two — way travel time (ms) map of the opal — A to opal — CT horizon in the Grip High 3 — D survey. Location of the survey is shown in Fig. 2.1. Exploration wells in the area are also shown.

232

A2.10. Amplitude map of the opal — A to opal — CT horizon in the Grip High 3 — D survey. Location of the survey is shown in Fig. 2.1. Exploration wells in the area are also shown.

233

Grip High 3D Seismic survey
Attribute map: DIP
Projection: Universal Transverse Mercator
Zone 31

N

A2.11. Dip map of the opal — A to opal — CT horizon in the Grip High 3 — D survey. Location of the survey is shown in Fig. 2.1. Exploration wells in the area are also shown.

234

Grip High 3D Seismic survey
Attribute map: DIP with locations of
faults 1-200
Projection: Universal Transverse Mercator
Zone 31

N

Time Dip (s/m)

-0
-50
-100
-150
-200
-250
-300
-350
-400
-450
-500

Meters

0   20000

A2.12. Dip map of the opal — A to opal — CT horizon in the Grip High 3 — D survey with the location of faults 1 to 205. Location of the survey is shown in Fig. 2.1. Exploration wells in the area are also shown.

A2.13. Estimated percentage of throw accumulated on the adjacent stratigraphic markers (above and below the A/CT reflection) after the diagenesis ceased for selected faults from the Gjallar and Ormen Lange areas. The values were calculated using the formula:

$$T_{ab} = \frac{T_{ab} - T_{A/CT}}{T_{ab}} \times 100$$, where T_{ab} is the throw on the stratigraphic marker adjacent to the

A/CT reflection (either above or below it) and $T_{A/CT}$ is the throw on the A/CT reflection. Digital data are presented in Appendices A2.14.1 and A2.14.2

Survey area	Fault no.	Percentage of throw (%)	
		Stratigraphic marker above A/CT	Stratigraphic marker below A/CT
Gjallar Ridge	8	19	35
	6	31	31
	5	0	35
	117	74	70
	129	54	33
	147	50	39
	87	58	62
	219	43	33
	246	20	0
	68	53	56
	344	63	57
	69	60	71
	301	25	45
	88	33	50
	309	22	53
Ormen Lange	21	13	28
	24	39	26
	59	17	33
	76	53	27

Appendix A2 Digital Files

Located on the attached CD:

A2.14.1. Spreadsheet containing Gjallar data

A2.14.2. Spreadsheet containing Ormen Lange data

A2.15. Spreadsheet with data related to selected faults from the three seismic surveys. Includes various plots, some presented in Chapter 5.

A2.16. Spreadsheet with data used to build the plot in Fig. 5.12. The plot shows the dip variation with normalised depth for a selection of faults that occur in the interval above the A/CT reflection in the Gjallar 3 – D survey.

A.2.17. Spreadsheet with the data used to build throw versus depth plots for a selection of faults from the three study areas. Includes a selection of plots, including those presented in Fig. 5.4.

Appendix A3 (additional data – Chapter 6)

A3.1. Interpolation parameters used for creating the grids on which the contour maps in Figs. 6.2, 6.6, 6.9, 6.10 and 6.13 are based on.

Marker horizon	Cell size for the TWT grid	Cell size for the isochron with the A/CT grid
Opal – A/CT	4400×4400	4500×4500 * *Isochron with present – day seabed
Top Kai Province 1	1400×1400	1400×1400
Top Kai Province 3	1300×1300	1400×1400
Reflection "N"	1500×1500	1400×1400
Reflection "R"	1400×1400	2500×2500

A3.2. The values of the thickness of the Naust, Kai and Brygge formations at different common deep points (CDP) along the seismic line presented in Fig. 6.7 used to build the burial history plot in Fig. 6.15a. The unconformities in the Naust Formation were not included in the plots because of the lack of data regarding the thickness and age of the missing sections.

Marker	CDP 250	CDP 2500	CDP 4000	CDP 5000	CDP 6500	CDP 8350	Age (Ma)
Seabed	1807	1260	1937	1447	1066	1318	0
Kai	1152	605	1418	936	727	1030	3.6
Brygge	835	605	857	425	554	796	23.8
Tare	0	0	0	0	0	0	55

A3.3. The values of the thickness of several selected markers at different common deep points (CDP) along the seismic line kfw98-127 used to build the burial history plot in Fig. 6.15b.

Marker	CDP 300	CDP 900	CDP 2250	Age (Ma)
Seabed	1872	1664	496	0
Kai	2440	2280	1216	3.6
Brygge	2848	2392	1648	23.8
A/CT	3072	2624	2250	55
Tare	3720	3120	3000	34
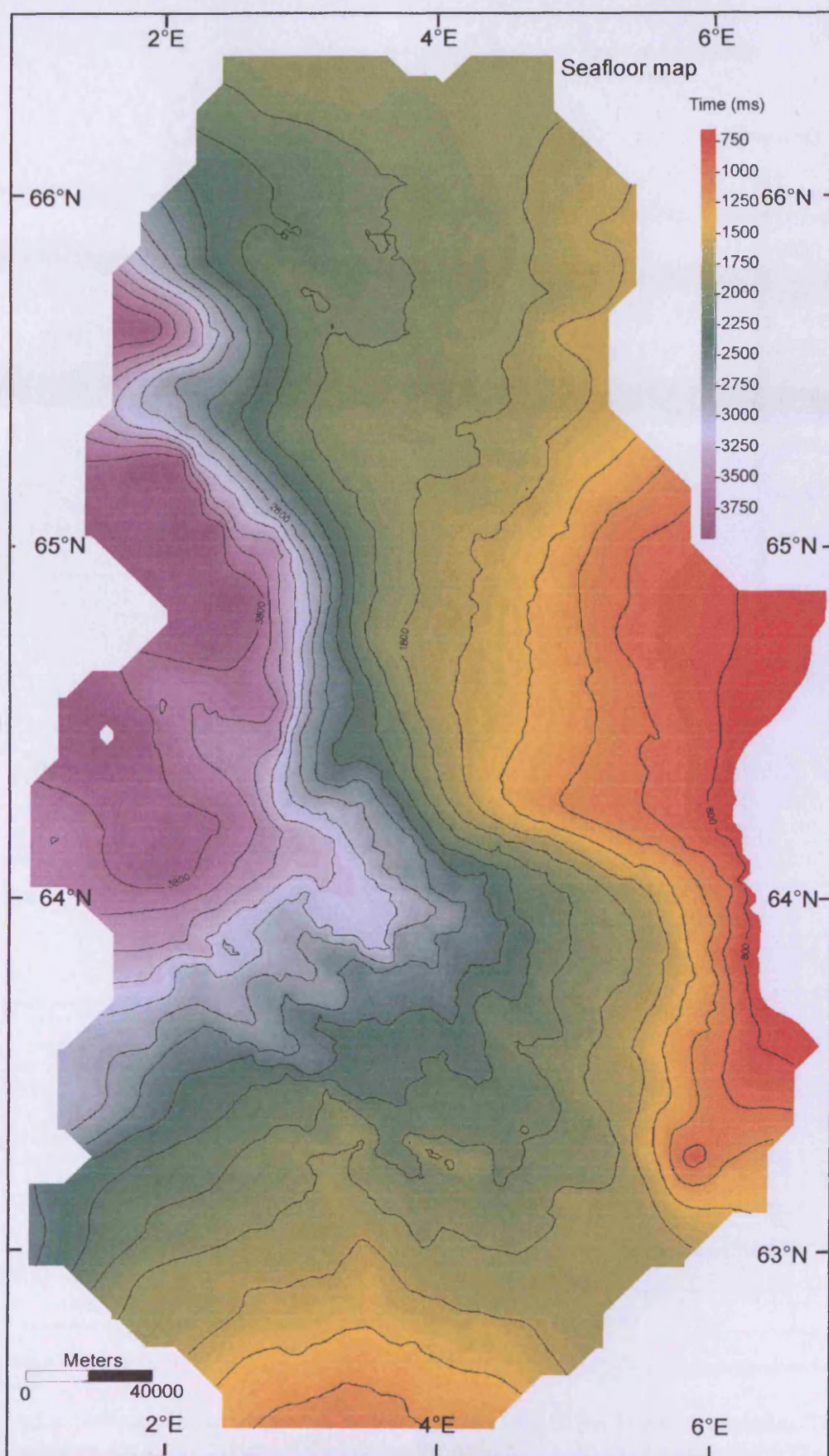
A3.4. Map of the two — way travel time (ms) of the seafloor reflection over the study area in Fig. 6.1. The map is based on interpolation of a grid of 2 – D seismic lines. The contour interval is 200 ms.

241
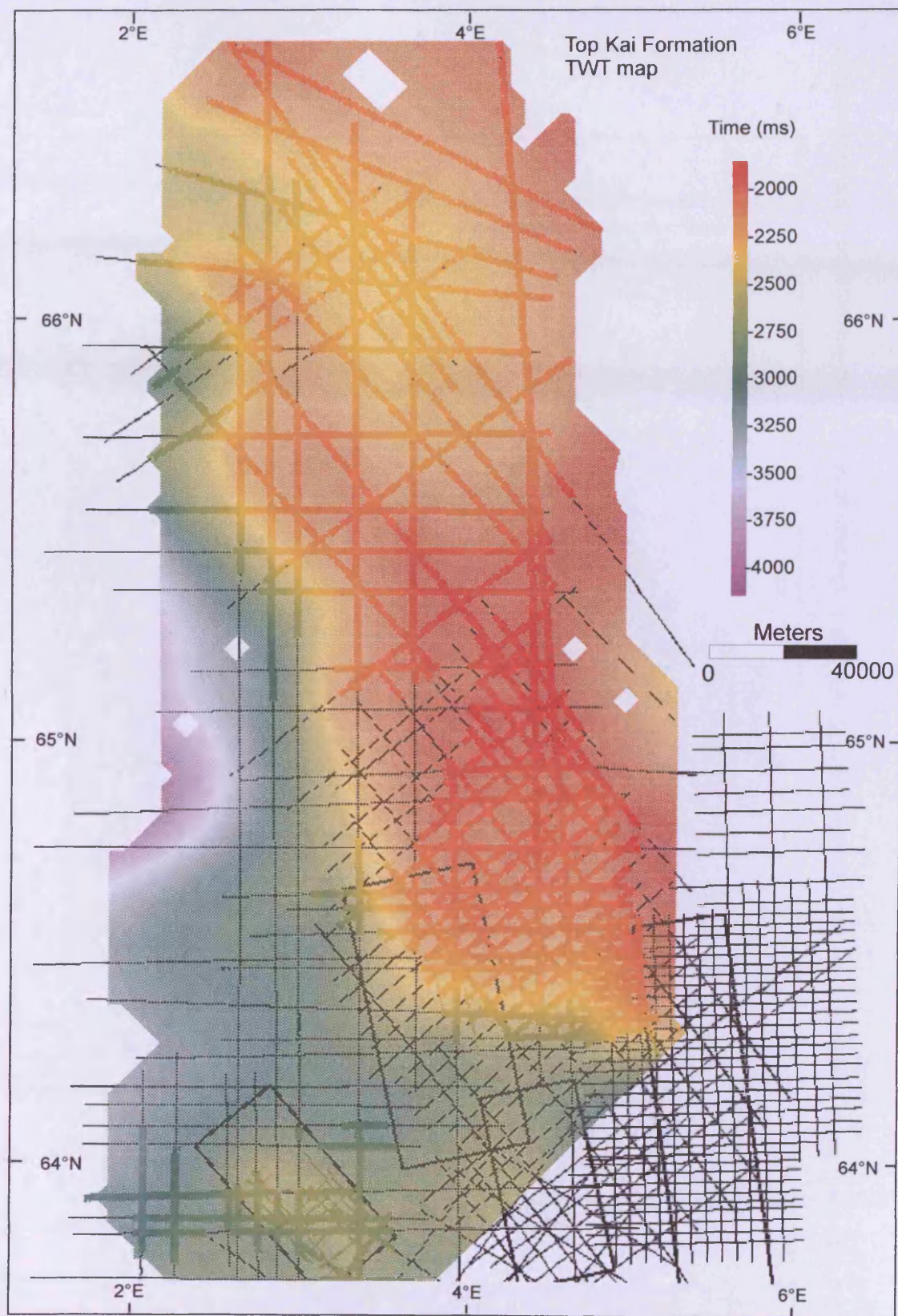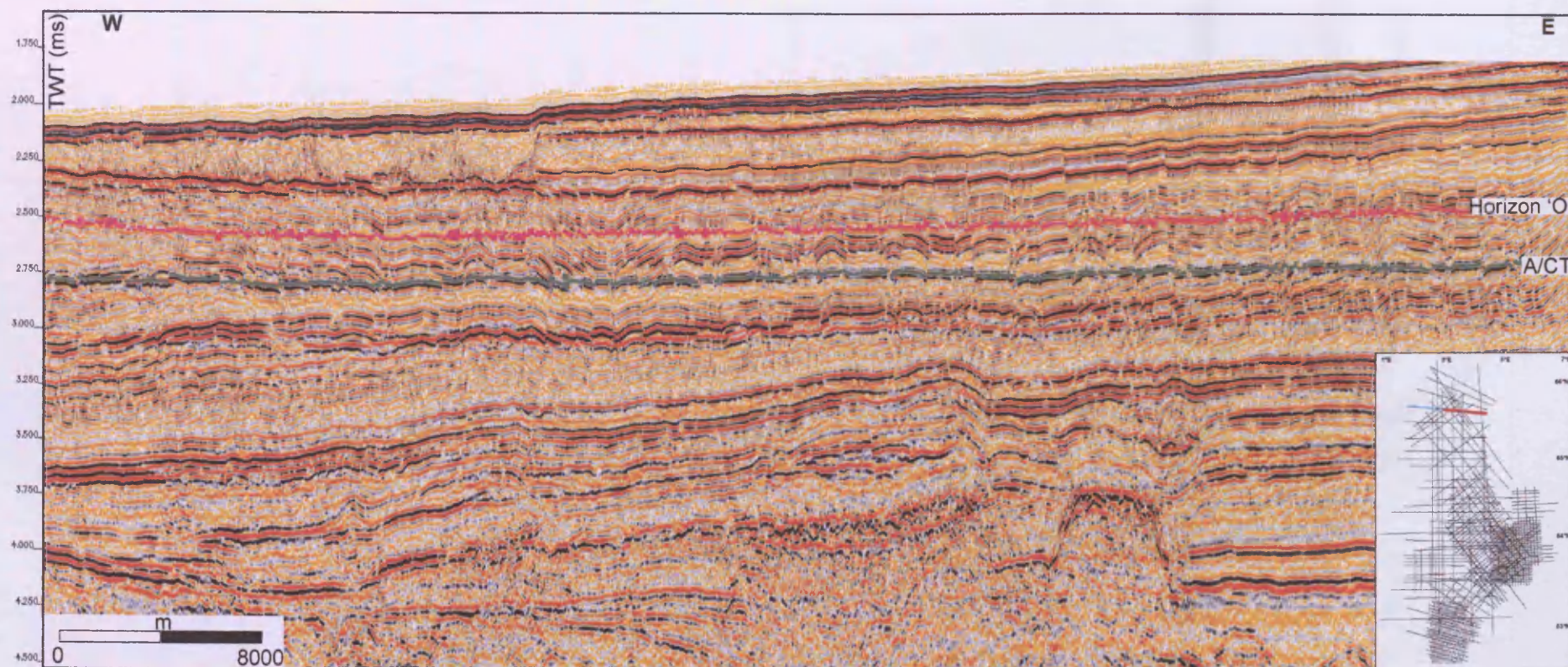
A3.5. Surface map of the two — way travel time (ms) of the Top Kai reflection. The map is based on the interpolation of the interpreted reflection TWT over a grid of 2 – D seismic lines.
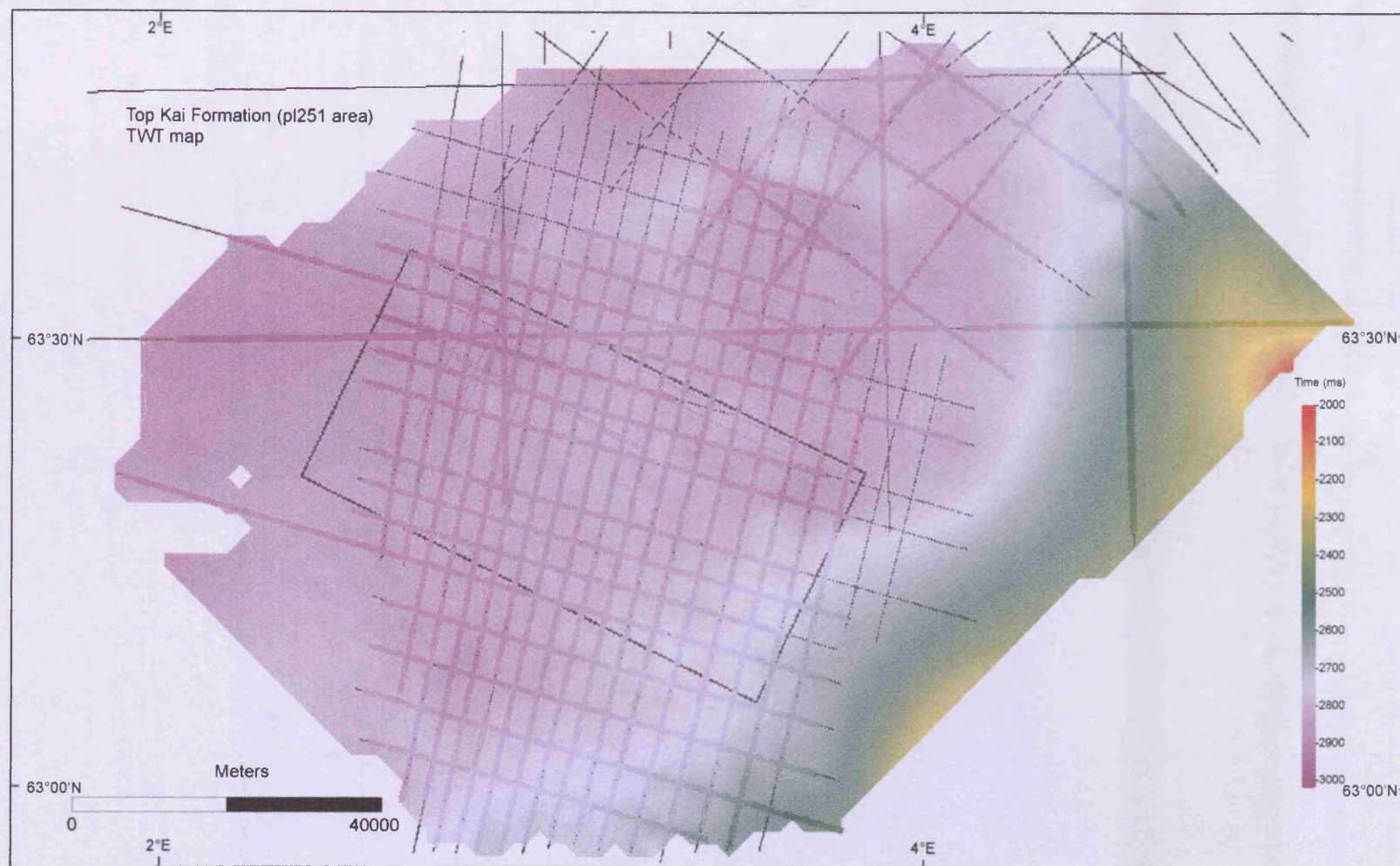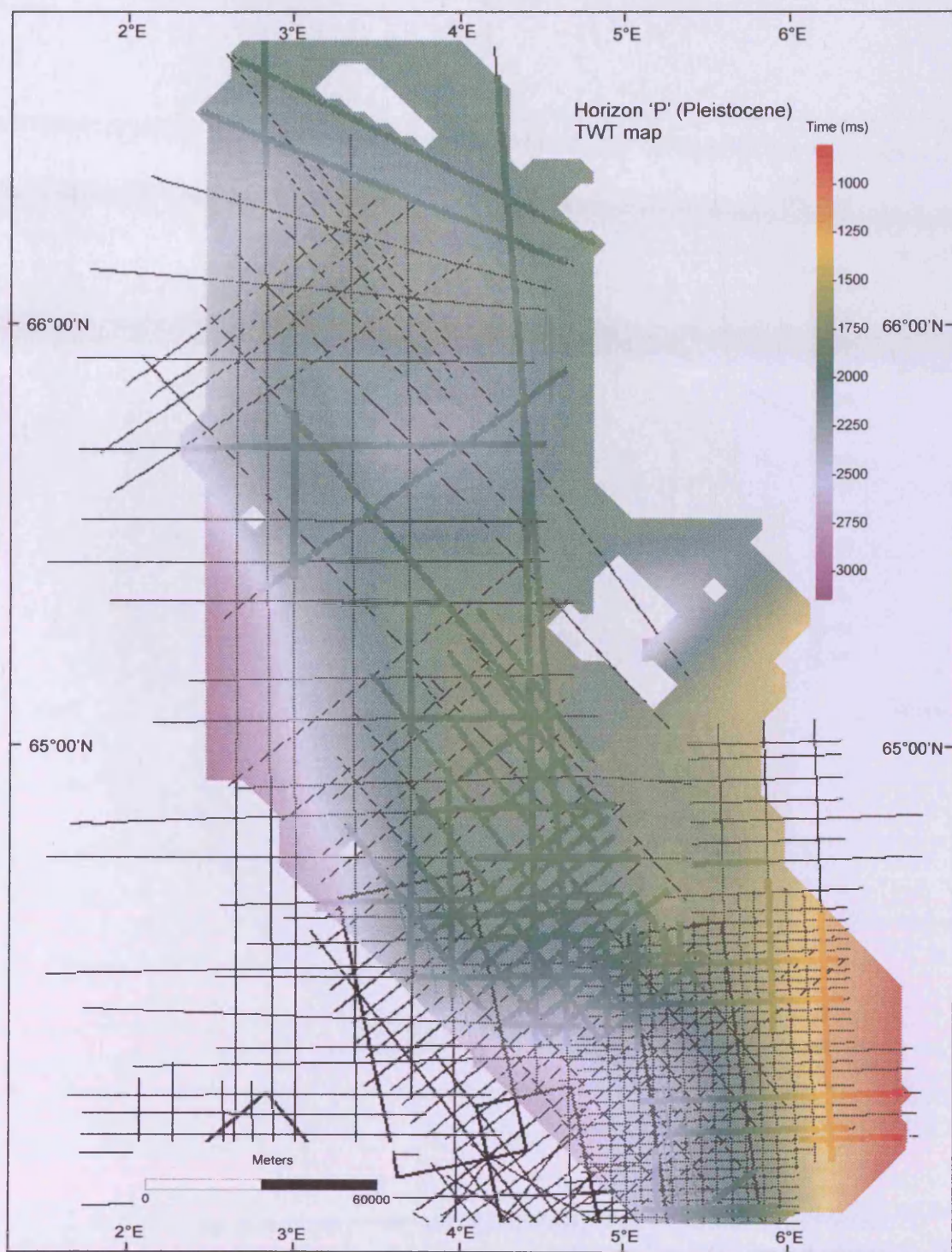
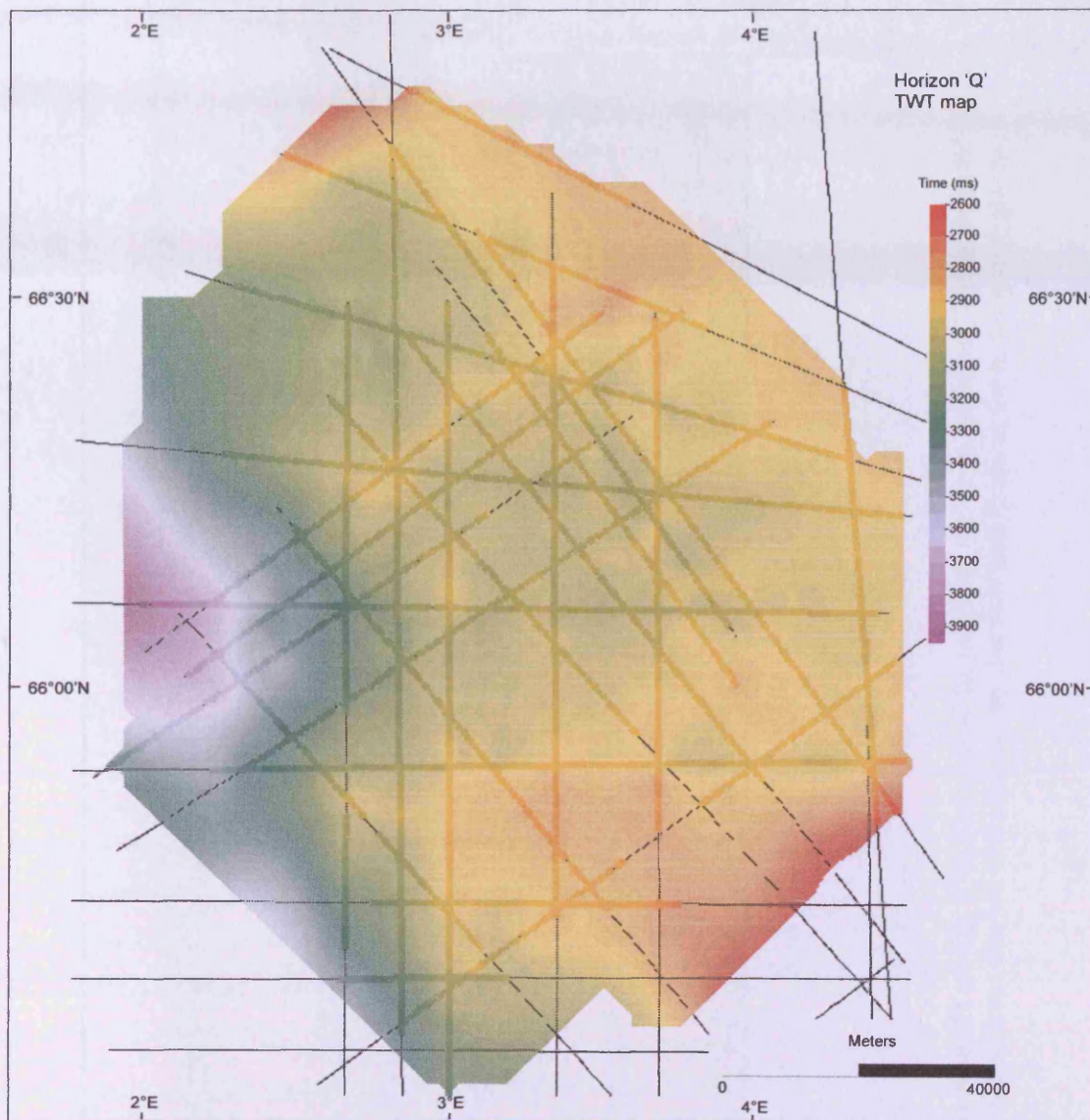A3.6. Surface map of the two — way travel time (ms) of the Top Kai reflection in P3 of Fig. 6.1. The map is based on the interpolation of the interpreted reflection TWT over a grid of 2 – D seismic lines.
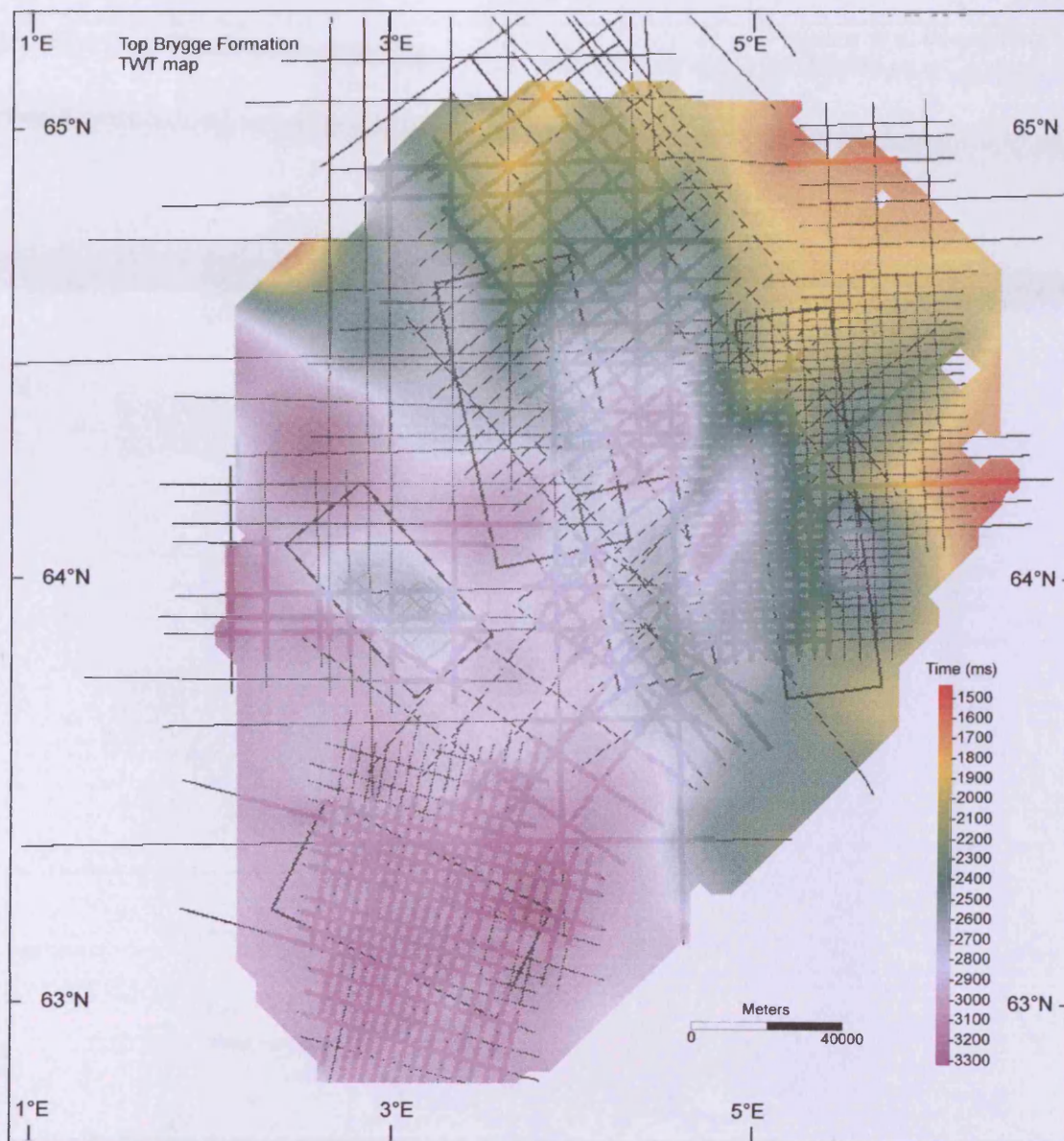
A3.7. Surface map of the two — way travel time (ms) of the Top Brygge reflection. The map is based on the interpolation of the interpreted reflection TWT over a grid of 2 – D seismic lines.
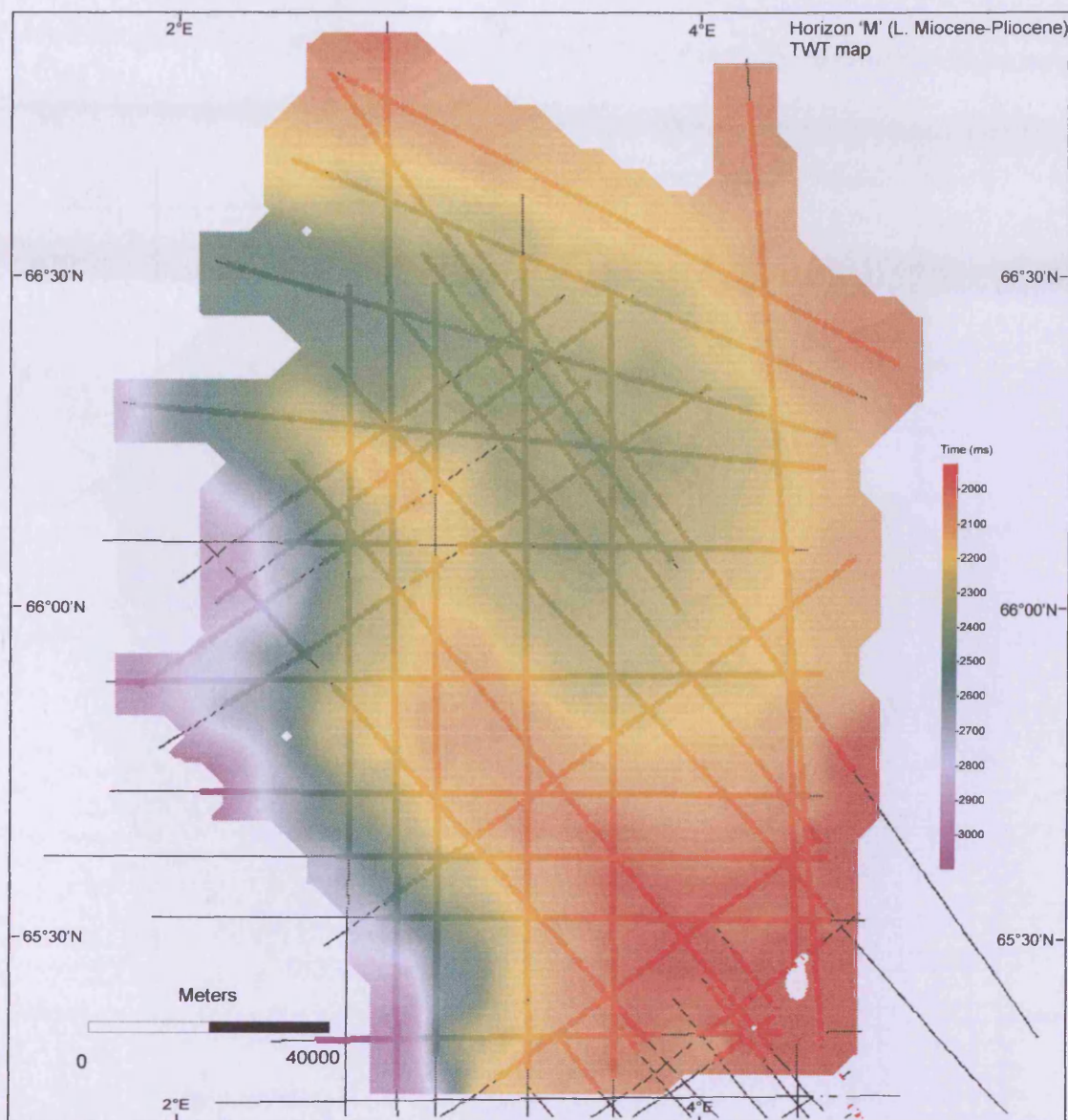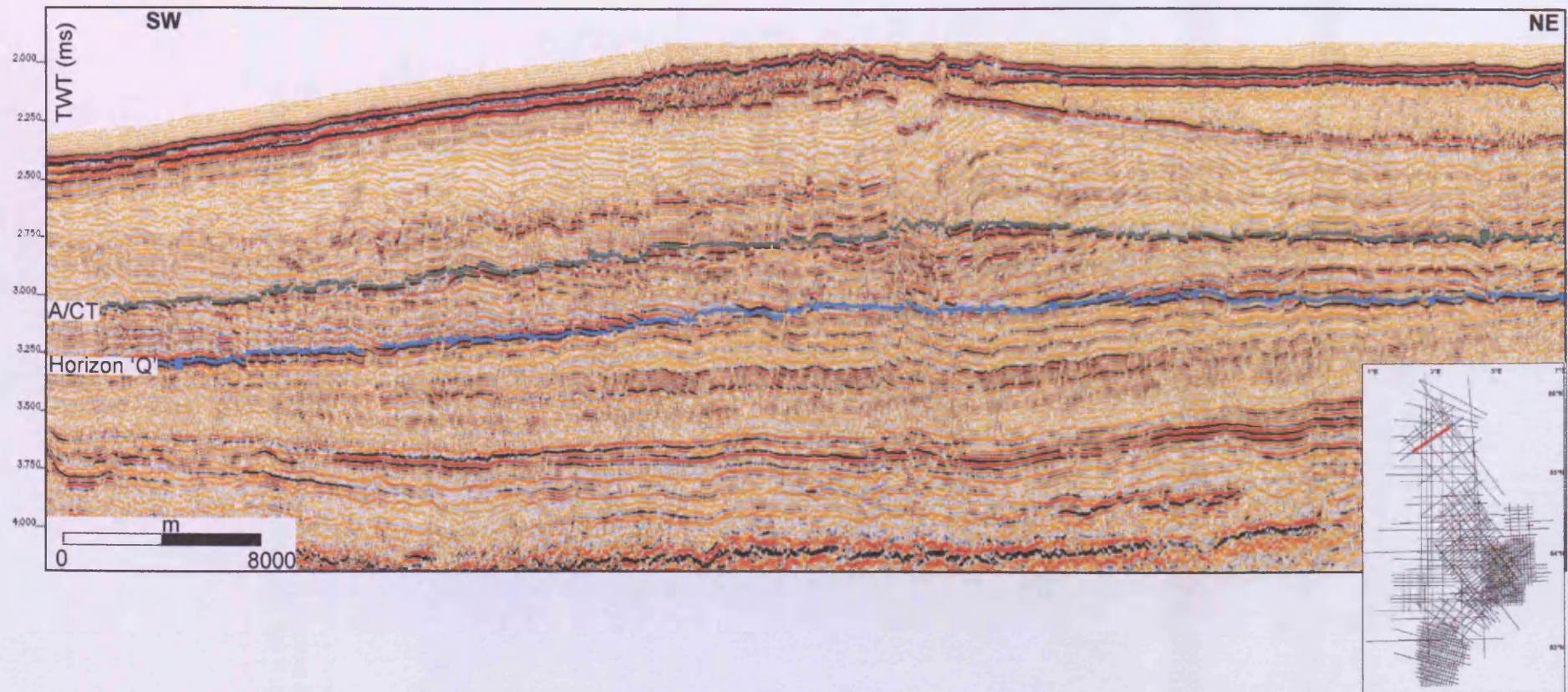
A3.8. Surface map of the two — way travel time (ms) of the reflection from Horizon 'M'. The map is based on the interpolation of the interpreted reflection TWT over a grid of 2 – D seismic lines.
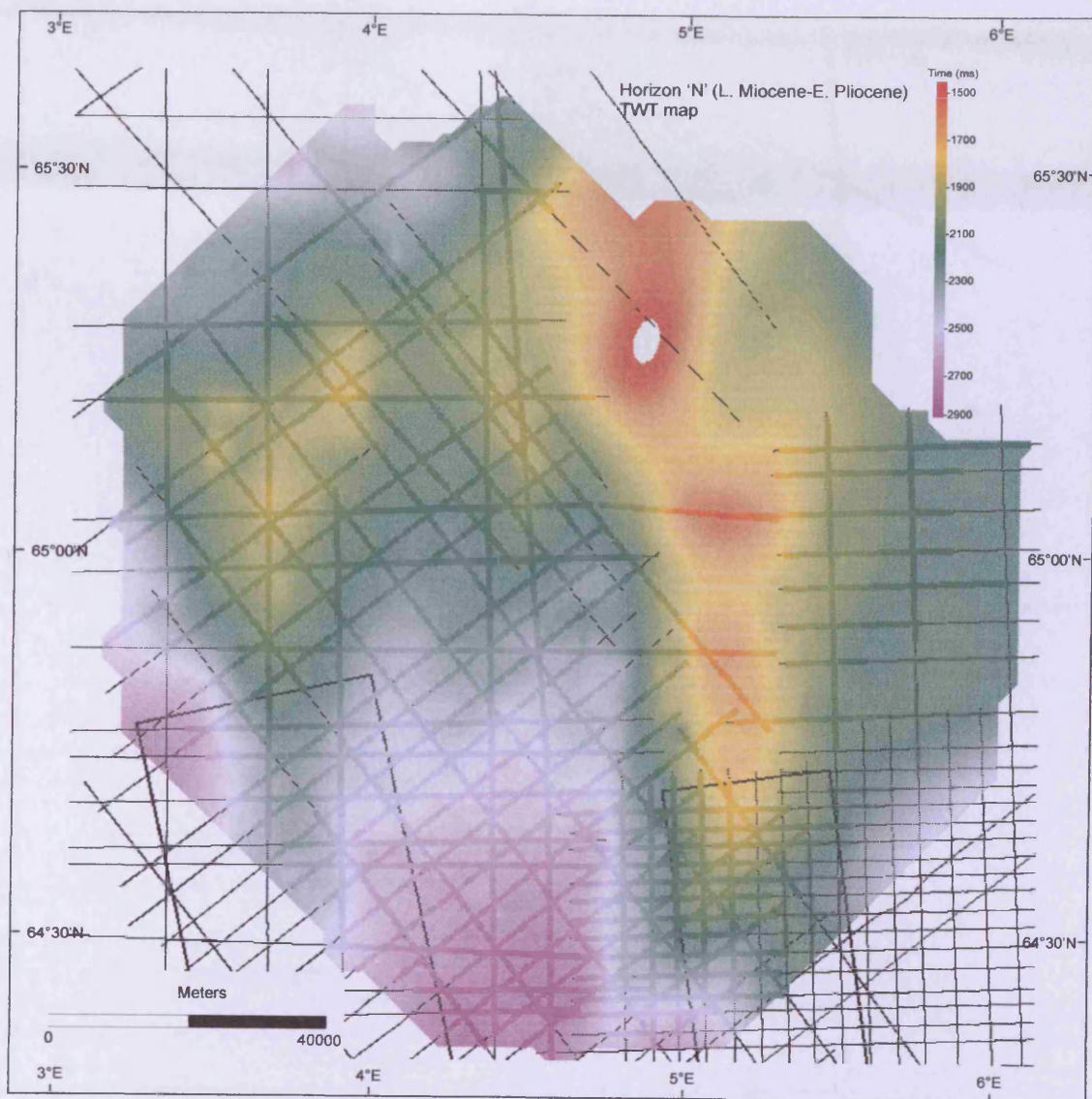
A3.9. Surface map of the two — way travel time (ms) of the reflection from Horizon 'N'. The map is based on the interpolation of the interpreted reflection TWT over a grid of 2 – D seismic lines.
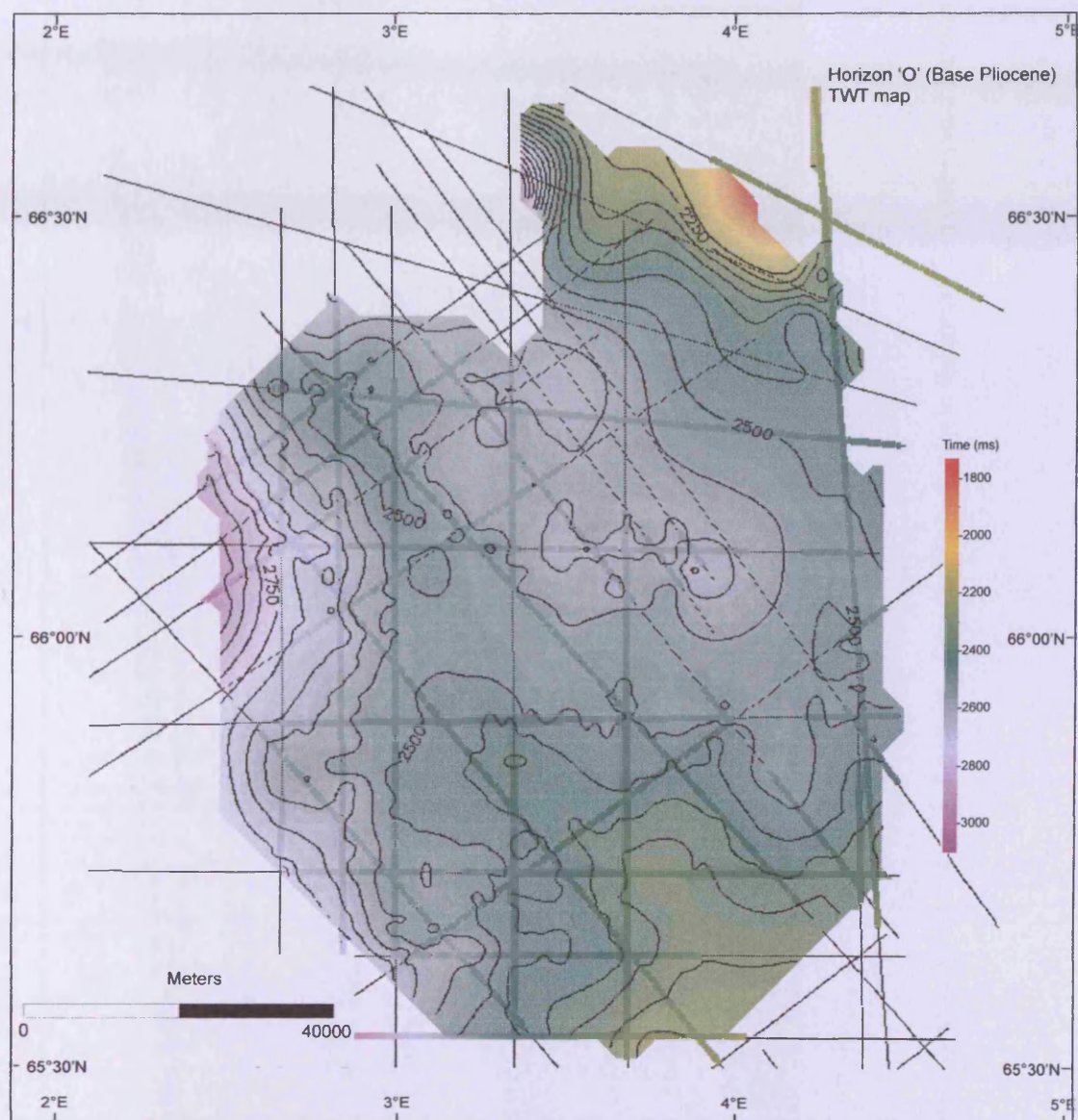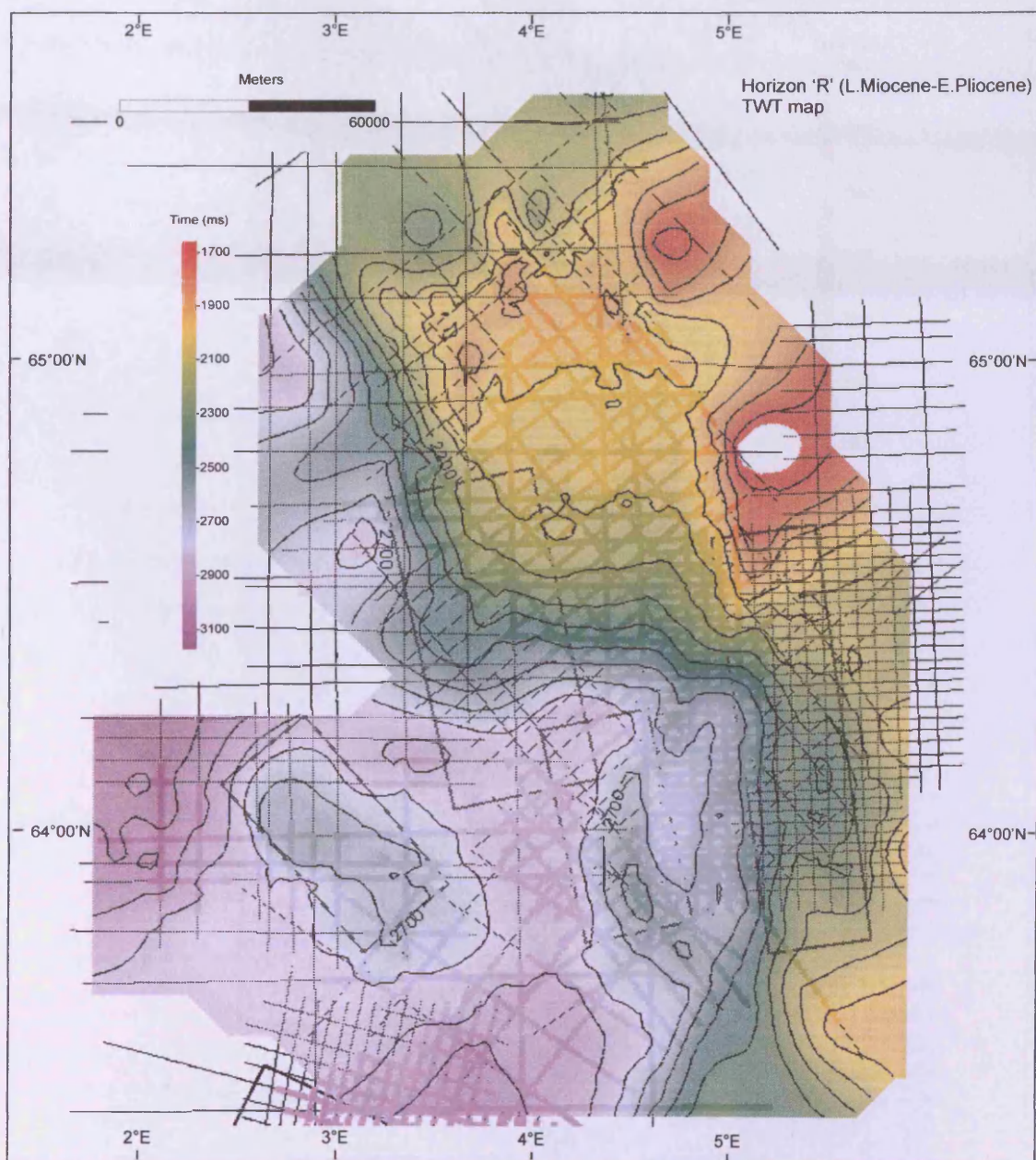
A3.10. Surface map of the two — way travel time (ms) of the reflection from Horizon 'O'. The map is based on the interpolation of the interpreted reflection TWT over a grid of 2 – D seismic lines.
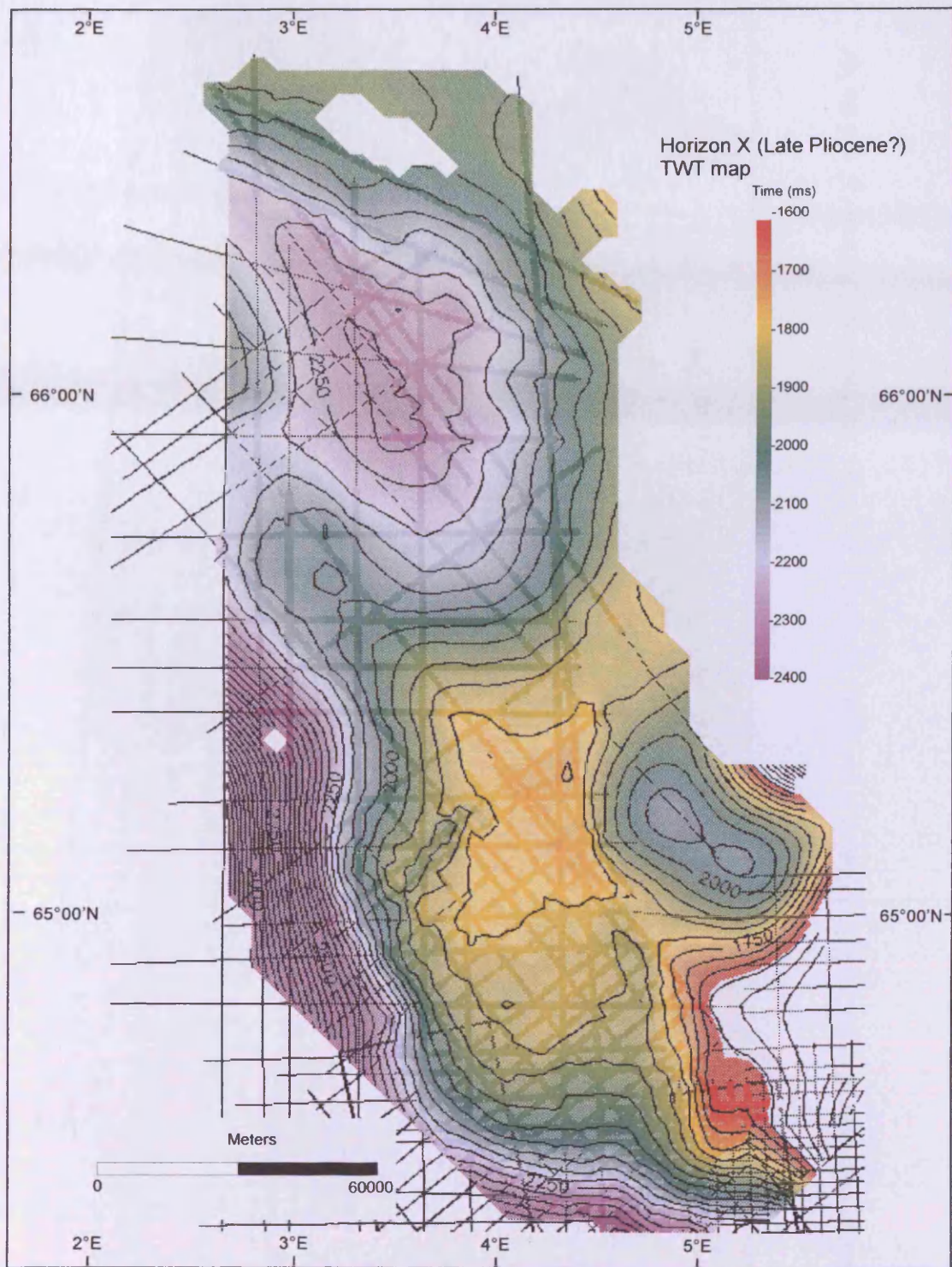
A3.11. Seismic profile from the northern study area (P1 on Fig. 6.1). Location of the profile is shown in the insert. The interpreted horizon 'O' and the 'A/CT' reflection are marked.

A3.12. Surface map of the two — way travel time (ms) of the reflection from Horizon 'P'. The map is based on the interpolation of the interpreted reflection TWT over a grid of 2 – D seismic lines.
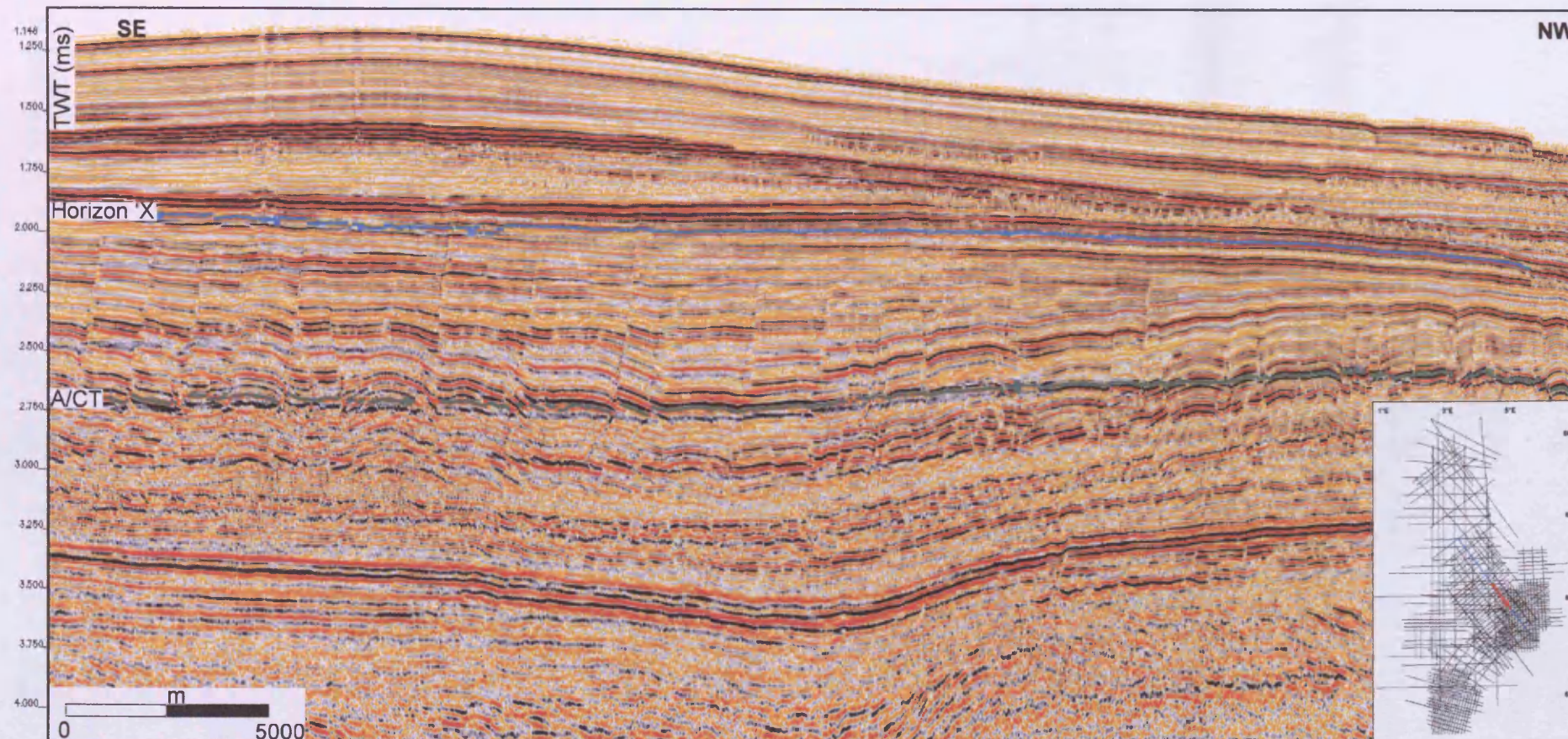
A3.13. Surface map of the two — way travel time (ms) of the reflection from Horizon 'Q'. The map is based on the interpolation of the interpreted reflection TWT over a grid of 2 – D seismic lines.

A3.14. Seismic profile from the northern study area (P1 on Fig. 6.1). Location of the profile is shown in the insert. The interpreted horizon 'Q' and the 'A/CT' reflection are marked. Note the concordance between the two horizons and the fact that both crosscut the hosting stratigraphy.

251

A3.15. Surface map of the two — way travel time (ms) of the reflection from Horizon 'R'. The map is based on the interpolation of the interpreted reflection TWT over a grid of 2 – D seismic lines.
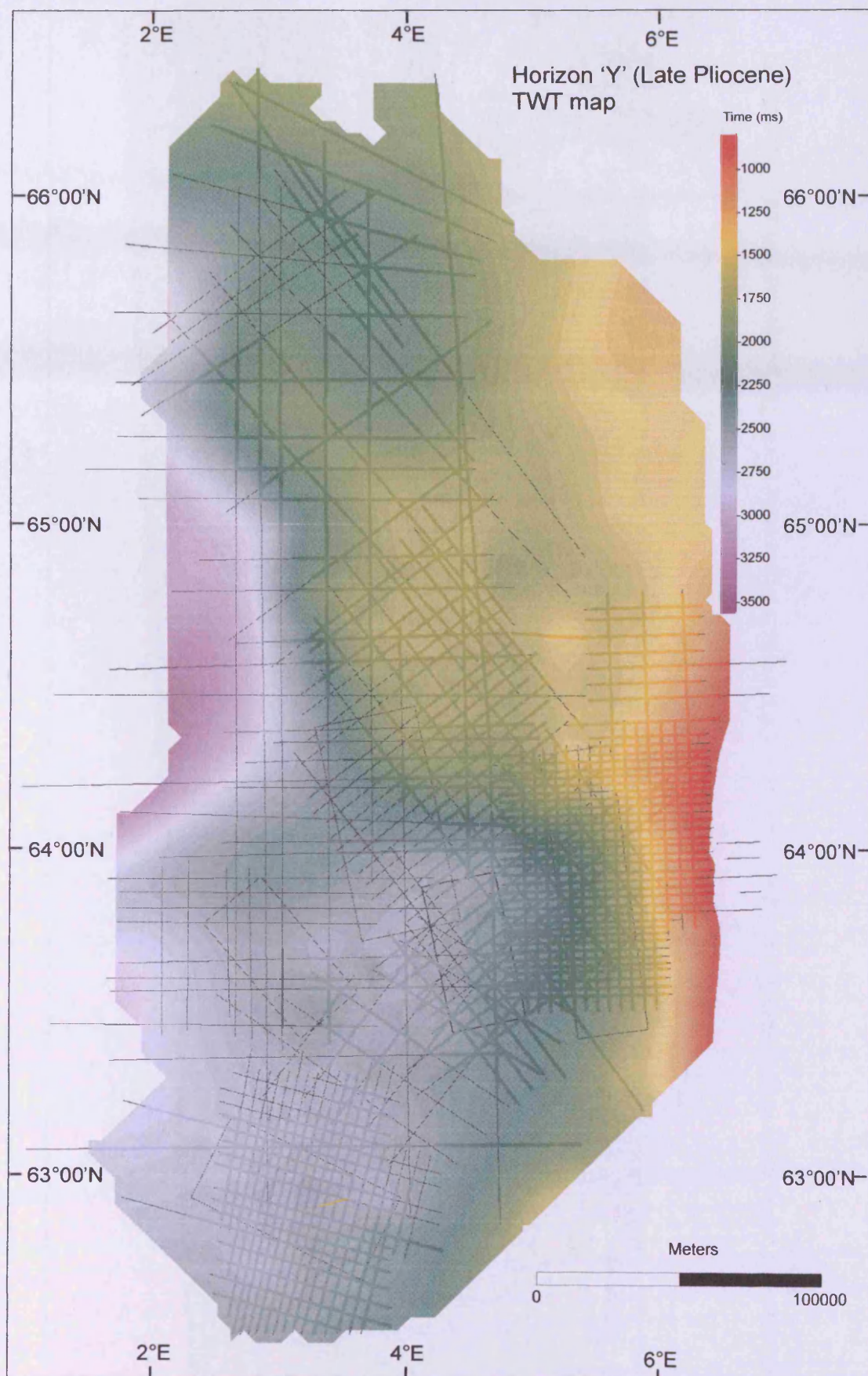
A3.16. Surface map of the two — way travel time (ms) of the reflection from Horizon 'X'. The map is based on the interpolation of the interpreted reflection TWT over a grid of 2 – D seismic lines.
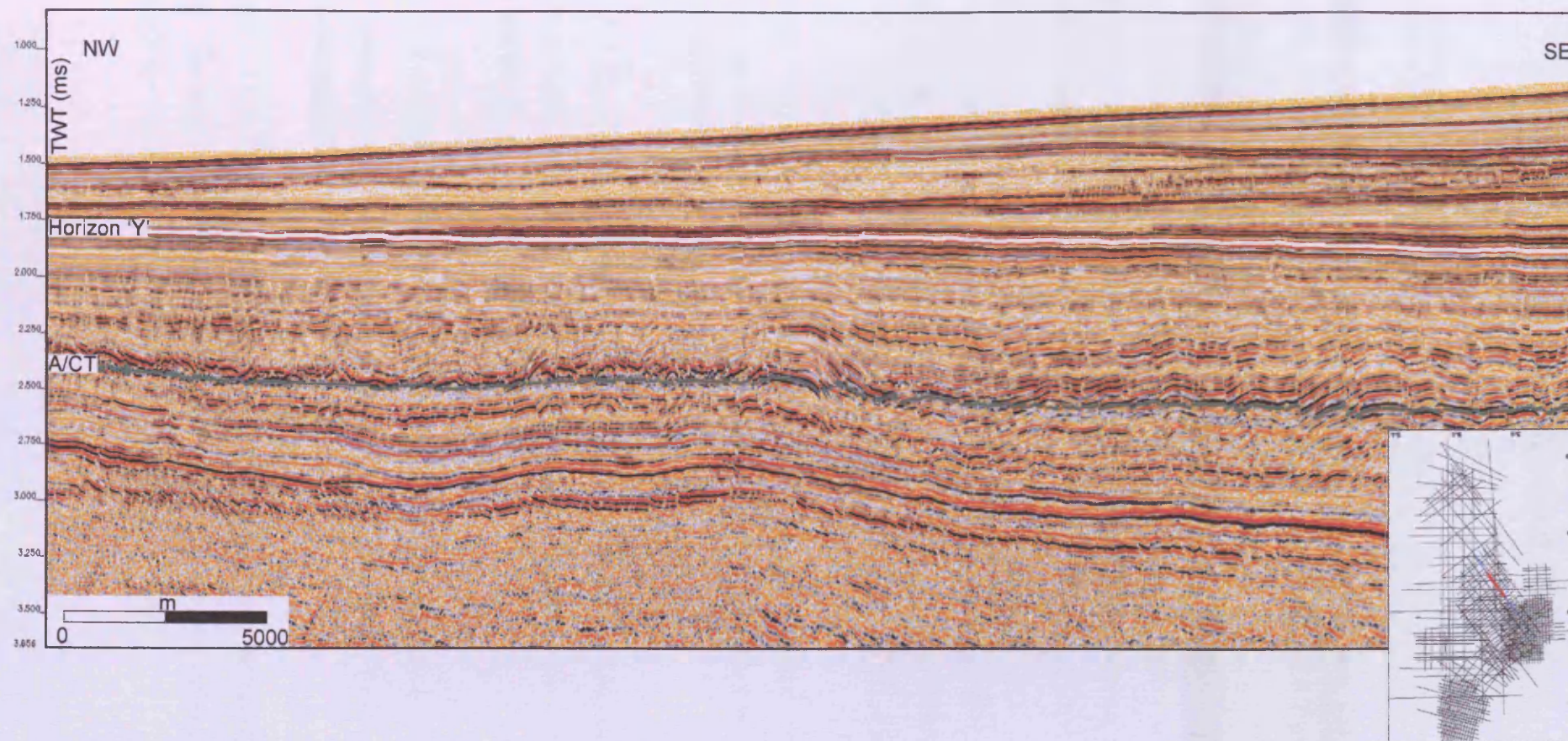
A3.17. Seismic profile from the central study area (P2.1 on Fig. 6.1). Location of the profile is shown in the insert. The interpreted horizon 'X' and the 'A/CT' reflection are marked.

Horizon 'Y' (Late Pliocene)
TWT map

Time (ms)

A3.18. Surface map of the two — way travel time (ms) of the reflection from Horizon 'Y'.
The map is based on the interpolation of the interpreted reflection TWT over a grid of 2 – D
seismic lines.

255

A3.19. Seismic profile from the northern study area (P1 on Fig. 6.1). Location of the profile is shown in the insert. The interpreted horizon 'Y' and the 'A/CT' reflection are marked.

Appendix A3 Digital Files

Located on the attached CD.

A3.5.1. Contour map of the two – way travel time of the Top Kai reflection. The map is based on the interpolation of the interpreted reflection TWT over a grid of 2 – D seismic lines. The contour interval is 50 ms.

A3.5.2. Seismic profile from the northern study area (P1 on Fig. 6.1). Location of the profile is shown in the insert. The interpreted horizon 'Top Kai' and the 'A/CT' reflection are marked.

A3.6.1. Contour map of the two – way travel time of the Top Kai reflection in P3 area of Fig. 6.1. The map is based on the interpolation of the interpreted reflection TWT over a grid of 2 – D seismic lines. The contour interval is 25 ms.

A3.6.2. Seismic profile from the southern study area (province P3 on Fig. 6.1). Location of the profile is shown in the insert. The interpreted horizon 'Top Kai' and the 'A/CT' reflection are marked.

A3.7.1. Contour map of the two – way travel time of the Top Brygge reflection. The map is based on the interpolation of the interpreted reflection TWT over a grid of 2 – D seismic lines. The contour interval is 100 ms.

A3.7.2. Seismic profile from the central study area (provinceP2.2 on Fig. 6.1). Location of the profile is shown in the insert. The interpreted horizon 'Top Brygge' and the 'A/CT' reflection are marked.

A3.8.1. Contour map of the two – way travel time of the reflection from Horizon 'M'. The map is based on the interpolation of the interpreted reflection TWT over a grid of 2 – D seismic lines. The contour interval is 100 ms.

A3.8.2. Seismic profile from the northern study area (P1 on Fig. 6.1). Location of the profile is shown in the insert. The interpreted horizon 'M' and the 'A/CT' reflection are marked.

A3.9.1. Contour map of the two – way travel time of the reflection from Horizon 'N'. The map is based on the interpolation of the interpreted reflection TWT over a grid of 2 – D seismic lines. The contour interval is 50 ms.

A3.9.2. Seismic profile from the central study area (P2.1 on Fig. 6.1). Location of the profile is shown in the insert. The interpreted horizon 'N' and the 'A/CT' reflection are marked.

A3.10.1. Contour map of the two – way travel time (ms) of the reflection from Horizon 'O'. The map is based on the interpolation of the interpreted reflection TWT over a grid of 2 – D seismic lines. The contour interval is 50 ms.

A3.12.1. Contour map of the two – way travel time of the reflection from Horizon 'P'. The map is based on the interpolation of the interpreted reflection TWT over a grid of 2 – D seismic lines. The contour interval is 100 ms.

A3.12.2. Seismic profile from the northern study area (P1 on Fig. 6.1). Location of the profile is shown in the insert. The interpreted horizon 'P' and the 'A/CT' reflection are marked.

A3.13.1. Contour map of the two – way travel time of the reflection from Horizon 'Q'. The map is based on the interpolation of the interpreted reflection TWT over a grid of 2 – D seismic lines. The contour interval is 50 ms.

A3.15.1. Contour map of the two – way travel time of the reflection from Horizon 'R'. The map is based on the interpolation of the interpreted reflection TWT over a grid of 2 – D seismic lines. The contour interval is 100 ms.

A3.15.2. Seismic profile from the central study area (P2.1 on Fig. 6.1). Location of the profile is shown in the insert. The interpreted horizon 'R' and the 'A/CT' reflection are marked.

A3.16.1. Contour map of the two – way travel time of the reflection from seismic Horizon 'X'. The map is based on the interpolation of the interpreted reflection TWT over a grid of 2 – D seismic lines. The contour interval is 50 ms.

A3.18.1. Contour map of the two – way travel time of the reflection from Horizon 'Y'. The map is based on the interpolation of the interpreted reflection TWT over a grid of 2 – D seismic lines. The contour interval is 100 ms.
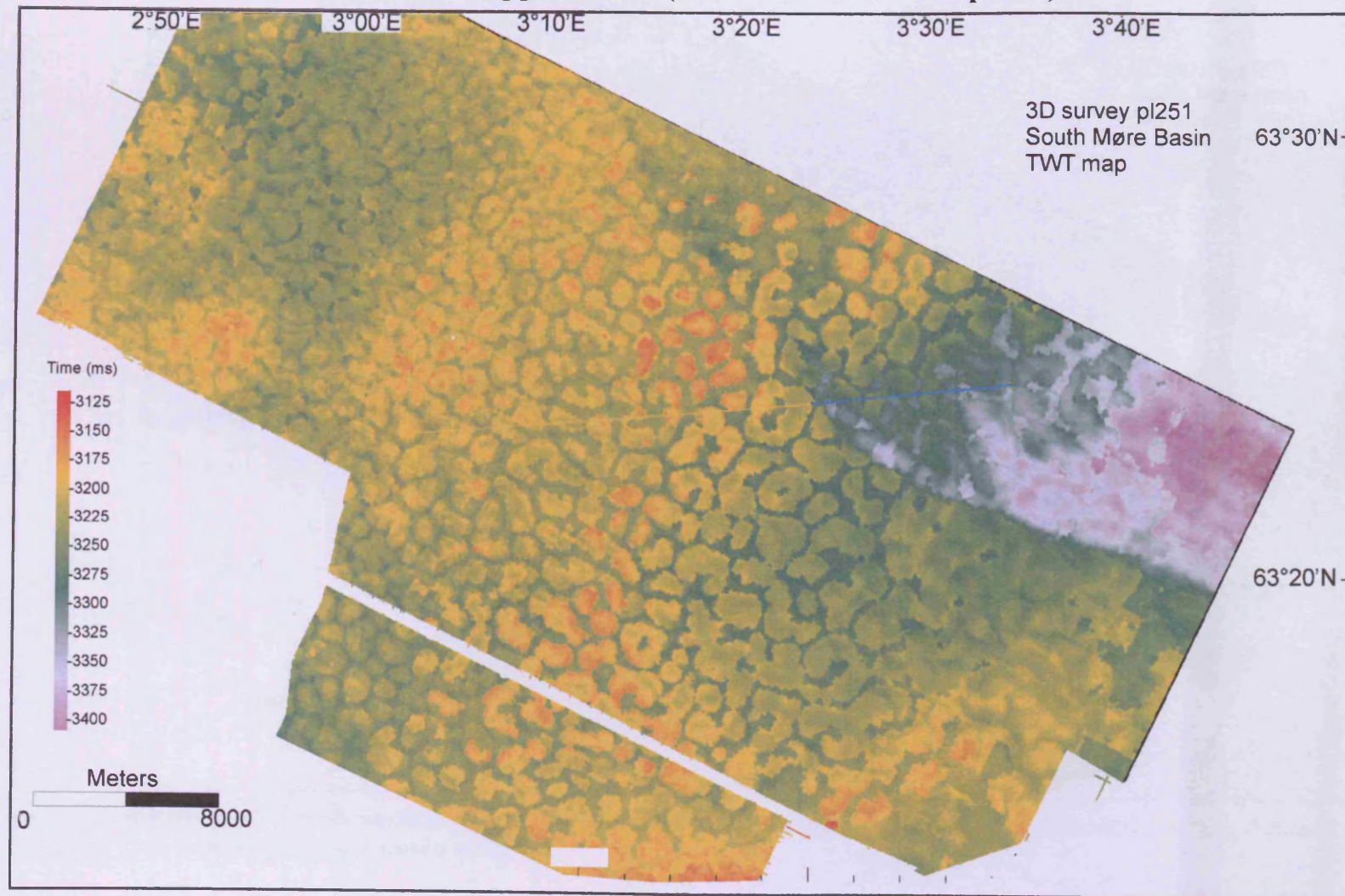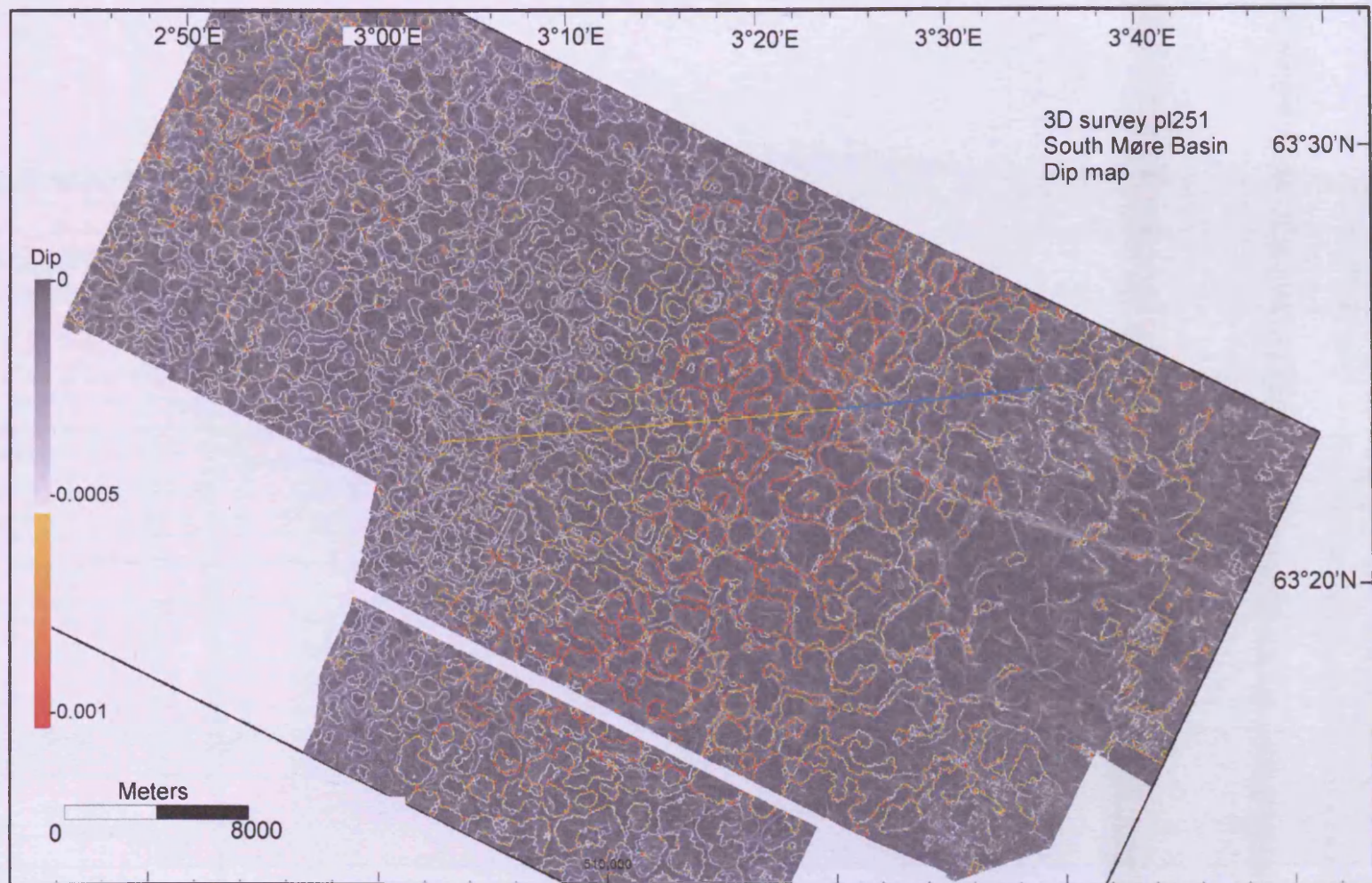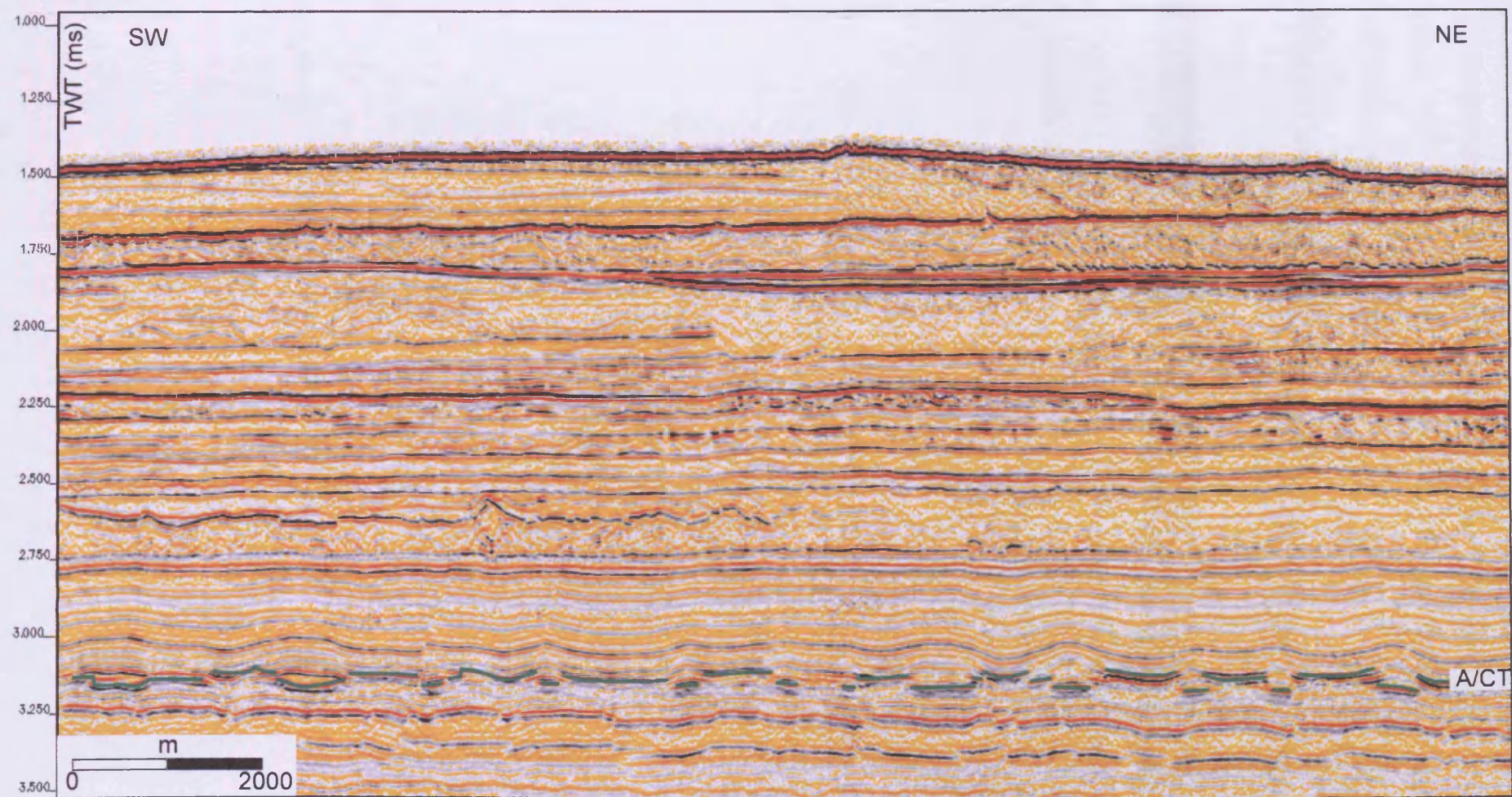
A4.1. Surface map of the TWT of the A/CT reflection in the pl251 seismic survey. Location of the survey was shown in Fig. 2.1.

A4.2. Dip map of the A/CT reflection from the pl251 seismic survey. Note the particular morphology of the A/CT surface, formed by cells separated by troughs. Location of the survey was shown in Fig. 2.1.

A4.3. Seismic profile from the pl251 seismic survey. Location of the profile is shown on the map in A4.1. The green line marks the interpreted A/CT reflection.

Appendix A5.

'Measurement of diagenetic compaction strain from quantitative analysis of fault plane dip'. Raluca Cristina Neagu, Joe Cartwright, Richard Davies. Journal of Structural Geology 32 (2010), 641 – 655. *(loose copy attached & digital copy available on CD)*

Appendix A6.

'Fossilisation of a silica diagenesis reaction front on the mid – Norwegian margin'. Raluca Cristina Neagu, Joe Cartwright, Richard Davies, Lars Jensen. Marine and Petroleum Geology 27 (2010), 2141 – 2155. *(loose copy attached & digital copy available on CD)*